

The Pennsylvania State University
The Graduate School
Department of Chemical Engineering

**CLEANUP OF BIOMASS GASIFICATION EFFLUENT
USING M-DOPED CERIA CATALYSTS**

A Dissertation in
Chemical Engineering
by
Matthew D. Krcha

© 2014 Matthew D. Krcha

Submitted in Partial Fulfillment
of the Requirements
for the Degree of

Doctor of Philosophy

August 2014

The dissertation of Matthew D. Krcha was reviewed and approved* by the following:

Michael J. Janik
Associate Professor of Chemical Engineering
Dissertation Advisor
Chair of Committee
Director of Graduate Program

Robert M. Rioux
Frederich G. Helfferich Associate Professor of Chemical Engineering

Scott T. Milner
Joyce Chair and Professor of Chemical Engineering

Adri C.T. van Duin
Associate Professor of Mechanical Engineering

*Signatures are on file in the Graduate School

ABSTRACT

Biomass conversion to liquid fuels may be accomplished through gasification to syngas followed by fuel synthesis processes, enabling a renewable energy source of liquid fuels. Prior to fuel synthesis catalysis, the syngas must be cleaned of sulfur and tar species. In a Department of Energy forecast for 2012, approximately 50% of the cost to produce ethanol through biomass gasification is involved in syngas cleanup. A tar reforming catalyst that can operate at high gasifier effluent temperatures and tolerate or, ideally act as a sulfur sorbent as well would help to reduce this cost associated with syngas cleanup. Ceria-based mixtures have shown promise in being able to reform hydrocarbons and remove sulfur at high temperatures.

This dissertation employs computational chemistry methods to design a ceria-based catalyst that can reform hydrocarbons into CO and H₂ as well as remove sulfur at high temperatures, thus making biomass gasification-based processes viable. Density functional theory (DFT+*U*) is used to generate structure-composition-function relationships for H₂S adsorption and hydrocarbon conversion. Transition metals can be doped into ceria to alter its reducibility and hydrocarbon activity. Considering all of the transition metals, we find the methane adsorption energy correlates with the oxygen vacancy formation energy for M-doped CeO₂. Using this correlation, the methane conversion rate follows a volcano relationship with surface reducibility. One of the dopants near the top of this volcano relationship is Mn, and to correctly represent the electronic structure of Mn-doped ceria, a correction to the energy of electrons in localized Mn *d*-states must be used. We utilized Mn-doped ceria as a system of focus to evaluate how this correction parameter, as well as the concentration and structure of Mn in the surface, affects the hydrocarbon activity. Employing the most stable structure of Mn-doped ceria and Zr-doped ceria, the reforming of propane over the surfaces are examined, along with developing an approach to model the complete oxidation of large hydrocarbons over an oxide. To clean up the effluent from biomass gasification, sulfur must also be removed and Mn-doped ceria also shows promise in being able to remove sulfur.

TABLE OF CONTENTS

List of Figures	vii
List of Tables	xviii
Acknowledgements.....	xx
Chapter 1 Introduction – Ceria for Biomass Gasification Effluent Cleanup	1
1.1. Background.....	1
1.2. Summary of Chapters.....	6
1.3. References.....	10
Chapter 2 Challenges in the Use of Density Functional Theory to Examine Catalysis by M-Doped Ceria Surfaces.....	14
2.1. Introduction.....	15
2.2. Challenges in representing M-doped CeO ₂ redox catalysis	17
2.3. DFT+U	19
2.4. Including a <i>U</i> -value on the <i>d</i> -states of transition metal dopants in CeO ₂	23
2.5. Hybrid functionals.....	26
2.6. Conclusions.....	27
2.7. References.....	29
Chapter 3 Periodic Trends of Oxygen Vacancy Formation and C-H Bond Activation over Transition Metal-Doped CeO ₂ (1 1 1) Surfaces	32
3.1. Introduction.....	33
3.2. Methods.....	36
3.2.1. Electronic structure method.....	36
3.2.2. Surface models	38
3.2.3. Oxygen vacancy formation energy.....	40
3.2.4. Methane dissociative adsorption energy	41
3.2.5. Methane activation barriers	42
3.3. Results and discussion	43
3.3.1 Correlation of C-H bond activation and surface reducibility	43
3.3.2. Density of States and Orbital Imaging	46
3.3.3. Site projected charge method	53
3.3.4. Periodic trends in dopant effects on surface reducibility	54
3.3.5. Implications for hydrocarbon conversion catalysis over M-doped CeO ₂ (1 1 1)	67
3.4. Conclusions.....	68
3.5. References.....	70
Chapter 4 Examination of Oxygen Vacancy Formation in Mn-Doped CeO ₂ (1 1 1) using DFT+ <i>U</i> and the Hybrid Functional HSE06	75
4.1. Introduction.....	76

4.2. Methods.....	79
4.2.1. Electronic structure method.....	79
4.2.2. Surface models	81
4.2.3. Surface formation energies.....	83
4.2.4. Oxygen vacancy formation energy.....	85
4.2.5. Determination of oxidation states.....	86
4.3. Results and Discussion.....	87
4.3.1. Assigning a Hubbard U -term to the d-states of Mn	87
4.3.2. Corroborating the U -value on Mn by comparison to the HSE06 hybrid functional.....	94
4.3.3. Mn concentration and distribution effects.....	95
4.4. Conclusions.....	105
4.5. References.....	106
 Chapter 5 Catalytic Propane Reforming Mechanism over Zr-Doped CeO ₂ (1 1 1).....	 109
5.1. Introduction.....	110
5.2. Methods.....	113
5.2.1. Electronic structure method.....	113
5.2.2. Surface models	115
5.2.3. Reaction Energies.....	117
5.2.4. Free Energies.....	119
5.2.5. Mechanistic choice for H* location and H ₂ O* desorption.....	120
5.2.6. Reaction path sequence determination	121
5.2.7. Initial condition of the catalyst before decomposition	122
5.3. Results and discussion	123
5.3.1. Propane oxidation in an oxidizing environment (0.1 atm O ₂).....	123
5.3.2. Propane oxidation in a reducing environment (1x10 ⁻¹⁷ atm O ₂).....	127
5.3.3. Propane oxidation under extremely reducing conditions (8x10 ⁻²² atm O ₂)	129
5.3.4. Extent of surface reduction under the reforming environment.....	132
5.3.5. Desorb hydrogen atoms as H ₂ or H ₂ O.....	137
5.4. Conclusions.....	140
5.5. References.....	141
 Chapter 6 Catalytic Propane Reforming Mechanism over Mn-Doped CeO ₂ (1 1 1).....	 145
6.1. Introduction.....	146
6.2. Methods.....	149
6.2.1. Electronic structure method.....	149
6.2.2. Surface models	150
6.2.3. Reaction and Free Energies.....	152
6.2.4. Results from Zr-doped Paper	152
6.3. Results and discussion	153
6.3.1. Propane reforming in an oxidizing environment (0.1 atm O ₂).....	153
6.3.2. Propane reforming in a reducing environment (1x10 ⁻¹⁷ atm O ₂).....	157
6.3.3. Propane reforming in an extremely reducing environment (8x10 ⁻²² atm O ₂)	159
6.3.4. Differences between Mn- and Zr-doped CeO ₂	161
6.3.5. Desorption of intermediates and electronic structure analysis	162

6.4. Conclusions.....	165
6.5. References.....	166
Chapter 7 Ce-Mn Oxides for High-Temperature Gasifier Effluent Desulfurization	170
7.1. Introduction.....	171
7.2. Methods.....	172
7.3. Results and Discussion.....	173
7.3.1. Experimental Results.....	173
7.3.2. DFT Results.....	176
7.4. Conclusions.....	183
7.5. References.....	184
Chapter 8 Alkane Reforming on Partially Sulfided CeO ₂ (1 1 1) Surfaces	188
8.1. Introduction.....	189
8.2. Methods.....	192
8.2.1. Electronic structure method.....	192
8.2.2. Surface models	193
8.2.3. Reaction Energies.....	196
8.2.4. Determination of oxidation states.....	198
8.3. Results and discussion	198
8.3.1. Initial C-H bond activation.....	198
8.3.2. Complete methane dehydrogenation with and without sulfur present	205
8.3.3. Electronic structure analysis during dehydrogenation on CeO ₂	212
8.3.4. Initial reforming of propane over a sulfided surface	215
8.4. Conclusions.....	216
8.5. References.....	218
Chapter 9 Summary, Conclusions, and Recommendations for Future Study.....	221
9.1. Hydrocarbon activity on M-doped CeO ₂ (1 1 1) surfaces.....	221
9.2. Effect of sulfur in effluent from biomass gasification	226
9.3. Perspectives and Suggestions for Future Studies.....	227
9.4. References.....	233
Appendix A Supplemental Material for Chapter 3	234
A.1. Site Projected Charge Method.....	238
A.2. Structural Assignment Categorization Scheme	242
Appendix B Supplemental Material for Chapter 4.....	251
Appendix C Supplemental Material for Chapter 5.....	253
Appendix D Supplemental Material for Chapter 6	269
Appendix E Supplemental Material for Chapter 8.....	275

LIST OF FIGURES

- Figure 1-1. Schematic of a typical biomass gasifier producing syngas (CO and H₂). (<http://www.steam-boilers.org/wp-content/uploads/2010/10/gasification-2.jpg>)3
- Figure 1-2. Cost to convert biomass into ethanol through biomass gasification. (U.S. Department of Energy Biomass Program, http://www1.eere.energy.gov/biomass/pdfs/biomass_deep_dive_pir.pdf)3
- Figure 2-1. Adsorbed intermediate (C₃H₅) in the oxidation of propane catalyzed by the surface of Mn-doped CeO₂ (1 1 1). The oxygen atoms associated with the hydrocarbon originate from the surface and remain associated with Ce atoms as well. The extent of electron localization on the Ce atoms due to the partial reduction will depend on DFT electronic structure approach used. Ce is displayed as tan (light), Mn as light blue (gray), and O as red (dark). 18
- Figure 2-2. Dissociative methane adsorption energy and surface oxygen vacancy formation energy versus U -value. (▲) pure CeO₂ (1 1 1) surface, (■) Zr-doped CeO₂ (1 1 1) surface, and (●) Pd-doped CeO₂ (1 1 1) surface. Closed circles represent oxygen vacancy formation energies and open circles represent methane adsorption energies. (Reproduced with permission from [ACS Publications], Mayernick et al., *J. Phys. Chem. C*. **2008**, 112, 14955)21
- Figure 2-3. (a) Total density of states for an oxygen vacant surface of pure CeO₂ (1 1 1) with no U -value on the f -states of ceria (upper) and a U -value of 5 eV on the f -states of Ce (lower). The double peak near the Fermi level in the bottom DOS is due to the slight asymmetry in the mirrored slab. Isodensity surface of an oxygen vacant surface of CeO₂ (1 1 1) (b) with no U -value on the f -states of ceria and (c) with a U -value of 5 eV on the f -states of ceria over the energy range -0.28 to 0.00 eV (relative to Fermi level). The isodensity surface with no U -value was taken to be an iso-change increase surface between the intact surface of ceria and the oxygen vacant surface of ceria.23
- Figure 2-4. (a) Total DOS for oxygen vacant Mn-doped CeO₂ (Mn²⁺) while varying the U -value on the d -states of Mn with a U -value of 5 eV on the f -states of Ce. (b) Surface oxygen vacancy formation energy vs. U -value on the d -states of Mn with a U -value of 5 eV on the f -states of Ce. Depending upon the U -value on the d -states of Mn, Mn reduces to different oxidation states (local minimum energy structures) upon formation of an oxygen vacancy. Mn reducing to: (◆) Mn³⁺, (■) Mn²⁺, and (▲) Mn⁴⁺ upon formation of an oxygen vacancy. (—) best fit line. (Adapted with permission from [ACS Publications], Krcha et al., *Langmuir* **2013**, 29 10120)25
- Figure 3-1. Side and top views of the slab model of M-doped CeO₂ (1 1 1). Ce is displayed as tan (light), M-dopant as light blue (gray), and O as red (dark). The three nearest neighbors (NN) and the next nearest neighbor (NNN) oxygen atom to the dopant are labeled.39
- Figure 3-2. Methane dissociative adsorption energy (ΔE_{ads}) vs. oxygen vacancy formation energy (ΔE_{vac}). The point for pure CeO₂ (1 1 1) is labeled as a square. The energy to

- refill oxygen vacancies ($-\Delta E_{vac} = \Delta E_{refill}$) from $O_2(g)$ at 0 K is greater than the methane activation barrier to the left of the dashed line.....45
- Figure 3-3. Total DOS plotted versus energy (referenced to Fermi level) for (a) intact Ag-doped CeO_2 (1 1 1), and (b) oxygen vacant Ag-doped CeO_2 (1 1 1). Spin-down density of states is plotted on the negative y axis. (c) Isodensity surfaces representing electronic states for oxygen vacant Ag-doped CeO_2 over the energy range -0.23 to 0.00 eV (relative to Fermi level).47
- Figure 3-4. Total DOS plotted versus energy (referenced to Fermi level) for (a) intact V-doped CeO_2 (1 1 1), and (c) oxygen vacant V-doped CeO_2 (1 1 1). Spin-down density of states is plotted on the negative y axis. Isodensity surfaces representing electronic states for (b) intact V-doped CeO_2 over the energy range -0.19 to 0.00 eV (relative to Fermi level) and (d) oxygen vacancy V-doped CeO_2 over the energy range -0.37 to 0.00 eV.49
- Figure 3-5. Total DOS plotted versus energy (referenced to Fermi level) for (a) intact Mn-doped CeO_2 (1 1 1), and (c) oxygen vacant Mn-doped CeO_2 (1 1 1). Spin-down density of states is plotted on the negative y axis. Isodensity surfaces representing electronic states for (b) intact Mn-doped CeO_2 over the energy range -0.87 to 0.00 eV (relative to Fermi level) and oxygen vacancy Mn-doped CeO_2 over the energy range (d) -1.06 to -0.66 eV and (e) -0.39 to 0.00 eV.51
- Figure 3-6. Total DOS plotted versus energy (referenced to Fermi level) for (a) intact Mn-doped CeO_2 (1 1 1), and (c) oxygen vacant Mn-doped CeO_2 (1 1 1) with Mn^{2+} . Spin-down density of states is plotted on the negative y axis. Isodensity surfaces representing electronic states for (b) intact Mn-doped CeO_2 over the energy range -0.90 to 0.00 eV (relative to Fermi level), and (d) oxygen vacancy Mn-doped CeO_2 with Mn^{2+} over the energy range -1.17 to 0.00 eV. These results were obtained with a U -value of 4.0 on the d -states of Mn, in addition to the U -value of 5 for Ce f -states.52
- Figure 3-7. Four common oxygen coordination environments about a M-dopant in CeO_2 (1 1 1). (a-c) represent fully-oxidized structures, whereas there is an oxygen vacancy in (d). (a) V coordinated in a trigonal pyramidal coordination, (b) Zr coordinated in a tetrahedral configuration, (c) Ag coordinated in a square planar configuration, and (d) Cd coordinated in a trigonal prismatic coordination. Ce is displayed as tan (light), M-dopant as light blue (gray), and O as red (dark). The O atoms labeled with X's would be in the first coordination shell of a Ce atom, but have rearranged such that they are at substantially larger distances than the first coordination shell O atoms of the dopant.55
- Figure 3-8. Periodic trends in the M-dopant electronic behavior upon the formation of a nearest neighbor surface oxygen vacancy or upon adsorption of $CH_3^* + H^*$ on M-doped CeO_2 (1 1 1).57
- Figure 3-9. Trends observed in M-doped CeO_2 (1 1 1) vacancy formation energies. (a) The vacancy formation energy (ΔE_{vac}) plotted versus M-dopant column in the periodic table. (◆) Row 4 dopants, (■) Row 5 dopants, and (▲) Row 6 dopants. (b) The range of vacancy formation energies (ΔE_{vac}) is illustrated grouped by whether the dopant

- reduces, both the dopant and one cerium atom reduces, or two cerium atoms reduce. The vacancy formation energies (ΔE_{vac}) are plotted versus (c) the dopant-oxygen bond enthalpy and (d) the atomic radii of the dopant atom. The vacancy formation energy for pure ceria is 2.76 eV. (—) best fit line.60
- Figure 3-10. (a) Initial state, (b) transition state, (c) pseudo-transition state and (d) final state (rotated 90°) for dissociative methane adsorption on the surface of Ag-doped CeO₂ (1 1 1). Ce is displayed as tan (light), M-dopant as light blue (gray), and O as red (dark).....64
- Figure 3-11. (a) A Brønsted-Evans-Polanyi relationship for the dissociative adsorption of methane on the surface of M-doped CeO₂ (1 1 1) for 10 selected dopants. For Ag, Ni, V, W, Zn and Zr both pseudo-transition states and true transition states are displayed (vanadium true and pseudo transition states are very close in energy and only show as one point). (b) Reaction energy diagram for the dissociative adsorption of methane over Ag-doped CeO₂. (c) Vacancy refilling energy and activation energy versus vacancy formation energy. Intersection between activation energy and vacancy refilling energy lines represents the point at which both vacancy refilling and methane activation require the same 0 K energy input. (◆) Pseudo-transition state, (■) true transition state, (----) best fit line for true transition states, (—) best fit line for pseudo-transition states, (— —) vacancy refilling line.....66
- Figure 4-1. Top and side views of the slab model of fully oxidized (intact) Mn-doped CeO₂ (1 1 1). (a) top view of $p(2 \times 2)$ unit expansion, (b) top view of $p(2 \times 3)$ unit expansion, (c) side view of $p(2 \times 2)$ unit expansion, and (d) side view of $p(2 \times 3)$ unit expansion. Ce is displayed as tan (light), Mn as light blue (gray), and O as red (dark).....82
- Figure 4-2. Surface oxygen vacancy formation energy vs. U -value on the d -states of Mn in a $p(2 \times 2)$ unit cell expansion with a 25% surface Mn concentration. Mn reduces to different oxidation states upon formation of an oxygen vacancy. Mn reducing to: (◆) Mn³⁺, (■) Mn²⁺, and (▲) Mn⁴⁺ upon formation of an oxygen vacancy. (—) best fit line.....88
- Figure 4-3. Possible spin arrangements after the formation of an oxygen vacancy in a mirrored $p(2 \times 2)$ unit cell expansion of a mirrored slab with a 25% surface Mn concentration. Each state represents a single occupied, localized Ce f or Mn d orbital. (a-h) Mn stays as Mn⁴⁺ (spin of 3) and two Ce atoms reduce per side, (i-m) Mn reduces to Mn³⁺ (spin of 4) and one Ce atom reduce per side, (n-o) Mn reduces to Mn²⁺ (spin of 5). Total spin of each system: (a, i, n) 10, (b, j) 8, (c, k) 6, (d, e) 4, (f, g, l) 2, (h, m, o) 0.....90
- Figure 4-4. Total DOS plotted versus energy (referenced to Fermi level) for (a) intact Mn-doped CeO₂ (1 1 1) with $U = 0$ eV on d -states of Mn (total spin of 6), and (c) intact Mn-doped CeO₂ (1 1 1) with $U = 4$ eV on d -states of Mn (total spin of 6). Spin-down density of states is plotted on the negative y axis. Isodensity surfaces representing electronic states for (b) intact Mn-doped CeO₂ with $U = 0$ eV on d -states of Mn over the energy range -0.87 to 0.00 eV (relative to Fermi level) and (d) intact Mn-doped CeO₂ with $U = 4$ eV on d -states of Mn over the energy range -4.93 to -4.23 eV.91

Figure 4-5. Total DOS plotted versus energy (referenced to Fermi level) for (a) oxygen vacant Mn-doped CeO₂ (1 1 1) with $U = 4$ eV on d -states of Mn and Mn reducing to Mn²⁺ (total spin of 10), and (c) oxygen vacant Mn-doped CeO₂ (1 1 1) with $U = 4$ eV on d -states of Mn and Mn reducing to Mn³⁺ (total spin of 6). Spin-down density of states is plotted on the negative y axis. Isodensity surfaces representing electronic states for (b) oxygen vacant Mn-doped CeO₂ with $U = 4$ eV on d -states of Mn and Mn reducing to Mn²⁺ over the energy range -0.34 to 0.00 eV (relative to Fermi level) and oxygen vacant Mn-doped CeO₂ with $U = 4$ eV on d -states of Mn and Mn reducing to Mn³⁺ over the energy range (d) -0.29 to 0.00 eV and (e) -5.59 to -5.78 eV. The X's represent the locations where the oxygen was removed.93

Figure 4-6. Four structures of a $p(2 \times 3)$ unit cell expansion of 2Mn-doped CeO₂ (1 1 1). (a) intact structure with Mn atoms diagonal to each other, (b) surface oxygen vacant structure with one Mn atom in a surface position and a second in a subsurface position in a row, (c) subsurface oxygen vacant structure with two Mn atoms in a surface short row, and (d) doubly surface oxygen vacant structure with two Mn atoms in a surface long row. Ce is displayed as tan (light), Mn as light blue (gray), and O as red (dark). The X's represent the locations where the oxygen was removed.97

Figure 4-7. First and second oxygen vacancy formation energies for Mn-doped CeO₂ (1 1 1) with $U = 4$ eV on d -states of Mn. The second oxygen vacancy energy is calculated relative to a structure with the first surface oxygen vacancy formed. (⊘) One surface oxygen vacancy, (⊞) One subsurface oxygen vacancy, (⊚) Two surface oxygen vacancies (⊛) One surface and one subsurface oxygen vacancy.....98

Figure 4-8. Formation energies for Mn-doped CeO₂ (1 1 1) and pure ceria at (a) 1000 K and $PO_2 = 10^{-13}$ atm and (b) 1000 K and $PO_2 = 10^{-18}$ atm. (⊘) Forming Mn-doped CeO₂ with 1 oxygen vacancy referencing an intact surface of CeO₂ (1 1 1), bulk CeO₂ and bulk MnO₂ (Equation 2 and chemical equation B), (⊞) forming 1 oxygen vacancy in CeO₂ (1 1 1) (Equation 3 and chemical equation C), (⊚) forming Mn-doped CeO₂ with 1 oxygen vacancy referencing an oxygen vacant surface of CeO₂ (1 1 1), bulk CeO₂ and bulk MnO₂ (Equation 4 and chemical equation D). The sum of (⊞) and (⊚) is (⊘).104

Figure 5-1. Side and top views of a $p(2 \times 3)$ unit cell expansion of Zr-doped CeO₂ (1 1 1). Ce is displayed at tan (light), Zr as light blue (gray) and O as red (dark)..... 116

Figure 5-2. Four selected structures of propane oxidation intermediates over Zr-doped CeO₂. (a) H*, (b) CH₃C*HCH₃, (c) C*H₂C*HC*H₂, (d) C*HC*C* (end C with 2 oxygens). Ce is displayed as tan (light), Zr as light blue (gray), O as red (dark). 124

Figure 5-3. Propane oxidation reaction energy diagram over the Zr-doped CeO₂ (1 1 1) surface in an oxidative environment (0.05 atm H₂O, 0.234 atm H₂, 0.1 atm O₂, 0.32 atm CO, 0.32 atm CO₂ and 0.1 atm propane at 1000 K). The blue (dark grey) denotes steps that are equivalent under more reducing environments in Figures 5-4 and 5-5..... 125

Figure 5-4. Propane oxidation reaction energy diagram over the Zr-doped CeO₂ (1 1 1) surface in a reducing environment (0.05 atm H₂O, 0.234 atm H₂, 1×10^{-17} atm O₂,

- 0.32 atm CO, 0.32 atm CO₂ and 0.1 atm propane at 1000 K). The blue (dark grey) denotes the steps that follow the same sequence regardless of oxidation conditions considered (equivalent in Figures 5-3 and 5-5) and the red (light grey) denotes steps that are equivalent under the more reducing conditions of Figure 5-5. 128
- Figure 5-5. Propane oxidation reaction energy diagram over the Zr-doped CeO₂ (1 1 1) surface under extremely reducing conditions (0.05 atm H₂O, 0.234 atm H₂, 8x10⁻²² atm O₂, 0.32 atm CO, 0.32 atm CO₂ and 0.1 atm propane at 1000 K). The blue (dark grey) denotes steps equivalent to the more oxidizing conditions used in Figures 5-3 – 5-5 and the red (light grey) denotes steps equivalent under the more oxidizing conditions in Figure 5-4. 131
- Figure 5-6. The energy to absorb ½ H₂ (g) onto the surface of Zr-doped CeO₂ (1 1 1) with varying number of surface oxygen vacancies and number of hydrogen atoms on the surface. The energy to absorb each hydrogen atom is calculated progressively in each step. The partial pressure of hydrogen is 0.234 atm and for oxygen is 6x10⁻²⁰ atm. The number of H* adsorbed in the 2x3 unit cell is denoted by bars of (white) 1 H*, (orange or lightest gray) 2 H*, (red or light gray) 3 H*, (green or medium gray) 4 H*, (purple or dark gray) 5 H*, (black) 6 H*..... 133
- Figure 5-7. The phase diagram for the number of hydrogen atoms absorbed and the number of surface oxygen vacancies present in a *p*(2 x 3) unit cell of pure CeO₂ (1 1 1) while varying the partial pressure of hydrogen and oxygen. The O represents the gas phase composition for the oxidizing case, R for the reducing case and ER for the extremely reducing case. (b) is zoomed in on the center of (a) to give a more detailed picture. 134
- Figure 5-8. The phase diagram for the number of hydrogen atoms absorbed and the number of surface oxygen vacancies present in a *p*(2 x 3) unit cell of Zr-doped CeO₂ (1 1 1) while varying the partial pressure of hydrogen and oxygen. The O represents the gas phase composition for the oxidizing case, R for the reducing case and ER for the extremely reducing case..... 135
- Figure 5-9. The pressure-temperature curves as to whether the hydrogen on the surface of Zr-doped ceria will desorb as H₂ or H₂O. (—) the division between whether the hydrogen will desorb as H₂ (below line) or H₂O (above line) based on the lower axis. The division on whether the hydrogen will desorb as (—) H₂, or (-----) H₂O, upper axis. Above the dotted/dashed lines, the hydrogen will exergonically desorb and below they will not. The X's represent the gas phase conditions considered in Sections 5.3.1-5.3.3 relative to whether H₂ or H₂O will desorb. The O's represent the conditions relative to the dotted/dashed lines indicating whether hydrogen desorption is exergonic. (a) represents the surface starting with 6 hydrogens absorbed on the surface (oxidizing and reducing conditions) and (b) represents the surface starting with 3 hydrogens and 3 surface oxygen vacancies (extremely reducing, gasifier effluent conditions)..... 139
- Figure 6-1. Side and top views of a *p*(2 x 3) unit cell expansion of Mn-doped CeO₂ (1 1 1). Ce is displayed at tan (light), Mn as light blue (gray) and O as red (dark). The X's represent the location of the oxygen vacancy. 151

- Figure 6-2. Four selected structures of propane reforming intermediates over Mn-doped CeO₂ (1 1 1). (a) CH₃C*HCH₃, (b) C*HC*CH₃, (c) C*HC*C*H (oxete like structure), (d) C*HC*C* (end C with 2 oxygens). Ce is displayed at tan (light), Mn as light blue (gray) and O as red (dark). 154
- Figure 6-3. Propane reforming reaction energy diagram over Mn-doped CeO₂ (1 1 1) surface in a oxidizing environment (0.05 atm H₂O, 0.234 atm H₂, 0.1 atm O₂, 0.32 atm CO, 0.32 atm CO₂ and 0.1 atm propane at 1000 K). The blue (dark grey) denotes steps that are equivalent under more reducing environments in Figures 6-4 and 6-5. 155
- Figure 6-4. Propane reforming reaction energy diagram over Mn-doped CeO₂ (1 1 1) surface in a reducing environment (0.05 atm H₂O, 0.234 atm H₂, 1x10⁻¹⁷ atm O₂, 0.32 atm CO, 0.32 atm CO₂ and 0.1 atm propane at 1000 K). The blue (dark grey) denotes the steps that follow the same sequence regardless of oxidation conditions considered (equivalent in Figures 6-3 and 6-5) and the red (light grey) denotes steps that are equivalent under the more reducing conditions of Figure 6-5. 158
- Figure 6-5. Propane reforming reaction energy diagram over Mn-doped CeO₂ (1 1 1) surface in an extremely reducing environment (0.05 atm H₂O, 0.234 atm H₂, 8x10⁻²² atm O₂, 0.32 atm CO, 0.32 atm CO₂ and 0.1 atm propane at 1000 K). The blue (dark grey) denotes steps equivalent to the more oxidizing conditions used in Figures 6-3 and 6-4 and the red (light grey) denotes steps equivalent under the more oxidizing conditions in Figure 6-4. 160
- Figure 6-6. Lewis structures for propane reforming over Mn-doped CeO₂ (1 1 1) in an oxidizing environment. Numbers near partial bonds represent the total of electrons associated with the partial bonds. 164
- Figure 7-1. Sulfur adsorption capacity at 903 K using a synthetic gasifier effluent with 32% CO₂. All capacities are the average of three cycle, not using the first cycle. Air regeneration was used at 873 K for 30 minutes. The numbers in parentheses are the wt% Al₂O₃ for supported materials. 175
- Figure 7-2. Normalized XANES spectra of Mn K pre-edge region. All samples were sulfided and reduced for several cycles prior to analysis. 176
- Figure 7-3. Side views of the surface unit cell for Mn-doped CeO₂ (1 1 1): (a) Intact 2 Mn-doped; (b) oxygen vacant 1 Mn-doped; (c) doubly oxygen vacant 2 Mn-doped; and (d) Sulfur adsorbed oxygen vacancy, 2 Mn-doped. Ce is displayed as tan (white), Mn as light blue (gray), O as red (dark), and S as yellow (light). 178
- Figure 8-1. Top and side views of the p(2 x 2) unit cell expansion of sulfided M-doped CeO₂ (1 1 1). (a) side view, and (b) top view. The X is the position of the subsurface oxygen vacancy (the X denotes an oxygen vacancy in front of the labeled oxygen). The oxygen /sulfur atoms 1-4 labels are used in referring to surface adsorbate positions. Ce is displayed at tan (light), M as light blue (light gray), O as red (dark) and S as yellow (dark gray)..... 194

- Figure 8-2. Four selected structures of hydrogen and a propyl derivative adsorbed onto the surfaces of sulfided and un-sulfided M-doped CeO₂. (a) H* (on O1) on the un-sulfided surface, (b) H* (on S1 (O1 position)) on the sulfided surface, (c) C*H₂C*HC*H₂ (on O1, O3, and O4) on the un-sulfided surface, (d) C*H₂C*HC*H₂ (on S1 (O1), O3, and O4) on the sulfided surface. Ce is displayed as tan (light), M as light blue (light gray), O as red (dark) and S as yellow (dark gray).....201
- Figure 8-3. Thermodynamic cycle decomposition of the steps involved in the abstraction of R₂ from R₁ forming a R₁ radical in the gas phase. On the sulfided case where R₂ is bound to a sulfur, the O would be replaced with S.202
- Figure 8-4. Reaction energy diagram of methane decomposition over sulfided and un-sulfided surfaces of pure CeO₂ (1 1 1). The solid lines represents each hydrogen abstraction (product desorption) on the un-sulfided surface and the dashed lines for the sulfided surface. For the pseudo-transition state (CH₃• + H*), the long dash represents H abstraction on a sulfur atom and the short dash represents on an oxygen atom.....207
- Figure 8-5. Structures of methane decomposition intermediates over (a-e) un-sulfided and (f-j) sulfided (1 1 1) surfaces of pure CeO₂. Isodensity surfaces representing isolated electron states on adsorbates are displayed in (b-c) and (g-i). The represent state appearing in the ceria band gap in the energy ranges of (b) -0.72 to -0.60 eV, (c) -1.24 to -1.10 eV, (g) -0.48 to -0.36 eV, (h) -0.55 to -0.35 eV, and (i) -0.36 to -0.13 eV (relative to the Fermi level). Total density of states for these structures are given as Figures E-9 and E-10. Ce is displayed as tan (light), O as red (dark), S as yellow (dark grey).209
- Figure 8-6. Reaction energy diagram of methane decomposition over sulfided and un-sulfided surfaces of Mn-doped CeO₂ (1 1 1). The solid lines represents each hydrogen abstraction (product desorption) on the un-sulfided surface and the dashed lines for the sulfided surface. For the pseudo-transition state (CH₃• + H*), the long dash represents H abstraction on a sulfur atom and the short dash represents on an oxygen atom.....211
- Figure 8-7. Lewis structures for methane decomposition surface intermediates over (a-e) surface oxygen atoms and (f-j) surface sulfur atoms over pure CeO₂ (1 1 1). Every image corresponds to the structure with the same letter displayed in Figure 8-5.213
- Figure 9-1. C-H activation of methane and CH₃• adsorption energies versus the oxygen vacancy formation energy of various oxide surfaces for oxidative coupling of methane. (◆) C-H activation energy of methane, (■) adsorption energy of CH₃•, (—) best fit line for C-H activation and CH₃• adsorption, (----) C₂H₆ formation energy in gas phase.232
- Figure A-2. Difference in number of electrons between a Ce⁴⁺ atom and Ce³⁺ atom (◆) and maximum variation of number of electrons counted for all Ce⁴⁺ (■) vs. the RWIGS value on Ce. An RWIGS value of 0.7 was used to determine which cerium atoms reduced in this study.239

- Figure A-3. Number of electrons around every cerium atom in a reduced CeO_2 (1 1 1) surface counted by the site projected method using an RWIGS value of 0.7 (■) and the Bader atoms-in-molecules method (◆). Ce atoms number 10 and 18 are Ce^{3+} and all others are Ce^{4+}240
- Figure A-4. Number of electrons counted in each orbital of the cerium atoms by the site projected charge method (RWIGS = 0.7). The number of s (◆), p (■) and d (▲) electrons is relatively constant, whereas the f (●) electron count changes significantly for the two Ce^{3+} atoms (10 and 18(for 18, the circle and square overlap)) and is relatively constant for all other non-reduced cerium atoms (Ce^{4+}).241
- Figure A-5. Five possible oxygen coordination environments about an intact M-dopant in CeO_2 (1 1 1). (a) Mn coordinated in pyramidal, (b) Ag coordinated in square planar, (c) V coordinated in trigonal pyramidal, (d) Zr coordinated in tetrahedral, and (e) Pd coordinated in octahedral. Ce is displayed as tan (light), M-dopant as light blue (gray), and O as red (dark). The oxygen atoms labeled with X's are the oxygen atoms not bonded, but are part of the 7 closest oxygen atoms.244
- Figure A-6. Six oxygen coordination environments with an oxygen vacancy in M-doped in CeO_2 (1 1 1). (a) Cu coordinated in T-shaped, (b) Fe coordinated in square planar, (c) Ni coordinated in trigonal pyramidal, (d) Hg coordinated in square pyramidal, (e) Ru coordinated in 4, and (f) Cd coordinated in trigonal prismatic. Ce is displayed as tan (light), M-dopant as light blue (gray), and O as red (dark). The oxygen atoms labeled with X's are the oxygen atoms not bonded, but are part of the 6 closest oxygen atoms.245
- Figure A-7. Seven oxygen coordination environments with methane dissociatively adsorbed on M-doped CeO_2 (1 1 1). (a) Os coordinated in see-saw, (b) Fe coordinated in square planar, (c) Ni coordinated in trigonal pyramidal, (d) Ru coordinated in square pyramidal, (e) W coordinated in 1, (f) Cr coordinated in 2, (g) Ir coordinated in octahedral. Ce is displayed as tan (light), M-dopant as light blue (gray), and O as red (dark). The oxygen atoms labeled with X's are the oxygen atoms not bonded, but are part of the 7 closest oxygen atoms.246
- Figure C-1. Structures for first 9 steps (excluding desorption of H^* as H_2O and refilling of the $\frac{1}{2} \text{V}_\text{O}$) to reform propane in an oxidizing environment. Ce is displayed as tan (light), Zr as light blue (gray), O as red (dark).....253
- Figure C-2. Structures for last 8 steps (excluding desorption of H^* as H_2O and refilling of the $\frac{1}{2} \text{V}_\text{O}$) to reform propane in an oxidizing environment. Ce is displayed as tan (light), Zr as light blue (gray), O as red (dark).....254
- Figure C-3. Structures for first 9 steps (excluding desorption of H^* as H_2O and refilling of the $\frac{1}{2} \text{V}_\text{O}$) to reform propane in a reducing environment. Ce is displayed as tan (light), Zr as light blue (gray), O as red (dark).....255

- Figure C-4. Structures for last 7 steps (excluding desorption of H^* as H_2O and refilling of the $\frac{1}{2} V_O$) to reform propane in a reducing environment. Ce is displayed as tan (light), Zr as light blue (gray), O as red (dark).....256
- Figure C-5. Structures for all of the steps (excluding desorption of H^* as H_2O and refilling of the $\frac{1}{2} V_O$) to reform propane under extremely reducing (gasifier effluent) conditions. Ce is displayed as tan (light), Zr as light blue (gray), O as red (dark).....257
- Figure C-6. Structures for hydrogen adsorption on an intact Zr-doped CeO_2 surface. Ce is displayed as tan (light), Zr as light blue (gray), O as red (dark).259
- Figure C-7. Structures for hydrogen adsorption on a Zr-doped CeO_2 surface with 1 oxygen vacancy. Ce is displayed as tan (light), Zr as light blue (gray), O as red (dark).260
- Figure C-8. Structures for hydrogen adsorption on a Zr-doped CeO_2 surface with 2 and 3 oxygen vacancy. Ce is displayed as tan (light), Zr as light blue (gray), O as red (dark).261
- Figure C-9. Structures for hydrogen adsorption on a Zr-doped CeO_2 surface with 4 and 5 oxygen vacancy. Ce is displayed as tan (light), Zr as light blue (gray), O as red (dark).262
- Figure C-10. The energy to absorb $\frac{1}{2} H_2$ (g) onto the surface of pure CeO_2 varying number of surface oxygen vacancies and number of hydrogen atoms on the surface. The energy to absorb each hydrogen atom is calculated progressively in each step. The partial pressure of hydrogen is 0.234 atm and for oxygen is 6×10^{-20} atm. (white) 1 hydrogens, (orange or lightest gray) 2 hydrogens, (red or light gray) 3 hydrogens, (green or medium gray) 4 hydrogens, (purple or dark gray) 5 hydrogens, (black) 6 hydrogens.263
- Figure C-11. The pressure-temperature curves as to whether the hydrogen on the surface of pure ceria will desorb as H_2 or H_2O for a pure ceria surface with 6 hydrogens. (—) the division between whether the hydrogen will desorb as H_2 (lower) or H_2O (upper) based on the lower axes. The division on whether the hydrogen will desorb as (—) H_2 , or (-----) H_2O , upper axes. Above these lines the hydrogen will desorb and below they will not. The X's represent the composition of the gas when the H_2 or H_2O will desorb and the O's represent the conditions if the hydrogen will desorb.264
- Figure C-12. Structures for hydrogen adsorption on an intact CeO_2 surface. Ce is displayed as tan (light), O as red (dark).265
- Figure C-13. Structures for hydrogen adsorption on a CeO_2 surface with 1 oxygen vacancy. Ce is displayed as tan (light), O as red (dark).266
- Figure C-14. Structures for hydrogen adsorption on a CeO_2 surface with 2 and 3 oxygen vacancy. Ce is displayed as tan (light), O as red (dark).267
- Figure C-15. Structures for hydrogen adsorption on a CeO_2 surface with 4, 5 and 6 oxygen vacancy. Ce is displayed as tan (light), O as red (dark).268

Figure D-1. Structures for the first 9 steps (excluding desorption of H* as H ₂ O and refilling of the ½ V _O) to reform propane in an oxidizing environment. Ce is displayed as tan (light), Zr as light blue (gray), O as red (dark).....	269
Figure D-2. Structures for the last 7 steps (excluding desorption of H* as H ₂ O and refilling of the ½ V _O) to reform propane in an oxidizing environment. Ce is displayed as tan (light), Zr as light blue (gray), O as red (dark).....	270
Figure D-3. Structures for the first 9 steps (excluding desorption of H* as H ₂ O and refilling of the ½ V _O) to reform propane in a reducing environment. Ce is displayed as tan (light), Zr as light blue (gray), O as red (dark).....	271
Figure D-4. Structures for the last 7 steps (excluding desorption of H* as H ₂ O and refilling of the ½ V _O) to reform propane in a reducing environment. Ce is displayed as tan (light), Zr as light blue (gray), O as red (dark).....	272
Figure D-5. Structures for the first 9 steps (excluding desorption of H* as H ₂ O and refilling of the ½ V _O) to reform propane under extremely reducing (gasifier effluent) conditions. Ce is displayed as tan (light), Zr as light blue (gray), O as red (dark).....	273
Figure D-6. Structures for the last 4 steps (excluding desorption of H* as H ₂ O and refilling of the ½ V _O) to reform propane under extremely reducing (gasifier effluent) conditions. Ce is displayed as tan (light), Zr as light blue (gray), O as red (dark).....	274
Figure E-1. Structures of the adsorption of H* onto the 4 surface oxygens in the un-sulfided surface of M-doped CeO ₂ . Ce is displayed as tan (light), M as light blue (gray) and O as red (dark).	275
Figure E-2. Structures of the reforming of methane on the un-sulfided surface of M-doped CeO ₂ . Ce is displayed as tan (light), M as light blue (gray) and O as red (dark). The X represents the position of the additional surface oxygen vacancy.	276
Figure E-3. Structures of the first three steps in the reforming of propane on the un-sulfided surface of M-doped CeO ₂ . Ce is displayed as tan (light), M as light blue (gray) and O as red (dark).	277
Figure E-4. Structures of the adsorption of H* onto the 4 surface oxygens in the sulfided surface of M-doped CeO ₂ . Ce is displayed as tan (light), M as light blue (light gray), O as red (dark) and S as yellow (dark gray).....	278
Figure E-5. Structures of the reforming of methane on the sulfided surface of M-doped CeO ₂ . Ce is displayed as tan (light), M as light blue (light gray), O as red (dark) and S as yellow (dark gray). The X represents the position of the additional surface oxygen vacancy.....	279
Figure E-6. Structures of the first three steps in the reforming of propane on the sulfided surface of M-doped CeO ₂ . Ce is displayed as tan (light), M as light blue (light gray), O as red (dark) and S as yellow (dark gray).....	280

- Figure E-7. Reaction energy diagram of methane decomposition over sulfided and un-sulfided surfaces of La-doped CeO_2 (1 1 1). The solid lines represents each hydrogen abstraction (product desorption) on the un-sulfided surface and the dashed lines for the sulfided surface. For the pseudo-transition state ($\text{CH}_3\bullet + \text{H}^*$), the long dash represents H abstraction on a sulfur atom and the short dash represents on an oxygen atom.....281
- Figure E-8. Reaction energy diagram of methane decomposition over sulfided and un-sulfided surfaces of Tb-doped CeO_2 (1 1 1). The solid lines represents each hydrogen abstraction (product desorption) on the un-sulfided surface and the dashed lines for the sulfided surface. For the pseudo-transition state ($\text{CH}_3\bullet + \text{H}^*$), the long dash represents H abstraction on a sulfur atom and the short dash represents on an oxygen atom.....282
- Figure E-9. Total density of states (DOS) plotted versus energy (referenced to Fermi level) for (a) C^*H_3 , (b) C^*H_2 , (c) C^*H , and (d) C^* on the un-sulfided pure CeO_2 (1 1 1) surface. Spin-down density of states is plotted on the negative y axis. All reduced cerium atoms have a spin-up f electron, and any spin paired states below the Fermi level and above the valence band are associated with electrons on the carbon atom.283
- Figure E-10. Total density of states (DOS) plotted versus energy (referenced to Fermi level) for (a) C^*H_3 , (b) C^*H_2 , (c) C^*H , and (d) C^* on the sulfided pure CeO_2 (1 1 1) surface. Spin-down density of states is plotted on the negative y axis. All reduced cerium atoms have a spin-up f electron, and any spin paired states below the Fermi level and above the valence band are associated with electrons on the carbon atom.284

LIST OF TABLES

Table 3-1. Nearest neighbor (NN) and next nearest neighbor (NNN) oxygen vacancy formation energies (ΔE_{vac}) in M-doped CeO ₂ (eV).....	59
Table 4-1. Oxygen vacancy formation energies (ΔE_{vac}) using the Hubbard <i>U</i> -correction and the HSE06 hybrid functional.....	95
Table 4-2. Mn oxidation states and number of reduced Ce atoms (# Ce ³⁺) for different concentrations and orientations of Mn dopants in the CeO ₂ (1 1 1) surface.....	99
Table 4-3. Formation energy of doping Mn into the surface of CeO ₂ at 1000 K and $P_{O_2} = 10^{-18}$ atm.	102
Table 5-1. Reaction types and reaction energy definitions for elementary steps involved in propane oxidation/reforming over CeZrO _x	118
Table 6-1. Energies for C _z intermediate desorption, abstracting a hydrogen and re-oxidizing the surface under oxidizing conditions	163
Table 7-1. Sample Names and Basic Properties.	174
Table 7-2. Oxygen vacancy formation (ΔE_{vac}) and H ₂ S adsorption (ΔE_{ads}) energies for CeO ₂ (1 1 1) with 1 Mn atom doped in the surface (isolated) and 2 Mn atoms doped in the surface (non-isolated), with one and two oxygen vacancies in the surface. The oxidation states of Mn are listed for each case, as well as the number of cerium atoms that reduce from Ce ⁴⁺ to Ce ³⁺	179
Table 7-3. Reaction energies ($\Delta E_{reaction}$, in eV) for conversion of H ₂ S _{gas} and O-vacant surfaces to H ₂ gas and an S-incorporated surface (Reaction A).....	182
Table 8-1. Reaction types and reaction energy definitions for all reactions included in this paper.....	197
Table 8-2. Adsorption and dehydrogenation energies for methane and propane reforming on sulfided and un-sulfided surfaces of pure, La-, Tb- and Mn-doped CeO ₂ (1 1 1). The oxygen numbers refer to which oxygen the species is adsorbed to from the labels in Figure 8-1. O1 is the sulfur atom position in the sulfided cases. The * represent which carbon(s) or hydrogen are bound to oxygen or sulfur atoms. Reaction types are defined in Table 8-1.	200
Table 8-3. Energies associated with the thermodynamic cycle decomposition of the abstraction of a hydrogen from a methane forming a methyl radical in the gas phase and a hydrogen adsorbed on the surface (on O1 for un-sulfided or S1 for sulfided) for pure, La-, Tb- and Mn-doped CeO ₂ (1 1 1). This cycle is represented graphically in Figure 8-3, if the R ₁ represents CH ₃ and R ₂ represents hydrogen. Step 2 is the sum of steps 2a-c and E _{act} is the sum of steps 1 and 2. Step 2b and 2c are the energies associated with the thermodynamic cycle breakdown for the adsorption of a methyl radical on the surface.	204

Table 8-4. The number of reduced cerium atoms and the oxidation state of the dopant atoms for methane and propane reforming surface intermediate over sulfided and un-sulfided surfaces of pure, La-, Tb- and Mn-doped CeO ₂ (1 1 1). La- and Tb-doped ceria had the same extent of reduction in the surface for every step and the dopant is represented by M. The oxygen numbers refer to which oxygen the species is adsorbed to from the labels in Figure 8-1. O1 is the sulfur atom in the sulfided surfaces. The * represent which carbon or hydrogen is bound to the oxygen or sulfur atom, and the oxygen numbers represent which oxygen (sulfur) the carbon or hydrogen are bound to.....	214
Table A-1. Subsurface oxygen vacancy formation energies.....	234
Table A-2. Valence configurations for the transition metal dopants used in this study.	235
Table A-3. Number of layers convergence. Vacancy formation energies are not calculated for non-mirrored slabs.....	236
Table A-4. Nearest neighbor oxygen vacancy formation energy and nearest neighbor dissociative methane adsorption energy.....	237
Table A-5. Number of layers convergence. Vacancy formation energies are not calculated for non-mirrored slabs.....	243
Table A-6. Bond lengths for dopant to 7 closest oxygens (6 with oxygen vacancy). Highlighted ones for the methane adsorbed structure are oxygens with the hydrogen or the methyl radical adsorbed to.	247
Table A-7. Adsorption energies and vacancy formation energies demonstrating the increasing of the number of layers in slab used to correct non-symmetries.	248
Table A-8. Activation barriers to the pseudo-transition and true transition states as well as the dissociative methane adsorption energies.	250
Table B-1. Surface oxygen vacancy formation energies at different values of U on d -states of Mn in a $p(2 \times 2)$ unit cell expansion with a 25% surface Mn concentration.	251
Table B-2. Surface, subsurface and 2 nd oxygen vacancy formation energies for Mn-doped CeO ₂ (1 1 1) with $U = 4$ eV on d -states of Mn. The second oxygen vacancy is calculated relative to a structure with the first surface oxygen vacancy formed.	252
Table C-1. 0 K oxygen vacancy formation energies for pure CeO ₂ (111) and Zr-doped CeO ₂ (111). Each successive oxygen vacancy formation energy is calculated relative to a surface with one less vacancy. The 6 th oxygen vacancy in Zr-doped CeO ₂ is not electronically possible due the number of cerium atoms that would have to reduce, see Section 5.3.4.....	258

ACKNOWLEDGEMENTS

I want to thank my advisor Michael Janik for providing all of his passionate help and technical direction throughout my studies. He is an excellent advisor, dedicating his time and talents to teaching others. I feel very lucky to have him as my advisor. I am appreciative of the senior students in our group for teaching me the computational techniques and methods used throughout my studies. I would like to particularly mention Adam Mayernick, whose previous work spurred my research project, and former members of the Janik group, Gholarmreza Rostamikia, Kuan-Yu Yea and Kyungtae Lee. I appreciate help and support from the other member of the Janik group and wish the best of luck to them, specifically Thomas Senftle, Siddharth Sitamraju, Nate Gifford, Huai-Suen Shiau, Hao Kuang, Sneha Akhade, Ian McCrum, Joel Bombile, and Gaurav Kumar. It has been a great pleasure to work with some of the brightest and kindest individuals while I have been at Penn State and the experience was irreplaceable.

I'd like to thank my parents and sister for their continuous support and encouragement. Finally, I'd like to thank Keslee Rice for her endless support and always being there for me over the past couple of years, you will always be in my heart. I'm forever grateful for the opportunities I have been fortunate enough to have, and offer thanks to all those who have helped along the way.

Chapter 1

Introduction – Ceria for Biomass Gasification Effluent Cleanup

1.1. Background

For the past 100 or so years, fossil hydrocarbons have been the main source of energy for the world (oil, coal and natural gas). These hydrocarbon sources can either be used directly through oxidation, or they can be converted to other types of fuel molecules. Biomass may partially replace fossil fuels in a future, renewable energy infrastructure. Biomass can be converted to precursors for fuel molecules through torrefaction, gasification or pyrolysis. The effluent from these processes would have to then be purified. For gasification, gas cleanup includes reforming methane and higher hydrocarbons and removing sulfur. The efficiency of the purification of this effluent, conversion to other hydrocarbons and hydrocarbon fuel utilization relies on conversion catalysts.

Ceria is useful in catalysis because it has a high thermal stability,¹⁻⁴ large oxygen storage capacity,⁵⁻⁷ high catalytic activity,⁸⁻⁹ and its properties can be improved by adding other transition metals to it.⁸⁻¹⁶ Ceria is already widely used in automotive catalysts, due to its ability to act as an oxygen reservoir and its ability to exchange oxygen atoms with reactants.⁵⁻⁷ Other applications which benefit similarly from ceria's ability to act as an oxygen reservoir are steam reforming,¹⁷⁻¹⁸ the water gas shift reaction¹⁹⁻²¹ and catalytic combustion.⁸⁻⁹ Pure ceria doesn't have the necessary redox properties and catalytic activity to work as an efficient conversion catalyst. The redox properties^{10,22-24} and catalytic activity⁸⁻¹⁶ of ceria can be improved with the addition of other transition metals. The ability to tailor the properties of ceria using other transition metals is essential for the use of ceria based catalysts in energy conversion and production processes. This dissertation utilizes density functional theory (DFT) to examine the catalytic activity and stability of transition

metal doped ceria surfaces. The cleanup of the effluent from biomass gasification is a specific target application. In addition, this work expands our knowledge of how to use DFT to model hydrocarbon activity on oxide systems.

Gasification involves the heating of the biomass (trees, grasses and other plant matter) to elevated temperatures (>1000 K) and combining with a specific amount of oxygen to form carbon monoxide and hydrogen, Figure 1-1.²⁵ This method can be considered a brute force method to convert any type of biomass into a useable fuel. The resulting carbon monoxide and hydrogen mixture (syngas) can be used directly in a solid oxide fuel cell to produce electricity,²⁶ used to produce electricity in a heat cycle,²⁷ or reacted over a catalyst to form hydrocarbon fuels including ethanol or synthetic crude oil through the Fischer–Tropsch process.²⁸ Biomass gasification results in high methane breakthrough (methane not converted to CO and H₂), up to 10% as well as tars up to 3.5% and small amounts of H₂S and NO_x.²⁹ To reform the methane using commercially available nickel based catalysts, one must first adsorb the sulfur, crack the tars and adsorb the NO_x in separate steps.³⁰⁻³¹ H₂S removal processes requires lower the effluent temperature below reforming temperatures, thereby creating an energy inefficiency. With this process, the conversion of biomass to ethanol using biomass gasification the greatest cost is the cleanup of the syngas, which currently is approximately 50% of the cost, Figure 1-2.³² The overall cost to produce syngas is projected to decrease, however the cleanup still comprises a large amount of the production costs. Currently, nickel on aluminum oxide catalysts are used to crack tars up to CH₄ and CO_x at 900 K, however the catalyst deactivates due to coking (carbon build-up). The nickel based catalyst can be promoted with cerium oxide which improves coking resistance.³⁰ A catalyst that can operate at high temperatures (1100 K) would be beneficial in decreasing the cleanup costs, by allowing the effluent to be cleaned at temperatures approaching the temperature of the gasifier without cooling the stream causing efficiency losses. The catalyst should be able to tolerate sulfur in the syngas or, ideally act as a sulfur sorbent as well as to reform hydrocarbons.

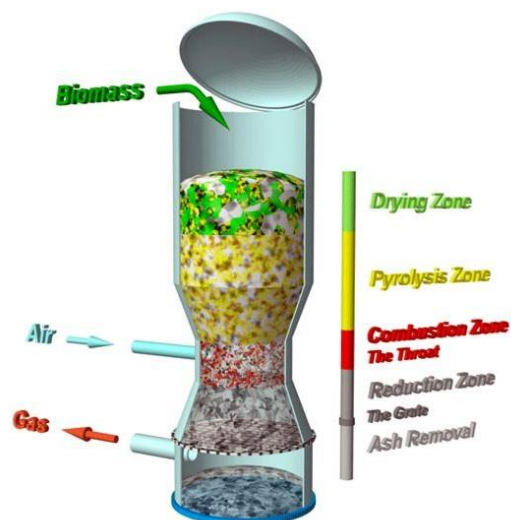


Figure 1-1. Schematic of a typical biomass gasifier producing syngas (CO and H₂). (<http://www.steam-boilers.org/wp-content/uploads/2010/10/gasification-2.jpg>)

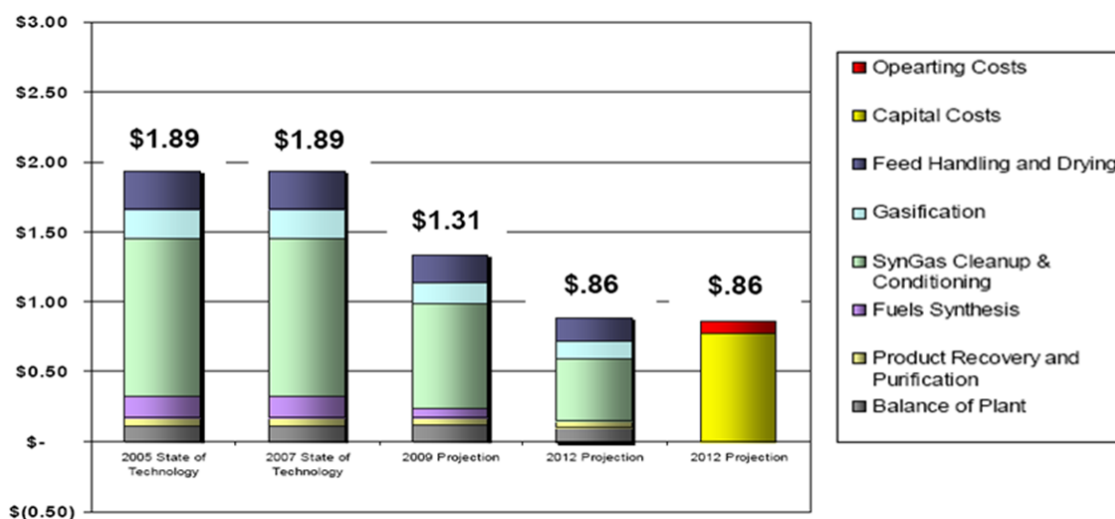


Figure 1-2. Cost to convert biomass into ethanol through biomass gasification. (U.S. Department of Energy Biomass Program, http://www1.eere.energy.gov/biomass/pdfs/biomass_deep_dive_pir.pdf)

Most metal oxide supports such as silica and alumina are a non-reducible support and only provide a physical support to maximize the active metal surface area with only a small interaction between the transition metal and the support oxide. Ceria, contrarily, is a reducible support and has a strong interaction between the transition metals, imparting a unique catalytic activity. As stated above, ceria can serve as an oxygen reservoir and easily exchange oxygen atoms with reacting species. This ability because the cerium can easily change oxygen states between Ce^{4+} and Ce^{3+} .³³ Having the oxygen reservoir allows ceria to increase the oxidation rate for a reaction as well as reduce coking, by giving “stored” oxygen atoms to the reactant that would normally not be available with a traditional metal oxide support. The addition of transition metals to ceria offers the potential for improved hydrocarbon oxidation catalysts and sulfur sorbents, where the ceria serves as both a support for the transition metals and acts as an active catalytic component in the system.

Computational chemistry can examine elementary reaction energetics and structural details on a catalyst at the atomic level, providing electronic level detail which is difficult to obtain experimentally. DFT along with *ab initio* thermodynamics can provide free energy differences for surface processes and elementary reaction steps under catalytic operating conditions. With free energies, the thermodynamically stable surfaces for a catalyst can be determined under operating conditions. This can identify whether a transition metal maybe stable doped into the ceria surface and if there will be oxygen vacancies present in the surface. During the catalytic cycle, the surface will undergo oxidation and reduction through either filling or forming oxygen vacancies or reforming of hydrocarbons. DFT is able to identify when the surface reduces, in addition to determining whether the cerium atoms will reduce from Ce^{4+} to Ce^{3+} or if the dopant atoms will act as reduction centers. With the ability to examine individual elementary steps for hydrocarbon reforming reactions, the lowest energy path can be determined. Studies of transition metal-ceria systems is limited to small unit cells due to the computational intensity of DFT. Consideration of transition metal particles on the surface of ceria is not possible due to the length scale and cell sizes

(<200 atoms) computationally practical in DFT. With these limitations, most DFT studies are limited to having one or two transition metals doped into the ceria lattice^{16,34-37} or supported adatoms on the surface.³⁸⁻³⁹ This dissertation uses DFT and *ab initio* thermodynamics to evaluate relative free energies of various transition metal dopants with and without surface sulfidation and their oxidation states and elementary reaction steps for methane and propane reforming on those M-doped ceria surfaces. Propane is used as a model hydrocarbon because it is the smallest hydrocarbon which contains a secondary carbon atom and can be used to model carbon-carbon breaking steps.

Representation of the electronic structure and redox chemistry on ceria surfaces is challenging for standard DFT methods. Typical generalized gradient approximation (GGA) exchange-correlation functionals fail in describing the partial occupation of the Ce *4f* orbitals upon the formation of oxygen vacancies in ceria, or during any process that reduces ceria.⁴⁰⁻⁴² Due to the self-interaction error inherent to standard DFT, DFT incorrectly predicts the delocalization of the Ce *4f* electrons when cerium atoms reduce from Ce⁴⁺ to Ce³⁺. To correct this error the DFT+*U* method introduces the Hubbard *U*-term as an on-site Coulombic interaction to the *f*-states of cerium.⁴³⁻⁴⁴ The introduction of the *U*-term on the *f*-states of cerium can force the localization of an electron onto a specific cerium atom by penalizing the delocalization of the electron across multiple cerium atoms. The localized *f* orbital appears between the valence band and the conduction band for reduced ceria (CeO_{2-x}).⁴⁰⁻⁴² The value of *U* chosen for the *f*-states of cerium affects the band gap, the lattice constant, reduction energies as well as other physical properties of ceria. With all of these properties being affected by the *U* value, the quantitative results contained herein might not match experimental results precisely, however, all of the qualitative results are reasonable. A value of *U* = 5 eV on the *f*-states of cerium is used for all calculations presented here, which is consistent with previous studies.^{39,45-48}

DFT is also known to have problems representing the *d*-states of other metal oxides. DFT+*U* has also been utilized on these metal oxides to help alleviate some of these problems. It, however, has not been well established if a *U*-value on the *d*-states of metals is needed when they are doped into another metal oxide, like ceria, and if so, how to determine what the *U*-value on the metal dopant should be. For some of the metals dopants used herein, a *U*-value has been added to the *d*-states to better improve the representation of the surfaces. For certain metal dopants, a *U*-value is necessary to correctly model the electronic behavior of the system, but for others, a *U*-value on the dopant would not change the behavior. The *U*-value chosen for the dopant can change whether the dopant or cerium atoms act as reduction centers. The challenges of using the DFT+*U* method for M-doped ceria systems is detailed in Chapter 2.

Instead of using DFT+*U* to correct the self-interaction error of ceria and of other metal dopants, hybrid functionals can be used.⁴⁹⁻⁵¹ Hybrid functionals incorporate a specified amount of nonlocal exact exchange together with a GGA or LDA functional. This exact exchange can alleviate the pure-GGA self-interaction error. Hybrid functionals have been shown to match experimental lattice constants, as well as the relative stabilities of surface and subsurface oxygen vacancies in ceria, they also correctly predict the localization of the *f* electrons of cerium.⁵⁰⁻⁵³ One major drawback on hybrid functionals is their computational intensity is much greater than that compared to DFT+*U* and therefore it is difficult to use hybrid functionals for large systems or large numbers of systems. In Chapter 4, we utilize the Heyd-Scuseria-Ernzerhof (HSE06) functional⁵⁴⁻⁵⁶ to compare against values obtained using the DFT+*U* method for Mn-doped CeO₂.

1.2. Summary of Chapters

This dissertation examines the ability of M-doped ceria (111) to reform hydrocarbons (Chapters 3-6) and to remove sulfur (Chapters 7 and 8) from the effluent from biomass gasification.

Chapter 2 clarifies the challenges to represent M-doped CeO₂ surface catalytic properties with DFT+*U* and hybrid functionals. The objective is to illustrate the difficulties and summarize current approaches, towards further motivating improved approaches practical for surface reactivity studies.

Chapter 3 examines the effect of transition metal dopants in the lattice of CeO₂ on oxygen vacancy formation and dissociative methane adsorption. Our group previously reported a correlation between the vacancy formation energy and the dissociative adsorption energy of methane for various surface terminations of Zr- and Pd-doped CeO₂.⁵⁷ Chapter 3 demonstrates that this same correlation holds across transition metal dopants in ceria. The ability of a M-doped CeO₂ to serve as a hydrocarbon oxidation catalyst depends upon the ability to activate C-H bonds and to heal oxygen vacancies. A volcano relationship is expected between oxidation activity and reducibility of the surface: dopants leaving the surface too reducible are limited by the ability to heal vacancies, those not reducible enough are limited by slow C-H bond activation. Periodic trends are demonstrated for the oxidation states of dopants before and after surface reduction.

The analysis of periodic trends in transitional metal-doped ceria of Chapter 3 suggests Mn-doped ceria could be an active, stable, and inexpensive material for use in biomass gasifier effluent cleanup. Chapter 4 determines the effect of a *U*-value on the *d*-states of Mn doped into the fluorite lattice of CeO₂. Depending on the *U*-value chosen for the *d*-states, the most stable oxidation state for Mn in a partially reduced surface can be either Mn³⁺ or Mn²⁺. In this chapter, a *U*-value of 4 eV on *d*-states of Mn is utilized. To help confirm this *U*-value, the hybrid functional HSE06 is used for one system and compared to the results from DFT+*U*. The oxidation state of Mn and Ce in the oxidized and reduced cases match the oxidation states as determined with XANES. With the reliability of a *U* = 4 eV value established, the reduction and formation energies for surfaces with various Mn concentrations are examined. The concentration and distribution of Mn doped in the surface of CeO₂ has a large impact on the first and second oxygen vacancy formation energies, as

well as the most stable oxidation states for Mn. The formation energies of the Mn-doped CeO₂ system to examine the stability of Mn-doping at various oxidation states are reported. This detailed computational examination of Mn-doped ceria provides basic electronic structure insight into a material found useful for H₂S absorption, as described in Chapter 6.

The cleanup of the effluent from biomass gasification requires the reforming of larger hydrocarbons where carbon-carbon bonds must be broken and propane can be used as a model hydrocarbon. Zr is one of the most common dopants in ceria due to its thermal stability, increase in surface area, and increase in oxygen storage capacity.¹⁻⁴ The reforming path for propane over Zr-doped ceria is examined in Chapter 5. Some of the mechanistic and modeling questions necessary to develop a formulaic approach for modeling this complex reaction sequence on an oxide surface are considered. A significant mechanistic question is when to add oxygen atoms onto the surface, re-oxidizing the surface during the intermediate steps of propane oxidation. An *ab initio* thermodynamics approach is used to determine the sequence of propane decomposition, surface re-oxidation and product desorption. The dependence of the mechanism on the O₂ chemical potential is observed. Reaction paths are reported for both highly oxidizing conditions (combustion) and reducing (reforming) conditions.

Using the same approach developed in Chapter 5 to model the reforming of propane over Zr-doped CeO₂, Chapter 6 examines the reforming of propane over Mn-doped CeO₂. We establish a possible reforming path for propane in an oxidizing, reducing and extremely reducing environment and compare the mechanism back to the Zr-doped surface as described in Chapter 5. We also examine the possibility for the desorption of all intermediates on the surface, as well as developing a detailed picture of the electronic structure along the reforming path.

In Chapter 7 uses a combination of the thermal stability and low H₂S equilibrium concentration of mixed REOs with the rapid sulfidation kinetics and high sulfur capacity of MnO_x to create a better sulfur sorbet from gasification effluent. Our collaborators examined the mixed

MnO_x and REO mixture over a range of MnO_x compositions and determine its sulfur capacities using a stream closely resembling the composition of effluent from a gasifier. X-ray adsorption near-edge spectroscopy (XANES) and density functional theory (DFT) are combined to understand the role Mn plays in the increased adsorption capacity of MnO_x/REO mixtures.

Using the thermodynamically stable structures established in Chapter 7 and in previous work,⁵⁸ Chapter 8 compares reforming of methane and the initial steps of reforming propane over sulfided and un-sulfided pure and M-doped CeO₂ (1 1 1) (M = La, Tb, Mn). Our initial structure contains one subsurface oxygen vacancy with no surface oxygen vacancies, so the catalyst will cycle between having a surface oxygen vacancy and not having a surface oxygen vacancy. We show that the initial steps for the reforming of methane over the sulfided surfaces (methyl group bound to sulfur) are similar in energy and only the later oxidation steps are energetically impacted compared to the un-sulfided surfaces. We also further examine how the state of the reduction of the ceria surface changes along the methane reforming path. Chapter 9 summarizes the key results from Chapters 2-8 and discusses recommendations for future work.

1.3. References

1. D. Terribile, A. Trovarelli, C. de Leitenburg, A. Primavera, G. Dolcetti. *Catalysis Today* **1999**, *47*, 133-140.
2. M. Boaro, C. de Leitenburg, G. Dolcetti, A. Trovarelli. *Journal of Catalysis* **2000**, *193*, 338-347.
3. P. Fornasiero, R. Dimonte, G. R. Rao, J. Kaspar, S. Meriani, A. Trovarelli, M. Graziani. *Journal of Catalysis* **1995**, *151*, 168-177.
4. G. Zhou, P. R. Shah, T. Kim, P. Fornasiero, R. J. Gorte. *Catalysis Today* **2007**, *123*, 86-93.
5. G. W. Graham, H. W. Jen, R. W. McCabe, A. M. Straccia, L. P. Haack. *Catalysis Letters* **2000**, *67*, 99-105.
6. H. W. Jen, G. W. Graham, W. Chun, R. W. McCabe, J. P. Cuif, S. E. Deutsch, O. Touret. *Catalysis Today* **1999**, *50*, 309-328.
7. Y. Nagai, T. Hirabayashi, K. Dohmae, N. Takagi, T. Minami, H. Shinjoh, S. i. Matsumoto. *Journal of Catalysis* **2006**, *242*, 103-109.
8. S. Colussi, A. Gayen, M. F. Camellone, M. Boaro, J. Llorca, S. Fabris, A. Trovarelli. *Angewandte Chemie-International Edition* **2009**, *48*, 8481-8484.
9. L. H. Xiao, K. P. Sun, X. L. Xu, X. N. Li. *Catalysis Communications* **2005**, *6*, 796-801.
10. E. Aneggi, M. Boaro, C. d. Leitenburg, G. Dolcetti, A. Trovarelli. *Journal of Alloys and Compounds* **2006**, *408-412*, 1096-1102.
11. Q. Fu, H. Saltsburg, M. Flytzani-Stephanopoulos. *Science* **2003**, *301*, 935-938.
12. G. Jacobs, P. M. Patterson, L. Williams, E. Chenu, D. Sparks, G. Thomas, B. H. Davis. *Applied Catalysis A: General* **2004**, *262*, 177-187.
13. G. Jacobs, S. Ricote, U. M. Graham, P. M. Patterson, B. H. Davis. *Catalysis Today* **2005**, *106*, 259-264.

14. S. H. Oh, G. B. Hoflund. *Journal of Physical Chemistry A* **2006**, *110*, 7609-7613.
15. D. Pierre, W. Deng, M. Flytzani-Stephanopoulos. *Topics in Catalysis* **2007**, *46*, 363-373.
16. V. Shapovalov, H. Metiu. *Journal of Catalysis* **2007**, *245*, 205-214.
17. G. Jacobs, R. A. Keogh, B. H. Davis. *Journal of Catalysis* **2007**, *245*, 326-337.
18. X. Wang, R. J. Gorte. *Applied Catalysis A: General* **2002**, *224*, 209-218.
19. T. Bunluesin, R. J. Gorte, G. W. Graham. *Applied Catalysis B: Environmental* **1998**, *15*, 107-114.
20. W. Deng, M. Flytzani-Stephanopoulos. *Angewandte Chemie* **2006**, *118*, 2343-2347.
21. X. Wang, R. J. Gorte, J. P. Wagner. *Journal of Catalysis* **2002**, *212*, 225-230.
22. A. Bensalem, F. Bozon-Verduraz, V. Perrichon. *Journal of the Chemical Society, Faraday Transactions* **1995**, *91*, 2185-2189.
23. P. Fornasiero, G. Balducci, R. Di Monte, J. Kaspar, V. Sergo, G. Gubitosa, A. Ferrero, M. Graziani. *Journal of Catalysis* **1996**, *164*, 173-183.
24. G. Zhou, R. J. Gorte. *Journal of Physical Chemistry B* **2008**, *112*, 9869-9875.
25. A. V. Bridgwater. *Fuel* **1995**, *74*, 631-653.
26. R. Suwanwarangkul, E. Croiset, E. Entchev, S. Charojrochkul, M. D. Pritzker, M. W. Fowler, P. L. Douglas, S. Chewathanakup, H. Mahaudom. *Journal of Power Sources* **2006**, *161*, 308-322.
27. L. Wang, C. L. Weller, D. D. Jones, M. A. Hanna. *Biomass and Bioenergy* **2008**, *32*, 573-581.
28. K.-W. Jun, H.-S. Roh, K.-S. Kim, J.-S. Ryu, K.-W. Lee. *Applied Catalysis A: General* **2004**, *259*, 221-226.
29. S. J. Juutilainen, P. A. Simell, A. O. I. Krause. *Applied Catalysis B-Environmental* **2006**, *62*, 86-92.
30. L. Devi, K. J. Ptasinski, F. Janssen. *Biomass & Bioenergy* **2003**, *24*, 125-140.

31. M. Jazbec, K. Sendt, B. S. Haynes. *Fuel* **2004**, *83*, 2133-2138.
32. U.S. Department of Energy Biomass Program.
http://www1.eere.energy.gov/biomass/pdfs/biomass_deep_dive_pir.pdf (accessed 6/21/2012).
33. D. Y. Lu, P. Liu. *Journal of Chemical Physics* **2014**, *140*, 084101.
34. X. Wang, J. A. Rodriguez, J. C. Hanson, D. Gamarra, A. Martinez-Arias, M. Fernandez-Garcia. *Journal of Physical Chemistry B* **2005**, *109*, 19595-19603.
35. H.-L. Chen, S.-H. Liu, J.-J. Ho. *Journal of Physical Chemistry B* **2006**, *110*, 14816-14823.
36. J. A. Rodriguez, X. Wang, J. C. Hanson, G. Liu, A. Iglesias-Juez, M. Fernandez-Garcia. *Journal of Chemical Physics* **2003**, *119*, 5659-5669.
37. Z. Yang, G. Luo, Z. Lu, T. K. Woo, K. Hermansson. *Journal of Physics: Condensed Matter* **2008**, *20*, 035210.
38. Z. Chafi, N. Keghouche, C. Minot. *Surface Science* **2007**, *601*, 2323-2329.
39. Z. Yang, L. A. Zhansheng, G. Luo, K. Hermansson. *Physics Letters A* **2007**, *369*, 132-139.
40. S. Fabris, S. de Gironcoli, S. Baroni, G. Vicario, G. Balducci. *Physical Review B* **2005**, *71*, 041102.
41. S. Fabris, S. de Gironcoli, S. Baroni, G. Vicario, G. Balducci. *Physical Review B* **2005**, *72*, 237102.
42. G. Kresse, P. Blaha, J. L. F. Da Silva, M. V. Ganduglia-Pirovano. *Physical Review B* **2005**, *72*, 237101.
43. V. I. Anisimov, O. Gunnarsson. *Physical Review B* **1991**, *43*, 7570-7574.
44. J. F. Herbst, R. E. Watson, J. W. Wilkins. *Physical Review B* **1978**, *17*, 3089-3098.
45. B. Herschend, M. Baudin, K. Hermansson. *Surface Science* **2005**, *599*, 173-186.
46. M. Nolan, S. C. Parker, G. W. Watson. *Surface Science* **2005**, *595*, 223-232.
47. M. Nolan, S. Grigoleit, D. C. Sayle, S. C. Parker, G. W. Watson. *Surface Science* **2005**, *576*, 217-229.

48. Z. Yang, G. Luo, Z. Lu, K. Hermansson. *The Journal of Chemical Physics* **2007**, *127*, 074704.
49. J. L. F. Da Silva, M. V. Ganduglia-Pirovano, J. Sauer, V. Bayer, G. Kresse. *Physical Review B* **2007**, *75*, 045121.
50. M. Nolan. *Journal of Physical Chemistry C* **2011**, *115*, 6671-6681.
51. M. Nolan. *Journal of Materials Chemistry* **2011**, *21*, 9160-9168.
52. G. Kresse, P. Blaha, J. L. F. D. Silva, M. V. Ganduglia-Pirovano. *Physical Review B* **2005**, *72*, 237101.
53. M. V. Ganduglia-Pirovano, J. L. F. Da Silva, J. Sauer. *Physical Review Letters* **2009**, *102*, 026101.
54. J. Heyd, G. E. Scuseria, M. Ernzerhof. *Journal of Chemical Physics* **2003**, *118*, 8207-8215.
55. J. Heyd, G. E. Scuseria. *Journal of Chemical Physics* **2004**, *121*, 1187-1192.
56. J. Heyd, G. E. Scuseria, M. Ernzerhof. *Journal of Chemical Physics* **2006**, *124*, 219906.
57. A. D. Mayernick, M. J. Janik. *Journal of Physical Chemistry C* **2008**, *112*, 14955-14964.
58. A. D. Mayernick, R. Li, K. M. Dooley, M. J. Janik. *Journal of Physical Chemistry C* **2011**, *115*, 24178-24188.

Chapter 2

Challenges in the Use of Density Functional Theory to Examine Catalysis by M-Doped Ceria Surfaces

This chapter is published as: M. D. Krcha, M. J. Janik. *International Journal of Quantum Chemistry*, 2014, 114, 8-13.

ABSTRACT: For CeO₂ or M-doped CeO₂ catalysts, reliable energetics associated with surface reactivity requires accurate representation of oxidized and reduced metal states. Density functional theory is used extensively for metals and metal oxides; however, for strongly correlated electron materials, conventional DFT fails to predict both qualitative and quantitative properties. This is the result of a localized electron self-interaction error that is inherent to DFT. DFT+*U* has shown promise in correcting energetic errors due to the self-interaction error, however, its transferability across processes relevant to surface catalysis remains unclear. Hybrid functionals, such as HSE06, can also be used to correct this self-interaction error. These hybrid functionals are computationally intensive, and especially demanding for periodic surface slab models. This perspective details the challenges in representing the energetics of M-doped ceria catalyzed processes and examines using DFT extensions to model the localized electronic properties.

2.1. Introduction

Density functional theory (DFT) is widely employed in catalysis studies. Though numerous successful applications to metal catalysts have been achieved, the reliability of standard generalized gradient approximation (GGA) DFT approaches for metal oxide systems is more suspect.¹⁻⁴ Metal oxides with localized, strongly correlated electrons are more difficult for DFT to accurately represent. Extensions to standard GGA-DFT are often used to model these systems.⁵ Catalytic activity on metal oxides is directly related to the ability of metal atoms to cycle between oxidation states.⁶ It is essential to develop computational methods that accurately capture energetics associated with metal oxidation state changes during metal oxide catalyzed reaction cycles.

Ceria-based catalysts are particularly difficult for conventional DFT due to the self-interaction error that emerges when modeling localized f -states in partially reduced surfaces.⁷ Recently a review on the status of DFT+ U has been published.⁸ This self-interaction error causes GGA-DFT methods to improperly delocalize f -electrons in reduced ceria systems. The most widely used method to correct this self-interaction error is the addition of the Hubbard U -term to the cerium f -states.⁷ The Hubbard U -term adds a semi-empirical energetic penalty to partial occupation of the orbitals to which is it applied (i.e. f -states of Ce). The empirical U -term may be chosen to match known material properties, or calculated self-consistently using the linear-response approach.⁷ The empirical approach is most typically used, however, a U -value determined to match one property (i.e. band gap) may not necessarily give proper surface reduction energetics. Self-consistent U determination provides an approach to return the full *ab initio* nature to DFT by determining an appropriate U -value for a given physical model. However, system energies cannot be trivially compared with different U -values, leaving an empirical choice of a constant U to apply within a catalytic cycle when the self-consistent U -values vary along the reaction path.

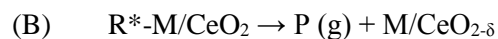
The addition of other transition metals to the ceria lattice, often occupying cerium lattice sites, can offer improved catalytic properties. Numerous studies have employed DFT approaches to these “doped” ceria surfaces. Often, an onsite U -potential is added only to the f -states of cerium on these doped systems.¹ For many metal oxides, accurate material properties require DFT+ U methods with U -corrections on the d -states of the metals.⁹ A second approximation to these mixed metal oxide systems is to also include a U -value to the dopant d -states.¹⁰ Correspondingly, a reasonable U -value for the d -states of these metals must also be determined. A U -value applied to the p -states of oxygen can also lead to a better estimate of the band gaps and reduction energies of ceria.¹¹ An additional complexity is that a different U -potential can be applied to the same atom in different geometric arrangements (surface versus subsurface, near dopant versus far from dopant). Sholl and co-workers recently used a position dependent version of DFT+ U (DFT+ $U(\mathbf{R})$) to correctly reproduce the properties of FeO_x .¹² As approaches are not standardized, comparisons between DFT examinations of M-doped CeO_2 reactivity are challenging.

A different approach from the DFT+ U method is the use of a hybrid exchange-correlation functional.¹³ Hybrid functionals add exact exchange and limit the pure GGA inaccuracies in canceling the self-repulsion, therefore avoiding the empiricism of adding U -corrections. The amount of exact exchange to use must still be chosen, retaining empiricism in hybrid functional implementation. The hybrid functional HSE06, along with other hybrid functionals, has been shown to accurately model oxygen vacancies in pure ceria.¹⁴ Recently, the HSE06 functional was used to examine oxygen vacancy formation and charge transfer for divalent and trivalent dopants in ceria.¹⁵⁻¹⁶

In this perspective, we clarify the challenge to represent M-doped CeO_2 surface catalytic properties with DFT+ U and hybrid functionals. Our objective is to illustrate the difficulties and summarize current approaches, towards further motivating improved approaches practical for surface reactivity studies.

2.2. Challenges in representing M-doped CeO₂ redox catalysis

M/CeO₂ systems are useful in CO oxidation,¹ CH₄ oxidation,^{2,17-18} and sulfur adsorptive desulfurization.¹⁹⁻²⁰ In all of these processes, the surface cycles between oxidized and reduced conditions. CH₄ and CO oxidation cycles begin with the gas phase reactant and the oxidized surface, then form an adsorbed intermediate (R*-M/CeO₂, example in Figure 2-1) that partially reduces the surface. An oxidized product desorbs, leaving a reduced surface (M/CeO_{2-δ}). The surface is then re-oxidized by an oxidant and the cycle repeats.



To model these cycles, we need accurate energetics for transformation among the oxidized, partially reduced and reduced surfaces. For oxidized and reduced surfaces, integer formal reduction of metal atoms often occurs. However, for adsorbed intermediates (Figure 2-1) and partially reduced surfaces (CO, CH₃ or H adsorbed to an oxygen atom, for example), it is unclear if a localized, reduction of a metal atom should occur. As characterization of adsorbed intermediates is limited and typically non-existent if the intermediate is unstable, it is unclear if sufficient experimental data exists to verify the accuracy of DFT representation of these intermediate species. For M-doped CeO₂ catalysts, it is not always known whether the dopant or the cerium atom should reduce upon intermediate formation or surface reduction.

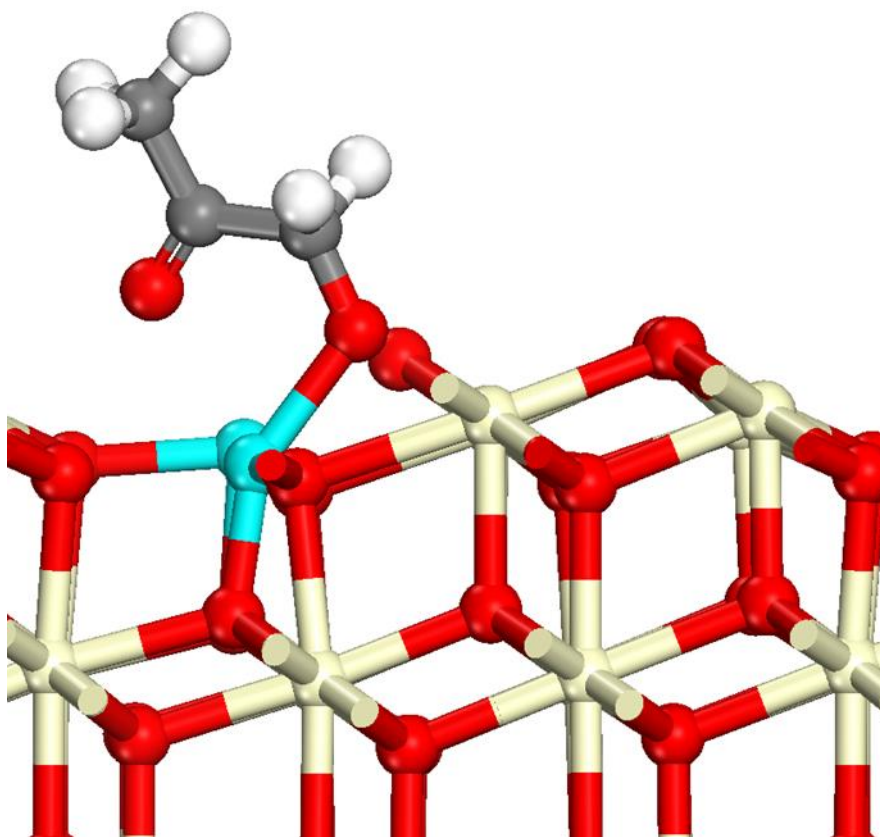


Figure 2-1. Adsorbed intermediate (C_3H_5) in the oxidation of propane catalyzed by the surface of Mn-doped CeO_2 (1 1 1). The oxygen atoms associated with the hydrocarbon originate from the surface and remain associated with Ce atoms as well. The extent of electron localization on the Ce atoms due to the partial reduction will depend on DFT electronic structure approach used. Ce is displayed as tan (light), Mn as light blue (gray), and O as red (dark).

Both Pd- and Mn-doped CeO₂ show promise as catalysts, however the role of the dopant in the catalytic process is not fully understood. In Pd-doped CeO₂, the Pd atom reduces and the cerium oxidation state is unchanged upon adsorption of methane or oxygen vacancy formation.¹⁸ For Mn-doped CeO₂, the U -value chosen for the d -states of the Mn atom changes whether the Mn atom(s) reduce or the cerium atom(s) reduce upon oxygen removal.²¹ We have recently evaluated whether the dopant serves as the reduction center or alters Ce reducibility for all transition metal doped CeO₂ (1 1 1) surfaces.¹⁷ As the reductant adsorption and oxygen vacancy formation energetics often correlate, the energetics of formation oxygen vacancies in the surface of M-doped CeO₂ is a good descriptor for the catalytic properties.¹⁷

In the following sections, we briefly review the DFT+ U method and discuss its application to pure and M-doped CeO₂ systems with a U -value on the cerium f -states. We then discuss the addition of a U -term on the oxygen p -states and dopant d -states. Lastly we examine the use of hybrid functionals for these M-doped CeO₂ systems.

2.3. DFT+U

Strongly-correlated electron materials (SCEMs), including middle-to-late transition metal oxides, are difficult for conventional DFT to represent. These metal oxides contain electrons in partially filled d or f shells, which are localized onto each metal atom. Conventional GGA-DFT uses spatially averaged approximations for exchange and correlation, which does not properly cancel out the electron self-interactions in localized states. This yields values for electron-electron repulsion that are artificially increased.⁵ These large values of electron-electron repulsion cause the electrons to delocalize, and often changes the metal oxides from an insulator to a conductor.

To correct these self-interaction errors, the electronic structure may be separated into localized and delocalized states. The two different states can be treated with different electronic

structure methods. A common method to do this is DFT+ U . The most common DFT+ U implementation uses a parameterized Hamiltonian in the framework of DFT instead of an explicit Hartree-Fock calculation. The energy from DFT+ U is calculated as:

$$E^{DFT+U}[\rho, \{n_{ilm\sigma}\}] = E^{DFT}[\rho] + \sum_{I,l,m,\sigma} \frac{(U_{II} - J_{II})}{2} (n_{ilm\sigma} - n_{ilm\sigma}^2) \quad (1)$$

where $E^{DFT}[\rho]$ is the energy from conventional DFT, U_{II} is the average Coulombic interaction, J_{II} is the exchange interaction, and n is the number of electrons in a localized orbital with a given spin and magnetic quantum number. I represents the atom type, l is the angular momentum (s, p, d, or f), m is the magnetic quantum number and σ is the spin. U_{II} and J_{II} are tunable parameters that may be chosen to match measurable experimental properties of the material, such as band gaps and magnetic moments. Alternatively, constrained DFT calculations, where the number of electrons on a specific site is fixed and the remaining electrons are allowed to relax, can be used to determine a U -value.⁵ As the Hamiltonian only uses the difference between U_{II} and J_{II} (Equation 1), we will take U to represent the difference, U_{eff} .

Several studies have examined what Ce- f U -value give reasonable electronic behavior for reduced CeO₂. Recommended U -values vary between 0.2 eV and 7 eV depending on the experimental properties being matched and the methods used to fit U . Dissociative methane adsorption energies and surface oxygen vacancy formation energies both greatly depend on the U -value chosen for Ce, as shown in Figure 2-2.² The exchange-correlation functional (LDA or which GGA) chosen can influence the U -value. Using this method, Lutfall et al. determined a U -value (PBE functional) of 0.2 eV on the f -states of Ce to closely match the experimental CeO₂ to Ce₂O₃ reduction energy of 138 kJ mol⁻¹.²² A U -value of 6.3 eV (LDA) matches the experimental band gaps of the $2p-4f$ and the $2p-5d$.²³ This U -value also reasonably predicts the lattice constant and

bulk modulus of ceria. A U of less than 5 eV (PW91) on Ce results in improper delocalization of electrons across cerium atoms of the reduced CeO_2 (1 0 0) surface.²⁴ A U -value of 5 eV results in the reduction of two Ce atoms from Ce^{4+} to Ce^{3+} near the oxygen vacancy as well as the appearance of a single spin peak in the density of states (DOS) between the CeO_2 valence band and the Fermi level (Figure 2-3a). Using both the LDA and GGA functional to match the band gaps, a U -value of 6 eV and 5 eV, respectively, was recommended.²⁵ To correctly replicate the insulating properties of reduced ceria (CeO_{2-x}), $U \geq 6$ eV (LDA) and $U \geq 5$ eV (GGA) are required, as can be seen in Figure 2-3. Figures 2-3b and 2-3c illustrates that the addition of the U -terms localizes the electrons onto two cerium atoms. Overall, most studies agree that U -values of around 4.5-6 eV are adequate to represent the measurable properties of ceria. Values for U lower than 4.5 eV tend to improperly delocalize electrons in the reduced surface.

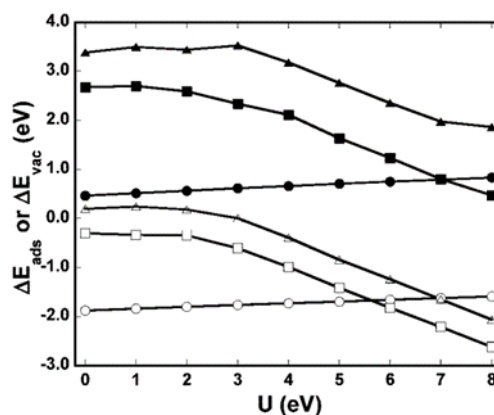


Figure 2-2. Dissociative methane adsorption energy and surface oxygen vacancy formation energy versus U -value. (▲) pure CeO_2 (1 1 1) surface, (■) Zr-doped CeO_2 (1 1 1) surface, and (●) Pd-doped CeO_2 (1 1 1) surface. Closed circles represent oxygen vacancy formation energies and open circles represent methane adsorption energies. (Reproduced with permission from [ACS Publications], Mayernick et al., *J. Phys. Chem. C*. **2008**, 112, 14955)

Our group has examined how the U -value on cerium affects the dissociative methane adsorption energy and oxygen vacancy formation energy for Zr- and Pd-doped ceria (Figure 2-2).² In Zr-doped CeO_2 , like pure CeO_2 , the Ce- f U -value influences both methane adsorption and oxygen vacancy formation energies. However, for Pd-doped CeO_2 surfaces, the Ce U -value does not have a significant influence on the two energies. Surface cerium atoms reduce when Zr-doped CeO_2 is reduced by either oxygen vacancy formation or dissociated methane adsorption. Therefore, the Ce- f U -value impacts reduction energetics. For Pd-doped CeO_2 , the Pd atom reduces and the Ce- f U -value therefore does not have a significant influence. Examining all transition metal dopants, the dopants on the left side of the periodic table are similar to Zr in that the dopant alters the reducibility of the cerium atoms. Late transition metal dopants, like Pd, become the reduction centers.¹⁷ The U -value on Ce f -states does not have a great influence on reduction energetics or surface electronic structure for dopants on the right side of the periodic table. The use of DFT+ U (with U only on cerium) provides qualitative and quantitative reduction energetics for early and late transition metal dopants. The application of a U -value to the d -states of late transition metal dopants, however, can alter the reduction energetics. For dopants in the middle of the periodic table, the application of a U -term to transition metal d -states will qualitatively and quantitatively alter the electronic structure of the doped surface.

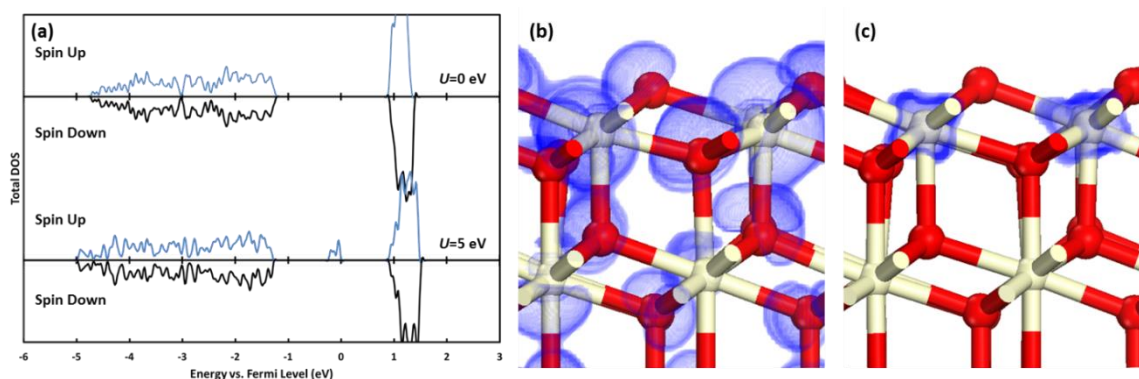


Figure 2-3. (a) Total density of states for an oxygen vacant surface of pure CeO_2 (1 1 1) with no U -value on the f -states of ceria (upper) and a U -value of 5 eV on the f -states of Ce (lower). The double peak near the Fermi level in the bottom DOS is due to the slight asymmetry in the mirrored slab. Isodensity surface of an oxygen vacant surface of CeO_2 (1 1 1) (b) with no U -value on the f -states of ceria and (c) with a U -value of 5 eV on the f -states of ceria over the energy range -0.28 to 0.00 eV (relative to Fermi level). The isodensity surface with no U -value was taken to be an iso-change increase surface between the intact surface of ceria and the oxygen vacant surface of ceria.

2.4. Including a U -value on the d -states of transition metal dopants in CeO_2

A U -correction can be added to the p -states of oxygen or to the d -states of a metal dopant atom to better match experimental measurable properties. The additional U -value on oxygen can lead to a better estimation and description of the lattice parameters, band gaps, formation energies, reduction energies and electronic properties for ceria.³ An oxygen hole (one 2p orbital with only one electron instead of two) results when a lower valency metal atom is doped into an oxide with a higher valency (trivalent dopant in ceria, for example). With a U -value only on the Ce atoms, the oxygen hole is delocalized across multiple oxygen atoms for La-doped CeO_2 .¹¹ To correct this, a U -value is added to the p -states of oxygen, thereby localizing the oxygen hole onto one oxygen atom.

A U -value must also be added to the d -states of many transition metal oxides to correct the self-interaction error that results in overestimation of oxidation energies as well as band gaps and

magnetic moments.^{9,26} However, it has not been clearly established if this additional U -correction should be added to the d -states of metal atoms doped into ceria to obtain correct energies and electronic behaviors, and if so how to choose the U -value. One way to choose the U -value can be from fitting a U -value in bulk oxides to match experimental lattice constants and band gaps, and then using this U -value for the metal dopant. This was done for Pr- and Mn-doped CeO₂ and the U -value chosen for M d -states was 4.5 eV.¹⁰ Varying the value of U changes the Mn-O bond lengths, as well the electronic structure.⁴ Figure 2-4a illustrates how the density of states changes for Mn-doped CeO₂ in the oxygen vacant surface (Mn²⁺) as the U -value on Mn changes. As the Mn- d U -value increases, the valence band slowly approaches the Fermi level and shifts the antibonding Mn-oxygen states into the valence band. Ultimately, Cen et al. also settle on a U -value of 4.5 eV on the d -states of Mn.⁴ Our group also examined how the U -value on Mn affects Mn-doped CeO₂ electronic properties.²¹ The most stable Mn oxidation state in reduced Mn-doped CeO₂ (1 1 1) depends on the U -value on Mn (Figure 2-4b). At low U -values, the most stable oxidation state for Mn in oxygen vacant Mn-doped CeO₂ is Mn³⁺, and at U -values greater than 3.5 eV the most stable structure has Mn reducing to Mn²⁺. A U -value of 4 eV, as determined by Wang et al.⁹ for pure MnO_x, also has Mn²⁺ as the oxidation state in reduced Mn-doped CeO₂, in agreement with XANES studies of Mn/CeO₂ oxides.¹⁹ The addition of the U -value to the d -states of metal dopants helps to get the correct surface reducibility, and is especially necessary for mid-periodic table transition metal dopants.

In conventional DFT+ U , the U -value is fixed for a given atom and electronic state. The self-interaction error, however, can vary for an atom in various geometric arrangements (surface versus subsurface, near dopant versus far from dopant). In each of these different arrangements, a different U -value might be necessary to reproduce an accurate electronic structure. One method that shows promise in being able to accomplish this is DFT+ $U(\mathbf{R})$.¹² In this method, the U -value is determined by examining the linear-response value of U with respect to position, (\mathbf{R}), of every

atom. This method provides promise for removing, to some extent, the empiricism of the DFT+ U method. However, the linear-response value of U may also vary along the catalytic reaction coordinate, and comparison of energies at varying U -values is not trivial, returning some degree of empiricism in choosing a constant value. To our knowledge, the $U(\mathbf{R})$ method has not been applied to investigate catalytic properties of transition metal doped ceria surfaces.

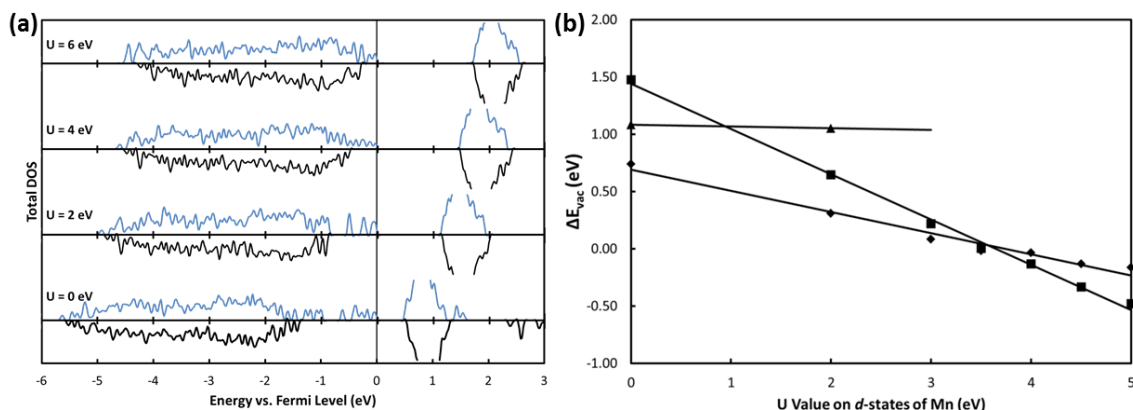


Figure 2-4. (a) Total DOS for oxygen vacant Mn-doped CeO₂ (Mn²⁺) while varying the U -value on the d -states of Mn with a U -value of 5 eV on the f -states of Ce. (b) Surface oxygen vacancy formation energy vs. U -value on the d -states of Mn with a U -value of 5 eV on the f -states of Ce. Depending upon the U -value on the d -states of Mn, Mn reduces to different oxidation states (local minimum energy structures) upon formation of an oxygen vacancy. Mn reducing to: (◆) Mn³⁺, (■) Mn²⁺, and (▲) Mn⁴⁺ upon formation of an oxygen vacancy. (—) best fit line. (Adapted with permission from [ACS Publications], Krcha et al., *Langmuir* **2013**, 29 10120)

2.5. Hybrid functionals

A hybrid exchange-correlation functional may be used to alleviate the self-interaction error and improper electron delocalization. A hybrid functional combines a specified amount of non-local exact exchange with a GGA functional. This specified amount of exact exchange must be chosen, and therefore this method also contains empirical dependencies; around 25% exact exchange is typically used. The non-local exchange added to conventional DFT more accurately captures the reduced CeO₂ electronic structure, however it also greatly increases the computational intensity (for periodic systems), making large systems or large numbers of species along a catalytic reaction pathway computationally prohibitive. Hybrid functionals can be used on smaller systems to help confirm or calibrate U -values for use in DFT+ U calculations.

The relative stabilities of surface to subsurface oxygen vacancies in CeO₂ (1 1 1) are accurately captured by using the hybrid functional Heyd-Scuseria-Ernzerhof (HSE06), as well as PBE+ U and LDA+ U functionals.¹³ The vacancy formation energies between these three functionals do not match, though the HSE06 vacancy formation energy matches well with the PBE0 functional and an embedded cluster model.²⁷ The adsorption energies of water on the CeO₂ (1 1 1) surface using the HSE06 functional and the PBE+ U functional are within 0.2 eV, and the differences in energies of various adsorption structures are within 0.1 eV.²⁸ Other hybrid functionals can be used such as PBE0 or B3LYP.¹⁴ Of the many hybrid functionals that have been examined, all produced cell parameters that were within 2.5% of the experimental values, with the PBE0 functional providing the most accurate results.¹⁴ The major differences between functionals are the predicted band gaps, where the amount of exact Hartree-Fock exchange included greatly changed the band gaps as well as the reduction energies (B1-WC functional performed best).¹⁴

Doped CeO₂ has also been examined with hybrid functionals, which could remove the “double empiricism” of choosing Ce- f and M- d U -values in DFT+ U . For doping of divalent (2+

oxidation state) cations (Pd and Ni) in ceria, DFT+ U ($U = 5.0$ eV on Ce f -states) and HSE06 yield the same qualitative descriptions of oxygen vacancy formation; however, the two functionals yield quantitatively different results.¹⁵ The first oxygen vacancy formation energy with HSE06 is lower than that predicted by DFT+ U , and to match oxygen vacancy formation energies a U -value of 10 eV would have to be used, which causes large deviation in other properties, such as shifting the Ce³⁺ states into the valence band. These methods still give quantitatively different results, even when a correction to the DFT O₂ bond energy (0.7 eV per O atom) is added. Correcting the overestimation of the DFT O₂ bond energy actually increases the difference in energy between DFT+ U and HSE06 for oxygen vacancy formation. The hybrid functional HSE06 also correctly shows the formation of an oxygen hole with doping of trivalent atoms in the surface.¹⁶ In both of Nolan's studies, the author did not examine how the addition of a U -term on the dopant would match with the hybrid functional HSE06. We examined how the addition of a U -term on the d -states of Mn (coupled with a U -term of Ce f -states) compares with the results from an HSE06 optimization.²¹ The qualitative preferences for Mn oxidation state match when an appropriate U -value on Mn is used ($U = 4.0$ eV on d -states of Mn and $U = 5.0$ eV on Ce f -states). The absolute quantitative oxygen vacancy formation energies do not match.

2.6. Conclusions

Though DFT+ U and hybrid functional methods can be chosen to match experimental properties of ceria and M-doped ceria systems, the transferability to surface catalytic activity is unclear. For catalytic studies, accurate reaction energies and activation barriers for transforming among reactant, adsorbed species and products is needed. These transformations include reduction and re-oxidation of the M-doped CeO₂ surface, challenging accurate energetics determination with tractable DFT methods. Despite these limitations, DFT+ U methods have provided qualitative

insight into catalytic mechanisms and trends with dopant variations for methane and carbon monoxide oxidation and desulfurization.

To help reduce and mitigate some of these challenges faced when using DFT to study catalytic properties of M-doped ceria systems, further standardization of current “best practices,” and greater availability of experimental model systems for benchmarking would help clarify the reliability of the methods being used. Differences between studies in model construction (slab thickness, the use of mirrored slabs, the U -value applied, and variance in exchange-correlation functionals) complicate comparison among DFT+ U studies. All DFT+ U studies should be careful to test convergence or sensitivity to model parameters, and should show a full awareness of the models used by others such that we may collectively clarify sensitivity to these differences and narrow the variety. Experimental benchmark studies of single crystal, M-doped ceria surfaces, especially probing reducibility and surface reactivity, would allow for further benchmarking to establish the reliability and limitations in DFT+ U . The choice of U -values or hybrid functionals in DFT may be better tuned to match experimental properties and testing of their transferability could be established. More advanced approaches, such as the DFT+ $U(\mathbf{R})$ method, can then be tested versus benchmarks and reliability in examining surface energetics can be tested. The greater use and testing of hybrid functionals would also be a clear avenue of future work if these can be made computationally tractable within a plane-wave basis set approach. Comparison between computation and experiment M-CeO₂ systems will continue be challenged by the structural complexities of these systems. The further development of DFT(+ U)-based reactive force-fields will allow for more direct comparisons that include structural inhomogeneity in doping and nano-structure, and for comparison with experimental properties defined on longer length or time scales accessible to electronic structure methods.

ACKNOWLEDGMENTS: This material is based upon work supported as part of the Center for Atomic Level Catalyst Design, an Energy Frontier Research Center funded by the U.S. Department of Energy, Office of Science, Office of Basic Energy Sciences under Award Number DE-SC0001058.

2.7. References

1. L. C. Hsu, M. K. Tsai, Y. H. Lu, H. T. Chen. *Journal of Physical Chemistry C* **2013**, *117*, 433-441.
2. A. D. Mayernick, M. J. Janik. *Journal of Physical Chemistry C* **2008**, *112*, 14955-14964.
3. J. J. Plata, A. M. Marquez, J. F. Sanz. *Journal of Chemical Physics* **2012**, *136*, 041101.
4. W. L. Cen, Y. Liu, Z. B. Wu, H. Q. Wang, X. L. Weng. *Physical Chemistry Chemical Physics* **2012**, *14*, 5769-5777.
5. N. J. Mosey, E. A. Carter. *Physical Review B* **2007**, *76*, 155123.
6. A. Gupta, U. V. Waghmare, M. S. Hegde. *Chemistry of Materials* **2010**, *22*, 5184-5198.
7. S. Fabris, G. Vicario, G. Balducci, S. de Gironcoli, S. Baroni. *Journal of Physical Chemistry B* **2005**, *109*, 22860-22867.
8. B. Himmetoglu, A. Floris, S. de Gironcoli, M. Cococcioni. *International Journal of Quantum Chemistry* **2013**, *114*, 14-49.
9. L. Wang, T. Maxisch, G. Ceder. *Physical Review B* **2006**, *73*, 195107.
10. Y. H. Tang, H. Zhang, L. X. Cui, C. Y. Ouyang, S. Q. Shi, W. H. Tang, H. Li, J. S. Lee, L. Q. Chen. *Physical Review B* **2010**, *82*, 125104.
11. I. Yeriskin, M. Nolan. *Journal of Physics-Condensed Matter* **2010**, *22*, 135004.
12. H. J. Kulik, N. Marzari. *The Journal of Chemical Physics* **2011**, *135*, 194105.

13. M. V. Ganduglia-Pirovano, J. L. F. Da Silva, J. Sauer. *Physical Review Letters* **2009**, *102*, 026101.
14. J. Graciani, A. M. Márquez, J. J. Plata, Y. Ortega, N. C. Hernández, A. Meyer, C. M. Zicovich-Wilson, J. F. Sanz. *Journal of Chemical Theory and Computation* **2010**, *7*, 56-65.
15. M. Nolan. *Journal of Materials Chemistry* **2011**, *21*, 9160-9168.
16. M. Nolan. *Journal of Physical Chemistry C* **2011**, *115*, 6671-6681.
17. M. D. Krcha, A. D. Mayernick, M. J. Janik. *Journal of Catalysis* **2012**, *293*, 103-115.
18. A. D. Mayernick, M. J. Janik. *Journal of Catalysis* **2011**, *278*, 16-25.
19. R. Li, M. D. Krcha, M. J. Janik, A. D. Roy, K. M. Dooley. *Energy & Fuels* **2012**, *26*, 6765-6776.
20. A. D. Mayernick, R. Li, K. M. Dooley, M. J. Janik. *The Journal of Physical Chemistry C* **2011**, *115*, 24178-24188.
21. M. D. Krcha, M. J. Janik. *Langmuir* **2013**, *29*, 10120-10131.
22. S. Lutfalla, V. Shapovalov, A. T. Bell. *Journal of Chemical Theory and Computation* **2011**, *7*, 2218-2223.
23. Y. Jiang, J. B. Adams, M. van Schilfgaarde. *Journal of Chemical Physics* **2005**, *123*, 064701.
24. M. Nolan, S. Grigoleit, D. C. Sayle, S. C. Parker, G. W. Watson. *Surface Science* **2005**, *576*, 217-229.
25. D. A. Andersson, S. I. Simak, B. Johansson, I. A. Abrikosov, N. V. Skorodumova. *Physical Review B* **2007**, *75*, 035109.
26. J. F. Herbst, R. E. Watson, J. W. Wilkins. *Physical Review B* **1978**, *17*, 3089-3098.
27. A. M. Burow, M. Sierka, J. Dobler, J. Sauer. *Journal of Chemical Physics* **2009**, *130*, 174710.

28. D. Fernandez-Torre, K. Kosmider, J. Carrasco, M. V. Ganduglia-Pirovano, R. Perez.
Journal of Physical Chemistry C **2012**, *116*, 13584-13593.

Chapter 3

Periodic Trends of Oxygen Vacancy Formation and C-H Bond Activation over Transition Metal-Doped CeO₂ (1 1 1) Surfaces

This chapter is published as: M. D. Krcha, A. D. Mayernick, M. J. Janik. *Journal of Catalysis* **2012**, 293, 103-115.

ABSTRACT: Substitutional transition metal dopants in the cerium oxide surface can alter the surface reducibility and catalytic activity for hydrocarbon conversion. Density functional theory (DFT+*U*) methods are used to examine the electronic and structural effects of transition metal dopants (groups IV through XII) in the CeO₂ (1 1 1) surface. Surface reducibility (oxygen vacancy formation) and dissociative adsorption of methane (forming H* and CH₃*) are considered. Both the methane dissociative adsorption energy and activation barriers correlate linearly with the surface oxygen vacancy formation energy. Charge analysis is used to determine the role of dopant metal in serving as a reduction center or altering the Ce reducibility. Dopants in groups IV and V alter the reducibility of the surface and dopants in groups X through XII become the reduction center. The dopant plays the same role in both oxygen vacancy formation and methane adsorption. A Brønsted-Evans-Polanyi relationship is established between the methane activation barrier, through H-abstraction, and the dissociative adsorption energy. The sensitivity of quantitative and qualitative trends to the inclusion of *U*-terms for the dopant transition metal d-states is considered. The optimal M/CeO₂ dopant for methane conversion to CO or CO₂ follows a volcano relationship with oxygen vacancy formation: highly reducible surfaces will be limited by re-oxidation whereas surfaces difficult to reduce will show high barriers for C-H bond activation. Transition metal dopants near the peak region of the volcano are Pd, Co, Ni, and Mn.

3.1. Introduction

Transition metal oxides can form a solid solution with ceria (CeO_2) that alters redox properties¹⁻³ and hydrocarbon conversion activity relative to pure CeO_2 .⁴⁻¹⁰ At relatively low M inclusion in $\text{M}_{1-x}\text{Ce}_x\text{O}_2$, the ceria fluorite lattice is maintained and the added transition metal can substitutionally dope into the Ce lattice positions.^{6-7,11-13} The dopant metal may either alter the reducibility of the ceria metal atoms or the dopant can become the reduction center.¹⁴⁻¹⁷ Several experimental^{8-13,18-19} and theoretical studies^{1-3,20-29} have examined how one or two transition metal dopants can affect the activity of the ceria surface; however an electronic level explanation remains incomplete. For example, density functional theory (DFT) studies have demonstrated that Pd becomes the reduction center for O-vacancy formation or methane conversion when doped into CeO_2 .²⁷⁻³⁰ Herein, density functional theory (DFT+ U) is used to examine the energetic and electronic structure effects of all Groups IV-XII transition metal dopants on CeO_2 (1 1 1) reducibility and C-H bond activation.

Cu,^{9,31} Pd,^{6-7,32} and Zr^{9,11-13} doped CeO_2 materials, with the transition metal substituting for Ce at fluorite lattice sites, have been synthesized and examined for catalytic applications. With the choice of optimal dopant and its concentration, the catalytic activity can be improved for preferential CO oxidation,³¹ catalytic oxidation of hydrocarbons⁸⁻¹⁰ and in the water-gas-shift reaction.³³ The hydrocarbon conversion activity of CeO_2 can be improved with a CeO_2 - ZrO_x solid solution, with a maximum catalytic activity demonstrated at $\text{Ce}_{0.92}\text{Zr}_{0.08}\text{O}_2$.⁹ A further improvement in the activity of the catalyst can be achieved with small amounts of MnO_x or CuO dissolved into the solid solution of CeO_2 - ZrO_x .⁹ Avgouropoulos and Ioannides showed that ultrafine, nanocrystalline Cu/ CeO_2 catalysts are very active and stable in the selective oxidation of CO.³¹ Palladium doped CeO_2 has also been shown to be a good catalyst for methane oxidation.^{6,32} $\text{Pd}^{\delta+}$

substitutionally mixed in the lattice of CeO_2 has a higher CH_4 oxidation rate per mass of Pd than Pd supported on the surface or pure CeO_2 .⁶

The capability of some transition metals to substitutionally dope as well as modify the reducibility or catalytic activity of ceria is established. Mixtures of zirconia oxide and cerium oxide can form solid solutions, which are more thermally stable and reducible than pure ceria.¹¹⁻¹³ Zirconia doped into the cerium oxide lattice results in replacement of Ce with Zr in the lattice.¹²⁻¹³ The addition of Zr into the lattice of CeO_2 results in a greater mobility of oxygen atoms in the lattice. The bulk diffusion coefficient of O^{2-} ions increases by 2 orders of magnitude with Zr in the lattice, as measured by ionic conductivity.¹¹ Palladium can also be incorporated into the lattice of CeO_2 using a solution-combustion synthesis.⁶⁻⁷ The Pd/ceria mixture that was prepared by this method contains Pd^{2+} cations incorporated into the cubic fluorite lattice, as identified by XPS, X-ray diffraction (XRD) and extended X-ray absorption fine structure (EXAFS).⁷ Colussi et al. also showed that Pd^{2+} ions are substituted for Ce^{4+} using high-resolution transmission electron microscopy (HRTEM), with image interpretation aided by DFT calculations.⁶ We seek to establish periodic trends across transition metals for their impact on both reducibility and oxidation activity as well as to correlate these two properties.

Though the aforementioned studies demonstrate the potential of $\text{M}_x\text{Ce}_{1-x}\text{O}_2$ materials to enhance catalytic activity, it is extremely difficult to construct experimental model systems for these catalysts. As such, active site identification and elementary reaction mechanism determination is challenging. For example, the majority of these studies do not attempt to report turnover frequency values as the counting of active sites for $\text{M}_x\text{Ce}_{1-x}\text{O}_2$ materials is not trivial. Further, the complex materials used in these studies surely expose a range of surface structures. Density functional theory may be used to construct models of active sites in these systems and examine the impact of site structure on surface properties.

Several computational studies have examined model surfaces with transition metals doped or absorbed onto cerium oxide. Similarly to the experimental studies, some of the dopants that have been thoroughly examined are Au,^{20,22-23} Cu,^{3,24,26} Pd,^{3,21,25,27-29} and Zr,^{1,16,34-35} with concentration on surface reducibility as well as CO, CH₄, H₂, or H₂O interactions with the surface. Using Au as a dopant in the CeO₂ lattice for CO oxidation allows the surface oxygen atoms to become reactive, but not too reactive that the oxygen vacancies will not heal. With Cu doped in the surface of CeO₂, formation of the first oxygen vacancy is spontaneous (leading to Cu²⁺) and a second vacancy forms with less endothermic energy than for pure CeO₂.³⁶ Several studies examined how Pd-doped into the surface of CeO₂ can affect methane oxidation activity and vacancy formation. Our group previously reported that the vacancy formation energy and the methane adsorption energy of Pd-doped CeO₂ are correlated over different surface terminations.²⁷ Upon the formation of an oxygen vacancy, a Pd⁴⁺ dopant is reduced to a Pd²⁺ state.^{21,25,27} When Zr is doped into the lattice of CeO₂, it takes on a Zr⁴⁺ oxidation state.¹ Upon the formation of a surface oxygen vacancy, two cerium atoms reduce rather than the zirconia.³⁴ High-valence dopants have only a local effect on oxygen atoms next to them whereas low-valence dopants have both long and short-range effects.³⁷ We extend upon these studies by 1) examining reducibility and C-H bond activation across *d*-block dopants, and 2) examining the variance of energetics with inclusion of a *U*-correction terms for dopant *d*-states.

This study examines the effect of transition metal dopants in the lattice of CeO₂ on oxygen vacancy formation and dissociative methane adsorption. We have previously observed a correlation between the vacancy formation energy and the dissociative adsorption energy of methane for various surface terminations of Zr- and Pd-doped CeO₂.²⁷ We demonstrate that this same correlation holds true across transition metal dopants. The ability of a M-doped CeO₂ to serve as a hydrocarbon oxidation catalyst depends upon the ability to activate C-H bonds and to heal oxygen vacancies. A volcano relationship is expected between oxidation activity and reducibility of the

surface: dopants leaving the surface too reducible are limited by the ability to heal vacancies, those not reducible enough are limited by slow C-H bond activation. The DFT+ U method is used to examine the electronic and structural effects of the various dopants. Periodic trends are demonstrated for the oxidation states of dopants before and after surface reduction.

3.2. Methods

3.2.1. Electronic structure method

Calculations were carried out using the Vienna *ab initio* simulation program (VASP), an *ab initio* total-energy and molecular dynamics program developed at the Institute for Material Physics at the University of Vienna.³⁸⁻⁴⁰ The projector augmented wave (PAW) method is used to represent the ion-core electron interactions.⁴¹ The valence electrons were represented using a plane wave basis set with an energy cutoff of 450eV. All calculations were spin polarized. The valence configuration for cerium was $5s^25p^66s^24f^5d^1$, $2s^22p^4$ for oxygen, $1s^1$ for hydrogen and $2s^22p^2$ for carbon. Valence configurations for the metal dopants considered are given in Table A-2. k -point sampling of (2 x 2 x 1) was performed using the Monkhorst Pack scheme,⁴² with the third vector perpendicular to the surface. The Perdew-Wang (PW91) version of the generalized gradient approximation (GGA) was used to incorporate exchange and correlation energies.⁴³ Forces on all atoms were minimized to $0.05 \text{ eV}\cdot\text{\AA}^{-1}$ using structural optimization steps. A force convergence criteria of $0.02 \text{ eV}\cdot\text{\AA}^{-1}$ was tested, for oxidized and reduced systems with three dopants, and the maximum absolute total energy difference was less than 0.02 eV from a convergence criteria of $0.05 \text{ eV}\cdot\text{\AA}^{-1}$. The convergence criteria of $0.05 \text{ eV}\cdot\text{\AA}^{-1}$ required significantly less computational time with no significant sacrifice in accuracy.

DFT has difficulties accurately representing the nature of $4f$ orbitals of cerium,⁴⁴⁻⁴⁶ therefore we implemented the DFT+ U approach.⁴⁷⁻⁴⁸ The DFT+ U method introduces an on-site Coulombic interaction (U -term) which penalizes non-integer occupation of localized orbitals, effectively penalizing delocalization of electrons. We introduced a U -term on the $4f$ orbitals of ceria to properly describe the localization of electrons in reduced cerium oxide (CeO_{2-x}). We used a U -value of 5 eV, which is consistent with values used in previous DFT studies of ceria.^{1,20,25,27-29,35,49-51} Our previous study examined the dependence of oxygen vacancy and methane activation on the Hubbard U -term on CeO_2 and $\text{Pd}_x\text{Ce}_{1-x}\text{O}_2$. The vacancy formation (ΔE_{vac}) and methane adsorption (ΔE_{ads}) energies increase in exothermicity linearly with increasing Ce f U -value,²⁷ though there is only a slight slope for $\text{Pd}_x\text{Ce}_{1-x}\text{O}_2$. With this dependence of vacancy formation and methane adsorption energies on the U -value, all quantitative results are inherently dependent on the U -value. The U -value of 5 eV accurately describes the electronic structure of reduced ceria and provides qualitative comparisons for the oxygen vacancy formation energies as well as the adsorption energies of methane.

DFT is also known to have difficulty representing d -states of metal oxides.^{26,52} We did not generally include a U -correction term for the d -states of metal dopants. We examined the addition of a d U -term on two dopants, V and Mn, to evaluate the quantitative and qualitative impact on energetics and electronic structure. Different U -values on the d -states of Mn and V can change the oxidation state of Mn and V in a reduced surface as well as the vacancy formation energy. As will be discussed in Section 3.3.2, we observed that reduction of M- CeO_2 typically results in electrons localizing on Ce or dopant metal atoms, and significant delocalization is not observed.

3.2.2. Surface models

The ceria (1 1 1) surface is modeled as a slab of cubic fluorite CeO₂ separated by 15 Å of vacuum space in the direction perpendicular to the surface. The bulk CeO₂ crystal structure is the same as used in previous work, and the methods used herein replicate the experimental lattice constant with 1% deviation.²⁷ A $p(2 \times 2)$ expansion of the surface unit cell is used. The (1 1 1) surface is used as it is the lowest energy surface among single crystal terminations of ceria^{22,27,53} and therefore will represent a large portion of a polycrystalline CeO₂ surface. Mirrored slabs of 12 atomic layers (Ce₁₆O₃₂) were chosen to model the CeO₂ surface, with the number of layers converged to surface formation energy and vacancy formation energy. Mirrored slabs were chosen to minimize the spurious slab to slab interactions that can result from a net surface dipole moment upon the formation of oxygen vacancies or methane adsorption. This surface model will result in a surface termination of four oxygen atoms per side of the unit cell. In the layer below there are 4 Ce atoms, as seen in Figure 3-1. All layers were relaxed during structural optimization. With a small number of M dopants, 12 atomic layers are not sufficient to prevent the top and bottom surfaces from interacting, and the slabs become asymmetric upon optimization. In these cases, as noted when presented below, the number of layers was increased to 15, 18 and 21 atomic layers. Table A-3 contains dissociative methane adsorption and oxygen vacancy formation energies for 12, 15 and 18 atomic layers for Ag, V and W-doped CeO₂.

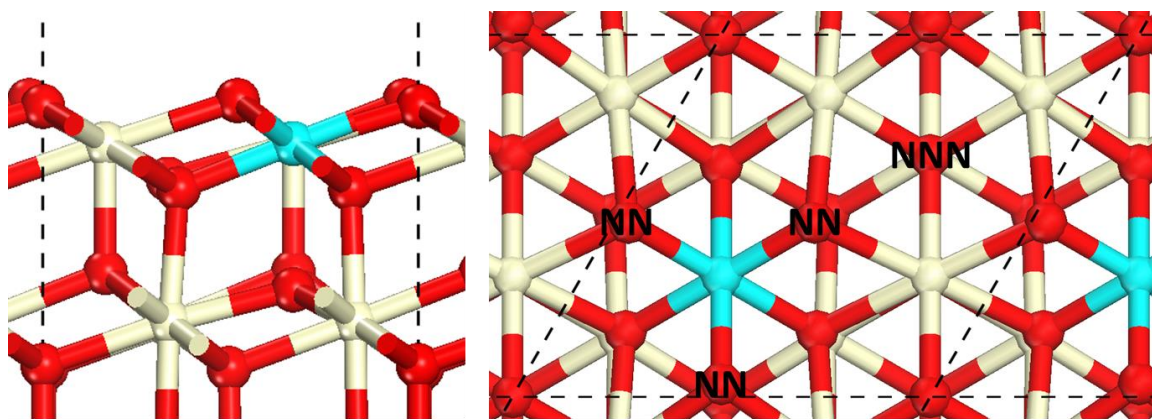


Figure 3-1. Side and top views of the slab model of M-doped CeO_2 (1 1 1). Ce is displayed as tan (light), M-dopant as light blue (gray), and O as red (dark). The three nearest neighbors (NN) and the next nearest neighbor (NNN) oxygen atom to the dopant are labeled.

A non-mirrored slab of 12 atomic layers is used when locating the methane C-H bond dissociation activation barriers. Dissociative methane adsorption energies for 6, 9 and 12 atomic layers on non-mirrored V and W-doped CeO_2 slabs is contained in Table A-3. With the introduction of the non-mirrored slab, a net surface dipole moment can develop. To decrease the effect of this spurious interaction on energetics, dipole corrections are added to the calculations within the electronic self-consistent field cycle.⁵⁴⁻⁵⁵ A comparison of mirrored slab with non-mirrored, dipole corrected results can be found in Section 3.3.4.2.1. The bottom three atomic layers of the non-mirrored slab were held fixed at the lattice positions of bulk CeO_2 .

The surfaces of the mirrored slab of CeO_2 were “doped” by substituting for one surface cerium atom on each side of the mirrored surface, as can be seen in Figure 3-1. The dopant is forced into CeO_2 without regard for stability of the dopant to enter the lattice, or to take on a 4+ oxidation state. For some dopants, the 4+ oxidation state is relative unstable and oxygen vacancy formation is exothermic. The dopants considered in this study are the first three rows of transition metals in groups IV to XII, other than the synthetic technetium (Tc) atom. Similarly, in the non-mirrored

models, one surface cerium atom on one surface is replaced with the dopant. The replacement of one cerium atom on each surface represents a 25% dopant surface concentration. The surface cell lateral dimensions were not allowed to relax, thus neglecting any possible changes in the optimal lattice parameter due to the dopant. This model represents a hypothetical system with surface segregation of a low bulk concentration dopant.

The starting geometry of the reduced or $(\text{CH}_3 + \text{H})^*$ system can have a great effect as to whether the system finds a local versus a global minimum energy structure. Depending upon the starting geometry of the system, the two electrons freed by reduction can localize on different metal atoms. To check whether the system reached a global minimum, slight variations to the starting structure were made and the structure optimized. For example, the cerium atoms near an oxygen vacancy can be motivated to reduce, by perturbing the initial positions towards the vacancy relative to their original lattice positions. For some dopants, the dopant will reduce if this perturbation is not made, regardless of which is a lower energy structure. The lowest energy structure located is reported, unless noted otherwise.

3.2.3. Oxygen vacancy formation energy

Reduced surfaces of CeO_2 were optimized by removing one surface oxygen atom, creating a 25% vacancy concentration in the surface. To maintain mirrored slab symmetry, one surface oxygen atom was removed from each slab side. Even though the subsurface oxygen vacancies in pure CeO_2 (1 1 1) have lower vacancy formation energies;⁵⁶ surface vacancies were mainly examined. For some dopants (Ir, Os, Re and Ru) subsurface oxygen vacancies were optimized and their vacancy formation energy is less than for their surface oxygen vacancy counterpart (Table A-1). We mainly consider surface vacancies because the surface oxygen would be expected to participate in the methane oxidation reaction, and it provides a measure of surface reducibility

that is found to correlate with activity for C-H dissociation. The surface oxygen atom that was removed is a nearest-neighbor oxygen atom to the dopant (an oxygen atom coordinated to the dopant).

The oxygen vacancy formation energy is calculated as:

$$\Delta E_{vac} = \frac{E_{Ce_nO_{2n-2}} + E_{O_2} - E_{Ce_nO_{2n}}}{2} \quad (1)$$

where $E_{Ce_nO_{2n-2}}$ is the energy of the reduced unit cell, E_{O_2} is the energy of a gas-phase O_2 molecule, $E_{Ce_nO_{2n}}$ is the energy of the stoichiometric surface slab, and the division of two results from the use of a mirrored slab. Due to the well-established DFT overestimation of the O_2 binding energy, the oxygen vacancy formation energies reported in this study cannot be directly compared with experimental reduction enthalpies.⁵⁷ A correction term can be added to the O_2 binding energy to directly compare with experiment. Mayernick illustrated that the oxygen vacancy formation energy of bulk CeO_2 doped with Zr from DFT+ U agrees well with the oxidation enthalpy determined experimentally.²⁷ In this study, trends are examined rather than absolute values, and therefore a constant correction is not applied. Zero-point vibrational energy and temperature free energy corrections were not added to the electronic energy herein because these corrections will be similar across all dopants and trends are of interest.

3.2.4. Methane dissociative adsorption energy

The dissociative adsorption of methane on the surface of CeO_2 was considered by adding CH_3^* and H^* adsorbates on each surface side. Molecular adsorption of methane is weak to all surfaces (<0.05 eV) due to the lack of dative bonding and the underestimation of non-bonded Van

der Waals interactions with the PW91 exchange-correlation functional. Dissociative adsorption places H* and CH₃* fragments atop of two different surface oxygen atoms. The energy of dissociative adsorption of methane was calculated as:

$$\Delta E_{ads} = \frac{E_{2(CH_3^* + H^*)} - (E_{Ce_nO_{2n}} + 2E_{CH_4})}{2} \quad (2)$$

where $E_{2(CH_3^* + H^*)}$ is the energy of a surface slab with adsorbed H* and CH₃* fragments on each side, $E_{Ce_nO_{2n}}$ is the energy of the clean surface, and E_{CH_4} is the energy of an isolated CH₄ molecule. Dividing by two accounts for the use of a mirrored slab.

3.2.5. Methane activation barriers

This study examines the first C-H bond activation involved in the dissociative adsorption of methane. The first C-H bond activation is the rate limiting step in methane combustion over the clean CeO₂ (1 1 1) surface.^{29,58} A 12 atomic layers, non-mirrored slab is used to calculate the methane activation barrier. To isolate the transition state for CH₄(g) → CH₃* + H*, we used the climbing image nudged elastic band method (CI-NEB).⁵⁹⁻⁶¹ The CI-NEB method uses a series of images along the reaction path, with the images optimized while constrained along the reaction coordinate. The highest energy image is made to climb along the minimum energy path to estimate the saddle point.⁶⁰ The transition state was identified as the highest energy image with a force tangent to the reaction coordinate less than 0.05 eV·Å⁻¹ as well as all atomic forces less than 0.05 eV·Å⁻¹. The harmonic vibrational modes were calculated for the transition state image to confirm a single imaginary vibrational frequency.

3.3. Results and discussion

The (1 1 1) surface of CeO₂ can be doped with various transition metals, which can alter the reducibility of the doped surface as well as the activity of C-H bonds on the surface. First a correlation between C-H bond activation and surface reducibility is illustrated in Section 3.3.1. We then examine density of states and orbital images to identify what atoms reduce their oxidation state when the surface of doped CeO₂ is reduced in Section 3.3.2. In Section 3.3.3, the Bader atoms-in-molecules method and the site projected charge method are examined for their utility to rapidly identify what atoms reduce. With a method that can rapidly identify which metal atoms reduce, the reduction of the doped surface is examined in Section 3.3.4. To reduce the surface, one surface oxygen atom is removed from the surface and the electronic structure along with the vacancy formation energies in the surfaces are reported in Section 3.3.4.1. In Section 3.3.4.2, the dissociative adsorption of methane on the surface is examined and similarities to oxygen vacancy formation are drawn. A Brønsted-Evans-Polanyi (BEP) is developed for the dissociative adsorption of methane on the surface. The catalytic implications in choosing the optimal dopant for hydrocarbon conversion are discussed.

3.3.1 Correlation of C-H bond activation and surface reducibility

Figure 3-2 displays a correlation of the C-H bond activation of methane (ΔE_{ads}) and the surface reducibility (ΔE_{vac}) of the CeO₂ (1 1 1) surface doped with the transition metals. The vacancy formation energies and methane adsorption energies (ΔE_{vac}) are given in Table A-4. All dopants shift the vacancy formation energy to less endothermic values relative to pure CeO₂ (1 1 1). For the pure CeO₂ (1 1 1), surface ΔE_{vac} is 2.76 eV and ΔE_{ads} is -0.76 eV. The correlation between C-H bond activation and surface reducibility has been established over Zr-doped and Pd-

doped CeO₂ (1 1 1), (1 1 0), and (1 0 0) surfaces by Mayernick and Janik.²⁷ The data in Figure 3-2 indicates that this correlation exists across numerous transition metal surface dopants. The following dopant metals decrease the vacancy formation energy (increase the reducibility) and decrease the methane adsorption energy (increase the C-H bond activity) below that of Pd: Co, Sc, Ni, Ag, Hg, Cd, Cu, and Zn. Nickel-ceria exhibits catalytic activity for steam reforming.⁶²⁻⁶³ Both steam reforming and direct oxidation require facile C-H bond breaking.

Neglecting stability considerations, these calculations would suggest any dopants appearing to the left of Pd in Figure 3-2 could impart greater methane conversion catalytic activity than Pd_xCe_{1-x}O₂. Methane oxidation activity, however, also requires refilling of the oxygen vacancy created by desorption of H₂O(g), CO, or CO₂(g). Effectively, we expect that some of the dopants will be highly unstable in the MO₂ stoichiometry, and will show little catalytic activity due to an inability to reach this 4+ oxidation state. Transition metals which appear to the left of the dashed line in Figure 3-2 correspond to those that lower the oxygen vacancy formation energy to the extent that refilling of the vacancy from O₂ (g) ($E_{vac} = -E_{refill}$) at 0 K is more difficult than the 0 K methane activation barrier. This line would then estimate the peak of a volcano curve, though a more precise estimate requires considering the actual hydrocarbon and O₂ chemical potentials in the reacting environment. Stability considerations and re-oxidation requirements therefore suggest Mn, Pd, Co, Au, Ni and Pt as interesting candidates for providing potential for improved methane combustion activity. Differentiation among these would portray greater accuracy than our calculations contain, when taking into account the absolute variance with U -values and the range of local dopant configuration likely exposed in a real catalyst.

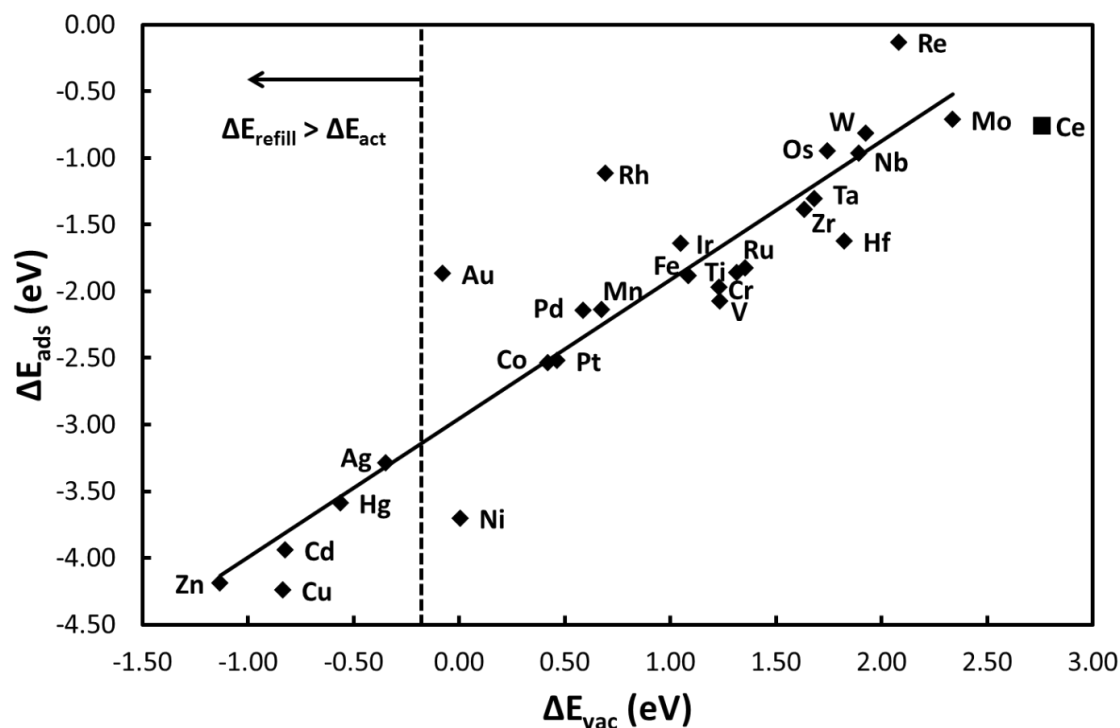


Figure 3-2. Methane dissociative adsorption energy (ΔE_{ads}) vs. oxygen vacancy formation energy (ΔE_{vac}). The point for pure CeO_2 (1 1 1) is labeled as a square. The energy to refill oxygen vacancies ($-\Delta E_{vac} = \Delta E_{refill}$) from $\text{O}_2(\text{g})$ at 0 K is greater than the methane activation barrier to the left of the dashed line.

As described above in Section 3.2.3, a subsurface oxygen vacancy is more stable for some dopants than a surface oxygen vacancy. After a surface oxygen vacancy is formed, a subsurface oxygen could move to the surface leaving a subsurface vacancy. Were this to occur, the reaction energy/barrier for the oxygen vacancy refilling step in the mechanism would increase. This increase in energy for the oxygen vacancy refilling step would shift the peak volcano plot to the left for dopants where a subsurface oxygen vacancy is much more stable than a surface oxygen vacancy.

We examine the electronic structure of the intact and reduced M/CeO_2 (1 1 1) surfaces to characterize the role the dopant metal plays in reducibility and C-H bond activation.

3.3.2. Density of States and Orbital Imaging

When the (1 1 1) surface of a doped cerium oxide is reduced, two electrons previously involved in M-O bonding return to reduce metal atoms. The surface dopant may serve as the reduction center, with both electrons occupying states associated with the d -orbitals of the dopant. Both electrons may instead localize in Ce f -states, with the dopant altering the Ce reducibility. A third possibility is that one of the two electrons localizes on M d -states and the second in a Ce f -state. When the electrons localize in the Ce f -states and some M-dopant d -states, an occupied electronic state appears between the top of the valence band and the bottom of the conduction band.

The transition metal dopant may serve as the reduction center (M^{n+} to $M^{(n-2)+}$) when an oxygen vacancy is formed. The occupied d orbital then occurs between the valence band and the conduction band in the reduced state. If two electrons localize on the dopant, they typically occupy the same orbital. Figure 3-3 illustrates the density of states and orbital images for intact and reduced Ag-doped CeO₂ (1 1 1). In the intact surface, Ag⁴⁺ is a d^7 metal, and a number of unoccupied d -states appear in the CeO₂ band gap. Upon surface reduction, Ag⁴⁺ is reduced to Ag²⁺ and Ag gap states move below the Fermi level (Figure 3-3b) with ΔE_{vac} of -0.35 eV. For dopants which serve as 2e⁻ reduction centers, no occupied Ce f -states are observed in the DOS plot, which is further confirmed through projected DOS analysis and atomic charge variations, as discussed in Section 3.3.3. Figure 3-3c images the occupied gap states formed upon Ag/CeO₂ reduction, showing clearly they are rather local to the Ag dopant. Most late transition metal dopants serve as 2e⁻ reduction centers as discussed in Section 3.3.4. For these metals, we expect the absolute value of the surface vacancy formation energy to be dependent on the value of any U -term applied to the dopant d -states. Any applied U -values will further motivate localization to the d -states.

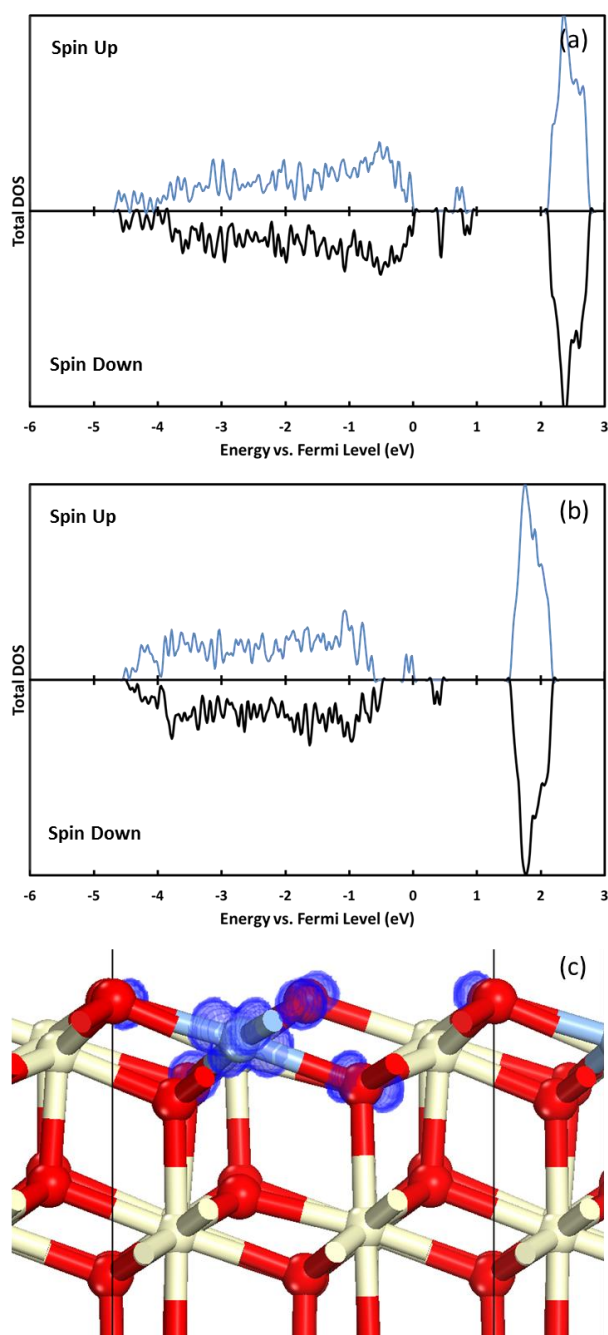


Figure 3-3. Total DOS plotted versus energy (referenced to Fermi level) for (a) intact Ag-doped CeO₂ (1 1 1), and (b) oxygen vacant Ag-doped CeO₂ (1 1 1). Spin-down density of states is plotted on the negative y axis. (c) Isodensity surfaces representing electronic states for oxygen vacant Ag-doped CeO₂ over the energy range -0.23 to 0.00 eV (relative to Fermi level).

The density of states and select orbital images for intact and reduced V-doped CeO₂ (1 1 1) can be seen in Figure 3-4. In the intact surface, the vanadium dopant takes on the V⁵⁺ (*d*⁰) oxidation state. There is one filled orbital that appears between the valence band and the conduction band which is attributed to the reduction of one Ce⁴⁺ to Ce³⁺. This orbital is imaged in Figure 3-4b, and is clearly a localized Ce *f*-electron. The cerium atom reduces to accommodate the excess electron from the vanadium being in a 5+ oxidation state. Upon vacancy formation, the vanadium stays in a 5+ oxidation state and two additional cerium atoms reduce from Ce⁴⁺ to Ce³⁺, with additional gap states being formed (Figure 3-4c). The difference in the three localized *f*-state energies can be attributed to a difference in relative position of the reduced Ce atoms to the surface, vacancy, or dopant. Figure 3-4d illustrates the 3 local *f*-electrons on Ce³⁺ atoms in the reduced state. The V atom dopant alters the reducibility of the cerium atoms, as ΔE_{vac} of V-doped ceria is 1.23 eV compared to 2.76 eV for pure CeO₂ (1 1 1). No additional *d*-state orbitals are filled upon the reduction of the surface. Most early transition metal dopants alter the reducibility of the surface and the cerium atoms reduce as discussed in Section 3.3.4.

With the addition of a *U*-value on the *d*-states of vanadium, the role that vanadium plays in the intact surface and when the surface is reduced can change. Using a recommended *U*-value of 3.1 as described by Wang, Maxish and Ceder,⁵² which was determined by matching magnetic moments and band gaps of VO, VO₂, V₂O₃ and V₂O₅ to experimental data, vanadium in the fully oxidized, intact state becomes V⁴⁺ rather than V⁵⁺ with no *d*-state *U*-term. With the formation of an oxygen vacancy, the oxidation state of the V-dopant remains V⁴⁺ with two cerium atoms reducing. The oxygen vacancy formation energy with a *U*-value of 3.1 becomes 1.18 eV, a shift of only 0.05eV relative to no *U* inclusion on V *d*-states.

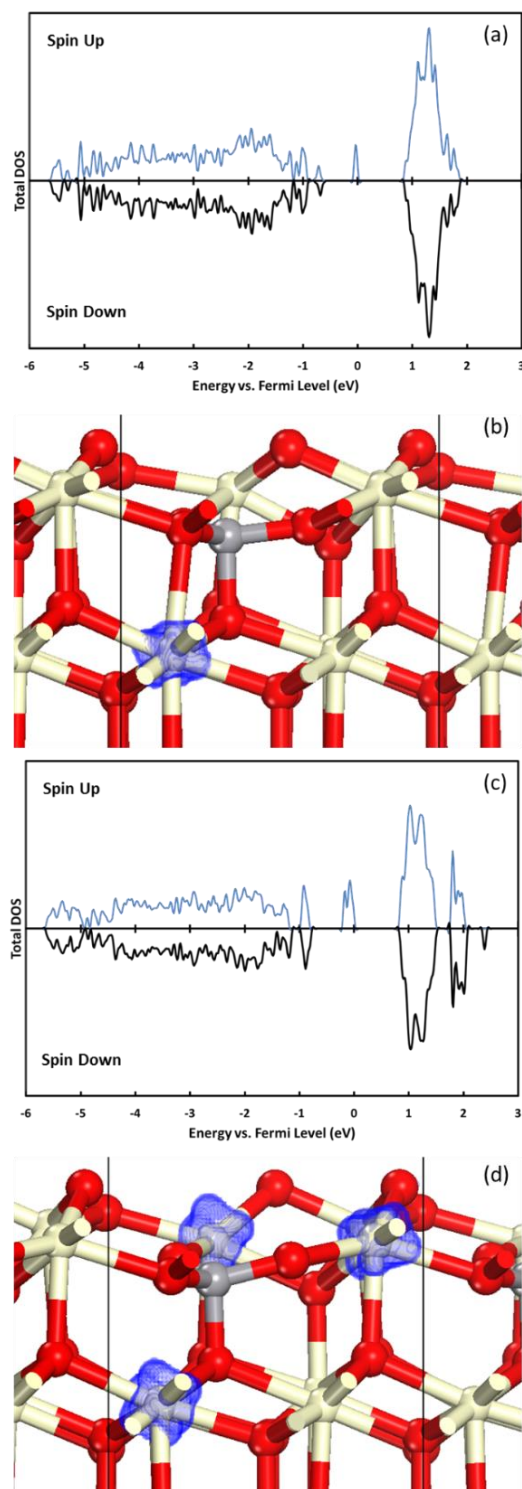


Figure 3-4. Total DOS plotted versus energy (referenced to Fermi level) for (a) intact V-doped CeO_2 (1 1 1), and (c) oxygen vacant V-doped CeO_2 (1 1 1). Spin-down density of states is plotted on the negative y axis. Isodensity surfaces representing electronic states for (b) intact V-doped CeO_2 over the energy range -0.19 to 0.00 eV (relative to Fermi level) and (d) oxygen vacancy V-doped CeO_2 over the energy range -0.37 to 0.00 eV.

For some middle *d*-block dopants, the dopants serves as a $1e^-$ reduction center and the second electron localizes in a Ce *f*-state. Two occupied orbitals form between the valence band and the conduction band, one for the $1e^-$ reduction on the dopant and the second for the electron localizing in the *f*-state of ceria. The $1e^-$ on the dopant results in a single spin state on the dopant. The density of state and orbital images for intact and reduced Mn-doped CeO₂ (1 1 1) are illustrated in Figure 3-5. In the intact surface, Mn⁴⁺ is a *d*³ metal, and a number of *d*-states appear in the CeO₂ band gap. Upon surface reduction, Mn⁴⁺ is reduced to Mn³⁺ and one Ce⁴⁺ is reduced to Ce³⁺ with additional gap states being formed (Figure 3-5b). In the case of Mn-doped CeO₂, the addition and value of a *U*-term to the *d*-states of Mn can change whether Mn serves as a $1e^-$ reduction center (with one Ce being reduced) or as a $2e^-$ reduction center with no Ce being reduced. With no *U*-term on the *d*-states of Mn, Mn serves as a $1e^-$ reduction center. Using a recommended *U*-value of 4 as described by Wang, Maxisch and Ceder,⁵² the most stable vacant structure has Mn serving as a $2e^-$ reduction center. The oxygen vacancy formation energy in Mn-doped CeO₂ decreases from 0.68 eV with no *U* on the *d*-states of Mn to -0.13 eV with a *U*-value of 4. Figure 3-6 illustrates the DOS and orbital images with a *U*-value of 4 on the *d*-states of Mn for the intact Mn-doped CeO₂ and Mn²⁺ oxygen vacant surface. Further discussion and implications of incorporating a *U*-value on the *d*-states of Mn-doped in CeO₂ is discussed in Chapter 4. Clearly, the inclusion of a *U*-term for the Mn *d*-states has significant impact on the calculated reducibility of the surface. The 0.81 eV variation in ΔE_{vac} , however, would still keep Mn in the range of encouraging dopants for hydrocarbon oxidation in Figure 3-2.

Though DOS and PDOS examination together with orbital imaging can provide a clear picture of the electronic modifications upon surface reduction, we evaluated atomic charge assignment schemes to provide a rapid and quantitative measure.

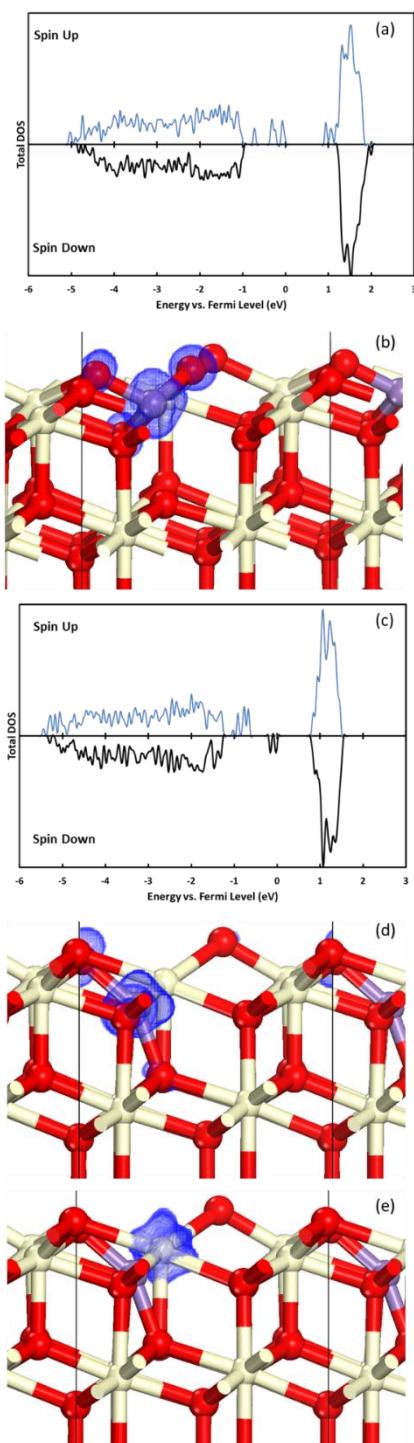


Figure 3-5. Total DOS plotted versus energy (referenced to Fermi level) for (a) intact Mn-doped CeO₂ (1 1 1), and (c) oxygen vacant Mn-doped CeO₂ (1 1 1). Spin-down density of states is plotted on the negative y axis. Isodensity surfaces representing electronic states for (b) intact Mn-doped CeO₂ over the energy range -0.87 to 0.00 eV (relative to Fermi level) and oxygen vacancy Mn-doped CeO₂ over the energy range (d) -1.06 to -0.66 eV and (e) -0.39 to 0.00 eV.

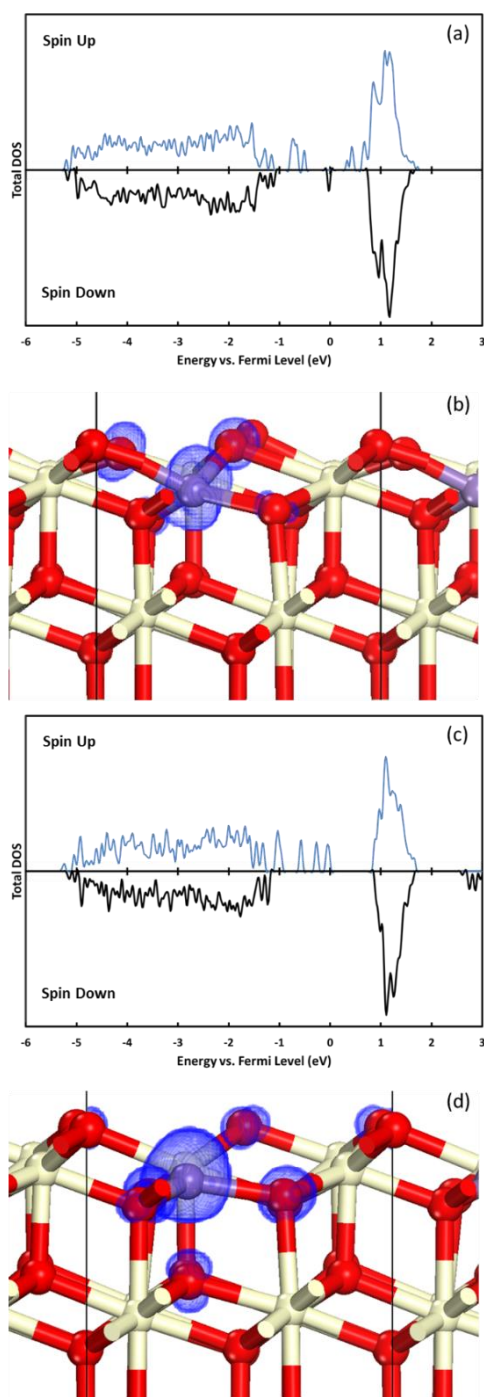


Figure 3-6. Total DOS plotted versus energy (referenced to Fermi level) for (a) intact Mn-doped CeO₂ (1 1 1), and (c) oxygen vacant Mn-doped CeO₂ (1 1 1) with Mn²⁺. Spin-down density of states is plotted on the negative y axis. Isodensity surfaces representing electronic states for (b) intact Mn-doped CeO₂ over the energy range -0.90 to 0.00 eV (relative to Fermi level), and (d) oxygen vacancy Mn-doped CeO₂ with Mn²⁺ over the energy range -1.17 to 0.00 eV. These results were obtained with a U -value of 4.0 on the d -states of Mn, in addition to the U -value of 5 for Ce f -states.

3.3.3. Site projected charge method

Though orbital imaging is useful in analyzing the electronic role of the dopant metals in CeO_2 , we desire a more facile method that uses atoms charge assignments. A popular method to identify the atoms that reduce is the Bader atoms-in-molecules method.¹⁴⁻¹⁷ In this method, atoms are divided by “zero-flux surfaces” which are 2-D planes where the gradient of the charge density is perpendicular to the plane.⁶⁴⁻⁶⁶ Using these surfaces, the volume drawn around each atom is variable. For our purposes, having a variable volume can lead to greater ambiguity in assigning atomic charges. Further, Bader volume determination should include core electron wave functions, and this requires a prohibitively fine grid with Ce and the PAW method. We found Bader charges based solely on valence electron distribution inconclusive in identifying which cerium atoms are in the 4+ oxidation state versus the 3+ oxidation state.

The site projected charge method proved reliable in determining whether individual Ce atoms are in the 4+ or 3+ oxidation state. In this method, the Wigner Seitz radius (RWIGS) is specified for each atom type. To identify the optimal value of RWIGS to differentiate 4+ and 3+ Ce atoms, a system with known Ce^{3+} atoms was used. The reduced cerium atoms were identified using projected DOS and orbital imaging. The value for RWIGS on the cerium was varied from 1.2 to 0.5 Å. As discussed in Appendix A.1 (Figure A-1), a value of 0.7 Å provided the largest charge difference between Ce^{4+} and Ce^{3+} atoms while maintaining a small difference among Ce^{4+} atoms.

3.3.4. Periodic trends in dopant effects on surface reducibility

In this section, we use site projected charges to determine how many Ce^{3+} ions are present in the intact, vacant and $\text{CH}_3^* + \text{H}^*$ states. The charge on the dopant metal atom is assigned based on the total Ce charge and assigning all O atoms as 2.

3.3.4.1. Vacancy formation

Substitutions of transition metal dopants into the intact surface of CeO_2 leads to structural rearrangement, often altering the coordination number of the dopant compared to the 7 coordinated surface Ce atoms. The dopant can coordinate with anywhere from 3 to 7 O atoms in its first coordination shell, as illustrated in Figure 3-7. In a trigonal pyramidal arrangement (Figure 3-7a) the dopant prefers to locate in an O subsurface plane below the uppermost Ce plane. The most common coordination environment for the transition metal dopants is 4, either in a tetrahedral arrangement (Figure 3-7b) or a square planar arrangement (Figure 3-7c). Appendix A.2 details a structural assignment categorization scheme and reports all coordination numbers and environments for dopants in the fully oxidized and reduced structures (Table A-5) as well as figures to illustrate all configurations (Figures A-4 – A-6). The distances between the seven (six for oxygen vacant) closest oxygen atoms to the dopant are reported in Table A-6.

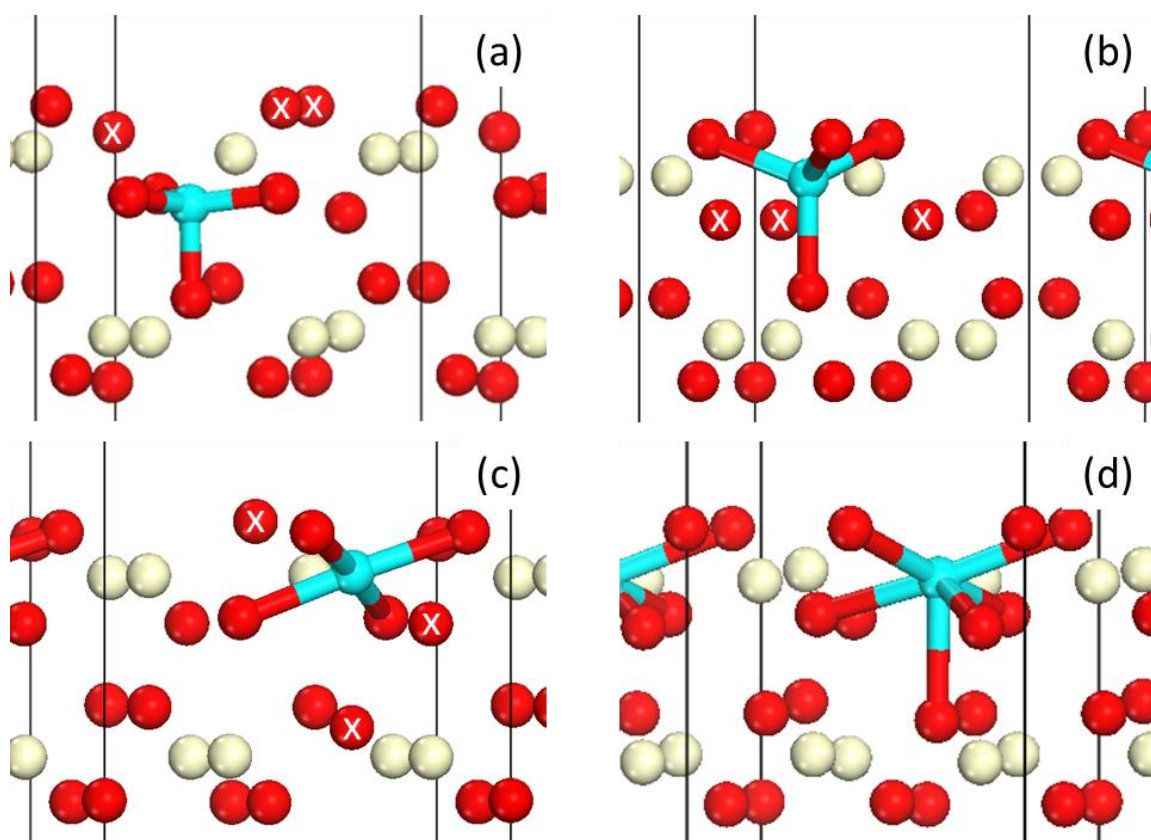


Figure 3-7. Four common oxygen coordination environments about a M-dopant in CeO₂ (1 1 1). (a-c) represent fully-oxidized structures, whereas there is an oxygen vacancy in (d). (a) V coordinated in a trigonal pyramidal coordination, (b) Zr coordinated in a tetrahedral configuration, (c) Ag coordinated in a square planar configuration, and (d) Cd coordinated in a trigonal prismatic coordination. Ce is displayed as tan (light), M-dopant as light blue (gray), and O as red (dark). The O atoms labeled with X's would be in the first coordination shell of a Ce atom, but have rearranged such that they are at substantially larger distances than the first coordination shell O atoms of the dopant.

In the intact structure, the dopant can take on an oxidation state of 4+, 5+, 6+, or 7+, with Ce^{4+} atoms reduced to Ce^{3+} if the dopant takes on a state greater than 4+. Due to the overall MO_2 stoichiometry and the inability of Ce to take on a formal oxidation states above 4+, the dopant metal may not take on lower oxidation states in the fully oxidized surface. Figure 3-8 illustrates the formal oxidation state of each dopant in the fully oxidized and oxygen vacant surface. These results are all without the inclusion of a U -term for the d -states; the possibility of differences with inclusion of a U -term were discussed in Section 3.3.2.

Generally, the transition metals on the left side of the periodic table (Groups IV and V) alter the reducibility of Ce atoms whereas transition metals on the right (Groups X, XI, XII) become the reduction center. The transition metals in the middle of the periodic table vary their role in altering surface reducibility. Elements in groups IV and V take on their stable oxidation state of 4+ for group IV and 5+ for group V. These oxidation states are maintained in both the oxidized and reduced surfaces. In groups X through XII, the oxidized surface dopant takes on a 4+ oxidation state. When the surface is reduced, the dopant reduces from a 4+ oxidation state to a 2+ oxidation state, as described in Section 3.3.1 for the Ag dopant. Gold is an exception to this trend, as gold goes from a fully-oxidized 4+ oxidation state to a reduced 3+ oxidation state with one cerium atom reduced. An oxidation state of 3+ is more stable than a 2+ oxidation state on gold.

Ti	V	Cr	Mn	Fe	Co	Ni	Cu	Zn
Zr	Nb	Mo	Tc	Ru	Rh	Pd	Ag	Cd
Hf	Ta	W	Re	Os	Ir	Pt	Au	Hg
Key	Fully Oxidized		Reduced		Atom Reduces			
	Dopant	Cerium	Dopant	Cerium				
	4+	All 4+	3+	1 – 3+	Cerium & Dopant			
	4+	All 4+	4+	2 – 3+	Cerium			
	5+	1 – 3+	5+	3 – 3+	Cerium			
	6+	2 – 3+	5+	3 – 3+	Cerium & Dopant			
	6+	2 – 3+	6+	4 – 3+	Cerium			
	7+	3 – 3+	6+	4 – 3+	Cerium & Dopant			
	4+	All 4+	2+	All 4+	Dopant			

Figure 3-8. Periodic trends in the M-dopant electronic behavior upon the formation of a nearest neighbor surface oxygen vacancy or upon adsorption of $\text{CH}_3^* + \text{H}^*$ on M-doped CeO_2 (1 1 1).

In groups VI through IX, trends are not as distinct. Group VI metals are doped into CeO_2 as M^{6+} . Upon the formation of an oxygen vacancy with Mo and W, two additional Ce atoms reduce. With Cr as the dopant, upon the formation of an oxygen vacancy, Cr^{6+} reduces to Cr^{5+} and one additional Ce atom reduces. The row 4 metals of groups VII, VIII and IX (Mn, Fe, Co) dope into CeO_2 as M^{4+} . Upon the formation of an oxygen vacancy, the dopant reduces to M^{3+} and one cerium atom reduces. The third ionization energies of Mn, Fe and Co are less than the fourth ionization of cerium, consistent with the lowest energy structure reducing Ce^{4+} to Ce^{3+} rather than M^{3+} reducing to M^{2+} . Re dopes into the surface of CeO_2 as Re^{7+} , and 3 Ce atoms reduce to Ce^{3+} . With the formation of an oxygen vacancy, the Re atom reduces to Re^{6+} with one additional Ce^{3+} formed.

Asymmetry between the dopant behaviors on the two mirrored slabs was observed for some dopants. Using 5 layer slabs, if the number of cerium atoms that reduce becomes large, inherent asymmetry in the model can allow restructuring in which the two sides effectively interact. Slight

asymmetries in the starting geometry (before optimization) also have a great impact on the converged structure. One case where the number of layers had to be increased to attain a symmetric mirrored slab is the Au-doped surface. The number of layers was increased for the Re-doped surface to attain adsorption energy convergence as the number of Ce that reduces is large and the two surfaces interact. In each of these cases, the number of layers was increased from 15 to 18 to 21 (Au only) and 24 (Au only) atomic layers to confirm convergence of vacancy formation energies with respect to the slab thickness (Table A-7).

The removal of the nearest neighbor (NN) oxygen to the dopant results in the lowest vacancy formation energy. In the $p(2 \times 2)$ unit cell, there are three equivalent NN oxygen atoms, with one next nearest neighbor (NNN) surface oxygen atom, as labeled in Figure 3-1. All NN vacancies are lower energy than NNN surface vacancies (Table 3-1). With most dopants, the vacancy formation energy for a NNN vacancy is lower than for a pure CeO_2 surface, so the dopant effect may be non-local. Larger unit cells are needed to consider the range of dopant effects on reducibility.

Table 3-1. Nearest neighbor (NN) and next nearest neighbor (NNN) oxygen vacancy formation energies (ΔE_{vac}) in M-doped CeO₂ (eV).

Dopant	NN Oxygen Vacancy (eV)	NNN Oxygen Vacancy (eV)
Ag	-0.35	0.63
Mn	0.68	- *
Ni	0.01	0.86
Pd	0.71	1.35
Pt	0.47	1.14
V	1.23	3.82
W	1.93	2.99
Zn	-1.13	0.51
Zr	1.63	2.61
Pure Ceria	2.76	2.76

*Unable to converge to a surface NNN oxygen vacancy.

Several periodic trends can be found in the oxygen vacancy formation energies. Moving the dopant across the periodic table from left to right, the vacancy formation energy generally decreases (less endothermic), as seen in Figure 3-9a. The vacancy formation energy generally increases as the dopant moves down a column of the periodic table. This trend holds on the far right and left side of the periodic table. This trend does not hold in the middle of the periodic table, as differences are observed in the electronic role of dopants in the same column. As shown in Figure 3-9b, it is also generally true that dopants serving as a reduction center give more favorable vacancy formation energies. Mixed reduction general leads to greater reducibility than when 2 Ce⁴⁺ atoms are reduced. However, when the dopant reduces, the range of vacancy formation energies is much greater than when only Ce reduces. Vacancy formation energy also correlates with the 298K,

diatomic M-O bond energy (Figure 3-9c).⁶⁷ As the M-O bond enthalpy increases, the vacancy formation energy also increases. As the atomic radii of the dopant increases, the vacancy formation energy generally increases (Figure 3-9d). The atomic radii are defined using self-consistent-field functions.⁶⁸ Though these last two correlations generally hold, deviation about a linear correlation is substantial.

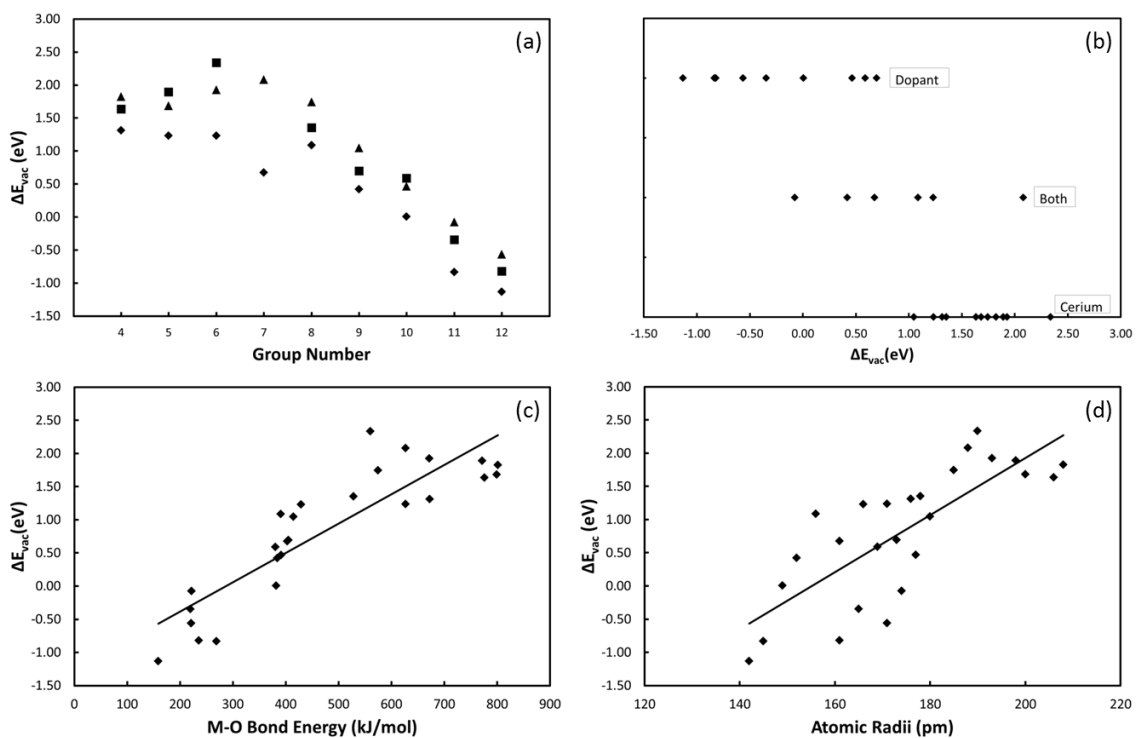


Figure 3-9. Trends observed in M-doped CeO_2 (1 1 1) vacancy formation energies. (a) The vacancy formation energy (ΔE_{vac}) plotted versus M-dopant column in the periodic table. (◆) Row 4 dopants, (■) Row 5 dopants, and (▲) Row 6 dopants. (b) The range of vacancy formation energies (ΔE_{vac}) is illustrated grouped by whether the dopant reduces, both the dopant and one cerium atom reduces, or two cerium atoms reduce. The vacancy formation energies (ΔE_{vac}) are plotted versus (c) the dopant-oxygen bond enthalpy and (d) the atomic radii of the dopant atom. The vacancy formation energy for pure ceria is 2.76 eV. (—) best fit line.

3.3.4.2. Methane Activation

Section 3.3.1 established a linear correlation between M-doped CeO₂ surface reducibility and the dissociative adsorption energy of methane. We expect similar trends in the dopant oxidation states upon vacancy formation or CH₃ + H adsorption, as both are processes that formally reduce the surface. Using the same oxidation state assignment approaches used for vacancy formation, exactly the same trends are observed in the CH₃ + H co-adsorbed state. Figure 3-8 therefore serves to describe the electronic structure of dopants in both vacancy formation and methane adsorption.

The dissociative adsorption of methane and formation of an oxygen vacancy are electronically similar. When an oxygen is removed from the surface with six valence electrons, two electrons are left behind in the surface. When methane is dissociatively adsorbed onto the surface, the hydrogen atom and the methyl radical fragments bond to surface oxygen atoms, with an electron from each species effectively donated to the surface. These two electrons reduce the surface M or Ce atoms similar to the 2 e⁻ returned by vacancy formation. The slope of the best fit line in Figure 3-2 is close to 1 (1.05). This suggests that the energetic effect of the dopant in both vacancy formation and dissociative methane adsorption is equivalent: the energy variation is due to the difference in energy associated with the two electron metal reduction, and the two energies are offset by a constant due to the differences in bonds broken and formed between methane adsorption and vacancy formation.

We considered which surface oxygen atoms preferentially bond CH₃ and H fragments. The lowest adsorption energies occur when both the methyl radical and the hydrogen atom adsorb onto oxygen atoms NN to the dopant. A structure with the H atom bound to a NNN O atom is approximately 0.2 eV higher in energy across sampled dopants. With this preference for the hydrogen atom and methyl radical to adsorb onto NN oxygen atoms, the dopant effect on the system

is relatively local. For both oxygen vacancy formation and methane adsorption, the dopant has a strong local effect and a generally smaller non-local effect.

3.3.4.2.1. Methane Activation Barrier

Non-mirrored slabs were used with the NEB method to locate transition states for CH₄ activation. Prior to considering barriers, we compared the energy necessary to convert methane to an adsorbed hydrogen atom and a gas-phase methyl radical between mirrored and non-mirrored slabs. As described below, methane activation proceeds through H atom abstraction, and this energy difference represents an approximate activation barrier than can be quickly evaluated without the need for a transition state search. For the majority of dopants, this approximate E_{act} on a 12-layer non-mirrored slab (with dipole corrections) is within 0.04 eV of the same value calculated for a mirrored slab. Figure A-7 illustrates that a minority of dopants show a larger deviation. The overall correlations presented herein are not impacted by the use of non-mirrored slabs, though quantitative differences in barriers between models are expected. Not including dipole corrections for non-mirrored slabs typically leads to adsorption energies that differ by 0.4-0.7 eV from the mirrored slab values.

The lowest energy path for CH₄ activation occurs through the surface abstraction of H. Figure 3-10 illustrates the initial, transition and final states for the dissociative adsorption of methane on Ag-CeO₂ (1 1 1). The highest energy state along this path has been previously identified as a gas-phase methyl radical and an adsorbed H atom, referred to here as a “pseudo-transition state” (Figure 3-10c).²⁷ In this pseudo-transition state, the methyl radical has no direct interaction with the surface. There is a slightly higher energy state that was located with careful NEB sampling for a subset of M-doped CeO₂ (1 1 1) surfaces. This true transition state is either slightly higher than or the same energy as the pseudo-transition state. For example, for W-doped CeO₂ (1 1 1), the

true transition state is 0.1 eV higher in energy than the pseudo-transition state. The true transition state contains a methyl radical close to the surface and a hydrogen atom interacts with both the methyl radical and a surface oxygen atom (Figure 3-10b). Analysis of the pseudo-transition state reveals that there is no imaginary vibrational frequency. The true transition states have a single imaginary vibrational frequency. In a few of the M-doped systems, such as V-doped CeO₂, a true transition state cannot be located. Figure 3-11b schematically illustrates a reaction energy diagram for this methane activation process.

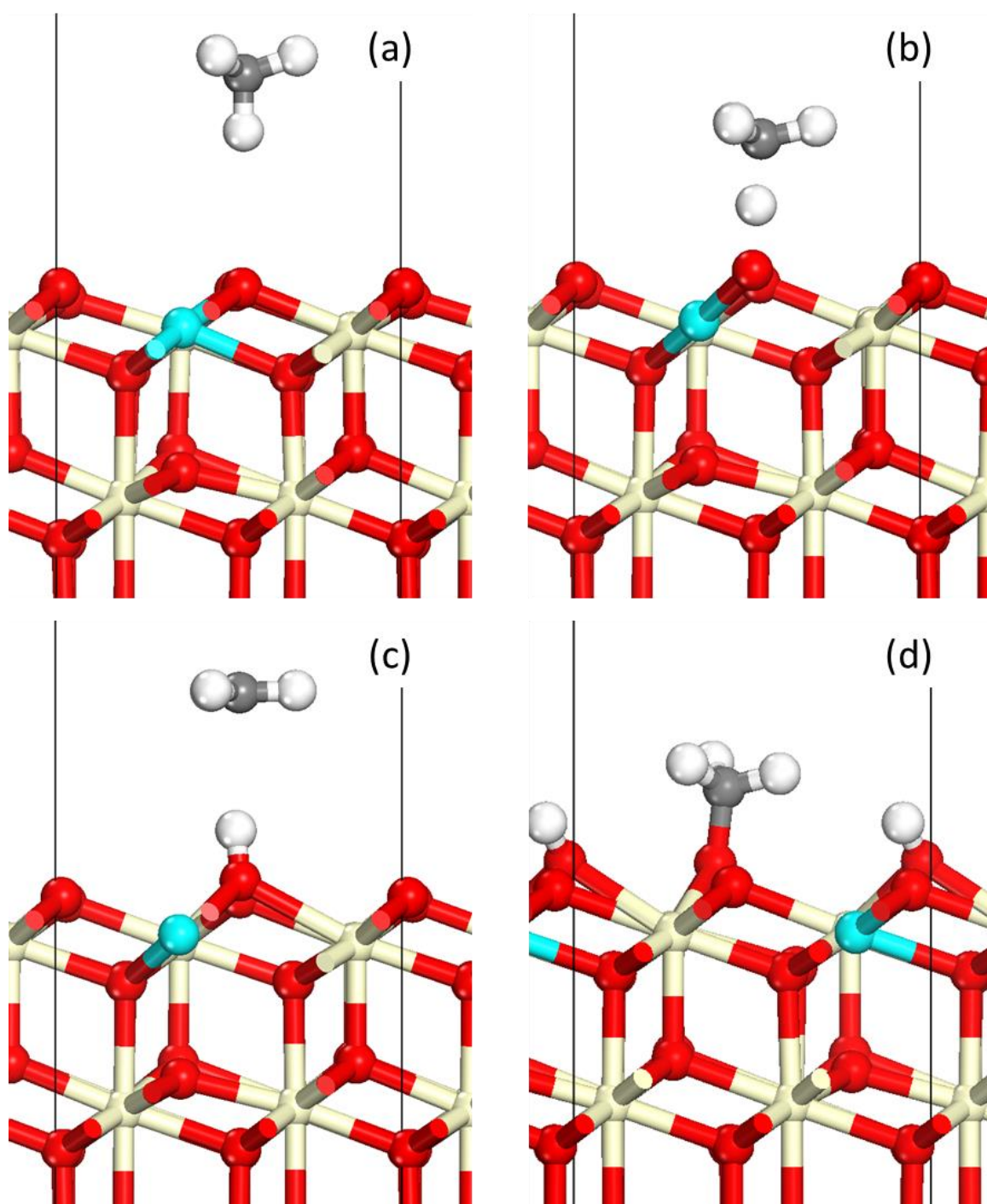


Figure 3-10. (a) Initial state, (b) transition state, (c) pseudo-transition state and (d) final state (rotated 90°) for dissociative methane adsorption on the surface of Ag-doped CeO₂ (1 1 1). Ce is displayed as tan (light), M-dopant as light blue (gray), and O as red (dark).

At the transition state for CH₄ activation, the O-H bond is effectively formed and a single electron donated to the surface. We used the adsorption of a hydrogen atom to identify which metal atoms reduce at the transition state. For dopants that reduce from M⁴⁺ to M²⁺ upon vacancy formation, a single reduction to M³⁺ is observed at the transition state. Similarly if two Ce atoms reduced with the adsorption of CH₃ + H, one Ce atom reduces at the transition state. When both the dopant and one Ce atom reduce upon 2 e⁻ reduction, the dopant will usually reduce to M³⁺ at the transition state. This is the case for the Mn dopant. Though these trends are generally followed, there are exceptions. For example, Pt does not have a stable 3+ oxidation state. When the hydrogen atom is adsorbed onto the surface, one Ce atom reduces. When the methyl radical then adsorbs the cerium atom returns to a 4+ oxidation state and the Pt reduces to a 2+ oxidation state.

A Brønsted-Evans-Polanyi (BEP)⁶⁹⁻⁷² relationship can be observed for adsorption of methane onto the surface of M-doped CeO₂. The activation barrier may consider as the energy needed to form either the pseudo-transition state or the true transition state, and the reaction energy is the dissociative adsorption energy of methane. Figure 3-11a illustrates the BEP relationship for ten of the 26 transition metal dopants examined. Table A-8 reports the values included in this plot. Four of the true transition states have been found and are represented by squares. The best fit lines for the true and pseudo-transition states are parallel with the true transition state line higher in energy than the pseudo-transition state line by 0.25 eV. Considerable deviation from linearity is observed for the pseudo-transition states.

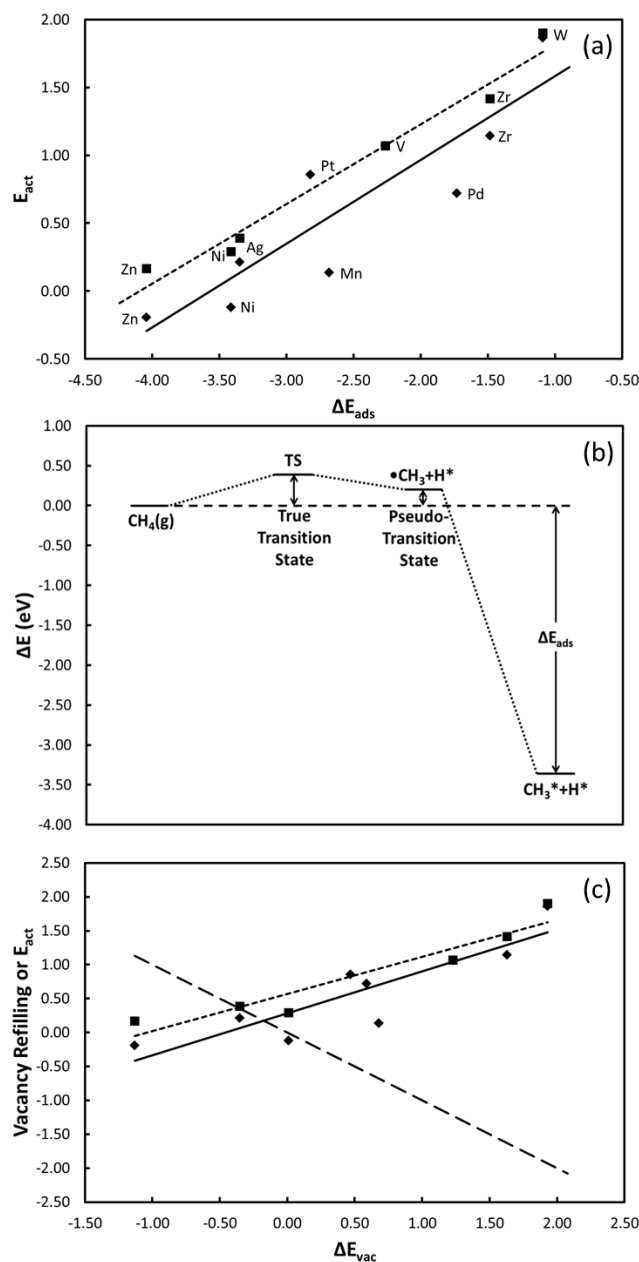


Figure 3-11. (a) A Brønsted-Evans-Polanyi relationship for the dissociative adsorption of methane on the surface of M-doped CeO₂ (1 1 1) for 10 selected dopants. For Ag, Ni, V, W, Zn and Zr both pseudo-transition states and true transition states are displayed (vanadium true and pseudo transition states are very close in energy and only show as one point). (b) Reaction energy diagram for the dissociative adsorption of methane over Ag-doped CeO₂. (c) Vacancy refilling energy and activation energy versus vacancy formation energy. Intersection between activation energy and vacancy refilling energy lines represents the point at which both vacancy refilling and methane activation require the same 0 K energy input. (◆) Pseudo-transition state, (■) true transition state, (----) best fit line for true transition states, (—) best fit line for pseudo-transition states, (—) vacancy refilling line.

3.3.5. Implications for hydrocarbon conversion catalysis over M-doped CeO₂ (1 1 1)

The activation energy for the selected dopants is plotted against the vacancy formation energy in Figure 3-11c. The vacancy refilling energy is also plotted against the vacancy formation energy, where the vacancy refilling energy is the negative of the vacancy formation energy. The intersection of these two lines represents the point at which vacancy refilling and methane activation require the same energy input. To the left of the intersection, oxygen vacancy refilling will limit the methane conversion rate and to the right methane activation will be limiting. The location of the intersection differs depending on whether the pseudo-transition state (ΔE_{vac} is 0.17 eV at intersection) or the true-transition state energy (ΔE_{vac} is 0.37 eV at intersection) is used.

We should qualify, however, that the data in Figure 3-11c represents 0 K values and also may suffer from inaccuracies in DFT calculations of the O₂ binding energy. As both vacancy refilling and methane activation involve the loss of entropy of a gas phase species, determination of the optimal dopant requires consideration of the gas phase oxygen and methane pressures. Considering our previous study of Pd-doped ceria,²⁹ which considered entropic factors and avoided DFT issues with O₂ binding energies, the optimal value under catalytic combustion conditions is at higher vacancy formation energies than the intersections in Figure 3-11c. A more reducing atmosphere (hydrocarbon reforming rather than combustion, for example) would push the optimal dopant further towards less exothermic vacancy formation energies (more facile vacancy refilling). If we consider larger hydrocarbons (with more active secondary or tertiary C-H bonds), the optimal dopant will also move towards less exothermic vacancy formation energies as lowering the barrier to C-H activation becomes less essential. Dopants offering vacancy formation energies between -0.5 eV and +1.0 eV will likely be towards the top of a volcano curve for hydrocarbon conversion over doped CeO₂ (1 1 1) surfaces, with the optimal catalyst depending on effective oxygen chemical potential, hydrocarbon pressure, and hydrocarbon identify. This range includes, in order of

increasing vacancy formation energy: Ag, Au, Ni, Co, Pt, Pd, and Mn dopants. Ir and Fe offer vacancy formation energies just above 1.0 eV.

Another approximation inherent in the analysis above is that only a “first” vacancy may participate in oxidation catalysis. For dopants with exoergonic vacancy formation energies, it is possible an oxygen atom remaining after vacancy formation could offer a more optimal active site. A “second” vacancy formation energy would be expected to be less exothermic than the first, pushing this second oxygen atom closer to the “optimal window.” Though this was not considered in our current study, we suggest that the potential for multiple vacancy formation does not alter the trade-offs in determining an optimal dopant. The need for multiple vacancy formation would suggest a reduced concentration of active oxygen atoms at the surface. For the majority of dopants that cause the first oxygen atom to be too easy to remove, the dopant transitions to a 2+ oxidation state following vacancy formation. Were the dopant to continue to act as the reduction center for a second oxygen atom to participate in oxidation catalysis, it would have to transition between 2+ and 0+ oxidation states during a catalytic cycle. It is questionable whether a dopant in the 0+ oxidation state could remain stable within the ceria lattice. The consideration of multiple dopants is similar to the consideration of coverage effects when considering the use of single atom binding energies in constructing volcano curves for transition metal surfaces. Coverage effects act to “flatten” a volcano relationship rather than relocate the peak, and a similar effect may be expected when considering the multiple vacancy formation for oxidation catalysis in doped ceria systems.

3.4. Conclusions

The electronic structure of transition metal doped CeO₂ (1 1 1) surfaces was investigated in the fully oxidized, reduced, and CH₃ + H adsorbed states. Upon the formation of a surface oxygen vacancy in the surface of M-doped CeO₂, the dopant can either become the reduction center or can

serve to alter the reducibility of the cerium atoms. On the left side of the periodic table, dopants act to alter the reducibility of the cerium atoms, whereas late transition metals serve as the reduction center. When methane adsorption reduces the surface, the dopants serve the same role. The U -value on the d -states of the dopant can change both the vacancy formation energy as well as the electronic role the dopant plays in surface reduction. The effect of the dopant has local and smaller non-local effects. The lowest oxygen vacancy formation and methane adsorption energies occur for the nearest neighbor to the dopant atom with a higher vacancy formation for the next nearest neighbor.

The vacancy formation energy and dissociative methane adsorption energy correlate across transition metal doped CeO_2 (1 1 1) surfaces. A BEP relationship exists for the activation of the C-H bond in methane over M-doped CeO_2 surfaces. Using this BEP relationship we determine that the methane activation and vacancy formation energies are also correlated. For dopants with the most exothermic (lowest) vacancy formation energy, hydrocarbon oxidation will be limited by oxygen vacancy refilling. For higher vacancy formation energies, methane activation will become rate limiting, leading to a volcano relationship between methane conversion activity and surface reducibility. Some of the dopants that look promising for hydrocarbon conversion are Ag, Au, Ni, Co, Pt, Pd, and Mn. These dopants have lower barriers for methane activation, but they are not so low that oxygen vacancy refilling will become rate limiting. The optimal dopant will depend on hydrocarbon pressure and identify as well as the redox environment.

One of the limitations in using DFT+ U is that the cell size for the model must remain small to make the optimizations computationally feasible. A $p(2 \times 2)$ surface cell was used, which gives a 25% surface dopant composition and a 50% coverage of surface O atoms in the $\text{CH}_3^* + \text{H}^*$ state. The use of a U -value on the d -states of the dopant is only briefly examined in this study. Chapter 4 studies how the dopant concentration in the surface and d -state U -value affect oxygen vacancy formation energies. Investigation of larger hydrocarbons will be discussed in Chapters 5 and 6.

ACKNOWLEDGEMENTS: This material is based upon work supported as part of the Center for Atomic Level Catalyst Design, an Energy Frontier Research Center funded by the U.S. Department of Energy, Office of Science, Office of Basic Energy Sciences under Award Number DE-SC0001058.

3.5. References

1. H. T. Chen, J. G. Chang. *Journal of Chemical Physics* **2010**, *132*, 214702.
2. Z. X. Yang, D. W. Ma, X. H. Yu, K. Hermansson. *European Physical Journal B* **2010**, *77*, 373-380.
3. A. Gupta, U. V. Waghmare, M. S. Hegde. *Chemistry of Materials* **2010**, *22*, 5184-5198.
4. S. Park, R. J. Gorte, J. M. Vohs. *Applied Catalysis A-General* **2000**, *200*, 55-61.
5. S. McIntosh, J. M. Vohs, R. J. Gorte. *Electrochemical and Solid State Letters* **2003**, *6*, A240-A243.
6. S. Colussi, A. Gayen, M. F. Camellone, M. Boaro, J. Llorca, S. Fabris, A. Trovarelli. *Angewandte Chemie-International Edition* **2009**, *48*, 8481-8484.
7. K. R. Priolkar, P. Bera, P. R. Sarode, M. S. Hegde, S. Emura, R. Kumashiro, N. P. Lalla. *Chemistry of Materials* **2002**, *14*, 2120-2128.
8. C. Bozo, N. Guilhaume, J. M. Herrmann. *Journal of Catalysis* **2001**, *203*, 393-406.
9. D. Terribile, A. Trovarelli, C. de Leitenburg, A. Primavera, G. Dolcetti. *Catalysis Today* **1999**, *47*, 133-140.
10. A. Yee, S. J. Morrison, H. Idriss. *Journal of Catalysis* **1999**, *186*, 279-295.
11. M. Boaro, C. de Leitenburg, G. Dolcetti, A. Trovarelli. *Journal of Catalysis* **2000**, *193*, 338-347.

12. P. Fornasiero, R. Dimonte, G. R. Rao, J. Kaspar, S. Meriani, A. Trovarelli, M. Graziani. *Journal of Catalysis* **1995**, *151*, 168-177.
13. G. Zhou, P. R. Shah, T. Kim, P. Fornasiero, R. J. Gorte. *Catalysis Today* **2007**, *123*, 86-93.
14. Z. Lu, Z. Yang, B. He, C. Castleton, K. Hermansson. *Chemical Physics Letters* **2011**, *510*, 60-66.
15. C. Spiel, P. Blaha, Y. Suchorski, K. Schwarz, G. Rupprechter. *Physical Review B* **2011**, *84*, 045412.
16. Z. X. Yang, Z. M. Fu, Y. W. Wei, Z. S. Lu. *Journal of Physical Chemistry C* **2008**, *112*, 15341-15347.
17. H. T. Chen, J. G. Chang. *Journal of Physical Chemistry C* **2011**, *115*, 14745-14753.
18. S. Sharma, Z. P. Hu, P. Zhang, E. W. McFarland, H. Metiu. *Journal of Catalysis* **2011**, *278*, 297-309.
19. W. Tang, Z. P. Hu, M. J. Wang, G. D. Stucky, H. Metiu, E. W. McFarland. *Journal of Catalysis* **2010**, *273*, 125-137.
20. M. Nolan. *Journal of Chemical Physics* **2009**, *130*, 144702.
21. M. Nolan. *Journal of Materials Chemistry* **2011**, *21*, 9160-9168.
22. M. Nolan, V. S. Verdugo, H. Metiu. *Surface Science* **2008**, *602*, 2734-2742.
23. V. Shapovalov, H. Metiu. *Journal of Catalysis* **2007**, *245*, 205-214.
24. Z. X. Yang, B. L. He, Z. S. Lu, K. Hermansson. *Journal of Physical Chemistry C* **2010**, *114*, 4486-4494.
25. Z. X. Yang, G. X. Luo, Z. S. Lu, K. Hermansson. *Journal of Chemical Physics* **2007**, *127*, 074704.
26. Z. X. Yang, Q. G. Wang, S. Y. Wei. *Physical Chemistry Chemical Physics* **2011**, *13*, 9363-9373.
27. A. D. Mayernick, M. J. Janik. *Journal of Physical Chemistry C* **2008**, *112*, 14955-14964.

28. A. D. Mayernick, M. J. Janik. *Journal of Chemical Physics* **2009**, *131*, 084701.
29. A. D. Mayernick, M. J. Janik. *Journal of Catalysis* **2011**, *278*, 16-25.
30. Z. Yang, L. A. Zhansheng, G. Luo, K. Hermansson. *Physics Letters A* **2007**, *369*, 132-139.
31. G. Avgouropoulos, T. Ioannides. *Applied Catalysis A-General* **2003**, *244*, 155-167.
32. G. B. Hoflund, H. A. E. Hagelin, J. F. Weaver, G. N. Salaita. *Applied Surface Science* **2003**, *205*, 102-112.
33. Q. Fu, H. Saltsburg, M. Flytzani-Stephanopoulos. *Science* **2003**, *301*, 935-938.
34. Z. X. Yang, Z. M. Fu, Y. W. Wei, K. Hermansson. *Chemical Physics Letters* **2008**, *450*, 286-291.
35. Z. X. Yang, Z. M. Fu, Y. N. Zhang, R. Q. Wu. *Catalysis Letters* **2011**, *141*, 78-82.
36. Z. S. Lu, Z. X. Yang, B. L. He, C. Castleton, K. Hermansson. *Chemical Physics Letters* **2011**, *510*, 60-66.
37. Z. P. Hu, H. Metiu. *Journal of Physical Chemistry C* **2011**, *115*, 17898-17909.
38. G. Kresse, J. Furthmuller. *Computational Materials Science* **1996**, *6*, 15-50.
39. G. Kresse, J. Furthmuller. *Physical Review B* **1996**, *54*, 11169-11186.
40. G. Kresse, J. Hafner. *Physical Review B* **1993**, *47*, 558-561.
41. G. Kresse, D. Joubert. *Physical Review B* **1999**, *59*, 1758-1775.
42. H. J. Monkhorst, J. D. Pack. *Physical Review B* **1976**, *13*, 5188-5192.
43. J. P. Perdew, J. A. Chevary, S. H. Vosko, K. A. Jackson, M. R. Pederson, D. J. Singh, C. Fiolhais. *Physical Review B* **1992**, *46*, 6671-6687.
44. S. Fabris, S. de Gironcoli, S. Baroni, G. Vicario, G. Balducci. *Physical Review B* **2005**, *71*, 041102.
45. S. Fabris, S. de Gironcoli, S. Baroni, G. Vicario, G. Balducci. *Physical Review B* **2005**, *72*, 237102.

46. G. Kresse, P. Blaha, J. L. F. Da Silva, M. V. Ganduglia-Pirovano. *Physical Review B* **2005**, 72, 237101.
47. V. I. Anisimov, O. Gunnarsson. *Physical Review B* **1991**, 43, 7570-7574.
48. J. F. Herbst, R. E. Watson, J. W. Wilkins. *Physical Review B* **1978**, 17, 3089-3098.
49. Y. Chen, J. Cheng, P. Hu, H. F. Wang. *Surface Science* **2008**, 602, 2828-2834.
50. Y. Chen, P. Hu, M. H. Lee, H. F. Wang. *Surface Science* **2008**, 602, 1736-1741.
51. N. C. Hernandez, R. Grau-Crespo, N. H. de Leeuw, J. F. Sanz. *Physical Chemistry Chemical Physics* **2009**, 11, 5246-5252.
52. L. Wang, T. Maxisch, G. Ceder. *Physical Review B* **2006**, 73,
53. M. Nolan, S. C. Parker, G. W. Watson. *Surface Science* **2005**, 595, 223-232.
54. G. Makov, M. C. Payne. *Physical Review B* **1995**, 51, 4014-4022.
55. J. Neugebauer, M. Scheffler. *Physical Review B* **1992**, 46, 16067-16080.
56. M. V. Ganduglia-Pirovano, J. L. F. Da Silva, J. Sauer. *Physical Review Letters* **2009**, 102, 026101.
57. L. Wang, T. Maxisch, G. Ceder. *Physical Review B* **2006**, 73, 195107.
58. D. Knapp, T. Ziegler. *Journal of Physical Chemistry C* **2008**, 112, 17311-17318.
59. G. Henkelman, H. Jonsson. *Journal of Chemical Physics* **2000**, 113, 9978-9985.
60. G. Henkelman, B. P. Uberuaga, H. Jonsson. *Journal of Chemical Physics* **2000**, 113, 9901-9904.
61. G. Mills, H. Jonsson, G. K. Schenter. *Surface Science* **1995**, 324, 305-337.
62. D. Srinivas, C. V. V. Satyanarayana, H. S. Potdar, P. Ratnasamy. *Applied Catalysis A-General* **2003**, 246, 323-334.
63. B. C. Zhang, X. L. Tang, Y. Li, Y. D. Xu, W. J. Shen. *International Journal of Hydrogen Energy* **2007**, 32, 2367-2373.
64. R. F. W. Bader. *Accounts of Chemical Research* **1985**, 18, 9-15.

65. G. Henkelman, A. Arnaldsson, H. Jonsson. *Computational Materials Science* **2006**, *36*, 354-360.
66. E. Sanville, S. D. Kenny, R. Smith, G. Henkelman. *Journal of Computational Chemistry* **2007**, *28*, 899-908.
67. Y.-R. Luo, *CRC Handbook of Chemistry and Physics 2008-2009: A Ready-Reference Book of Chemical and Physical Data*. CRC Press: Boca Raton, 2008.
68. E. Clementi, D. L. Raimondi. *Journal of Chemical Physics* **1963**, *38*, 2686.
69. M. G. Evans, M. Polanyi. *Transactions of the Faraday Society* **1938**, *34*, 0011-0023.
70. T. Bligaard, J. K. Nørskov, S. Dahl, J. Matthiesen, C. H. Christensen, J. Sehested. *Journal of Catalysis* **2004**, *224*, 206-217.
71. J. K. Nørskov, T. Bligaard, A. Logadottir, S. Bahn, L. B. Hansen, M. Bollinger, H. Benggaard, B. Hammer, Z. Sljivancanin, M. Mavrikakis, Y. Xu, S. Dahl, C. J. H. Jacobsen. *Journal of Catalysis* **2002**, *209*, 275-278.
72. A. Logadottir, T. H. Rod, J. K. Nørskov, B. Hammer, S. Dahl, C. J. H. Jacobsen. *Journal of Catalysis* **2001**, *197*, 229-231.

Chapter 4

Examination of Oxygen Vacancy Formation in Mn-Doped CeO₂ (1 1 1) using DFT+*U* and the Hybrid Functional HSE06

This chapter is published as: M. D. Krcha, M. J. Janik. *Langmuir* **2013**, 29, 10120-10131.

ABSTRACT: MnO_x-CeO_x mixed oxide systems exhibit interesting sulfur adsorption capacities and catalytic activity. We examined the electronic structure of Mn-doped fluorite CeO₂ bulk solid and surface using density functional theory (DFT) with the Hubbard *U*-term or the Heyd-Scuseria-Ernzerhof (HSE06) hybrid functional. We specifically evaluate the reducibility and formation energies of Mn-doped CeO₂ surfaces. The use of a *U*-value on the *d*-states of Mn is examined and a value of 4 eV is chosen based upon results from DFT+*U* calculations on bulk MnO_x,¹ XANES characterization of oxidation states in calcined and reduced Mn-doped CeO₂, and comparison with HSE06 hybrid functional results. Electronic structure impacts of the *U* inclusion are discussed. The concentration and orientation of Mn atoms doped into the surface of CeO₂ have a great influence on the reducibility of the surface. Based upon formation energies, Mn will not favor doping into the surface of CeO₂ in a fully oxidized system (Mn⁴⁺). Under reducing environments, Mn will dope into the surface with oxygen vacancies present (Mn³⁺ and Mn²⁺). The first oxygen vacancy is not likely catalytically important in fluorite MnO_x-CeO_x systems as formation of the fully oxidized surface is not stable. A greater degree of reduction would occur during a catalyzed redox reaction.

4.1. Introduction

Cerium oxide (CeO_2) can be doped with transition metals, altering its redox properties relative to pure CeO_2 . Manganese added to CeO_2 enhances its redox properties²⁻⁴ and catalytic oxidation activity,⁵⁻⁹ as well as sulfur adsorption capacity.¹⁰ Several experimental^{2,5-8,11-12} and computational studies^{3-4,9,13} have examined how Mn addition affects the properties of Mn-doped CeO_2 . A more complete understanding of the electronic structure impact of Mn-doping could explain the interesting properties. Herein, density functional theory (DFT), considering both the inclusion of the Hubbard U -term and the incorporation of exact exchange (HSE06 hybrid functional),¹⁴⁻¹⁶ is used to examine the electronic structure, formation and reduction energetics of the Mn-doped CeO_2 (1 1 1) surface. We find that a U -value on the d -states of Mn is necessary to arrive at electronic behavior consistent with experiment. The concentration and arrangement of Mn in the surface can have a large impact on surface reducibility.

Mn-doped CeO_2 materials have been synthesized, their properties have been characterized, and they have been examined for catalytic applications. Two methods used to synthesize Mn-doped CeO_2 are the solution combustion technique^{7,12} and the hydrothermal method.⁶ The solution combustion technique leads to a highly dispersed Mn species throughout the ceria, with Mn taking on Mn^{2+} and Mn^{3+} oxidation states.¹² X-ray diffraction shows that there is a fluorite phase but no MnO_x phase present, indicating the formation of $\text{Ce}_{1-x}\text{Mn}_x\text{O}_{2-\delta}$. Dissolving MnO_x into the ceria-zirconia lattice promotes the low-temperature reduction of Ce^{4+} to Ce^{3+} , improving the catalytic activity of the total oxidation of methane.⁸ Segregation of a Mn_3O_4 phase is seen with concentrations of 25% Mn and higher.⁷ The surface area of $\text{MnO}_x\text{-CeO}_2$ is greater than either one of the single oxide systems prepared by the same method, helping to achieve a more complete combustion of organic compounds.⁷

An electronic structure level explanation of the enhanced catalytic properties upon Mn-doping could guide further optimization. Density functional theory is known to have difficulties representing oxide systems,^{1,17-20} challenging accurate electronic structure determination. To model reduced ceria systems, a Hubbard U -correction can correct self-interaction errors that result from standard DFT methods.¹⁷⁻¹⁹ This self-interaction error results in improper delocalization of f -electrons in reduced ceria systems. A Hubbard U -correction is also needed to correctly represent the d -states of some metal oxides.^{1,20} The application and reliability of U -corrections to model mixed oxide systems is not well established. U -corrections can be added to both the f -states of cerium and the d -states of a metal dopant,^{3-4,21} though most Mn-doped ceria studies included a U -correction on f -states of cerium only. A hybrid functional, included exact exchange, may be used to avoid the empiricism of adding U -corrections, but still requires a choice of the amount of exact exchange to include.²²⁻²³ Though a practical, universal method is not available, systematic application of U -corrections may allow for realistic electronic structure representation.

Density functional theory has been used to construct models and determine active sites and electronic properties of Mn-doped ceria.^{3-4,9,13} Gupta examined the substitution of 4 Mn atoms for Ce atoms in a $2 \times 2 \times 2$ supercell of CeO_2 .¹³ Two oxygen atoms were removed from the supercell, allowing the Mn to be present in the Mn^{3+} oxidation state, and the Mn-O bond lengths were used to assess Mn oxidation states. Tang et al. also examined a $2 \times 2 \times 2$ bulk supercell, though they only substituted 1 Mn atom for a Ce atom.³ Both studies included a U -correction to Ce f -states, but Tang et al. also included an on-site Coulomb interaction (U -value of 4.5 eV) onto the d -states of Mn. The Mn atom dopes into the fluorite lattice as Mn^{4+} and, with the formation of an oxygen vacancy, the Mn reduces to Mn^{2+} . The oxygen vacancy formation energy decreases relative to pure CeO_2 , which is a result of electronic modification and structural distortion caused by doping Mn into CeO_2 .³ Hsu et al. used a $p(\sqrt{3} \times 2)$ CeO_2 (1 1 1) surface and replaced one Ce atom with an Mn atom to examine the effects of Mn on the adsorption and oxidation of CO.⁹ They only used a U -value on the f -states

of cerium. Hsu et al. found physisorbed CO, physisorbed CO₂ and chemisorbed CO on Mn-doped CeO₂ (1 1 1) and only physisorbed CO on pure CeO₂ (1 1 1).⁹ CO oxidation is promoted by the Mn dopant. Cen et al. used a $p(3 \times 3)$ surface with 9 atomic layers to substitute 1 Ce atom with an Mn atom.⁴ A U -value from 0 to 6 eV was examined on the d -states of Mn and they choose a U -value of 4.5 eV for most optimizations. Cen et al. argued that Mn dopes into the fully oxidized CeO₂ lattice as Mn³⁺ and the formation of an oxygen vacancy reduces the dopant to Mn²⁺. They did not explain, however the origin of the electrons which reduced Mn to 3⁺ in the overall MO₂ lattice. As shown by Tang et al. and Cen et al., a U -value on the d -states of Mn is needed to reasonably fit experimental lattice parameters and band gaps when modeling Mn-doped CeO₂. Wang used the magnetic moments of Mn in MnO_x to determine a U -value for the d -states of Mn in the bulk oxide, arriving at a U -value of 4 eV.¹

A hybrid functional can be utilized, alternatively to correct the self-exchange error by inclusion of exact exchange, thereby motivating proper electron localization. Though this can qualitatively overcome the false delocalization error, the extent of exact exchange inclusion is semi-empirical and typically does not fully correct the self-interaction error of strongly localized states. The use of hybrid functionals in a plane wave basis set code is computationally intense compared to the DFT+ U methods, and therefore cannot be widely utilized for investigating surface properties of mixed oxides. Comparison with HSE06 calculations can help to select or to verify a U -value on specific states. Ganduglia-Pirovano et al. compared the PBE+ U ($U = 4.50$ eV), LDA+ U ($U = 5.30$ eV) and HSE06 functionals for CeO₂ surfaces.²⁴ They found the LDA+ U and the HSE06 functional match the surface reduction energies more closely than the PBE+ U functional. Nolan also compared the HSE06 functional and DFT+ U methods to examine oxygen vacancies in Pd and Ni doped CeO₂²² and doping of trivalent elements into CeO₂.²³ In both studies, Nolan used a U of 5 eV on Ce f -states and in the study of trivalent dopants he used a U -value of 7 eV on O p -states

for comparison to the HSE06 functional. He did not utilize a U -value on the metal dopants in either study.

This study examines the effect of a U -value on the d -states of Mn doped into the fluorite lattice of CeO₂. Depending on the U -value chosen for the d -states, the most stable oxidation state for Mn in a partially reduced surface can be either Mn³⁺ or Mn²⁺. A U -value of 4 eV on d -states of Mn, as recommended for bulk MnO_x by Wang et al.,¹ is utilized for all optimizations unless otherwise stated. To help confirm this U -value, the hybrid functional HSE06 is used for one system and compared to the results from DFT+ U . With the reliability of a $U = 4$ eV value established, we consider the reduction and formation energies for surfaces with various Mn concentrations. The concentration and distribution of Mn doped in the surface of CeO₂ has a large impact on the first and second oxygen vacancy formation energies, as well as the most stable oxidation states for Mn. We also report formation energies of the Mn-doped CeO₂ system to examine the stability of Mn-doping at various oxidation states.

4.2. Methods

4.2.1. Electronic structure method

Calculations were carried out using the Vienna *ab initio* simulation program (VASP), an *ab initio* total energy and molecular dynamics program developed at the Institute for Material Physics at the University of Vienna.²⁵⁻²⁷ The ion-core interactions were represented by the projector-augmented wave (PAW) method.²⁸ Plane wave basis sets were used to expand the wave functions of valence electrons, with valence configurations for cerium being $5s^25p^66s^24f^15d^1$, $2s^22p^4$ for oxygen, and $3d^64s^1$ for Mn. The energy cutoff for the plane wave basis set was 450 eV. k -point sampling of (2 x 2 x 1) was performed using the Monkhorst Pack scheme,²⁹ with the third vector

perpendicular to the surface for all DFT+ U optimizations. The Perdew-Wang (PW91) version of the generalized gradient approximation (GGA) was used to incorporate exchange and correlation energies.³⁰ All optimizations were spin polarized. Structural optimizations were performed by minimizing the forces on all atoms to below $0.05 \text{ eV}\cdot\text{\AA}^{-1}$. A force criteria of $0.02 \text{ eV}\cdot\text{\AA}^{-1}$ has been previously examined on this system and we find both structures and energetics are converged at the courser value.³¹

Due to well-established difficulties within DFT to accurately represent the nature of the $4f$ state in ceria,¹⁷⁻¹⁹ we implement the DFT+ U approach.³²⁻³³ The DFT+ U method introduces an on-site Coulombic interaction (U -term) that penalizes non-integer occupation of localized orbitals, effectively penalizing delocalization of electrons. We use a Ce f U -value of 5 eV, which is consistent with values used in previous studies of ceria.^{4,31,34-39} We previously reported the dependence of methane activation and oxygen vacancy formation on the value of the Ce $4f$ Hubbard U -term for CeO_2 and $\text{Pd}_x\text{Ce}_{1-x}\text{O}_2$. The vacancy formation (ΔE_{vac}) and methane adsorption (ΔE_{ads}) energies increase in exothermicity linearly with increasing Ce f U -value,³⁴ though there is only a slight slope for $\text{Pd}_x\text{Ce}_{1-x}\text{O}_2$. Given the dependence of vacancy formation energy on the U -value for pure ceria, the quantitative values we calculate are inherently dependent on our specific choice of U -value. The U -value of 5 eV accurately describes the electronic structure of reduced ceria and provides qualitative comparisons for the oxygen vacancy formation energies.

DFT is generally known to have difficulties representing localized d -states of metal oxides.^{1,20} We included a U -term on the d -states of Mn, which is varied from 0 eV to 5 eV. A U -value of 4 eV on the d -states of Mn was used for all optimizations, as this value correctly predicts oxidation states for Mn in the intact and oxygen vacant cases that agree with XANES measurements.¹⁰ The Heyd-Scuseria-Ernzerhof (HSE06) hybrid functional was also utilized on a select subset of structures.¹⁴⁻¹⁶ The exact exchange contribution of 25% was utilized with a

screening length of 0.2 \AA^{-1} as utilized by Nolan.²²⁻²³ The surface was modeled using a Γ point only for all hybrid functional optimizations due to the computational intensity of the hybrid functional.²⁴

4.2.2. Surface models

The bulk CeO_2 cubic fluorite structure is the same as used in our previous work,^{31,34-36} and the lattice constant is reproduced within 1% of the experimental lattice constant.³⁴ The surface is modeled using the (1 1 1) surface of ceria separated by 15 \AA of vacuum space in the direction perpendicular to the surface. The lowest energy surface among single crystal terminations of ceria is the (1 1 1) surface,^{34,40-41} which will represent a large portion of a polycrystalline CeO_2 surface. Mirrored slabs of 12 atomic layers were utilized for all DFT+ U optimizations, with the number of layers converged to surface formation energy and vacancy formation energy. Mirrored slabs were chosen to minimize the slab-to-slab interactions that can result from a large net surface dipole moment upon the reduction in surface metal ions. A $p(2 \times 2)$ ($\text{Ce}_{16}\text{O}_{32}$) and a $p(2 \times 3)$ ($\text{Ce}_{24}\text{O}_{48}$) expansion of the surface cell were considered. The (1 1 1) termination of CeO_2 results in four oxygen atoms per side of the unit cell (six for the $p(2 \times 3)$ expansion) with four Ce atoms in the layer below (six for the $p(2 \times 3)$ expansion), as seen in Figure 4-1. A non-mirrored slab of 9 atomic layers ($\text{Ce}_{12}\text{O}_{24}$) is used for the hybrid functional HSE06 calculations.

The mirrored surfaces of CeO_2 were “doped” by replacing one or two cerium atoms (either 1 surface, 1 surface and 1 subsurface or 2 surface Ce atoms) with Mn atoms on each side of the mirrored surface (Figure 4-1). The Mn atom is forced to take on a 4^+ oxidation state when replacing a cerium atom in the fully oxidized surface. In the non-mirrored model for the hybrid functional, one Ce atom in the surface is replaced by a Mn atom. The surface cell lattice parameters were not allowed to relax and the dopant level was presumed low enough so as to not perturb this lattice

constant. By not allowing the lattice parameters to relax, this model would represent a system with surface segregation of a low bulk concentration dopant.

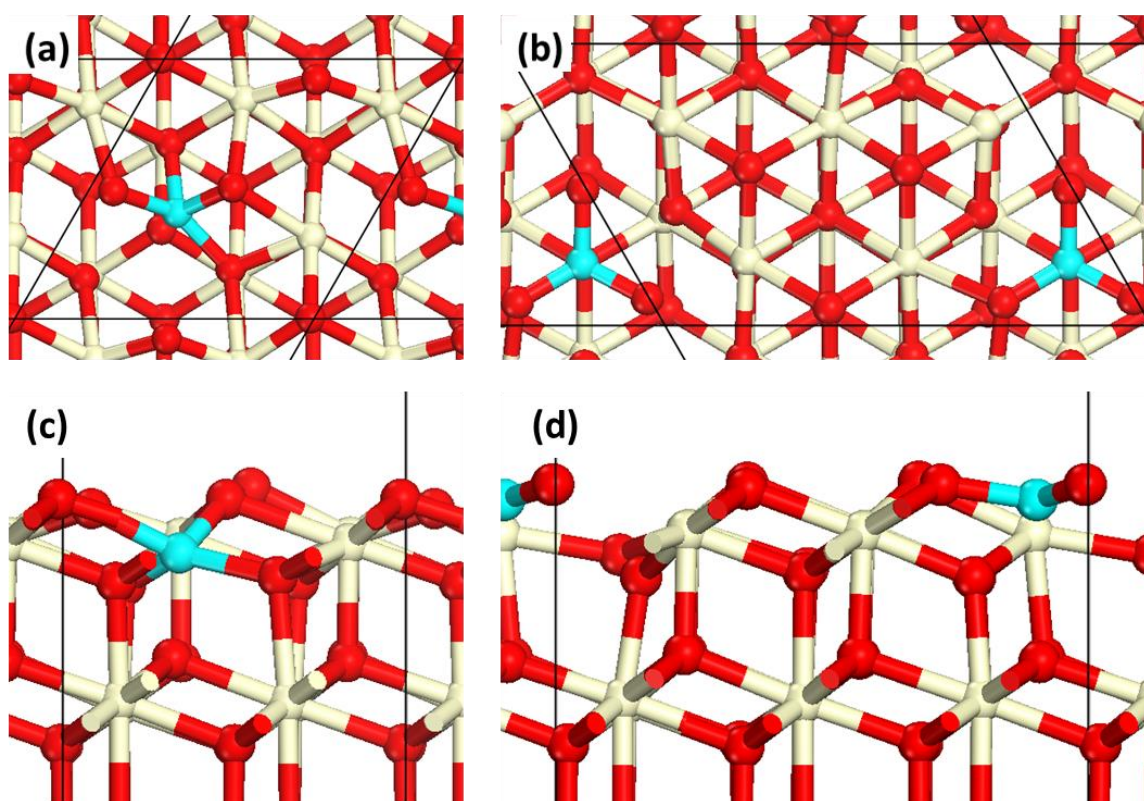
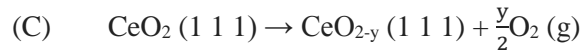
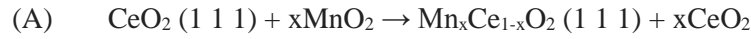


Figure 4-1. Top and side views of the slab model of fully oxidized (intact) Mn-doped CeO₂ (1 1 1). (a) top view of $p(2 \times 2)$ unit expansion, (b) top view of $p(2 \times 3)$ unit expansion, (c) side view of $p(2 \times 2)$ unit expansion, and (d) side view of $p(2 \times 3)$ unit expansion. Ce is displayed as tan (light), Mn as light blue (gray), and O as red (dark).

4.2.3. Surface formation energies

To determine the relative stability of different configurations and concentrations of Mn doped into CeO₂, a system formation energy is defined. The system formation energies were determined from the following set of chemical equations:



The MnO₂ and CeO₂ units are taken from and inserted in a bulk reservoir, respectively, and the gas phase oxygen is inserted into a reservoir of oxygen at a specified temperature and partial pressure of oxygen. Using the above chemical equations, the system formation energy is calculated at various extents of surface reduction:

$$\Delta G_{\text{CeO}_2 \rightarrow \text{Mn}/\text{inc}} = \frac{E_{\text{Mn}/\text{inc}} + 2\mu_{\text{CeO}_2} - (E_{\text{CeO}_2(111)} + 2\mu_{\text{MnO}_2})}{2} \quad (1)$$

$$\Delta G_{\text{CeO}_2 \rightarrow \text{Mn}/\text{inc}/V_{\text{O}}} = \frac{E_{\text{Mn}/\text{inc}/V_{\text{O}}} + 2\mu_{\text{CeO}_2} + \mu_{\text{O}_2} - (E_{\text{CeO}_2(111)} + 2\mu_{\text{MnO}_2})}{2} \quad (2)$$

$$\Delta G_{\text{CeO}_2 \rightarrow \text{CeO}_{2-y}/V_{\text{O}}} = \frac{E_{\text{CeO}_{2-y}(111)/V_{\text{O}}} + \mu_{\text{O}_2} - E_{\text{CeO}_2(111)}}{2} \quad (3)$$

$$\Delta G_{\text{CeO}_{2-y}/V_{\text{O}} \rightarrow \text{Mn}/\text{inc}/V_{\text{O}}} = \frac{E_{\text{Mn}/\text{inc}/V_{\text{O}}} + 2\mu_{\text{CeO}_2} - (E_{\text{CeO}_{2-y}(111)/V_{\text{O}}} + 2\mu_{\text{MnO}_2})}{2} \quad (4)$$

where $E_{Mn/inc}$ is the energy of the Mn-doped CeO_2 (1 1 1) system, μ_{CeO_2} is the chemical potential of bulk CeO_2 , $E_{CeO_2(1\ 1\ 1)}$ is the energy of a clean surface of CeO_2 , $E_{CeO_2(1\ 1\ 1)/V_O}$ is the energy of a surface of CeO_2 with an oxygen vacancy present, μ_{MnO_2} is the chemical potential of bulk MnO_2 , $E_{Mn/inc/V_O}$ is the energy of Mn incorporated into a Ce lattice position of CeO_2 (1 1 1) surface with an oxygen vacancy present, and μ_{O_2} is the chemical potential of oxygen at a given temperature and pressure. The division by two is a result of using a mirrored slab. The chemical potentials for bulk CeO_2 (MnO_2) were obtained from the energy of a 4 CeO_2 (4 MnO_2) unit cell and divided by 4 to obtain the energy for a single unit of CeO_2 (MnO_2). Equation 1 is representative of replacing a Ce atom with a Mn atom with no oxygen vacancies (reaction A). Equation 2 represents the formation energy to dope Mn while also creating an oxygen vacancy (reaction B). The oxygen vacancy formation energy for the pure CeO_2 (1 1 1) surface is given by Equation 3 (reaction C). Equation 4 represents the formation energy for a structure replacing a Ce atom with a Mn atom in an oxygen vacant surface (reaction D). Equation 2 is the sum of equations 3 and 4. To replace two Ce atoms, with Mn atoms, the coefficient of 2 in front of μ_{CeO_2} and μ_{MnO_2} is replaced with a 4. The effects of configurational entropy have not been examined in our model, as these contributions are quite small relative to the electronic energy contributions. The use of these equations to assess the preference of Mn atoms to dope in ceria versus remaining in a separate MnO_2 phase is discussed in Section 4.3.3.2.

The free energy of oxygen atoms, μ_{O_2} , is calculated as a function of oxygen partial pressure (P_{O_2}), and temperature (T).

$$\mu_{O_2} = E_o + ZPVE - TS + PV \quad (5)$$

where E_o is the DFT energy, $ZPVE$ is the zero-point vibrational energy correction, TS is the entropy calculated by statistical mechanics multiplied by temperature and PV is the pressure volume term.

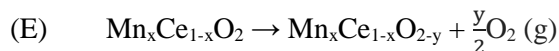
The entropy of O_2 is calculated as

$$S = S_{rot} + S_{vib} + S_{trans} + S_{el} \quad (6)$$

where S_{rot} is the entropy due to rotation, S_{vib} is the entropy due to vibration, S_{trans} is the entropy due to translation, and S_{el} is the entropy due to electronic excitations. The difference between the experimentally determined free energy for O_2 (using the NIST JANAF thermochemical tables)⁴² and the DFT-based free energy is minimal and therefore the DFT energy for O_2 was utilized.

4.2.4. Oxygen vacancy formation energy

The chemical equation for formation of the first oxygen vacancy in Mn-doped CeO_2 is:

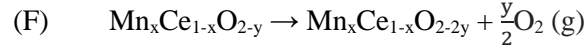


The first oxygen vacancy formation energy is calculated as:

$$\Delta E_{vac} = \frac{E_{Mn/inc/V_O} + E_{O_2} - E_{Mn/inc}}{2} \quad (7)$$

where $E_{Mn/inc/V_O}$ is the energy of the unit cell with one oxygen vacancy on each slab side, E_{O_2} is the energy of a gas phase O_2 molecule, $E_{Mn/inc}$ is the energy of the stoichiometric surface slab, and the division of two is a result from using mirrored slabs.

The chemical equation for the second oxygen vacancy formation in Mn-doped CeO₂ is:



The second oxygen vacancy formation energy is calculated as:

$$\Delta E_{vac} = \frac{E_{Mn/inc/2V_O} + E_{O_2} - E_{Mn/inc/V_O}}{2} \quad (8)$$

where $E_{Mn/inc/2V_O}$ is the energy of the unit cell with two oxygen vacancies on each side, E_{O_2} is the energy of a gas phase O₂ molecule, and the division of two is a result from using mirrored slabs. In both of the oxygen vacancy formation energy calculations, the DFT energy for O₂ is utilized, even though it is known that DFT overestimates the O-O binding energy.¹ A correction term can be added to directly compare the O₂ binding energy to experimental values. In this study, the oxygen vacancies formation energies are compared to establish qualitative trends, and therefore a constant correction term is not applied. For the calculation of oxygen vacancy formation energies, ZPVE and temperature free energy calculations were not added.

4.2.5. Determination of oxidation states

As described in Chapter 3,³¹ we use the site projected charge method to identify the number of cerium atoms reducing from the 4⁺ to the 3⁺ oxidation state. The formal charge on Mn dopant atoms was determined using the formal charge of the Ce atoms and assigning all oxygen atoms as 2-. The oxidation states of the Mn atoms were further confirmed by examining the system total spin.

4.3. Results and Discussion

Mn-dopants in the CeO₂ (1 1 1) surface alter surface reducibility. First, we examine a U -value correction on the d -states of Mn, and recommend a value of $U = 4$ eV which matches Mn XANES behavior (Section 4.3.1). The density of states and orbital structure are compared between standard DFT and DFT+ U methods with a U -value of 4 eV on Mn d -states. Comparing with hybrid HSE06 functional calculations, the U -value of 4 eV is confirmed to give consistent relative energies for oxidation states of Mn (Section 4.3.2). In Section 4.3.3, the concentration of Mn in the surface, as well as the orientation of Mn atoms to each other, is examined for its impact on surface stability and reducibility. Section 4.3.3.1 examines Mn-concentration effects on oxygen vacancy formation energies and Section 4.3.3.2 examines formation energies.

4.3.1. Assigning a Hubbard U -term to the d -states of Mn

Tang et al.³ and Cen et al.⁴ have shown that a U -value on the d -states of Mn in Mn-doped CeO₂ is needed to correctly represent the band gaps and lattice parameters. Figure 4-2 displays the correlation between the oxygen vacancy formation energy and the U -value on the d -states of Mn in a $p(2 \times 2)$ unit cell expansion with a 25% surface Mn concentration. Table B-1 reports the values included in this plot. There are multiple possible local minimum energy structures for each U -value tested, and each represents a different Mn oxidation state. We considered multiple initial structures which converged to these various oxidation states when an oxygen vacancy was created: (1) Mn remaining as Mn⁴⁺ (Mn dopes in as Mn⁴⁺ in the intact case due to the ceria fluorite lattice and remains Mn⁴⁺ after formation of an oxygen vacancy) and 2 Ce atoms reducing, (2) Mn reducing to Mn³⁺ and 1 Ce atom reducing, or (3) Mn reducing to Mn²⁺. In the fully oxidized structure, Mn takes on a 4⁺ oxidation state, as enforced by the MO₂ stoichiometry, irrelevant of U -value. At low U -

values ($U < 3.5$ eV), the most stable oxidation state for Mn after formation of an oxygen vacancy is Mn^{3+} . The impact of the Mn d -state U -correction is more significant for a more reduced Mn^{2+} state, which causes Mn^{2+} to become more stable for $U \geq 3.5$ eV. Using the U -value of 4 eV on the d -states of Mn, as recommended by Wang based on pure MnO_x behavior,¹ the most stable oxidation state is Mn^{2+} upon formation of an oxygen vacancy. Li et al. showed using XANES that when Mn-doped CeO_2 is reduced, a Mn^{2+} oxidation state is preferred, corroborating that a U -value of 4 eV on the d -states of Mn matches qualitatively experimental behavior.¹⁰ A U -value of 4 eV is also consistent with existence of both Mn^{3+} and Mn^{2+} in a calcined sample.¹⁰

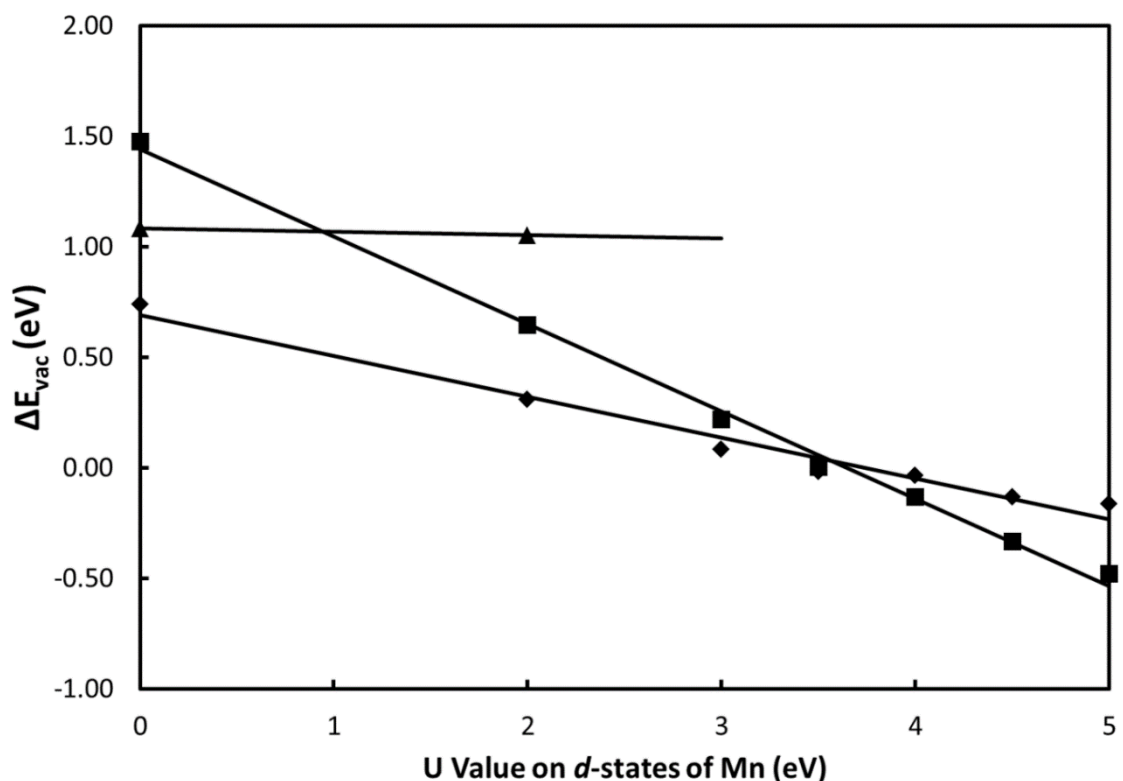


Figure 4-2. Surface oxygen vacancy formation energy vs. U -value on the d -states of Mn in a $p(2 \times 2)$ unit cell expansion with a 25% surface Mn concentration. Mn reduces to different oxidation states upon formation of an oxygen vacancy. Mn reducing to: (◆) Mn^{3+} , (■) Mn^{2+} , and (▲) Mn^{4+} upon formation of an oxygen vacancy. (—) best fit line.

When the Mn atom reduces to Mn^{3+} , there are 5 possible overall spin values for the system (utilizing a mirrored slab): 10, 8, 6, 2 and 0. All have the same energy (within 0.02 eV), indicating there is no spin-spin interaction among the localized Mn d or Ce f -states. In each of these cases, each Mn atom has a spin of 4, as enumerated in Figure 4-3. All possible overall spin states for Mn (Mn^{4+} , Mn^{3+} and Mn^{2+}) in the reduced structure are shown in Figure 4-3. The atomic spin for Mn^{4+} is 3 and the spin for Mn^{2+} is 5. In the intact case the overall spin can be either be 0 or 6.

The intact (fully oxidized) surface density of states and select orbital images for Mn-doped CeO_2 with Mn d -state U -values of 0 and 4 eV are shown in Figure 4-4. In both cases, Mn dopes into the surface as Mn^{4+} (d^3). With no U -value on the d -states of Mn, single spin occupied orbitals lie between the valence band and the conduction band, Figure 4-4a. The orbital image in Figure 4-4b confirms these states as Mn-oxygen anti-bonding states. The inclusion of a U -value on the d -states of Mn shifts single spin occupied d -states out of the valence band region to below the valence band. The Mn-oxygen anti-bonding orbitals are shifted into the valence band, Figure 4-4c and Mn-oxygen bonding orbitals from the valence band are shifted to below the valence band (between -5 and -4 eV), Figures 4-4c and 4-4d.

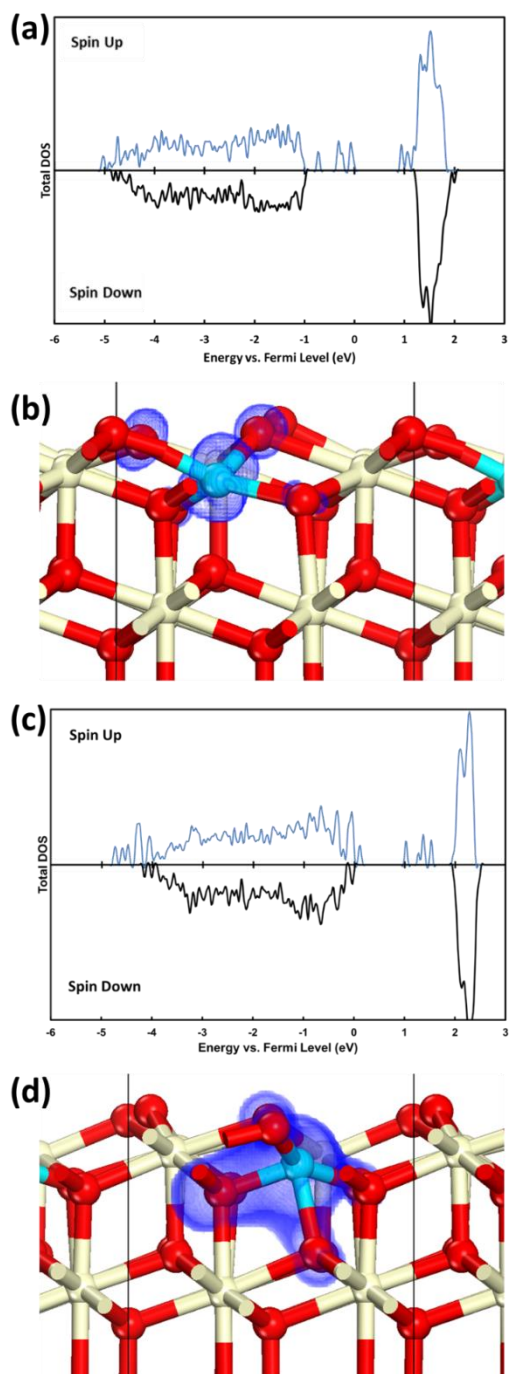


Figure 4-4. Total DOS plotted versus energy (referenced to Fermi level) for (a) intact Mn-doped CeO_2 (1 1 1) with $U = 0$ eV on d -states of Mn (total spin of 6), and (c) intact Mn-doped CeO_2 (1 1 1) with $U = 4$ eV on d -states of Mn (total spin of 6). Spin-down density of states is plotted on the negative y axis. Isodensity surfaces representing electronic states for (b) intact Mn-doped CeO_2 with $U = 0$ eV on d -states of Mn over the energy range -0.87 to 0.00 eV (relative to Fermi level) and (d) intact Mn-doped CeO_2 with $U = 4$ eV on d -states of Mn over the energy range -4.93 to -4.23 eV.

The oxygen vacant density of states for Mn-doped CeO₂, with a Mn *d*-state *U*-value of 4 eV, and for Mn reducing to Mn²⁺ or Mn³⁺, are displayed in Figure 4-5. Figure 4-5a contains the DOS for Mn reducing to Mn²⁺. There are a number of single spin states at the top of the valence band. Orbital images of these single spin states are displayed in Figure 4-5b, confirming these as anti-bonding Mn-oxygen states. The DOS for the slightly less favorable minimum of Mn reducing to Mn³⁺ is shown in Figure 4-5c. Here a number of single spin states can also be seen at the top and the bottom of the valence band, as well as the formation of another occupied *d* orbital between the valence and conduction bands. Orbital imaging of this orbital between the valence and conduction bands is shown in Figure 4-5d, confirming anti-bonding Mn-oxygen character. Figure 4-5e, illustrates the localized *d*-states on Mn at the bottom of the valence band. The single spin states just above the localized *d*-states on Mn are Mn-oxygen bonding states (~-5.5 to 5 eV). The density of states for Mn reducing to Mn³⁺ with no *U*-value on the *d*-states of Mn was previously published.³¹ In this Mn³⁺ DOS, occupied orbitals form between the valence and conduction band. One forms from the reduction of Ce⁴⁺ to Ce³⁺ and the second from Mn reducing to Mn³⁺. With the inclusion of the *U*-value on the *d*-states, the occupied orbital from the *d*-states of Mn stays between the valence and conduction bands. There should be an orbital resulting from the reduction of Ce⁴⁺ to Ce³⁺ based upon charge analysis; however there is no single spin state for cerium in the band gap. Therefore, the inclusion of a *U*-term on the *d*-states of Mn shifts the occupied orbital resulting from the reduction of Ce into the valence band.

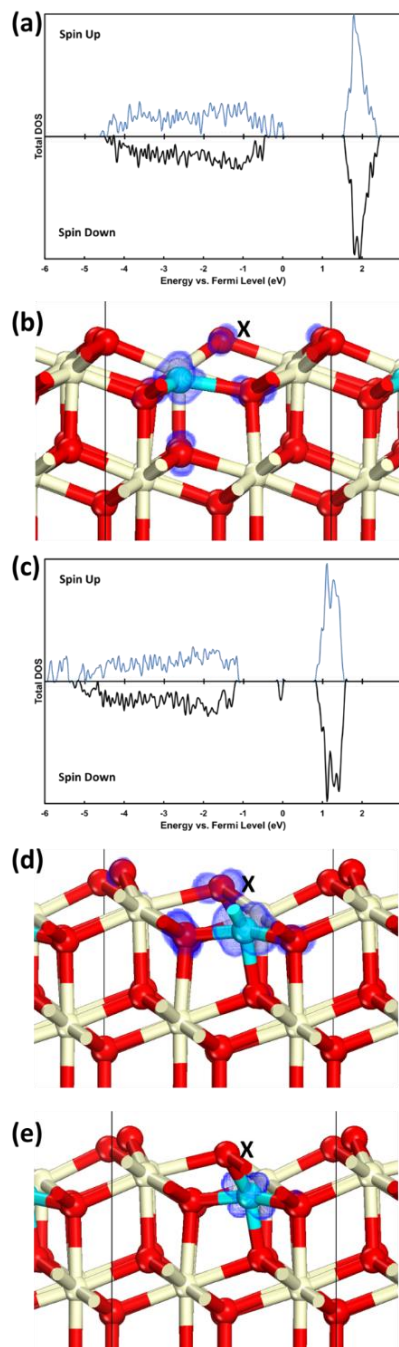


Figure 4-5. Total DOS plotted versus energy (referenced to Fermi level) for (a) oxygen vacant Mn-doped CeO_2 (1 1 1) with $U = 4$ eV on d -states of Mn and Mn reducing to Mn^{2+} (total spin of 10), and (c) oxygen vacant Mn-doped CeO_2 (1 1 1) with $U = 4$ eV on d -states of Mn and Mn reducing to Mn^{3+} (total spin of 6). Spin-down density of states is plotted on the negative y axis. Isodensity surfaces representing electronic states for (b) oxygen vacant Mn-doped CeO_2 with $U = 4$ eV on d -states of Mn and Mn reducing to Mn^{2+} over the energy range -0.34 to 0.00 eV (relative to Fermi level) and oxygen vacant Mn-doped CeO_2 with $U = 4$ eV on d -states of Mn and Mn reducing to Mn^{3+} over the energy range (d) -0.29 to 0.00 eV and (e) -5.59 to -5.78 eV. The X's represent the locations where the oxygen was removed.

The inclusion of U -terms clearly shifts the electronic behavior of the intact and vacant Mn-doped ceria surface, with the Ce and Mn U -terms having a combined effect. Though we have not assessed the accuracy of this representation due to a lack of available electronic characterization for the Mn-CeO₂(1 1 1) surface, we again note that the independent U -values of 5 eV on Ce f -states and 4 eV on Mn d -states replicate the separate bulk oxide behaviors. These values have also qualitatively captured the Mn XANES assigned Mn oxidation state in oxidized and reduced surfaces.

4.3.2. Corroborating the U -value on Mn by comparison to the HSE06 hybrid functional

The hybrid functional HSE06 has been used to model oxygen vacancy formation in pure CeO₂(1 1 1)²⁴ and oxygen vacancy formation in doped surfaces of CeO₂.²²⁻²³ These studies did not examine Mn as a dopant, nor was direct comparison between HSE06 and a U -value on the d -states of any dopant considered. As described above, in the lowest energy structure for Mn-doped CeO₂, Mn reduces to Mn²⁺ upon the formation of an oxygen vacancy with a U -value of 4 eV on the d -states of Mn. The HSE06 hybrid functional also predicts that the lowest energy structure upon formation of an oxygen vacancy is Mn reducing to Mn²⁺ (Table 4-1). The absolute oxygen vacancy formation energies (ΔE_{vac}) for DFT+ U and HSE06 functional are reasonably similar. The difference of ~0.5 eV is meaningful, highlighting the difficulty in using absolute reduction energies from DFT based methods for these systems. The extent to which these differences are due to the different number of layers or k -points could not be evaluated because of computational intensity and SCF convergence problems with the HSE06 calculations. The difference between the vacancy formation energies between Mn reducing to Mn²⁺ versus Mn³⁺ are in good agreement (0.10 eV for DFT+ U and 0.15 eV for HSE06). The matching of the difference between Mn²⁺ and Mn³⁺ is more important than the absolute values of vacancy formation energies in predicting the most stable oxidation states

for Mn in Mn-doped CeO₂. The HSE06 hybrid functional helps to confirm the U -value of 4 eV on the d -states for predicting, at least, qualitative redox behavior of Mn-doped ceria.

Table 4-1. Oxygen vacancy formation energies (ΔE_{vac}) using the Hubbard U -correction and the HSE06 hybrid functional.

Functional	Mn Reduces to	ΔE_{vac} (eV)
$U = 4$ on Mn, $U = 5$ on Ce ^a	Mn ³⁺	-0.03
$U = 4$ on Mn, $U = 5$ on Ce ^a	Mn ²⁺	-0.13
HSE06 ^b	Mn ³⁺	-0.54
HSE06 ^b	Mn ²⁺	-0.69

^a4-layer mirrored slab with 2 x 2 x 1 k -points. ^b3-layer non-mirrored slab with 1 x 1 x 1 k -points.

4.3.3. Mn concentration and distribution effects

In this section, we examine how the concentration and orientation of Mn dopants affect oxygen vacancy formation energies and surface formation energies. All results use DFT+ U with a U -value of 4 eV on the Mn d -states.

4.3.3.1. First and second oxygen vacancy formation energies

In the previous section, the concentration of Mn in the surface was 25% in a $p(2 \times 2)$ unit cell expansion, resulting in a surface oxygen vacancy formation energy of -0.03 eV. This exothermic vacancy formation, coupled with the favorable entropy of vacancy formation, suggests the fully oxidized Mn-doped CeO₂ (1 1 1) surface is unstable for this Mn concentration. To vary

the Mn concentrations, a $p(2 \times 3)$ unit cell expansion is utilized with either 1 Mn dopant (16.7% concentration) or 2 Mn dopants (33.3% concentration). With the inclusion of 2 Mn dopants, multiple configurations for Mn atoms are possible (short row, long row, diagonal, surface and subsurface). Also, there are multiple possibilities for the first oxygen vacancy position: an oxygen not bond to an Mn atom, an oxygen bond to one Mn, an oxygen bond to 2 Mn atoms as well as subsurface oxygen vacancies. Examining a second oxygen vacancy adds more possibilities for combinations of oxygen vacancy positions. Most of the possible arrangements for the configurations for Mn dopants were examined. Multiple positions for the first oxygen vacancy were examined and the lowest energy structure is reported. The starting structure to form a second vacancy was the lowest energy structure for the first oxygen vacancy and multiple positions for the second oxygen vacancy were examined. The lowest energy structure is reported.

A subset of the optimized structures and orientations for Mn dopants are shown in Figure 4-6. Two surface Mn atoms in a diagonal arrangement with no oxygen vacancies is shown in Figure 4-6a. Figures 4-6b through 4-6d contain optimized structures with either one or two oxygen vacancies with different orientations of Mn atoms. Figure 4-7 contains surface, subsurface, and 2nd oxygen vacancy formation energies for different concentrations and orientations of Mn dopants. Table B-2 reports the values included in this plot. In all cases for Mn-doped CeO₂ (1 1 1), the subsurface oxygen vacancy is higher in energy than the surface oxygen vacancy. The oxidation states of Mn in each case as well as the number of reduced Ce atoms are listed in Table 4-2. In all cases, the lowest energy structure for the formation of a surface or subsurface oxygen vacancy occurs by reducing Mn without reducing Ce atoms. When there is only one Mn present, the Mn reduces to Mn²⁺, and with two Mn present, they both reduce to Mn³⁺.

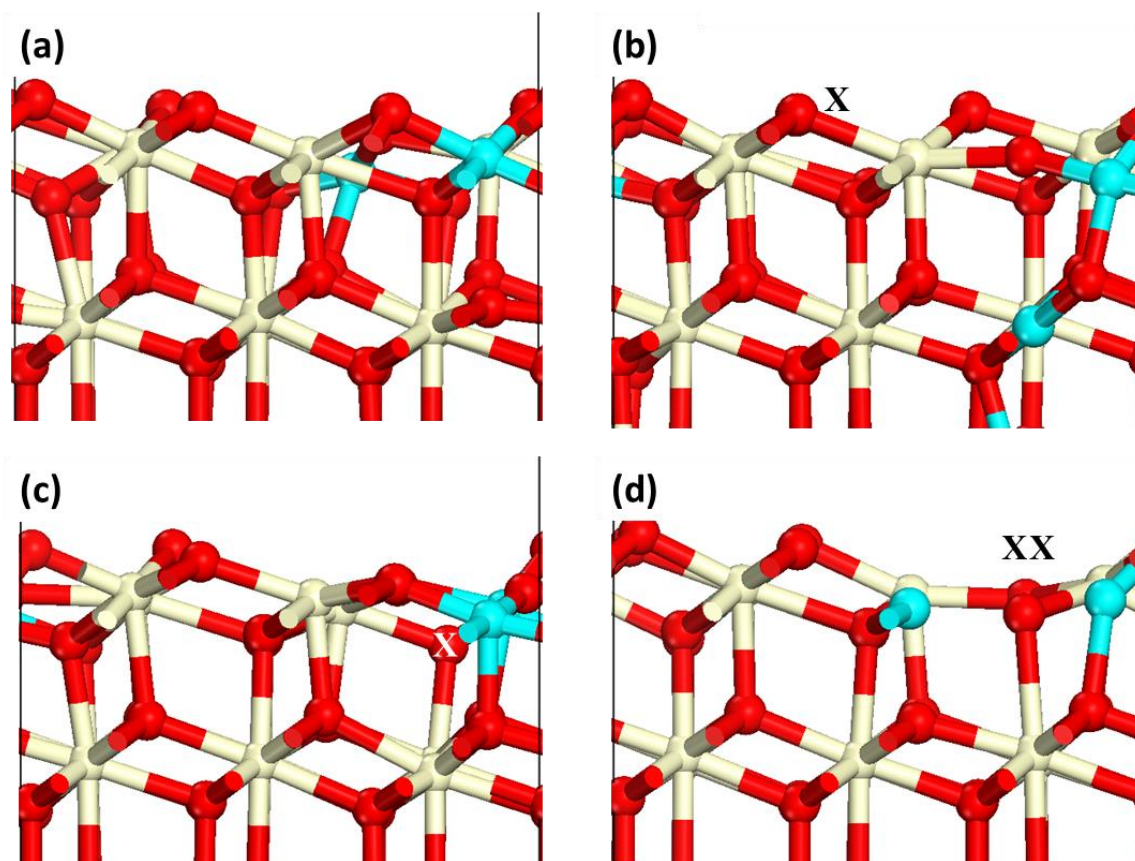


Figure 4-6. Four structures of a $p(2 \times 3)$ unit cell expansion of 2Mn-doped CeO_2 (1 1 1). (a) intact structure with Mn atoms diagonal to each other, (b) surface oxygen vacant structure with one Mn atom in a surface position and a second in a subsurface position in a row, (c) subsurface oxygen vacant structure with two Mn atoms in a surface short row, and (d) doubly surface oxygen vacant structure with two Mn atoms in a surface long row. Ce is displayed as tan (light), Mn as light blue (gray), and O as red (dark). The X's represent the locations where the oxygen was removed.

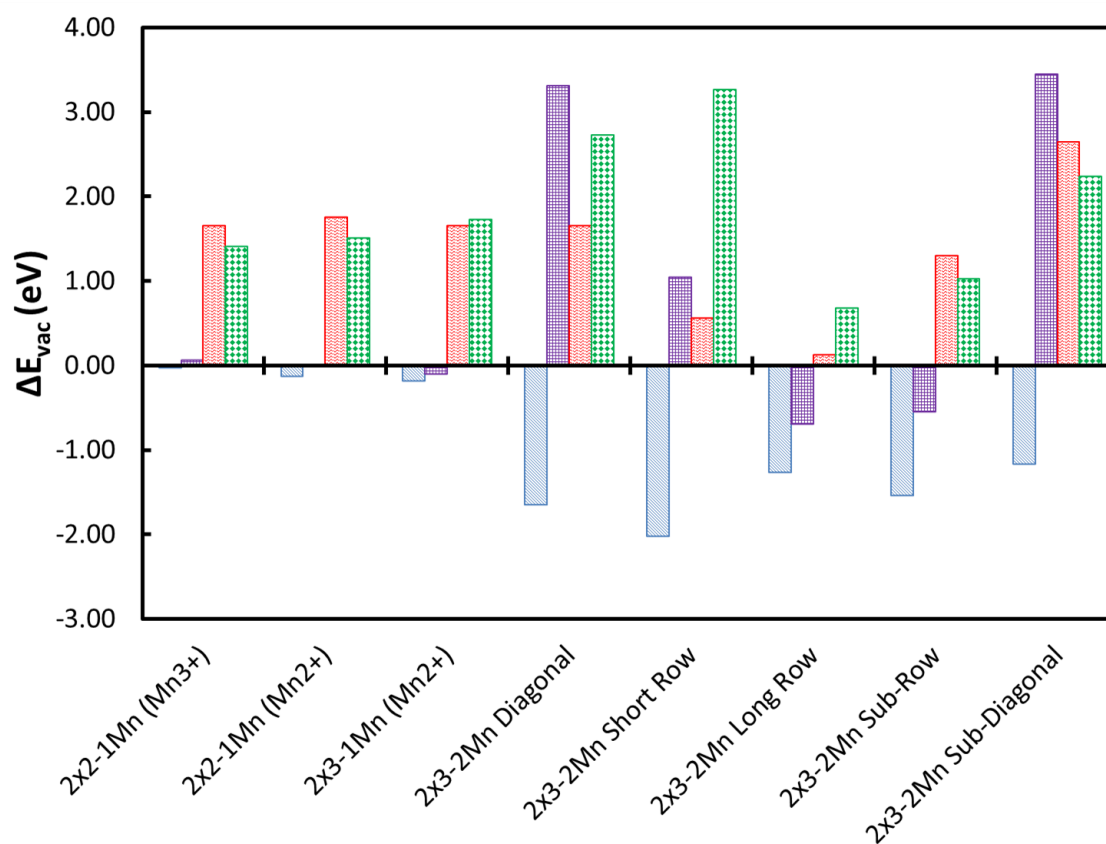


Figure 4-7. First and second oxygen vacancy formation energies for Mn-doped $\text{CeO}_2(1\ 1\ 1)$ with $U = 4$ eV on d -states of Mn. The second oxygen vacancy energy is calculated relative to a structure with the first surface oxygen vacancy formed. (▨) One surface oxygen vacancy, (▨) One subsurface oxygen vacancy, (▨) Two surface oxygen vacancies (▨) One surface and one subsurface oxygen vacancy.

Table 4-2. Mn oxidation states and number of reduced Ce atoms (# Ce³⁺) for different concentrations and orientations of Mn dopants in the CeO₂ (1 1 1) surface.

Configura tion	Bare Surface		Surface Oxygen Vacancy		Subsurface Oxygen Vacancy		2 Surface Oxygen Vacancies		1 Surface and 1 Subsurface Oxygen Vacancy	
	Mn	# Ce ³⁺	Mn	# Ce ³⁺	Mn	# Ce ³⁺	Mn	# Ce ³⁺	Mn	# Ce ³⁺
2x2 – 1 Mn (Mn ³⁺)	Mn ⁴⁺	0	Mn ³⁺	0	Mn ³⁺	0	Mn ²⁺	2	Mn ²⁺	2
2x2 – 1 Mn (Mn ²⁺)	Mn ⁴⁺	0	Mn ²⁺	0	-	-	Mn ²⁺	2	Mn ²⁺	2
2x3 – 1 Mn	Mn ⁴⁺	0	Mn ²⁺	0	Mn ²⁺	0	Mn ²⁺	2	Mn ²⁺	2
2x3 – 2 Mn Diagonal	Mn ⁴⁺	0	Mn ³⁺	0	Mn ³⁺	0	Mn ²⁺	0	Mn ²⁺ Mn ³⁺	1
2x3 – 2 Mn Short Row	Mn ⁴⁺	0	Mn ³⁺	0	Mn ³⁺	0	Mn ²⁺ Mn ³⁺	1	Mn ²⁺ Mn ³⁺	1
2x3 – 2 Mn Long Row	Mn ⁴⁺	0	Mn ³⁺	0	Mn ³⁺	0	Mn ²⁺	0	Mn ²⁺ Mn ³⁺	1
2x3 – 2 Mn Sub- Row	Mn ⁴⁺	0	Mn ³⁺	0	Mn ³⁺	0	Mn ²⁺ Mn ³⁺	1	Mn ²⁺ Mn ³⁺	1
2x3 – 2 Mn Sub- Diagonal	Mn ⁴⁺	0	Mn ³⁺	0	Mn ³⁺	0	Mn ²⁺	0	Mn ²⁺ Mn ³⁺	1

For a single Mn surface dopant, the first oxygen vacancy formation energy is slightly negative. With 2 Mn dopants, all first oxygen vacancy formation energies are highly exothermic. The first oxygen vacancy is therefore spontaneous upon doping Mn into the surface. The second oxygen vacancy formation energy likely becomes more catalytically important in catalytic processes for which the surface oscillates between oxidation states.

Second oxygen vacancy formation energies, forming two surface oxygen vacancies or a surface and subsurface oxygen vacancy, are reported in Figure 4-7. The second vacancy formation energy is calculated relative to a surface with the first surface oxygen vacancy formed. With two Mn atoms doped into the surface, formation of two surface oxygen vacancies is preferred. When one of the two Mn atoms is doped into the subsurface layer, forming a surface and a subsurface vacancy becomes more favorable. This suggests that Mn-dopant short range effects (nearest neighbor, NN) on vacancy stability are much stronger than longer range effects (next NN, NNN). After one surface vacancy is formed, remaining surface oxygen atoms are NNN or farther away from the subsurface Mn. With one Mn atom doped into the surface, forming two surface oxygen vacancies or forming a surface and subsurface oxygen vacancy are equivalent in energy.

Formation of a second oxygen vacancy with one Mn present reduces two Ce atoms and the Mn remains as Mn^{2+} (Table 4-2). This vacancy formation energy is not nearly as favorable as the first vacancy formation energy, but is still more favorable than the formation of a single oxygen vacancy in pure CeO_2 (1 1 1). This is in agreement with Cen et al. showing Ce^{4+} reduction to Ce^{3+} is promoted by Mn doping.⁴ Formation of a second vacancy with two Mn present does not always reduce both Mn atoms to Mn^{2+} . When forming two surface vacancies, depending on the orientation, either one Mn atom can reduce from Mn^{3+} to Mn^{2+} and one Ce reduce, or both Mn atoms can reduce from Mn^{3+} to Mn^{2+} . Though all Mn atoms reducing to Mn^{2+} before any Ce atoms reduce might be expected, structural rearrangements would have to occur to allow both Mn atoms to reduce to Mn^{2+} . The small unit cell constrains these rearrangements. In some cases, the second oxygen vacancy

formation energy is less than 0. The second vacancy formation energy is always more favorable with 2 Mn atoms doped into the surface than with 1 Mn dopant and always more favorable than the first oxygen vacancy in pure CeO₂. This suggests a strong reducibility of the Mn-doped CeO₂ system.

As first vacancy formation energies are always favorable, Mn³⁺ or Mn²⁺ may be present in calcined surfaces of Mn-doped ceria. Second vacancy formation varies from slightly exothermic to endothermic, depending on Mn concentrations and positioning suggesting these oxygen atoms may be labile to participate in redox processes. Mn-CeO₂ will likely expose an array of various local sites, but all of these vacancy formation energies are in the optimal range for methane oxidation activity as described in Chapter 3.³¹

4.3.3.2. Formation energies

Up to this point, we have assumed that Mn will dope into the surface of CeO₂ without consideration of its stability. However, Mn may not prefer to dope into the fluorite CeO₂ structure, and the favorability of doping will depend on concentration, orientation and whether the surface is exposed to an oxidizing or reducing environment. Structural reorganization, especially upon multiple oxygen vacancy formation, is significant, further questioning the stability of the mixed oxide system. We considered formation energies to form the mixed oxide surface system from a pure CeO₂ surface (oxidized or reduced) and a bulk MnO₂ reservoir.

These formation energies can provide an indication of the stability of the Mn-doped surfaces at various concentrations and oxidation states, however, it is possible the synthetic procedures may isolate unstable configurations as well. The formation energies to dope Mn into the surface are listed in Table 4-3, as calculated by equations 1-4, at 1000 K and $P_{O_2} = 10^{-18}$ atm ($\mu_{O_2} = -15.82$ eV). For example, Equation 1 gives the formation energy of a Mn-doped, fully-

oxidized surface referenced to a pure (1 1 1) surface of CeO₂, where a MnO₂ unit from bulk MnO₂ replaces a CeO₂ unit and the CeO₂ unit is placed back into bulk CeO₂. Formation energies for the fully oxidized system calculated via Equation 1 are endergonic at any temperature and oxidizing or reducing environment. Therefore, Mn will not preferentially dope into the surface in a fully oxidized fluorite lattice.

Table 4-3. Formation energy of doping Mn into the surface of CeO₂ at 1000 K and $P_{O_2} = 10^{-18}$ atm.

	Formation energy of doping Mn into CeO ₂ (1 1 1) with no oxygen vacancies (eV)	Formation energy of doping Mn into CeO ₂ (1 1 1) with no oxygen vacancies forming an oxygen vacancy (eV)	Formation energy forming 1 oxygen vacancy in CeO ₂ (1 1 1) (eV)	Formation energy of doping Mn into CeO ₂ (1 1 1) with one oxygen vacancy (eV)
2x2-1Mn (Mn ³⁺)	2.30	-0.73	-0.24	-0.50
2x2-1Mn (Mn ²⁺)	2.30	-0.83	-0.24	-0.59
2x3-1Mn (Mn ²⁺)	2.37	-0.83	-0.44	-0.39
2x3-2Mn Diagonal	3.60	-1.06	-0.44	-0.63
2x3-2Mn Short Row	3.93	-1.10	-0.44	-0.66
2x3-2Mn Long Row	4.68	0.41	-0.44	0.84
2x3-2Mn Sub-Row	4.37	-0.18	-0.44	0.26
2x3-2Mn Sub-Diagonal	4.03	-0.15	-0.44	0.29

If instead an oxygen vacancy is formed with Mn doped into the surface, the doped surface is stable relative to the MnO_2 reference under certain environments. Figure 4-8 depicts 3 formation energy values for each Mn-doped ceria reduce surface. The first is the formation free energy relative to intact CeO_2 (1 1 1) (Equation 2). A negative value for this does not necessarily signify favorable doping as it neglects possible favorable pure CeO_2 (1 1 1) reduction in the reference state. The second value is the reduction free energy of CeO_2 (1 1 1) (Equation 3) with the same unit cell and the third is the difference between these (Equation 4). Negative values for this third column suggest favorable doping at that oxygen chemical potential. As seen in Figure 4-8, under more reducing environments, Mn doped into a reduced surface is favorable.

Under conditions where the environment is very reducing, the stable surface for pure CeO_2 surface will have oxygen vacancies (negative for the second value), Figure 4-8b. Relative to bulk MnO_2 under these conditions, Mn doped in the reduced surface of CeO_2 will be stable. Under somewhat less reducing environments, the stable surface of pure CeO_2 will be intact (positive for the second value, Figure 4-8a). A reduced surface with Mn-doped may be stable in these less reducing environments where it is unstable for ceria to have oxygen vacancies, due to the more favorable reducibility of the Mn-doped surface. Under even less reducing or approaching oxidizing environments, Mn-doping into the surface becomes unstable relative to separate oxide phases. Mn doped into the CeO_2 surface either in a diagonal arrangement to one another or forming a continuous row (short row) are the most stable structures. Doping 2 Mn atoms in the surface is more stable than doping 1 Mn atom because of the more favorable vacancy formation energy when Mn atoms are adjacent.

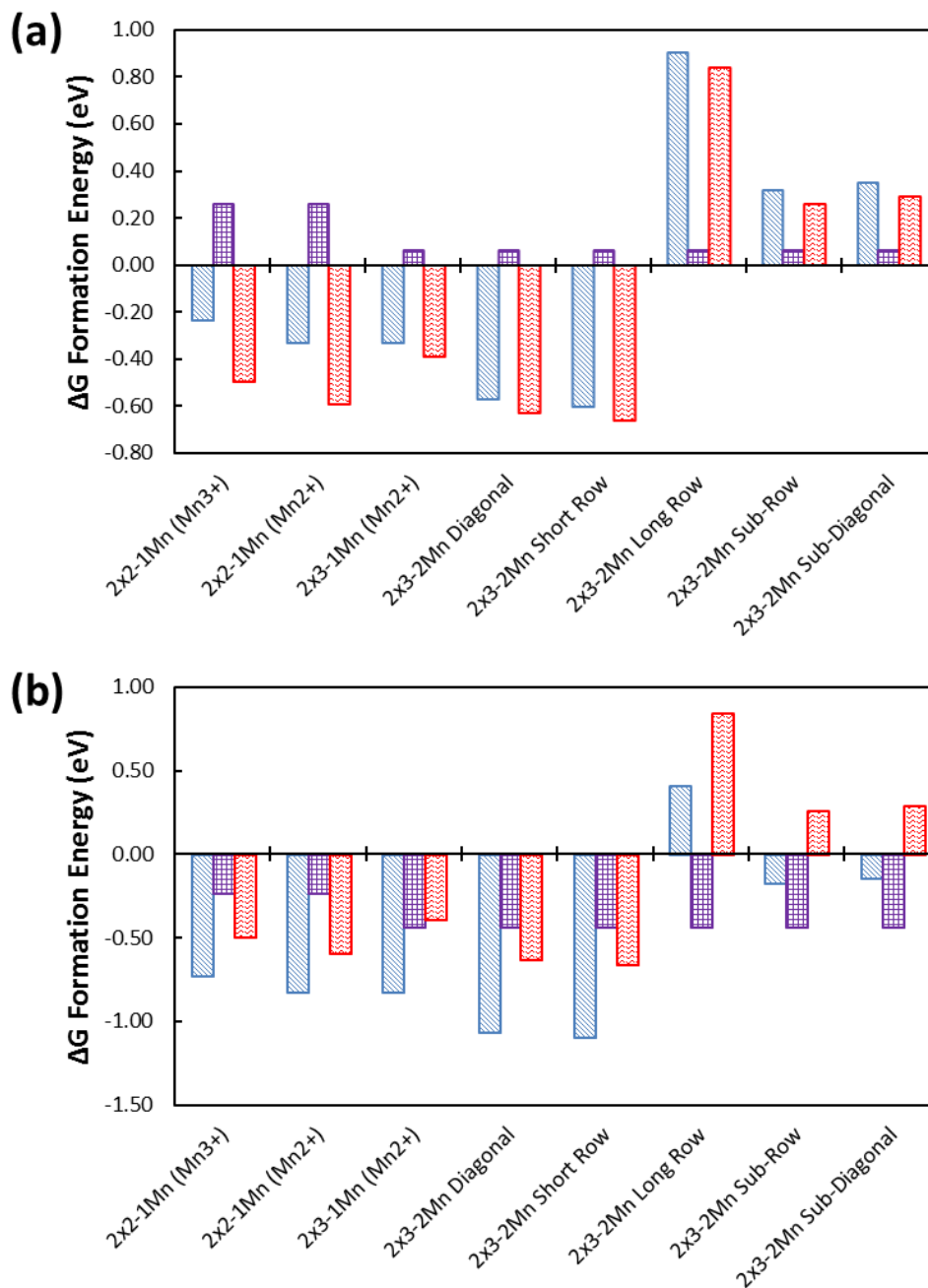


Figure 4-8. Formation energies for Mn-doped CeO_2 (1 1 1) and pure ceria at (a) 1000 K and $P_{\text{O}_2} = 10^{-13}$ atm and (b) 1000 K and $P_{\text{O}_2} = 10^{-18}$ atm. (▨) Forming Mn-doped CeO_2 with 1 oxygen vacancy referencing an intact surface of CeO_2 (1 1 1), bulk CeO_2 and bulk MnO_2 (Equation 2 and chemical equation B), (▣) forming 1 oxygen vacancy in CeO_2 (1 1 1) (Equation 3 and chemical equation C), (⊞) forming Mn-doped CeO_2 with 1 oxygen vacancy referencing an oxygen vacant surface of CeO_2 (1 1 1), bulk CeO_2 and bulk MnO_2 (Equation 4 and chemical equation D). The sum of (▣) and (⊞) is (▨).

The positive formation energies for Mn doping into pure CeO₂ without forming an oxygen vacancy is indicative that the Mn will not dope in the surface as Mn⁴⁺. Under highly oxidizing conditions, formation of a separate MnO₂ phase will be thermodynamically preferred. The negative formation energies, under reducing conditions, for Mn doping into CeO₂ with an oxygen vacancy is indicative that Mn will dope into the surface as Mn³⁺ and Mn²⁺. The formation of Mn-doped CeO₂ is metastable when formed under highly oxidizing environments, but under reducing environments, the system is stable.

4.4. Conclusions

To correctly represent the electronic structure and behavior of Mn in Mn-doped CeO₂ (1 1 1) surface, a U -correction on the d -states of Mn must be included. Depending upon the U -value chosen, the most stable oxidation state for Mn can vary. At low U -values, a $p(2 \times 2)$ unit cell expansion with 25% Mn concentration reduces Mn⁴⁺ to Mn³⁺ upon formation of an oxygen vacancy. Mn reduces instead to Mn²⁺ at high U -values. Using a U -value of 4 eV, as recommended by Wang et al.,¹ the most stable oxidation state for isolated Mn atoms in a reduced surface is Mn²⁺. The difference in energy between Mn reducing to Mn²⁺ and Mn³⁺ at a U -value of 4 eV is closely matched to the equivalent difference in energy as predicted by the HSE06 hybrid functional. This helps to confirm that a U -value of 4 eV is reasonable.

For all concentrations and arrangements of Mn atoms in the doped CeO₂ (1 1 1) surface without oxygen vacancies, the formation energy is endergonic and therefore Mn does not favorably dope into the surface. Under sufficiently reducing conditions, the formation energy is favorable for doping Mn into CeO₂ (1 1 1) with oxygen vacancies, indicating that Mn will dope into the reduced surface. The most favorable concentration and arrangement for Mn to dope into CeO₂ occurs when Mn atoms are diagonal to one another or when Mn atoms form a continuous row (short row). As

Mn is not stable doped into the surface of CeO₂ without oxygen vacancies, the first oxygen vacancy is not catalytically important. The second oxygen vacancy becomes catalytically important as it may form and reoxidize during catalyzed redox processes. The second oxygen vacancy formation energy is highly dependent upon the concentration and orientation of Mn atoms.

ACKNOWLEDGEMENTS: This material is based upon work supported as part of the Center for Atomic Level Design, an Energy Frontier Research Center funded by the U.S. Department of Energy, Office of Science, Office of Basic Energy Sciences under Award Number DE-SC0001058.

4.5. References

1. L. Wang, T. Maxisch, G. Ceder. *Physical Review B* **2006**, *73*, 195107.
2. G. S. Qi, R. T. Yang. *Journal of Physical Chemistry B* **2004**, *108*, 15738-15747.
3. Y. H. Tang, H. Zhang, L. X. Cui, C. Y. Ouyang, S. Q. Shi, W. H. Tang, H. Li, J. S. Lee, L. Q. Chen. *Physical Review B* **2010**, *82*, 125104.
4. W. L. Cen, Y. Liu, Z. B. Wu, H. Q. Wang, X. L. Weng. *Physical Chemistry Chemical Physics* **2012**, *14*, 5769-5777.
5. M. Abecassis-Wolfovich, M. V. Landau, A. Brenner, M. Herskowitz. *Journal of Catalysis* **2007**, *247*, 201-213.
6. H. F. Li, G. Z. Lu, Q. G. Dai, Y. Q. Wang, Y. Guo, Y. L. Guo. *Applied Catalysis B-Environmental* **2011**, *102*, 475-483.
7. D. Delimaris, T. Ioannides. *Applied Catalysis B-Environmental* **2008**, *84*, 303-312.
8. D. Terribile, A. Trovarelli, C. de Leitenburg, A. Primavera, G. Dolcetti. *Catalysis Today* **1999**, *47*, 133-140.

9. L. C. Hsu, M. K. Tsai, Y. H. Lu, H. T. Chen. *Journal of Physical Chemistry C* **2013**, *117*, 433-441.
10. R. Li, M. D. Krcha, M. J. Janik, A. D. Roy, K. M. Dooley. *Energy & Fuels* **2012**, *26*, 6765-6776.
11. C. Y. Kang, H. Kusaba, H. Yahiro, K. Sasaki, Y. Teraoka. *Solid State Ionics* **2006**, *177*, 1799-1802.
12. B. Murugan, A. V. Ramaswamy, D. Srinivas, C. S. Gopinath, V. Ramaswamy. *Chemistry of Materials* **2005**, *17*, 3983-3993.
13. A. Gupta, U. V. Waghmare, M. S. Hegde. *Chemistry of Materials* **2010**, *22*, 5184-5198.
14. J. Heyd, G. E. Scuseria, M. Ernzerhof. *Journal of Chemical Physics* **2003**, *118*, 8207-8215.
15. J. Heyd, G. E. Scuseria, M. Ernzerhof. *Journal of Chemical Physics* **2006**, *124*, 219906.
16. J. Heyd, G. E. Scuseria. *Journal of Chemical Physics* **2004**, *121*, 1187-1192.
17. S. Fabris, S. de Gironcoli, S. Baroni, G. Vicario, G. Balducci. *Physical Review B* **2005**, *71*, 041102.
18. S. Fabris, S. de Gironcoli, S. Baroni, G. Vicario, G. Balducci. *Physical Review B* **2005**, *72*, 237102.
19. G. Kresse, P. Blaha, J. L. F. Da Silva, M. V. Ganduglia-Pirovano. *Physical Review B* **2005**, *72*, 237101.
20. S. L. Dudarev, G. A. Botton, S. Y. Savrasov, C. J. Humphreys, A. P. Sutton. *Physical Review B* **1998**, *57*, 1505-1509.
21. Z. X. Yang, Q. G. Wang, S. Y. Wei. *Physical Chemistry Chemical Physics* **2011**, *13*, 9363-9373.
22. M. Nolan. *Journal of Materials Chemistry* **2011**, *21*, 9160-9168.
23. M. Nolan. *Journal of Physical Chemistry C* **2011**, *115*, 6671-6681.

24. M. V. Ganduglia-Pirovano, J. L. F. Da Silva, J. Sauer. *Physical Review Letters* **2009**, *102*, 026101.
25. G. Kresse, J. Furthmuller. *Computational Materials Science* **1996**, *6*, 15-50.
26. G. Kresse, J. Furthmuller. *Physical Review B* **1996**, *54*, 11169-11186.
27. G. Kresse, J. Hafner. *Physical Review B* **1993**, *47*, 558-561.
28. G. Kresse, D. Joubert. *Physical Review B* **1999**, *59*, 1758-1775.
29. H. J. Monkhorst, J. D. Pack. *Physical Review B* **1976**, *13*, 5188-5192.
30. J. P. Perdew, J. A. Chevary, S. H. Vosko, K. A. Jackson, M. R. Pederson, D. J. Singh, C. Fiolhais. *Physical Review B* **1992**, *46*, 6671-6687.
31. M. D. Krcha, A. D. Mayernick, M. J. Janik. *Journal of Catalysis* **2012**, *293*, 103-115.
32. V. I. Anisimov, O. Gunnarsson. *Physical Review B* **1991**, *43*, 7570-7574.
33. J. F. Herbst, R. E. Watson, J. W. Wilkins. *Physical Review B* **1978**, *17*, 3089-3098.
34. A. D. Mayernick, M. J. Janik. *Journal of Physical Chemistry C* **2008**, *112*, 14955-14964.
35. A. D. Mayernick, M. J. Janik. *Journal of Chemical Physics* **2009**, *131*, 084701.
36. A. D. Mayernick, M. J. Janik. *Journal of Catalysis* **2011**, *278*, 16-25.
37. H. T. Chen, J. G. Chang. *Journal of Chemical Physics* **2010**, *132*, 214702.
38. M. Nolan. *Journal of Chemical Physics* **2009**, *130*, 144702.
39. Z. X. Yang, G. X. Luo, Z. S. Lu, K. Hermansson. *Journal of Chemical Physics* **2007**, *127*, 074704.
40. M. Nolan, V. S. Verdugo, H. Metiu. *Surface Science* **2008**, *602*, 2734-2742.
41. M. Nolan, S. C. Parker, G. W. Watson. *Surface Science* **2005**, *595*, 223-232.
42. J. Chase, *NIST-JANAF Thermochemical Tables*. 4th ed.; ACS American Chemical Society: 1998.

Chapter 5

Catalytic Propane Reforming Mechanism over Zr-Doped CeO₂ (1 1 1)

This chapter is published as: M. D. Krcha, M. J. Janik. *Catalysis Science & Technology* **2014**, DOI: 10.1039/C4CY00619D.

ABSTRACT: Elucidation of the elementary reaction processes involved in hydrocarbon oxidation on oxide catalysts can help guide active site optimization. We use density functional theory (DFT) methods to examine the reforming of propane over the Zr-doped CeO₂ (1 1 1) surface. Numerous modeling and mechanistic questions arise in modeling this multistep reaction on oxides. The surface redox and coverage state in the reaction environment impacts energetics and must be considered. Phase diagrams of Zr-doped and pure CeO₂ (1 1 1) are created based upon the partial pressure of oxygen and hydrogen, demonstrating that the surface will be reduced under operating conditions. All elementary energetics along the preferential path for propane reforming were identified, and differences in path with oxygen pressure variance were identified. The reaction path varies depending on the oxygen chemical potential as this alters at which step in the mechanism the surface will re-oxidize.

5.1. Introduction

Small hydrocarbon oxidation and decomposition reactions over metal catalysts have been extensively investigated with density functional theory (DFT) methods, providing significant insights in the understanding these reaction mechanisms.¹⁻⁶ Even for small hydrocarbons, these reactions involve numerous possible elementary steps (36 for CH₄,⁷ over 800 for C₃H₈). The DFT investigation of complete oxidation/decomposition paths on oxides are rare, due to both the complexities in representing redox chemistry on oxides and difficulties in identifying active sites and adsorbate binding modes on oxide surfaces. Using pure ceria and M-doped ceria for oxidation and reforming of small hydrocarbons has been examined with DFT methods, where most studies use methane as a model to examine full oxidation paths.⁸⁻¹⁶ Propane partial oxidation and dehydrogenation has been investigated with DFT on V₂O₅ and Ga₂O₃.¹⁷⁻²⁰ Investigating the elementary mechanism of propane decomposition over oxides using DFT can help identify key elementary steps, thus informing design choices that improve catalyst performance for reforming larger hydrocarbons. Here, we employ DFT to examine the reaction path for the decomposition of propane over Zr-doped CeO₂. We identify and provide an example approach for key modeling and mechanistic questions involved in the decomposition of hydrocarbons over oxides, integrating an *ab initio* thermodynamics approach to evaluate redox environment effects on the catalytic hydrocarbon oxidation mechanism.

Zr-doped ceria catalysts have numerous promising properties for reforming hydrocarbons.^{16,21-23} Zr-doped ceria has been proposed to replace ceria in three-way catalysts, as it has a greater oxygen storage capacity compared to ceria.^{16,21} At temperatures approaching 700 K, Pd/Ce_{0.2}Zr_{0.8}O₂ yields a 90% conversion of propane and propene.²² La, Gd, or Sm doped Ce-ZrO₂ selectively produces H₂, CH₄, CO, and CO₂ instead of over C₂H₆ and C₂H₄, while La-doped Ce-ZrO₂ has the highest oxygen storage capacity and is the most active reforming catalyst.²³ Ceria

doped with other metals, such as copper, also has a high activity and selectivity toward oxidation of other hydrocarbons. Cu-doped ceria exhibits 100% selectivity toward CO₂ for the total oxidation of naphthalene.²⁴⁻²⁵ Surface oxygen vacancies play a crucial role in the catalytic behavior of naphthalene oxidation.²⁵

Despite the potential for oxide catalysis of hydrocarbon oxidation/decomposition, the detailed mechanism for the decomposition of propane has only been examined over metal catalysts. DFT uniquely allows the consideration of the numerous elementary steps in such complex mechanisms. Yang et al. examined the reaction path for propane decomposition over Pt (1 1 1) and Pt (2 1 1) using DFT.¹⁻² On Pt (1 1 1), they determined that the C-C bond breaking step likely occurs when propane dehydrogenates to propyne.¹ On a metal step site, the barriers for the dehydrogenation of propane decrease by approximately 0.4 eV, with the C-C bond breaking step still occurring with propyne.² Our group has similarly investigated the mechanism of propane reforming over Rh, Ni, and Rh-Ni catalysis with DFT.³ C-H or C-C bond breaking elementary steps generally limit hydrocarbon reforming rates over metal catalysts.²

The elementary mechanism of the oxidation/decomposition of propane over an oxide has not been examined with DFT, aside from isolated studies looking at the initial reaction steps.¹⁷⁻²⁰ DFT modeling of propane decomposition over an oxide raises additional complications that do not impact metal catalysts. On oxides, the addition of oxygen often requires lattice oxygen atoms in a Mars-van Krevelen mechanism, and as C-H or C-C breaking reactions occur on surface oxygen atoms, oxygen addition steps cannot be examined separately from C-H and C-C cleavage, as is typically done on metals. Intrinsic local effects cannot be easily approximated or ignored on oxides, as the size of the unit cell used will dictate the number of reducible surface sites. Though complete oxidation/decomposition has not been studied, selective oxidation of propane has been examined with DFT for vanadium catalysis.¹⁷⁻¹⁹ Alexopoulos et al. examined the selective oxidation of propane over the V₂O₅ (0 0 1) surface and determined that the rate limiting step for propane

selective oxidation (to propene and oxygenated products) is the initial hydrogen abstraction from the secondary carbon.¹⁷ A monolayer of vanadia over TiO₂ results in a lower activation barrier and alters the selectivity toward propene from i-propanol and acetone.¹⁷ The structure of the vanadium oxide monomers and dimers supported on anatase has a strong influence on the hydrogen abstraction energy, with the barrier 9 kcal mol⁻¹ lower on a square pyramidal cluster compared to a tetrahedral cluster.¹⁸ The dehydrogenation of propane has also been studied over a Ga₂O₃ (1 0 0) surface. Here again, the first C-H bond activation occurs through a hydrogen abstraction from the secondary carbon forming a propyl radical.²⁰ Liu et al. also determined that hydrogen atoms prefer to desorb as H₂. However, at high reaction temperatures the hydrogen could desorb as H₂O forming an oxygen vacancy.²⁰

Mayernick et al.¹¹ and Knapp et al.⁸ examined the reforming of methane over pure ceria and Pd-doped ceria. These two studies used two different approaches towards mixing of alkane decomposition and oxidized product (H₂O, CO₂) desorption steps. Mayernick et al. immediately desorbed H* from the surface as H₂O, forming an oxygen vacancy that was immediately refilled.¹¹ Knapp et al. collected all 4 H* species in their DFT unit cell before desorbing H₂O and refilling the oxygen vacancies as the last step of the mechanism.⁸ This second approach leads to an “over-reduced” surface and the incorrect conclusion that the highly unfavorable (at 0 K) desorption step limits reactivity. Immediately desorbing products as they are formed is equally arbitrary, though it better depicts the impact of product desorption on reactivity. For propane reforming, this modeling choice becomes more complicated, as the number of hydrogens that dissociate from the hydrocarbon increases and the depth of surface reduction attainable during reaction must be considered.

Herein, we examine the reforming path for propane over Zr-doped ceria. We first examine some of the mechanistic and modeling questions necessary to develop a formulaic approach for modeling this complex reaction sequence on an oxide surface. A significant mechanistic question

is when to add oxygen atoms onto the surface, re-oxidizing the surface during the intermediate steps of propane oxidation. We assume oxygen atoms are added anytime the reaction free energy for oxygen addition (re-oxidation) is more favorable than the subsequent propane decomposition step. We can then consider how the mechanism is affected by the O_2 chemical potential. Reaction paths are reported for both highly oxidizing conditions (combustion) and reducing (reforming) conditions. We initially evaluate the oxidation reaction catalyzed by an initially stoichiometric, bare MO_2 surface. We then examine the extent of equilibrium surface reduction, either through hydrogen adsorption or oxygen vacancy formation, as a function of the reaction environment. We conclude that reaction energetics evident on the fully-oxidized surface may not well-represent the operable reaction path due to surface reduction in the reaction environment. Finally, we examine how reaction conditions determine whether the oxidation product will be H_2 or H_2O .

5.2. Methods

5.2.1. Electronic structure method

Density functional theory calculations were carried out using the Vienna *ab initio* simulation program (VASP), an *ab initio* total energy, and molecular dynamics program developed at the Institute for Material Physics at the University of Vienna.²⁶⁻²⁸ The projector-augmented wave method (PAW) is used to represent the ion-core interactions.²⁹ A plane wave basis set with a cutoff of 450 eV is used to represent the valence electrons. The valence configuration for cerium is $5s^25p^66s^24f^15d^1$, $4s^24p^65d^25s^2$ for zirconium, $2s^22p^4$ for oxygen, $2s^22p^2$ for carbon and $1s^1$ for hydrogen. All optimizations were spin polarized. The Monkhorst Pack scheme was used to perform *k*-point sampling of (2 x 2 x 1), with the third basis vector perpendicular to the surface.³⁰ To incorporate the exchange and correlation energies, the Perdew-Wang (PW91) version of the

generalized gradient approximation (GGA) was utilized.³¹ Structural optimizations were performed by minimizing forces on all atoms to below $0.05 \text{ eV}\cdot\text{\AA}^{-1}$. In our previous study, we examined using a force criteria of $0.02 \text{ eV}\cdot\text{\AA}^{-1}$ and found that both the structure and energetics converged at the coarser value.⁹

We implemented the DFT+ U approach,³²⁻³³ due to the well-established difficulties for DFT to represent the nature of the $4f$ orbitals of ceria.³⁴⁻³⁶ The DFT+ U method penalizes non-integer occupation of localized orbitals by introducing an on-site Coulombic interaction (U -term), effectively penalizing delocalization of electrons. We utilize a U -value of 5 eV, consistent with other DFT+ U studies for ceria.^{9-11,37-41} Previously we examined the dependence of oxygen vacancy formation and methane adsorption energies against the value of U on the f -states of Ce for pure CeO₂, Zr-doped CeO₂ and Pd-doped CeO₂.¹⁰ The methane adsorption and oxygen vacancy formation energies increase slightly with Pd-doped CeO₂ and decrease with pure CeO₂ and Zr-doped CeO₂ with an increase of U -value on Ce f -states.¹⁰ The quantitative results presented herein are, therefore, dependent on the U chosen. A U -value of 5 eV accurately gives the electronic structure of pure CeO₂ and gives oxygen vacancy formation energies consistent with hybrid functional calculations and *ab initio* U -determination approaches.⁴² We expect the DFT-PW91- $U=5$ approach to provide qualitatively reasonable behavior for oxygen vacancy formation and hydrocarbon adsorption.

In Chapters 3 and 4, we showed that for certain dopants, a U -value must be added to the d -states of the dopant to correctly represent the electronic structure.^{9,37-38} For Zr-doped CeO₂, the zirconia retains a 4+ oxidation state as the surface is reduced,⁹ therefore a U -value on the d -states of Zr is not necessary.

5.2.2. Surface models

The bulk crystal structure of pure CeO₂ is the same as used in our previous studies, with the bulk lattice parameter (5.466 Å) reproduced within 1% of experimental values.^{9-11,37-39} A $p(2 \times 3)$ unit cell expansion of the (1 1 1) surface is used to model the surface with 15 Å of vacuum space perpendicular to the surface, with lattice parameters of 11.521 Å by 7.681 Å by 25.975 Å. The (1 1 1) surface is the lowest energy surface of ceria^{10,40,43} and therefore will represent a large portion of the surface of polycrystalline ceria. Mirrored slabs of 4 CeO₂ layers (12 atomic layers) were utilized for all optimizations with adsorbate/intermediates mirrored on top and bottom surfaces. The mirrored slabs were used to remove any slab-to-slab interactions that might result from a net surface dipole upon formation of oxygen vacancies and propane adsorption and reforming. All layers were allowed to relax during structural optimizations. The (1 1 1) termination of ceria will result in surface termination of 6 oxygen atoms per side with 6 Ce atoms in the layer below, as seen in Figure 5-1. The mirrored slab of ceria was doped with Zr by replacing one surface Ce atom with a Zr atom on each side of the mirrored surface, representing a 17% surface dopant concentration. The Zr dopes in with a 4+ oxidation state and remains as Zr⁴⁺ throughout all optimizations. We use the site-projected charge method to identify the number of cerium atoms that reduce from Ce⁴⁺ to Ce³⁺, as described in Chapter 3.⁹ The cell parameters were not allowed to relax, thereby not allowing any changes in the optimal lattice parameter due to the Zr-dopant. Our dopant model represents a system with surface segregation of a low bulk concentration dopant.

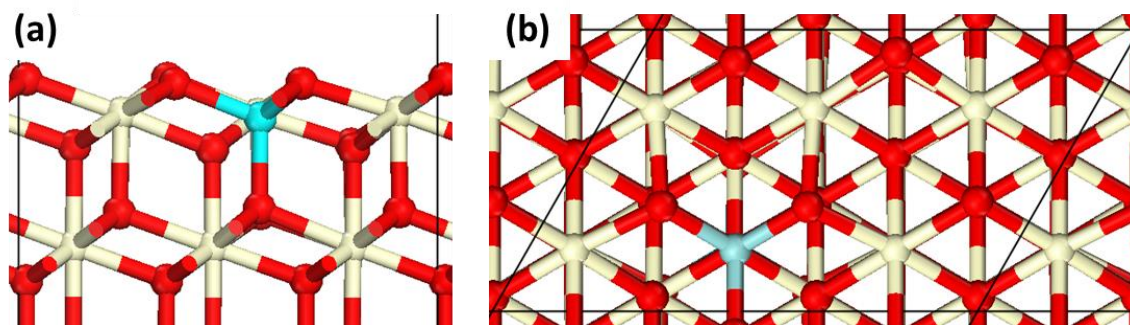


Figure 5-1. Side and top views of a $p(2 \times 3)$ unit cell expansion of Zr-doped CeO_2 (1 1 1). Ce is displayed at tan (light), Zr as light blue (gray) and O as red (dark).

5.2.3. Reaction Energies

The elementary reactions considered and the formulas for calculation of their reaction energies are given in Table 5-1.

The variables used in Table 5-1 are listed below:

E_S is the energy of the stoichiometric surface slab

E_{S/V_O} is the energy of the unit cell with one oxygen vacancy on each side of the slab

E_{S/nV_O} is the energy of the unit cell with n oxygen vacancies on each side of the slab

$E_{S/(n-1)V_O}$ is the energy of the surface unit cell with $(n-1)$ oxygen vacancies on each side of the slab

E_{S/H^*} is the energy of the surface unit cell with H absorbed

$E_{S/C_zH_n^*}$ is the energy of the surface unit cell with a C_zH_n molecule bound to the surface

$E_{S/xV_O/C_zH_n^*}$ is the energy of a C_zH_n molecule bound to the surface with x oxygen vacancies

$E_{S/nO/C_zH_m^*}$ is the energy of a C_zH_m molecule bound to the surface with n extra oxygens

μ_{O_2} is the chemical potential of gaseous oxygen at a given temperature and pressure

$\mu_{C_zH_n}$ is the chemical potential of a C_xH_n molecule in the gas phase

μ_{CO_x} is the chemical potential of CO_x in the gas phase

μ_{H_2} is the chemical potential of hydrogen in the gas phase

$\mu_{C_zH_mO_n}$ is the chemical potential of an oxygenated C_z intermediate in the gas phase

Table 5-1. Reaction types and reaction energy definitions for elementary steps involved in propane oxidation/reforming over CeZrO_x.

Reaction Type	Chemical Reaction	Reaction Energy
(A) Initial vacancy formation	(A) $Zr_xCe_{1-x}O_{2x} \rightarrow Zr_xCe_{1-x}O_{2x-y} + \frac{y}{2}O_2(g)$	$\Delta G_{vac} = \frac{E_{S/V_0} + \mu_{O_2} - E_S}{2} \quad (1)$
(B) Multiple vacancy formation	(B) $Zr_xCe_{1-x}O_{2x-(n-1)y} \rightarrow Zr_xCe_{1-x}O_{2x-ny} + \frac{y}{2}O_2(g)$	$\Delta G_{vac} = \frac{E_{S/nV_0} + \mu_{O_2} - E_{S/(n-1)V_0}}{2} \quad (2)$
(C) Alkane activation	(C) $C_zH_n(g) + * \rightarrow H^* + C_zH_{n-1}(g)$	$G_{act} = \frac{(E_{S/H^*} + 2*\mu_{C_zH_{n-1}}) - (E_S + 2*\mu_{C_zH_n})}{2} \quad (3)$
(D) Alkane adsorption	(D) $C_zH_n + * \rightarrow C_zH_n^*$	$\Delta G_{ads} = \frac{(E_{S/C_zH_n^*}) - (E_S + 2*\mu_{C_zH_n})}{2} \quad (4)$
(E) Surface C-H dissociation	(E) $C_zH_n^* + * \rightarrow H^* + C_zH_{n-1}^*$	$\Delta G_{C-H} = \frac{(E_{S/C_zH_{n-1}^*} + E_{S/H^*}) - (E_{S/C_zH_n^*} + E_S)}{2} \quad (5)$
(F) Surface C-C dissociation	(F) $C_zH_n^* + * \rightarrow C_{z-1}H_{n-x}^* + CH_x^*$	$\Delta G_{C-C} = \frac{(E_{S/C_{z-1}H_{n-x}^*} + E_{S/CH_x^*}) - (E_{S/C_zH_n^*} + E_S)}{2} \quad (6)$
(G) CO/CO ₂ desorption	(G) $C_zH_n^* \rightarrow C_{z-1}H_{n-x}^* + CO_x(g) + xV_0$	$\Delta G_{CO_x} = \frac{(E_{S/xV_0/C_{z-1}H_{n-x}^*} + 2*\mu_{CO_x}) - (E_{S/C_zH_n^*})}{2} \quad (7)$
(H) Alternative CO/CO ₂ desorption	(H) $C_2^* \rightarrow 2CO_x(g) + *$	$\Delta G_{CO_x} = \frac{(E_{S/nV_0} + 4*\mu_{CO_x}) - (E_{S/C_2^*})}{2} \quad (8)$
(I) Surface re-oxidation	(I) $Zr_xCe_{1-x}O_{2x-y}/C_zH_m^* + \frac{n}{2}O_2(g) \rightarrow Zr_xCe_{1-x}O_{2x-y+n}/C_zH_m^*$	$\Delta G_{re-ox} = \frac{(E_{S/C_zH_m^*}) - (E_{S/nO/C_zH_m^*} + \mu_{O_2})}{2} \quad (9)$
(J) Hydrogen desorption as H ₂	(J) $H^* \rightarrow \frac{1}{2}H_2(g) + *$	$\Delta G_{H_2} = \frac{(E_S + \mu_{H_2}) - (E_{S/H^*})}{2} \quad (10)$
(K) Hydrogen desorption as H ₂ O	(K) $H^* \rightarrow \frac{1}{2}H_2O(g) + *$	$\Delta G_{H_2O} = \frac{(E_S + E_{S/V_0} + \mu_{H_2O}) - (2*E_{S/H^*})}{2} \quad (11)$
(L) C _z intermediate desorption	(L) $Zr_xCe_{1-x}O_{2x-y}/C_zH_m^* \rightarrow Zr_xCe_{1-x}O_{2x-y-n} + C_zH_mO_n^*(g)$	$\Delta G_{des} = \frac{(E_{S/V_0} + \mu_{C_zH_mO_n}) - (E_{S/C_zH_m^*})}{2} \quad (12)$

Factors of two in the reaction energies of Table 5-1 are a result of using mirrored slabs. Oxygen vacancy refilling is the reverse of reaction types A and B. Our previous paper showed that the lowest energy H^* structure adsorbs H to an oxygen atom nearest neighbor (NN) to the dopant.⁹ All $C_zH_n^*$ and H^* adsorbates are bound to surface oxygen NN to the Zr dopant. Transition states were not examined in this study, and, as a first analysis of this complex mechanism, the reaction path is determined using only the elementary reaction 0 K and reaction condition-dependent free energies. The activation barrier for the initial propane activation is represented using the “pseudo-transition state” of an abstracted surface absorbed H^* and an isolated propyl radical. Chapter 3 suggested the pseudo-transition state is a reasonable approximation of the initial C-H activation transition state located by CI-NEB.⁹

5.2.4. Free Energies

All reaction energies in Table 5-1 are noted as free energies, though we neglect non-zero K corrections to surface bound states. The chemical potentials of gas phase species (O_2 , C_3H_8 , CO , CO_2 , H_2 , H_2O , etc.) are made temperature and pressure dependent using expressions derived from statistical mechanics. The free energy of oxygen (μ_{O_2}) is calculated as a function of temperature (T) and oxygen partial pressure (P_{O_2}) by

$$\mu_{O_2} = E_{O_2} + ZPVE + PV - TS \quad (12)$$

where E_{O_2} is the DFT energy of an isolated O_2 molecule, $ZPVE$ is the zero-point vibrational energy correction, PV is the pressure volume term, and TS is the entropy calculated by statistical mechanics multiplied by temperature. The entropy of gaseous O_2 is calculated as

$$S = S_{rot} + S_{vib} + S_{trans} + S_{el} \quad (13)$$

where S_{rot} is the entropy due to rotation, S_{vib} is the entropy due to vibration, S_{trans} is the entropy due to translation, and S_{el} is the entropy due to electronic excitations. Differences between the experimentally-determined free energy for O₂ (using NIST JANAF thermochemical tables⁴⁴) and the DFT-based free energy are minimal, and the DFT-based free energy is therefore used. Even though it is known that DFT overestimates the O-O binding energy, the DFT energy for O₂ is utilized.⁴⁵ A correction term can be added to directly compare the O₂ binding energy with experiments. We acknowledge that the oxygen partial pressure and temperatures we specify will be offset from experimental values. We are examining the qualitative differences in reaction paths depending on O₂ chemical potential, and the constant correction term would only change the absolute value for the partial pressure of oxygen. Free energies for all other molecules (C₃H₈, CO, CO₂, H₂, H₂O, etc.) in the gas phase are calculated in an equivalent approach.

5.2.5. Mechanistic choice for H* location and H₂O* desorption

When applying DFT to model oxidation chemistry on metals at low coverage, reaction dissociation products are often placed in separate cells to represent the lack of adsorbate-adsorbate interactions at low coverage. We make the same approximation in examining C-H and C-C dissociations, with the two dissociation products placed in separate unit cells when calculating reaction energies. The consequences of this choice on metals is often minor due to weak adsorbate-adsorbate interactions. However, H* retention in the oxide unit cell as successive C-H dissociations occur creates an unreasonable degree of local surface reduction. We placed dissociation products in separate unit cells to provide a more reasonable indication of oxidation catalysis of an extended

surface and a more consistent computational model for comparing oxide catalysts or reaction steps. The impact of H^* coverage on the oxidation reaction is an interesting topic for future study.

5.2.6. Reaction path sequence determination

Propane oxidation studies on metal catalysts have examined which C_zH_n intermediate forms a C-O bond, typically concluding it is late in the mechanism; for example, through C^* or CH^* intermediates over reforming catalysts.⁷ For reactions on oxides, separation of C-H/C-C dissociation and C-O bond formation is not as straightforward, as the dissociation products bind to surface oxygen atoms. Successive unsaturation of the hydrocarbon adsorbate leads to a greater degree of C-O bond formation and weakening of the surface M-O interactions. Whereas on metals, we ask for which intermediates will C-O bond formation be competitive with further decomposition, on oxides we ask at what points along the reaction path the surface would prefer to add/replace surface oxygen atoms compared to further C-H/C-C dissociation.

For each adsorbate $C_zH_n^*$, we consider whether it is more favorable to (1) dissociate to $C_zH_{n-1}^* + H^*$ (considering all non-equivalent H's and numerous adsorption configurations for $C_zH_{n-1}^*$), (2) to dissociate to $C_{z-1}H_{n-x}^*$ and CH_x^* , (3) to add an oxygen atom to the surface, or (4) to desorb $C_zH_n^*$, CO, or CO₂. The numerous non-preferred reaction steps (or non-global minimum energy structures we optimized) are not directly discussed, as we concentrate solely on the most favorable path. In comparing two surface reaction steps, we take that the step with the most exoergonic reaction free energy will be more favorable. The desorption of products were accepted as the next step only if the 0 K energy for the desorbed product was more favorable than the possible surface reaction steps, even if the free energy of product desorption was significantly more favorable. This assumption reflects the need for desorption to overcome an activation barrier similar to the 0 K unimolecular desorption energy. As surface reaction energies, rather than barriers,

are used for comparison, this approach could improperly favor further surface reaction over intermediate desorption. We find, however, that the relative energy between product desorption and further surface reaction favors surface reaction by at least 1.5 eV for all $C_zH_n^*$ intermediates prior to formation of the final CO_x species. This is not surprising, as Zr-doped ceria is not expected to be a good partial oxidation catalyst. We consider further reactions only from the most favorable outcome of the previous step. This approximation is necessitated by the numerous possible reaction paths possible if all plausible intermediates are to be considered.

5.2.7. Initial condition of the catalyst before decomposition

Our reaction energy analysis begins with the fully oxidized surface of Zr-doped ceria ($Zr_xCe_{1-x}O_2$). With this starting point, the reforming path of propane over the ceria surface under oxidizing conditions yields qualitatively reasonable results, though the final section discusses limitations in the analysis due to neglecting that the active catalyst form is reduced from the MO_2 stoichiometry. For future analysis, we also compute the surface reduction extent in equilibrium with the gas phase environment under reducing conditions. The coverage of intermediates and extent of surface reduction in the reaction environment is dictated by steady state conditions. Without a full kinetic model, we instead calculate the H^* coverage and extent of oxygen vacancy formation that would be expected in equilibrium with gas phase conditions.

5.3. Results and discussion

5.3.1. Propane oxidation in an oxidizing environment (0.1 atm O₂)

The first step in propane oxidation is secondary hydrogen abstraction. This step proceeds through a pseudo-transition state consisting of a secondary propyl radical in the gas phase and a hydrogen bound to a surface oxygen atom. H* preferentially adsorbs on an oxygen atom adjacent to the zirconia dopant, as illustrated in Figure 5-2a. The 0 K energy of propane activation to the pseudo-transition state is 0.68 eV. After H-abstraction, the secondary propyl radical binds to a surface oxygen atom (propyl radical adsorption energy -2.53 eV), again NN to a zirconia dopant (Figure 5-2b). Figure 5-3 contains the overall reaction free energy diagram for the reforming of propane over Zr-doped ceria in an oxidizing environment, and all intermediate structures are illustrated in Appendix C. After the adsorption of the propyl radical, the hydrogen atom desorbs from the surface as half of H₂O, forming half of an oxygen vacancy in the surface. The half oxygen vacancy is then refilled by oxygen present in the gas phase, returning the intact (fully oxidized) surface. Though this process does not stoichiometrically represent the elementary step, it provides a thermodynamic approach for incorporating hydrogen desorption as H₂O during the mechanism of reforming propane. This same process is repeated for every elementary step when a hydrogen atom is abstracted from the propane-derived intermediate. Whether the hydrogen stays on the surface or desorbs as H₂ or H₂O will be discussed in Section 5.3.5, but we will assume for now that the hydrogen will desorb as H₂O and the subsequent O-vacancy is refilled by O₂.

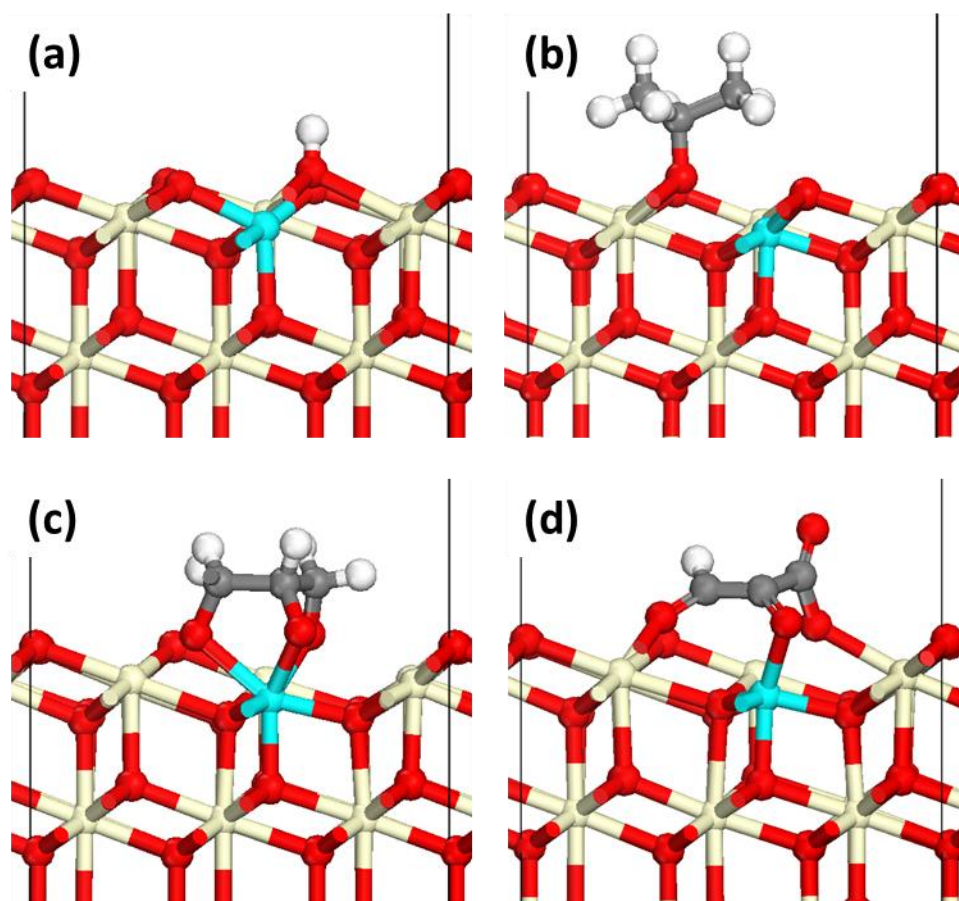


Figure 5-2. Four selected structures of propane oxidation intermediates over Zr-doped CeO₂. (a) H*, (b) CH₃C*HCH₃, (c) C*H₂C*HC*H₂, (d) C*HC*C* (end C with 2 oxygens). Ce is displayed as tan (light), Zr as light blue (gray), O as red (dark).

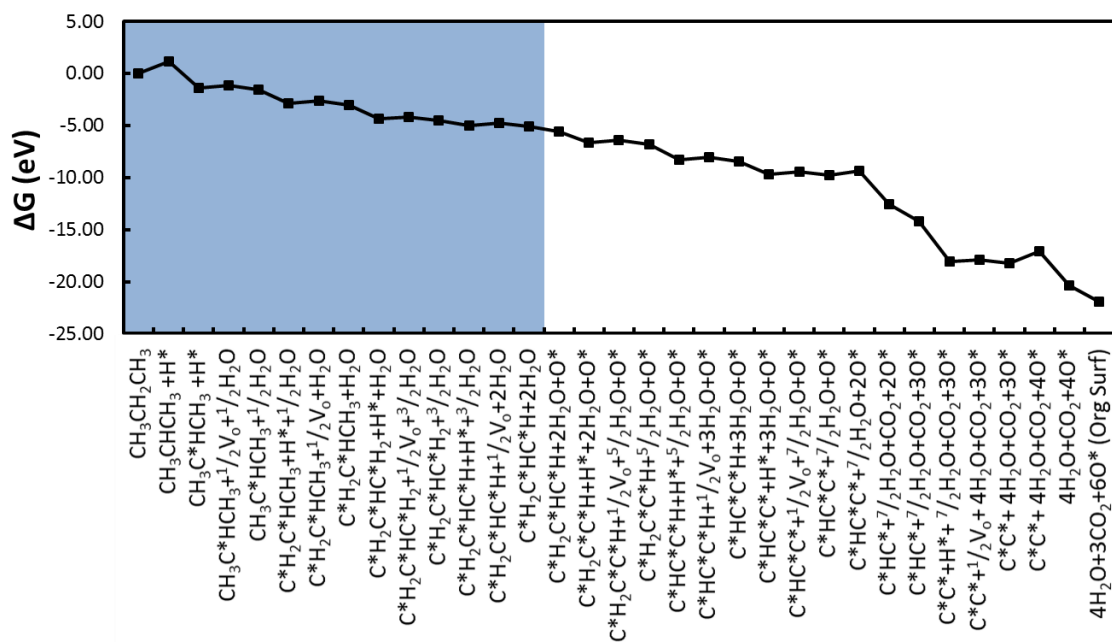


Figure 5-3. Propane oxidation reaction energy diagram over the Zr-doped CeO₂ (1 1 1) surface in an oxidative environment (0.05 atm H₂O, 0.234 atm H₂, 0.1 atm O₂, 0.32 atm CO, 0.32 atm CO₂ and 0.1 atm propane at 1000 K). The blue (dark grey) denotes steps that are equivalent under more reducing environments in Figures 5-4 and 5-5.

For every subsequent step, breaking a C-H bond or a C-C bond, desorption of the C_z intermediate and the possibility of re-oxidizing the surface with an oxygen atom was considered. When re-oxidation of the surface was considered, the initial position of added O atoms was placed where M-O bonds had been broken/weakened due to strong C-O bond formation. Please see the Appendix C for example structures. The 0 K energies for C_z intermediate desorption were compared to the surface reaction energies. For all species prior to CO/CO₂, product desorption was at least 1.5 eV less favorable than surface reaction, and we conclude that CO/CO₂ are the only majority C-containing products of propane oxidation over Zr-doped CeO₂ (1 1 1).

After the secondary propyl radical binds to the surface, the following step involves the abstraction of a hydrogen atom from one of the primary carbon atoms and the bonding of the same

primary carbon atom to one of the surface oxygen atoms NN to the zirconia, forming $C^*H_2C^*HCH_3$. The asterisks referring to carbon atoms bound to surface oxygen atoms. The next step, after water desorption and subsequent oxygen vacancy refilling, is the abstraction of a H atom from the other primary carbon and the bonding of that carbon to the last available oxygen atom NN to the Zr-dopant (total of 3 oxygen atoms NN to the Zr-dopant), forming $C^*H_2^*CHC^*H_2$ (Figure 5-2c). Another hydrogen atom is then abstracted from a primary carbon atom followed by the partial re-oxidization of the surface with an oxygen atom from O_2 (Figure C-1). The added O atom allows the terminal $-CHO$ moiety to break all M-O bonds, with the added O atom refilling the resulting surface O vacancy.

Three more hydrogen atoms are then abstracted from the C_3 intermediate, forming $C^*HC^*C^*$. This structure has 2 oxygen atoms bound to the end carbon, one resembling a carbon-oxygen double bond and the other a single bond (Figure 5-2d). The surface is then re-oxidized, followed by the end carbon breaking its carbon-carbon bond forming CO_2 in the gas phase and leaving behind C^*HC^* on the surface, along with forming an oxygen vacancy. The surface is again re-oxidized, and the last hydrogen is abstracted from the C_2 intermediate forming C^*C^* . One more oxygen atom re-oxidizes the surface forming a 2 carbon species on the surface, with each of the carbons bound to 2 oxygen atoms. The C-C bond breaks and the two CO_2 molecules desorb, leaving behind 2 oxygen vacancies. To complete the catalytic cycle, the surface is re-oxidized with two oxygen atoms, making the surface fully oxidized. All structures along this oxidation path can be seen in Figures C-1 and C-2.

Reforming of propane over Zr-doped ceria in an oxidative environment produced 4 H_2O and 3 CO_2 molecules ($C_3H_8 + 5O_2 \rightarrow 4H_2O + 3CO_2$) with an overall reaction free energy of -21.94 eV. Based on tabulated free energies of formation of the gas phase species, the overall gas phase reaction free energy would be -22.00 eV in these oxidizing conditions, which is in excellent agreement with our DFT results.⁴⁶ The overall oxidation reaction rate will be most influenced by

the first hydrogen abstraction from the propane forming a secondary propyl radical in the gas phase (0 K barrier of 0.68 eV, free energy barrier relative to gas phase propane of 1.12 eV) and the product CO₂ desorption energy (0.96 eV). As will be discussed in Section 5.3.4, it is likely the Zr-doped CeO₂ (1 1 1) surface would not be fully oxidized under reforming reaction conditions or under catalytic combustion conditions, having either adsorbed H* or O-vacancies. A higher degree of surface reduction could raise the propane activation energy, as this step further reduces the surface and requires available O sites. As our reaction path analysis considers whether it is stable to re-oxidize the surface, the extent of surface reduction is reasonably represented in our analysis at any point past the first re-oxidation, although with the exception of our neglecting the possible build-up of surface H* species in the unit cell. The presence of surface H* species could push CO desorption to become more competitive with CO₂ desorption.

5.3.2. Propane oxidation in a reducing environment (1×10^{-17} atm O₂)

As described above, the initial propane activation steps are the same in all environments we examined. In the reducing environment, the elementary steps until the formation of C*H₂C*HC*H are the same as the oxidizing environment. At this point, the paths diverge due to the lower partial pressure of oxygen. With a higher pressure of O₂, surface re-oxidation was favored over further C₃ decomposition surface reactions. Under the more reducing conditions, however, there are an additional three hydrogen abstractions before the surface is re-oxidized with an oxygen atom from O₂. The reaction free energy diagram under reducing conditions is given in Figure 5-4. When an O atom re-oxidizes the surface, it also forms a bond with the end carbon atom, giving this carbon atom 2 oxygen bonds (reaching the state of Figure 5-2d as in the oxidizing conditions, but through a different order of re-oxidation and C-H breaking steps). The last hydrogen is then abstracted, leaving behind C*C*C*. The surface is then re-oxidized again and the other primary

carbon forms a bond with oxygen leaving both of the primary carbon atoms with 2 oxygen atoms bound to them. One of the end carbon atoms breaks off as CO₂, leaving behind C*C* with an oxygen vacancy. An additional oxygen atoms re-oxidizes the surface, leaving both carbons with two C-O bonds. The C-C bond then breaks forming 2 CO₂ molecules and leaving the surface with 3 oxygen vacancies. To complete the catalytic cycle, 3 additional oxygen atoms re-oxidize the surface forming a fully oxidized surface.

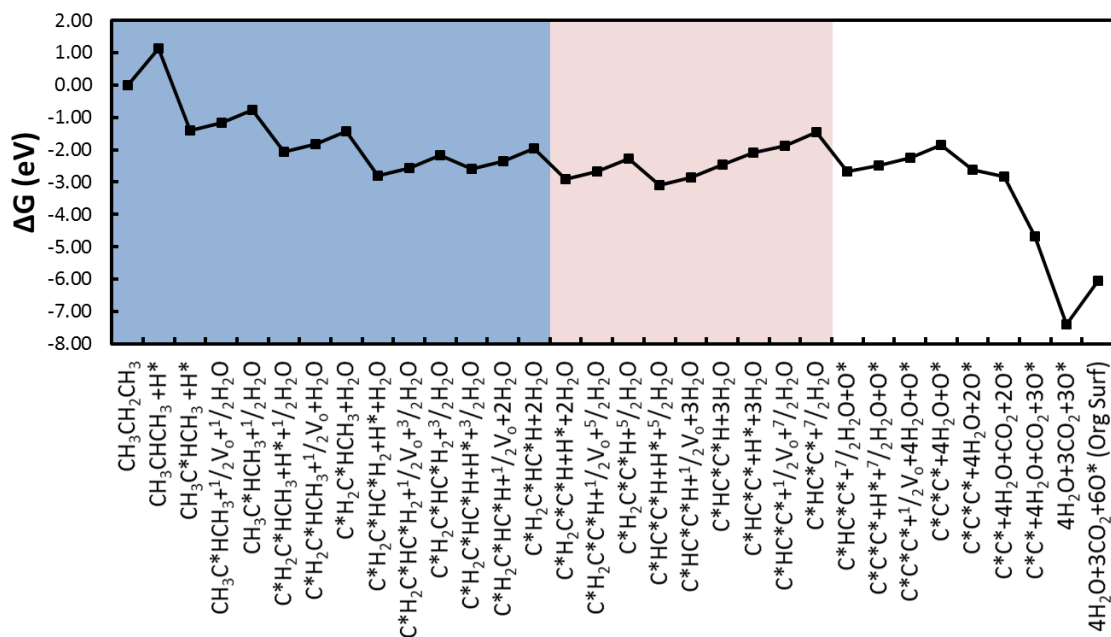


Figure 5-4. Propane oxidation reaction energy diagram over the Zr-doped CeO₂ (1 1 1) surface in a reducing environment (0.05 atm H₂O, 0.234 atm H₂, 1x10⁻¹⁷ atm O₂, 0.32 atm CO, 0.32 atm CO₂ and 0.1 atm propane at 1000 K). The blue (dark grey) denotes the steps that follow the same sequence regardless of oxidation conditions considered (equivalent in Figures 5-3 and 5-5) and the red (light grey) denotes steps that are equivalent under the more reducing conditions of Figure 5-5.

Under these reducing conditions, there are 3 CO₂ and 4 H₂O molecules produced during the oxidation of propane (C₃H₈ + 5O₂ → 4H₂O + 3CO₂). All structures along this reaction path can be seen in Figures C-3 and C-4. The highest energy reaction sequence is not the first hydrogen abstraction, as for the oxidative environment, but a series of steps in the middle of the overall reaction, giving a barrier of 1.62 eV. This high energy reaction sequence includes water desorption, refilling of oxygen vacancies, and a hydrogen abstraction from the C₃ intermediate. The rate of the first CO₂ desorption step may also impact the overall oxidation rate, with a 0 K desorption energy of 1.95 eV. The overall reforming reaction of propane in a reducing environment is very similar to the path in an oxidizing environment, with small differences in the point of surface re-oxidation. The fact that CO₂ products remain preferred over the expected CO in the reducing environment suggests that the absence of surface H* species in the unit cell could alter the product species formed. H* presence would further reduce the surface, which would then prefer desorption of less oxidized products. If the reaction were to proceed on a more deeply reduced surface, H₂ desorption might be favored over H₂O desorption and CO desorption over CO₂ desorption, thereby leading to different products and altering the higher energy reaction sequences.

5.3.3. Propane oxidation under extremely reducing conditions (8x10⁻²² atm O₂)

An O₂ partial pressure of 8x10⁻²² atm would be dictated by the equilibrium between H₂O and H₂ at 1000 K, $P_{H_2} = 0.234$ atm, and $P_{H_2O} = 0.05$ atm. These partial pressures are similar to the effluent from a biomass gasifier.³⁸ With this lower effective O₂ pressure, the propane oxidation path is the same as that in the previous section up until the first surface re-oxidation step. Instead of re-oxidizing the surface when there is only one hydrogen left on the C₃ intermediate, at this low P_{O₂}, the last hydrogen atom will be abstracted. The 3 carbon chain left behind forms a ring of carbons with each carbon having effectively a carbon-oxygen double bond. One carbon in this 3 carbon

chain will then break two of its carbon-carbon bonds forming a gas phase CO molecule and leaving behind C*C* on the surface. This C*C* will then also break its carbon-carbon bond forming two more CO molecules in the gas phase.

This reforming path under these extremely reducing conditions forms a total of 3 CO and 4 H₂O molecules in the gas phase ($C_3H_8 + 3.5O_2 \rightarrow 4H_2O + 3CO$). The reaction free energy diagram under these conditions is given in Figure 5-5, and all structures along the path are illustrated in Figure C-5. The high energy reaction sequences under these extremely reducing conditions are 1) the same H₂O desorption, vacancy refilling, and C-H bond dissociation sequence as under the more mildly reducing conditions, with an energy requirement of 2.03 eV and 2) the desorption of the first CO with a ΔE of 2.04 eV. The major differences in reaction path at this low oxygen pressure are the lack of surface re-oxidation until final oxidation products desorb, and the production of CO rather than CO₂ as the final product. The large energy requirements, as well as the surprising unimportance of C-H activation in impacting the overall rate, are likely a consequence of incorrect assumptions made in our modeling approach. For all steps prior to the first surface re-oxidation, our analysis has not properly represented the extent of surface reduction that would be present under the reaction conditions. As detailed in the next section, the active surface under these extremely reducing conditions would be highly reduced. As discussed in Section 5.3.5, it would be more favorable for H* species to form H₂ relative to H₂O under these conditions, so the use of the H₂O product also misrepresents the reaction path. C-H activation steps would become more kinetically relevant, requiring greater energy input, were the reaction occurring on a highly reduced surface. The CO desorption energy could also be effected. The high energy sequence beginning with H₂O desorption and including vacancy refilling would not occur in the dominant path, as forming H₂ is a lower energy process. Though our approach reasonably reflected the reaction path under oxidizing or mildly reducing conditions, the reaction path under

reducing conditions is greatly misrepresented due to the use of the fully-oxidized surface as the reactive surface and the assumption of formation of the H₂O product.

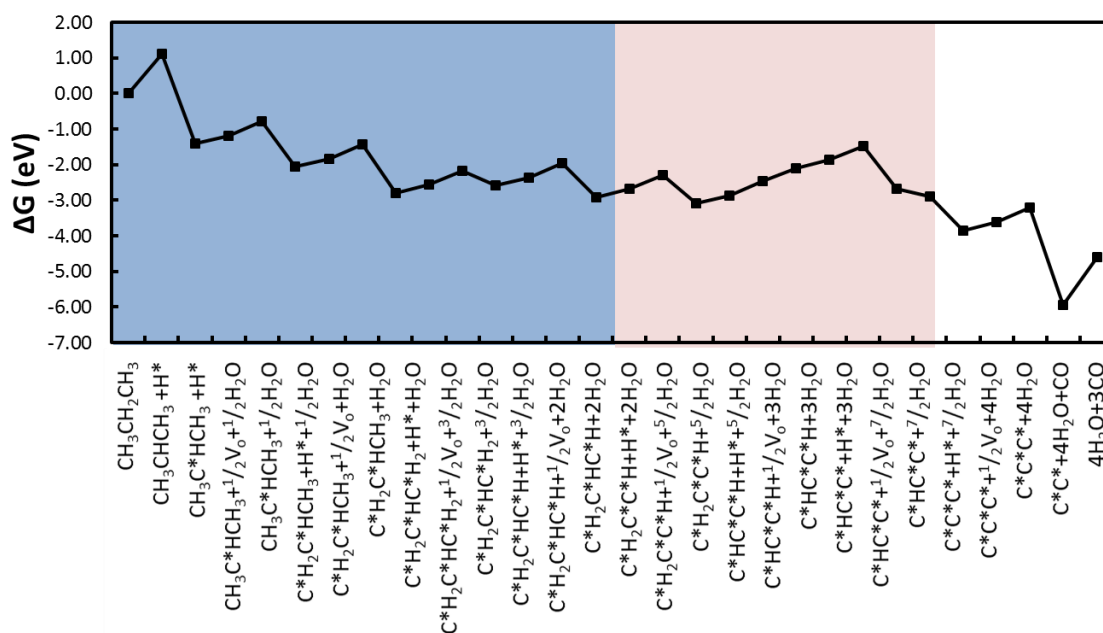


Figure 5-5. Propane oxidation reaction energy diagram over the Zr-doped CeO₂ (1 1 1) surface under extremely reducing conditions (0.05 atm H₂O, 0.234 atm H₂, 8x10⁻²² atm O₂, 0.32 atm CO, 0.32 atm CO₂ and 0.1 atm propane at 1000 K). The blue (dark grey) denotes steps equivalent to the more oxidizing conditions used in Figures 5-3 – 5-5 and the red (light grey) denotes steps equivalent under the more oxidizing conditions in Figure 5-4.

5.3.4. Extent of surface reduction under the reforming environment

Our reaction free energy analysis assumed that the starting surface for the reforming reaction has no oxygen vacancies present and no hydrogen or other species adsorbed. We presumed that any adsorbed hydrogen will immediately desorb as H₂O after abstraction. However, there can be hydrogen atoms adsorbed on the surface or oxygen vacancies in the surface (especially under reducing conditions), with the catalytic cycle oscillating between a reduced and further reduced surface without reaching the fully oxidized state.

We computed the $\frac{1}{2}$ H₂ dissociative adsorption free energy on the Zr-doped CeO₂ (1 1 1) surface with the oxide surface containing a variable number of O vacancies. These free energies are given in Figure 5-6. Each consecutive hydrogen adsorption energy is relative to the previous surface with one less hydrogen adsorbed. The energetics of forming of surface oxygen vacancies (some of the subsurface oxygen migrated towards the surface) and the addition of hydrogen atoms on surface oxygen were considered, leading to a maximum of 6 surface oxygen vacancies (reducing 12 Ce⁴⁺ to Ce³⁺), 6 hydrogen atoms on the surface (reducing 6 Ce⁴⁺ to Ce³⁺) or a combination of both adding from 0 to 6 (allowing reduction of between 0 and 12 Ce⁴⁺ to Ce³⁺ caused by any assortment O removal or H* formation). With a mirrored, 4 CeO₂-layered surface with 1 Zr dopant per side, a sixth surface oxygen vacancy is not energetically reasonable. A 12e⁻ reduction (per side of the mirrored slab) would force all Ce atoms and the Zr dopant to reduce, and the irreducibility of the Zr dopant leads to an extra electron that is not properly represented. The more the surface is reduced (more adsorbed H* or oxygen vacancies) the more endothermic each adsorption becomes. All structures associated with the data in Figure 5-6 are provided in the Appendix C, along with the 0 K oxygen vacancy formation energies in Table C-1. The same reduction energetics can be seen in Figure C-10 for pure CeO₂ (1 1 1), along with its associated structures.

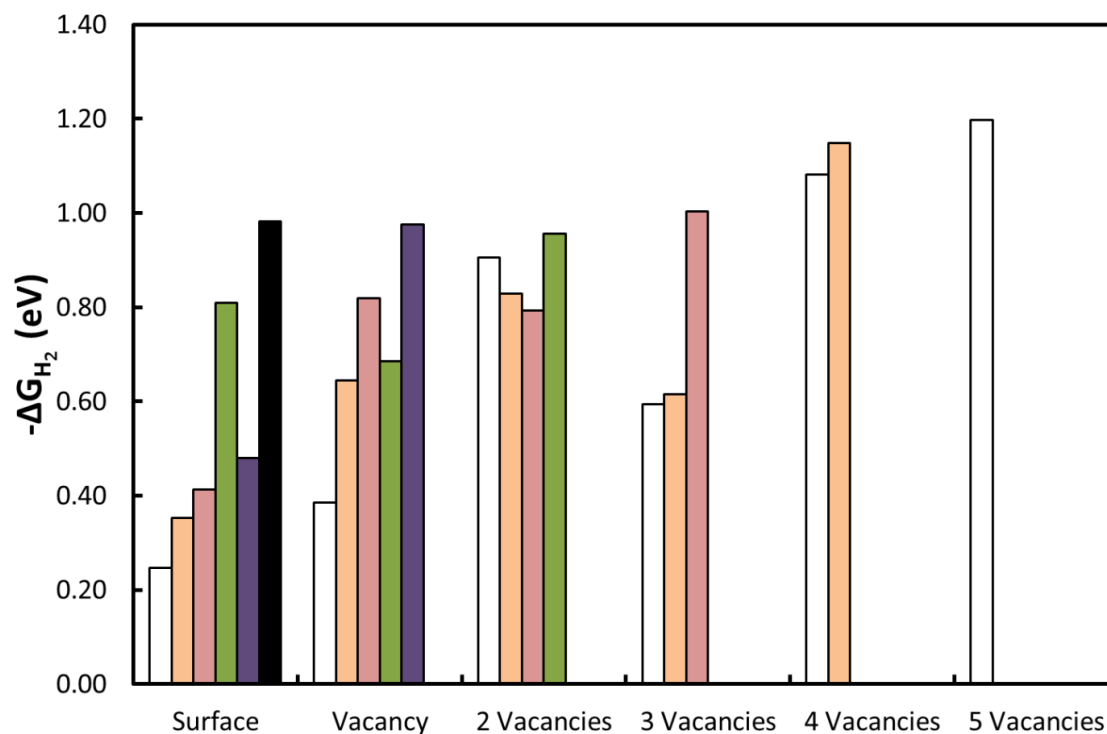


Figure 5-6. The energy to absorb $\frac{1}{2}$ H_2 (g) onto the surface of Zr-doped CeO_2 (1 1 1) with varying number of surface oxygen vacancies and number of hydrogen atoms on the surface. The energy to absorb each hydrogen atom is calculated progressively in each step. The partial pressure of hydrogen is 0.234 atm and for oxygen is 6×10^{-20} atm. The number of H^* adsorbed in the 2×3 unit cell is denoted by bars of (white) 1 H^* , (orange or lightest gray) 2 H^* , (red or light gray) 3 H^* , (green or medium gray) 4 H^* , (purple or dark gray) 5 H^* , (black) 6 H^* .

Though our reaction free energy analysis used a fully oxidized surface, we examined the stable surface reduction state as a function of H_2 and O_2 pressure to clarify the applicability of the surface model used and guide future work. Figure 5-7 illustrates the phase diagram for pure CeO_2 , varying the hydrogen and oxygen partial pressures. In all three above reaction environments (oxidizing, reducing and extremely reducing) the surface of pure CeO_2 will have no oxygen vacancies and every surface oxygen will have a hydrogen adsorbed (6 e^- reduction per side of the mirrored slab). The reaction environments we considered in Sections 5.3.1-5.3.3 are labeled as O (oxidizing), R (reducing), and ER (extremely reducing) on Figure 5-7.

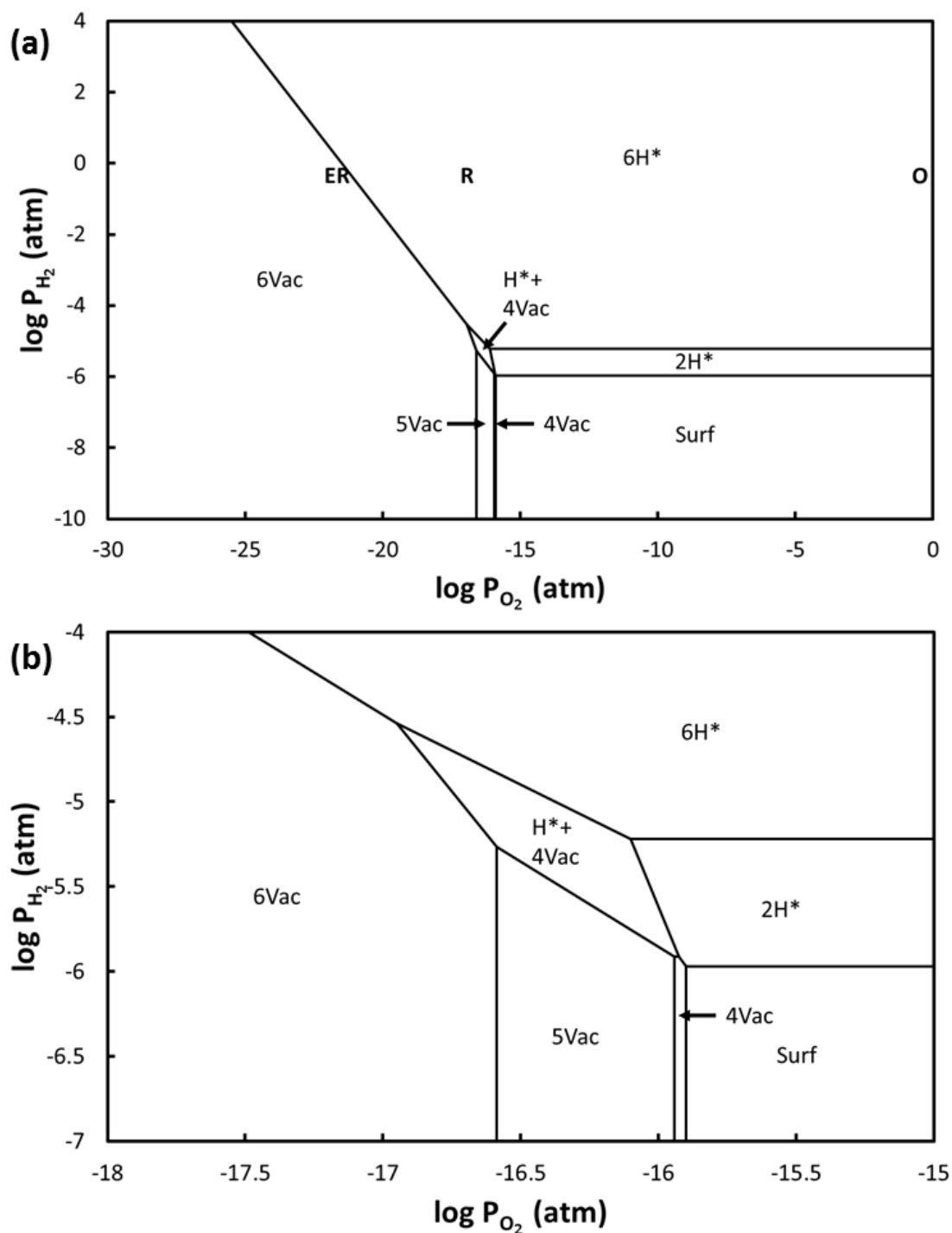


Figure 5-7. The phase diagram for the number of hydrogen atoms absorbed and the number of surface oxygen vacancies present in a $p(2 \times 3)$ unit cell of pure CeO_2 (1 1 1) while varying the partial pressure of hydrogen and oxygen. The O represents the gas phase composition for the oxidizing case, R for the reducing case and ER for the extremely reducing case. (b) is zoomed in on the center of (a) to give a more detailed picture.

Figure 5-8 represents the same phase diagram as above, but for Zr-doped CeO_2 (1 1 1). The scales for Figure 5-8 and for Figure 5-7a are the same, illustrating how the Zr-doping changes the overall shape and scale of the phase diagram. In the oxidizing and reducing environment (labeled as O and R, respectively) the surface of Zr-doped CeO_2 will be covered in hydrogen with no oxygen vacancies present ($6e^-$ reduction per side of the slab). However, in the extremely reducing environments (labeled as ER), the surface will have 3 surface oxygen vacancies present and the other 3 remaining surface oxygens will have hydrogen atoms absorbed onto them (a $9e^-$ reduction per side of the slab).

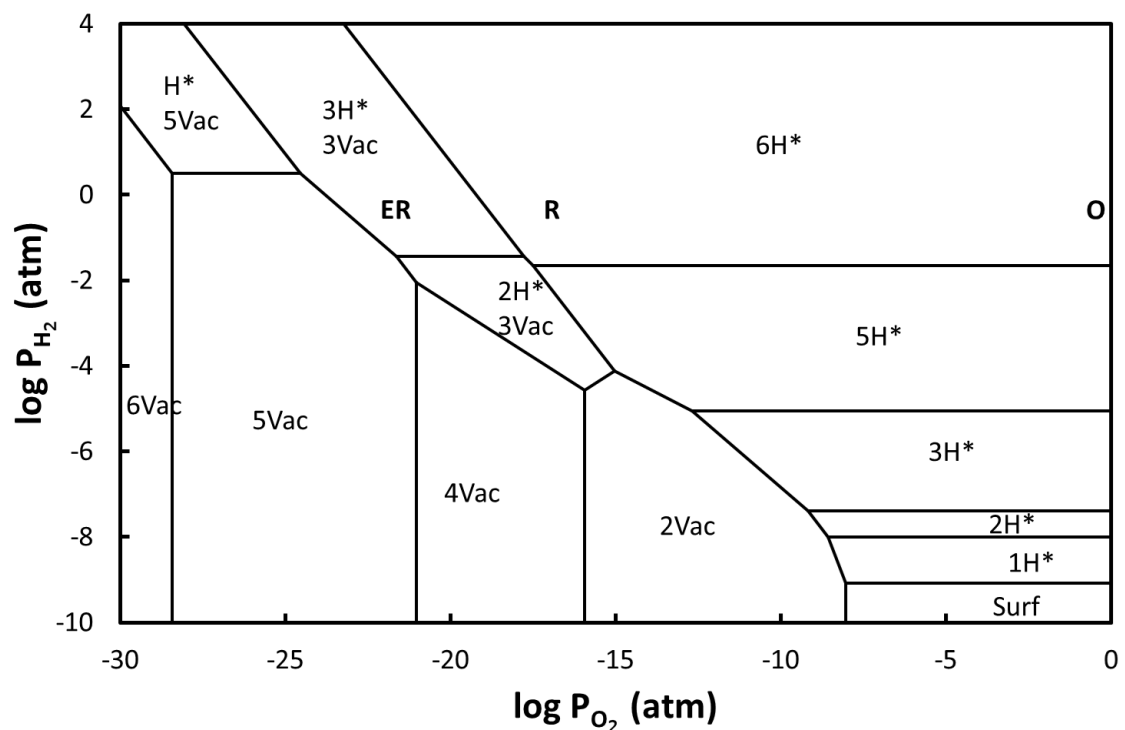


Figure 5-8. The phase diagram for the number of hydrogen atoms absorbed and the number of surface oxygen vacancies present in a $p(2 \times 3)$ unit cell of Zr-doped CeO_2 (1 1 1) while varying the partial pressure of hydrogen and oxygen. The O represents the gas phase composition for the oxidizing case, R for the reducing case and ER for the extremely reducing case.

The use of a fully-oxidized surface as the initial “bare” surface model on which propane oxidation catalysis occurs is not representative of the stable surface around which oxidation catalysis will occur in the reaction environments considered. Depending upon the H_2/O_2 environment, there will either be surface oxygen vacancies present and/or hydrogen adsorbed on the surface. Propane oxidation will require the opening of oxygen sites, through either vacancy refilling, H_2 desorption, or H_2O desorption followed by vacancy refilling, to allow for initial C-H bond activation. C-H and C-C breaking steps will be more energetically uphill than depicted in Figures 5-3 – 5-5 due these steps reducing a surface to a “deeper” reduction state than considered above in determining reaction energetics. Further C-H or C-C dissociation steps will require the opening of oxygen sites on the surface, and the probability of finding open sites adjacent to adsorbed hydrocarbon fragments may impact the rate of C_3 conversion. The desorption of oxidized products (H_2O , CO_2) will be more energetically uphill than indicated in Figures 5-3 – 5-5 due to the oscillation about a deeper reduction state. Surface re-oxidation (vacancy refilling) will be more facile than depicted in Figures 5-3 – 5-5 due to the oscillation about a deeper reduction state. CO desorption will become more competitive with CO_2 desorption. Changes in the path through reaction intermediates are also plausible. The use of a fully-oxidized surface provides mechanistic insight into site requirements and possible limiting steps, however, conclusions reached can clearly be significantly altered if this does not represent the active surface oxidation state through which the catalytic cycle will oscillate. Use of the stoichiometric, oxidized surface is most common in DFT studies of oxidation catalysis, however, we hope the conclusions reached herein will encourage the use of *ab initio* thermodynamic methods to first consider the metal oxide surface state under reaction conditions prior to considering the redox catalysis of the surface.

5.3.5. Desorb hydrogen atoms as H₂ or H₂O

In constructing reaction energy diagrams above, we have assumed that when hydrogen atoms desorb from the surface, they desorb as H₂O leaving behind a half of an oxygen vacancy in the surface. Depending upon the partial pressures of hydrogen and water and the temperature of the systems, hydrogen can desorb as either H₂ or water. Figure 5-9 illustrates a “desorption phase diagram,” for Zr-doped CeO₂ (1 1 1), demonstrating the temperature and partial pressure ranges over which H₂ or H₂O desorption has a more favorable free energy. Above the solid line (high T or high P_{H_2}) hydrogen would prefer to desorb from the surface as H₂O, whereas below the line hydrogen would prefer to desorb as H₂. The dotted lines delineate regions in which the desorption free energy is negative (above line) or positive (below line). These diagrams were created considering a differing numbers of H* adsorbed. Figure 5-9a, represents desorption from a surface with all 6 surface oxygen atoms having a hydrogen atom adsorbed onto them, which was determined as the most stable surface of Zr-doped CeO₂ (1 1 1) under oxidizing and reducing conditions. Figure 5-9b represents desorption from a surface with 3 hydrogen atoms and 3 surface oxygen vacancies (the most stable surface of Zr-doped CeO₂ (1 1 1) under gasifier effluent conditions). The desorption curves for pure CeO₂ are contained in Figure C-11.

The gas phase compositions are marked with an X for whether hydrogen will desorb as H₂ or H₂O (relative to the solid line) and with an O for whether the desorption is favorable (relative to the dotted line) under oxidizing and reducing conditions (Figure 5-9a) and for gasifier effluent conditions (Figure 5-9b). Under oxidizing and reducing conditions, H₂O desorption is thermodynamically preferred over H₂ desorption, as we used in our reaction path in Sections 5.3.1 and 5.3.2. However, under gasifier effluent conditions (Section 5.3.3), H₂ desorption is thermodynamically preferred over H₂O desorption. Though H₂O desorption was considered in constructing reaction free energy diagrams in our analysis above, H₂ production from propane

reforming will be favored under gasifier effluent conditions when the properly reduced surface is used as the catalytic surface.

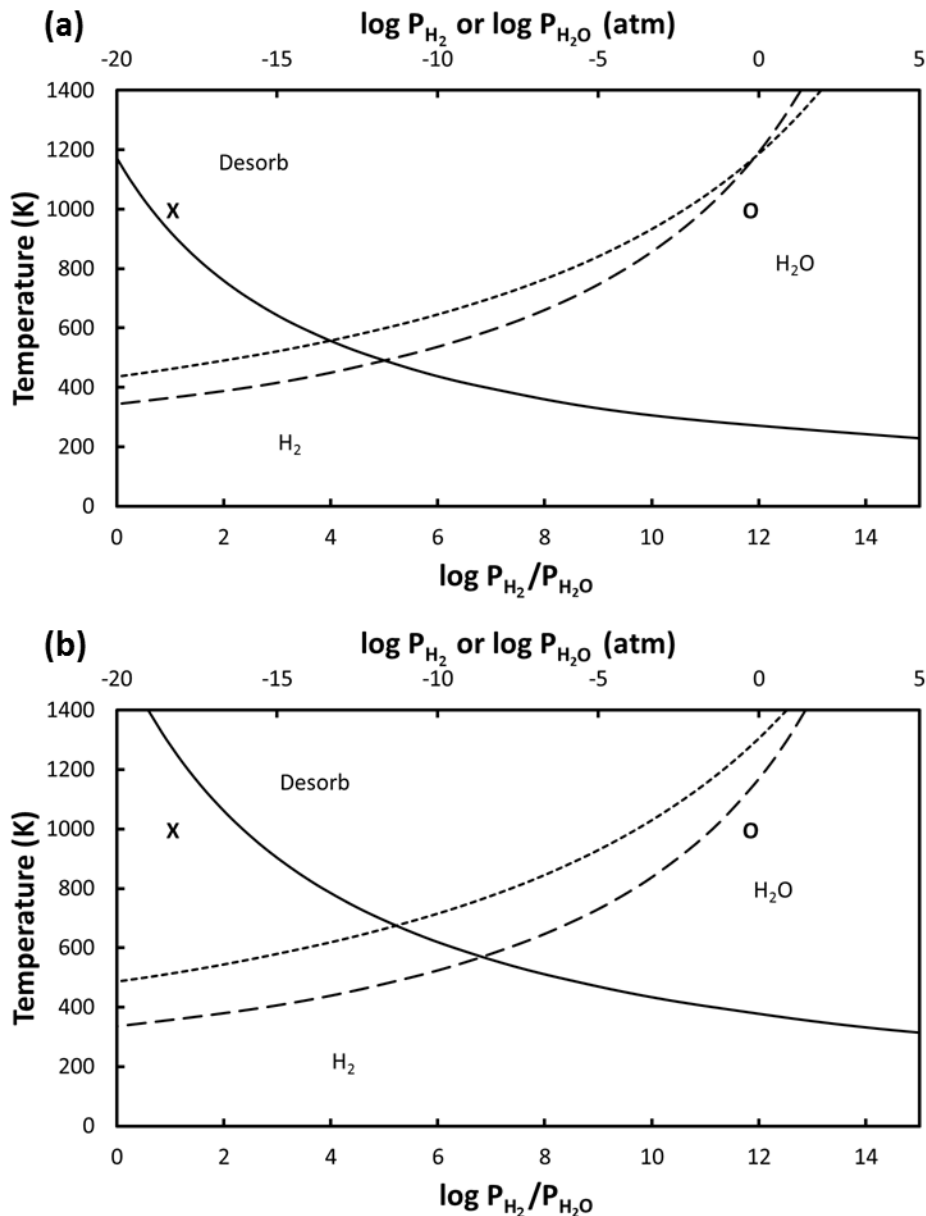


Figure 5-9. The pressure-temperature curves as to whether the hydrogen on the surface of Zr-doped ceria will desorb as H_2 or H_2O . (—) the division between whether the hydrogen will desorb as H_2 (below line) or H_2O (above line) based on the lower axis. The division on whether the hydrogen will desorb as (---) H_2 , or (-----) H_2O , upper axis. Above the dotted/dashed lines, the hydrogen will exergonically desorb and below they will not. The X's represent the gas phase conditions considered in Sections 5.3.1-5.3.3 relative to whether H_2 or H_2O will desorb. The O's represent the conditions relative to the dotted/dashed lines indicating whether hydrogen desorption is exergonic. (a) represents the surface starting with 6 hydrogens absorbed on the surface (oxidizing and reducing conditions) and (b) represents the surface starting with 3 hydrogens and 3 surface oxygen vacancies (extremely reducing, gasifier effluent conditions).

5.4. Conclusions

The bare, fully-oxidized Zr-doped CeO₂ (1 1 1) surface is not the active surface during the reforming of propane under the oxidizing, reducing or extremely reducing environments. Instead the surface will be either covered in hydrogen (oxidizing and reducing environments) or have half of the surface oxygen atoms covered in hydrogen and the other half vacant (extremely reducing environment). Therefore, for propane oxidation to occur, surface oxygen sites need to become available through either vacancy refilling, H₂ desorption, or H₂O desorption followed by vacancy refilling. Requiring these processes will alter the reaction path and could slow down the overall rate relative to a surface model where all surface O are available to reactants. Further reforming steps will also require the opening of additional oxygen sites which could also impact the rate. With the surface also being in a further reduced state, the reaction path in all of the environments could be altered. Our reaction path analysis, including re-oxidation, captures the oxidizing and reducing environments reasonably well, however, the reaction path under extremely reducing (gasifier effluent) conditions is highly misrepresented. The approach utilized in this study is able to differentiate the preferred oxidation products (H₂O or H₂, CO or CO₂) based on the reaction environment, and connect this distribution to elementary reaction processes. The oxidation environment influences the points during the propane decomposition path at which surface re-oxidation occurs. Our results demonstrate that erroneous mechanistic conclusions can be reached when examining redox catalysis over oxide surfaces if the initial surface oxidation state about which the catalytic cycle oscillates is not properly utilized.

ACKNOWLEDGEMENTS: This material is based upon work supported as part of the Center for Atomic Level Design, an Energy Frontier Research Center funded by the U.S. Department of Energy, Office of Science, Office of Basic Energy Sciences under Award Number DE-SC0001058.

5.5. References

1. M. L. Yang, Y. A. Zhu, C. Fan, Z. J. Sui, D. Chen, X. G. Zhou. *Journal of Molecular Catalysis A-Chemical* **2010**, *321*, 42-49.
2. M. L. Yang, Y. A. Zhu, C. Fan, Z. J. Sui, D. Chen, X. G. Zhou. *Physical Chemistry Chemical Physics* **2011**, *13*, 3257-3267.
3. K. Lee, E. Lee, C. Song, M. J. Janik. *Journal of Catalysis* **2014**, *309*, 248-259.
4. P. Gelin, M. Primet. *Applied Catalysis B-Environmental* **2002**, *39*, 1-37.
5. J. A. Labinger, J. E. Bercaw. *Nature* **2002**, *417*, 507-514.
6. G. C. Bond, D. T. Thompson. *Catalysis Reviews-Science and Engineering* **1999**, *41*, 319-388.
7. D. W. Blaylock, T. Ogura, W. H. Green, G. J. O. Beran. *The Journal of Physical Chemistry C* **2009**, *113*, 4898-4908.
8. D. Knapp, T. Ziegler. *Journal of Physical Chemistry C* **2008**, *112*, 17311-17318.
9. M. D. Krcha, A. D. Mayernick, M. J. Janik. *Journal of Catalysis* **2012**, *293*, 103-115.
10. A. D. Mayernick, M. J. Janik. *Journal of Physical Chemistry C* **2008**, *112*, 14955-14964.
11. A. D. Mayernick, M. J. Janik. *Journal of Catalysis* **2011**, *278*, 16-25.
12. W. Tang, Z. P. Hu, M. J. Wang, G. D. Stucky, H. Metiu, E. W. McFarland. *Journal of Catalysis* **2010**, *273*, 125-137.

13. D. Terribile, A. Trovarelli, C. de Leitenburg, A. Primavera, G. Dolcetti. *Catalysis Today* **1999**, *47*, 133-140.
14. L. H. Xiao, K. P. Sun, X. L. Xu, X. N. Li. *Catalysis Communications* **2005**, *6*, 796-801.
15. T. K. Das, E. L. Kugler, D. B. Dadyburjor. *Industrial & Engineering Chemistry Research* **2009**, *48*, 10796-10802.
16. C. deLeitenburg, A. Trovarelli, J. Llorca, F. Cavani, G. Bini. *Applied Catalysis a-General* **1996**, *139*, 161-173.
17. K. Alexopoulos, M. F. Reyniers, G. B. Marin. *Journal of Catalysis* **2012**, *289*, 127-139.
18. L. Cheng, G. A. Ferguson, S. A. Zygmunt, L. A. Curtiss. *Journal of Catalysis* **2013**, *302*, 31-36.
19. B. Beck, M. Harth, N. G. Hamilton, C. Carrero, J. J. Uhlrich, A. Trunschke, S. Shaikhutdinov, H. Schubert, H. J. Freund, R. Schlogl, J. Sauer, R. Schomacker. *Journal of Catalysis* **2012**, *296*, 120-131.
20. Y. Liu, Z. H. Li, J. Lu, K. N. Fan. *Journal of Physical Chemistry C* **2008**, *112*, 20382-20392.
21. M. Fernandez-Garcia, A. Martinez-Arias, A. Iglesias-Juez, A. B. Hungria, J. A. Anderson, J. C. Conesa, J. Soria. *Journal of Catalysis* **2003**, *214*, 220-233.
22. Q. Y. Wang, B. Zhao, G. F. Li, R. X. Zhou. *Environmental Science & Technology* **2010**, *44*, 3870-3875.
23. N. Laosiripojana, W. Sutthisripok, P. Kim-Lohsoontorn, S. Assabumrungrat. *International Journal of Hydrogen Energy* **2010**, *35*, 6747-6756.
24. A. Aranda, E. Aylon, B. Solsona, R. Murillo, A. M. Mastral, D. R. Sellick, S. Agouram, T. Garcia, S. H. Taylor. *Chemical Communications* **2012**, *48*, 4704-4706.
25. A. Aranda, S. Agouram, J. M. Lopez, A. M. Mastral, D. R. Sellick, B. Solsona, S. H. Taylor, T. Garcia. *Applied Catalysis B-Environmental* **2012**, *127*, 77-88.

26. G. Kresse, J. Furthmuller. *Computational Materials Science* **1996**, *6*, 15-50.
27. G. Kresse, J. Furthmuller. *Physical Review B* **1996**, *54*, 11169-11186.
28. G. Kresse, J. Hafner. *Physical Review B* **1993**, *47*, 558-561.
29. G. Kresse, D. Joubert. *Physical Review B* **1999**, *59*, 1758-1775.
30. H. J. Monkhorst, J. D. Pack. *Physical Review B* **1976**, *13*, 5188-5192.
31. J. P. Perdew, J. A. Chevary, S. H. Vosko, K. A. Jackson, M. R. Pederson, D. J. Singh, C. Fiolhais. *Physical Review B* **1992**, *46*, 6671-6687.
32. V. I. Anisimov, O. Gunnarsson. *Physical Review B* **1991**, *43*, 7570-7574.
33. J. F. Herbst, R. E. Watson, J. W. Wilkins. *Physical Review B* **1978**, *17*, 3089-3098.
34. S. Fabris, S. de Gironcoli, S. Baroni, G. Vicario, G. Balducci. *Physical Review B* **2005**, *71*, 041102.
35. S. Fabris, S. de Gironcoli, S. Baroni, G. Vicario, G. Balducci. *Physical Review B* **2005**, *72*, 237102.
36. G. Kresse, P. Blaha, J. L. F. Da Silva, M. V. Ganduglia-Pirovano. *Physical Review B* **2005**, *72*, 237101.
37. M. D. Krcha, M. J. Janik. *Langmuir* **2013**, *29*, 10120-10131.
38. R. Li, M. D. Krcha, M. J. Janik, A. D. Roy, K. M. Dooley. *Energy & Fuels* **2012**, *26*, 6765-6776.
39. A. D. Mayernick, M. J. Janik. *Journal of Chemical Physics* **2009**, *131*, 084701.
40. M. Nolan, V. S. Verdugo, H. Metiu. *Surface Science* **2008**, *602*, 2734-2742.
41. M. Nolan, S. Grigoleit, D. C. Sayle, S. C. Parker, G. W. Watson. *Surface Science* **2005**, *576*, 217-229.
42. D. Y. Lu, P. Liu. *Journal of Chemical Physics* **2014**, *140*, 084101.
43. M. Nolan, S. C. Parker, G. W. Watson. *Surface Science* **2005**, *595*, 223-232.

44. J. Chase, *NIST-JANAF Thermochemical Tables*. 4th ed.; ACS American Chemical Society: 1998.
45. L. Wang, T. Maxisch, G. Ceder. *Physical Review B* **2006**, 73, 195107.
46. J. A. Dean. *Lange's Handbook of Chemistry*. 15th ed.; McGraw-Hill, Inc.: 1999.

Chapter 6

Catalytic Propane Reforming Mechanism over Mn-Doped CeO₂ (1 1 1)

ABSTRACT: MnO_x/CeO_x mixed oxide systems exhibits a great hydrocarbon oxidation activity. Using density functional theory (DFT) methods, we examined the reforming path of propane over the Mn-doped CeO₂ (1 1 1) surface. The surface initially contains a surface oxygen vacancy, making the surface model closer to the true active surface of the catalyst. The reforming paths over Mn- and Zr-doped ceria are very similar with only slight differences in the path and the same final products. The possibility of intermediates during the reforming process desorbing from the surface is extremely low, with desorption energies of the intermediates being much higher than further surface reactions. The extent of surface reduction and the electronic structure of the propane intermediate is also examined.

6.1. Introduction

Manganese oxide (MnO_x) can be added to ceria and provides a greater catalytic oxidation activity compared to pure CeO_2 .¹⁻⁸ High concentrations of MnO_x in CeO_2 are stable with no presence of an MnO_x phase with x-ray diffraction (XRD).⁵ Density functional theory (DFT) has shown that Mn can be doped into the fluorite lattice of ceria when there are oxygen vacancies present nearby,³ and Mn-doped CeO_2 will have a high rate for reforming of methane.^{4,6} $\text{MnO}_x/\text{CeO}_2$ has also been shown to be able to oxidize hydrocarbons with chlorine (trichlorophenol¹ and trichloroethylene²), volatile organic compounds,⁷ toluene,⁹ tars (C_{10}H_8),⁸ and CO .¹⁰ With the ability of Mn-doped CeO_2 to reform hydrocarbons well established, we employ DFT to examine the path for the decomposition of propane over Mn-doped CeO_2 . We also examine the extent of reduction of the surface and the electronic configuration of the propane intermediate at every step.

Density functional theory (DFT) has been extensively used to model small hydrocarbon oxidation and decomposition over metal catalysts.¹¹⁻¹⁶ However, using DFT to examine the complete oxidation/decomposition of hydrocarbons over oxides are uncommon, due to the added complexities representing redox chemistry on oxides. DFT has been used to model oxidation and reforming of small hydrocarbons over pure and M-doped ceria, with most of the focus on methane.^{4,6,17-23} Most studies involving propane and DFT are on partial oxidation and dehydrogenation over V_2O_5 and Ga_2O_3 .²⁴⁻²⁷ Chapter 5 examined the reforming mechanism of propane over Zr-doped CeO_2 (1 1 1), and identified a number of key modeling and mechanistic questions involved in the decomposition of hydrocarbons over oxides.²⁸

$\text{MnO}_x/\text{CeO}_x$ mixed oxides has a high catalytic activity as well as high stability.⁹ Combining MnO_x and CeO_x in a nanorod structure was found to be very active for the total oxidation of toluene to CO_2 at temperatures as low as 225 °C.⁹ The catalytic activity of the total oxidation of *n*-hexane on $\text{MnO}_x/\text{CeO}_x$ supported on alumina is also high.²⁹ Mn-doped ceria has also shown promise in

reforming tars (modeled as $C_{10}H_8$) from gasifier effluents to at least methane and in some conditions to CO and H_2 at temperatures of 1100 K.⁸ The addition of other oxides to MnO_x/CeO_x mixtures can lead to an even higher catalytic activity. The addition of MnO_x to CeO_2-ZrO_2 mixtures increases the activity of reforming methane.⁶ MnO_x/CeO_x mixtures has also shown great promise in the low temperature catalytic combustion of volatile organic compounds (VOCs).^{1-2,7,30} At moderate conditions (100-140 °C), MnO_x/CeO_x mixed oxides is able to oxidize VOCs to HCl, Cl_2 , CO_2 and small amounts of CO.^{1,30} It is thought the Mn in the mixture helps to remove chlorine species from Ce active sites, allowing for a higher stability of the surface.² Compared with other oxides and metals that can be mixed with CeO_2 , MnO_x can increase the stability of the catalyst,⁹ as well as being less expensive than some oxides and metals (Ag, Au, Pt, Pd) that can increase the activity of ceria.^{4,31-33} Several DFT studies has also examined the catalytic activity of Mn-doped CeO_2 . We have previously shown that the reducibility of the surface is linearly correlated with the reducibility of the surface, so a surface which is more reducible, to an extent, will have a higher catalytic activity.⁴ Cen et al.,³⁴ Gupta et al.,³⁵ and Tang et al.³⁶ all showed that the addition of Mn to the ceria surface increases the reducibility of the surface. Chapter 4 showed that Mn will dope into the lattice of ceria with oxygen vacancies present and also increases the reducibility and catalytic activity of the surface.³⁻⁴

There has only been a detailed mechanism for the decomposition of propane over metal catalysts and not oxide catalysts, except for Chapter 5 where we examined the propane mechanism over Zr-doped CeO_2 (1 1 1).²⁸ Our group and Yang et al. has previously examined the mechanism for propane decomposition over Pt¹¹⁻¹² and Rh-Ni¹³ surface using DFT. Previously to our study,²⁸ only isolated studies examined the initial reaction steps of oxidation/decomposition of propane over oxides, with most of the studies focused on vanadia and selective oxidation.²⁴⁻²⁶ A similar study examined the initial dehydrogenation of propane over Ga_2O_3 and determined hydrogen atoms prefer to desorb at H_2 at low reaction temperatures.²⁷

Chapter 5 examined propane reforming over Zr-doped CeO₂ and discussed many modeling and mechanistic questions that arise in modeling complex multistep reactions on oxides.²⁸ Dissociation products during the reforming of propane are placed in separate unit cells to maintain a reasonable degree of local surface reduction. For every intermediate on the surface, we consider if it is more favorable to 1) dissociate to C_zH_{n-1}* + H*, (2) to dissociate to C_{z-1}H_{n-x}* and CH_x*, (3) to add an oxygen atom to the surface, or (4) to desorb C_zH_n*, CO, or CO₂. When comparing step, we only considered the most exoergonic free energy step as the more favorable step. The desorption of species were only considered if the 0 K energy for the desorbed species was more favorable than other possible surface reaction steps.

For the Zr-doped CeO₂ surface, we find that the active surface is not a bare-fully oxidized surface.²⁸ Depending upon the conditions, the surface is either fully covered in hydrogen or there is a combination of surface oxygens and hydrogen on the surface. We discussed if the active surface of Zr-doped CeO₂ was utilized instead of the bare-fully oxidized surface what parts of the reaction path could change. One of the main differences, is the surface will already be reduced before the reforming of propane and would therefore most likely increase any step along the reforming path that would further reduce the surface. Also with the presence of hydrogen on the surface, propane oxidation would require the opening of oxygen sites, either through H₂ or H₂O desorption or through oxygen vacancy refilling.

This study examines the reforming path for propane over Mn-doped CeO₂ (1 1 1). Using the mechanistic and modeling questions we established in our previous paper, we determine a possible reforming path for propane over Mn-doped ceria in an oxidizing, reducing and extremely reducing environment. We previously shown that the active surface of Zr-doped ceria is not a bare-fully oxidized surface, but has hydrogen on the surface, with the presence of some oxygen vacancies depending upon the oxygen partial pressure. We take a step closer to the active surface by incorporating a surface oxygen vacancy. We also compare the reforming path of propane on the

Mn- and Zr-doped ceria surface. Lastly, we examine the desorption of possible intermediates and a more detailed picture of the electronic structure at every intermediate step during the path is developed.

6.2. Methods

6.2.1. Electronic structure method

Density functional theory calculations were carried out using the Vienna *ab initio* simulation program (VASP), an *ab initio* total energy, and molecular dynamics program developed at the Institute for Material Physics at the University of Vienna.³⁷⁻³⁹ Plane wave basis sets were used with an energy cutoff of 450 eV. The ion-core interactions were represented using the projector-augmented wave (PAW) method.⁴⁰ The generalized gradient functional of Perdew-Wang (PW91) was utilized to incorporate the exchange and correlation energies.⁴¹ All calculations were spin polarized. The valence configurations of cerium is $5s^25p^66s^24f^15d^1$, manganese is $3d^64s^1$, oxygen is $2s^22p^4$, carbon is $2s^22p^2$, and hydrogen is $1s^1$. The Monkhorst Pack scheme⁴² was used for k -point sampling of $(2 \times 2 \times 1)$, with the third vector perpendicular to the surface. Structural optimization were performed by minimizing forces on all atoms to below $0.05 \text{ eV} \cdot \text{\AA}^{-1}$. We have previously shown that using a force criteria of $0.05 \text{ eV} \cdot \text{\AA}^{-1}$ is sufficient to provide converged structure and energetics compared with a force criteria of $0.02 \text{ eV} \cdot \text{\AA}^{-1}$.⁴

The DFT+ U approach was utilized, due to the difficulties standard DFT has in representing the nature of the $4f$ orbitals in ceria.⁴³⁻⁴⁵ This approach introduces an on-site Coulombic interaction (U -term) which penalizes non-integer occupation of localized orbitals effectively penalizing delocalization of electrons. A U -value of 5 eV was utilized on the f -states of cerium, consistent with previous studies of ceria.^{3-5,18-19,46-48} The oxygen vacancy formation and methane adsorption

energies depend upon the U -value of the f -states of cerium, as we have previously shown.¹⁸ The oxygen vacancy and methane adsorption energies decrease with increasing U -value for pure and Zr-doped CeO₂, with a slight increase in energies for Pd-doped CeO₂. With the dependence for oxygen vacancy and methane adsorption energies on the U -values chosen, the quantitative results presented herein dependent upon the U -value chosen. However, we expect the qualitative results presented herein to be reasonably correct with a U -value of 5 eV on the f -states of cerium.

It has been shown that for the Mn dopant in ceria, a U -value to Mn must be added to correctly represent the electronic structure of Mn-doped CeO₂.^{3-5,34-36,49} A U -value of 4 eV on the d -states of Mn has been confirmed using both XANES and results from the hybrid functional HSE06.^{3,5}

6.2.2. Surface models

The fluorite crystal structure of pure CeO₂ is the same as used in our previous studies, with a bulk lattice parameter of (5.466 Å) which is within 1% of experimental values.^{3-5,18-19,46} The (1 1 1) surface was utilized as it is the lowest energy surface of ceria and with therefore represent a large portion of the surface of polycrystalline ceria.^{18,47,50} The (1 1 1) termination of ceria results in surface termination of oxygen atoms with cerium atoms in the layer below, Figure 6-1. A $p(2 \times 3)$ unit cell expansion is used to model the surface with 15 Å of vacuum space perpendicular to the surface. To remove any slab-to-slab interaction that might result from a net surface dipole upon propane adsorption and reforming, as well as formation of oxygen vacancies, mirrored slabs were utilized. 4 CeO₂ layer (12 atomic layer) were utilized for all optimizations with adsorbate/intermediates mirrored on top and bottom surfaces. All layers were allowed to relax during structural optimizations. In our previous paper we showed that the most stable surface of Mn-doped CeO₂ with one oxygen vacancy in a $p(2 \times 3)$ expansion is by doping two Mn atoms

along the short side (replaces to Ce atoms and forming a continuous row of Mn) with a oxygen vacancy being in the surface.³ In this surface, the Mn atoms are in a 3+ oxidation state, and all cerium atoms remain as Ce⁴⁺. As described in our previous paper, the site projected charge method is utilized to identify the number of cerium atoms reducing from Ce⁴⁺ to Ce³⁺.⁴ The oxidation state of Mn was also identified using the site projected charge method (RWIGS of 0.7), using both the total number of electrons counted on an Mn atom as well as the spin on each Mn atom. An Mn atom in a 3+ oxidation state has ~3.5 electrons and in a 2+ oxidation state has ~3.7 electrons.

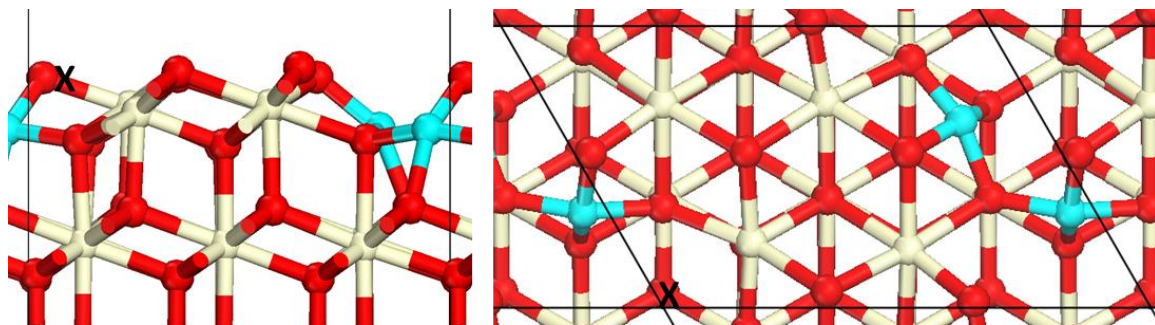


Figure 6-1. Side and top views of a $p(2 \times 3)$ unit cell expansion of Mn-doped CeO₂ (1 1 1). Ce is displayed at tan (light), Mn as light blue (gray) and O as red (dark). The X's represent the location of the oxygen vacancy.

6.2.3. Reaction and Free Energies

The elementary reactions and the formulas for their reaction energy are the same equations as we utilized in our previous paper.²⁸ As a first analysis, the reaction path is determined only using the elementary reaction 0 K and reaction condition-dependent free energies and no transition states are considered. All of the reaction energies calculated in this study use free energies of all gas phase species and the chemical potential of all gas phase species was calculated in the same method as our previous paper.²⁸ Even though it is known that DFT overestimates the O-O binding energy of oxygen, the DFT energy of O₂ is utilized.⁵¹ A correction term can be added, however it would only offset the oxygen partial pressures and temperatures we specify.

6.2.4. Results from Zr-doped Paper

We utilized the same 4 possible steps for every intermediate as our previous paper (as discussed in Section 6.1) when examining the path for reforming propane over Mn-doped CeO₂ (1 1 1) and only considered the most exoergonic free energy step.²⁸ It was also determined that the active surface of the catalyst is not a bare fully-oxidized surface, but is covered in hydrogen and has oxygen vacancies depending upon the partial pressure of oxygen. In this study we did not start with the active surface of Mn-doped CeO₂ under reaction conditions, however, we did take a step closer to the active surface, by incorporating a surface oxygen vacancy.

6.3. Results and discussion

6.3.1. Propane reforming in an oxidizing environment (0.1 atm O₂)

The initial step for propane oxidation over Mn-doped CeO₂ is a secondary hydrogen abstraction. This state forms a secondary propyl radical in the gas phase and a hydrogen bound to a surface oxygen atom, a pseudo-transition state. The 0 K energy from the secondary hydrogen abstraction is 0.63 eV. Following the hydrogen abstraction, the secondary propyl radical binds to a surface oxygen atom, with an adsorption energy of 2.67 eV, Figure 6-2a. The overall reaction free energy diagram for the reforming of propane over Mn-doped CeO₂ in an oxidizing environment is contained in Figure 6-3, along with all intermediates contained in the Appendix D. The hydrogen atom adsorbed on the surface, then desorbs from the surface as half an H₂O, forming a half of an oxygen vacancy in the surface. The half of an oxygen vacancy is then refilled using an oxygen present in the gas phase, returning the surface to the initial state of reduction. Desorbing as half an H₂O was shown to be thermodynamically preferable based upon the gas phase environment as shown in our previous paper.²⁸ This same process is repeated of desorbing the hydrogen as water immediately following the abstraction of the hydrogen from the C_z intermediate.

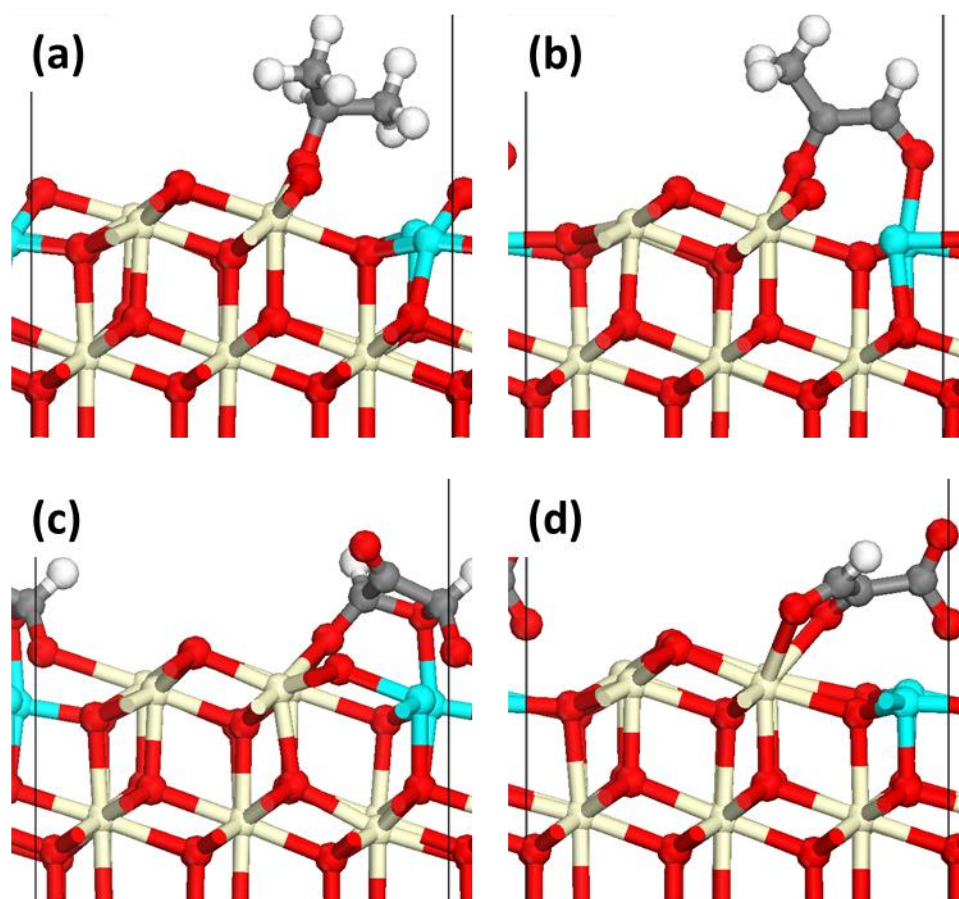


Figure 6-2. Four selected structures of propane reforming intermediates over Mn-doped CeO₂ (1 1 1). (a) CH₃C*HCH₃, (b) C*HC*CH₃, (c) C*HC*C*H (oxete like structure), (d) C*HC*C* (end C with 2 oxygens). Ce is displayed at tan (light), Mn as light blue (gray) and O as red (dark).

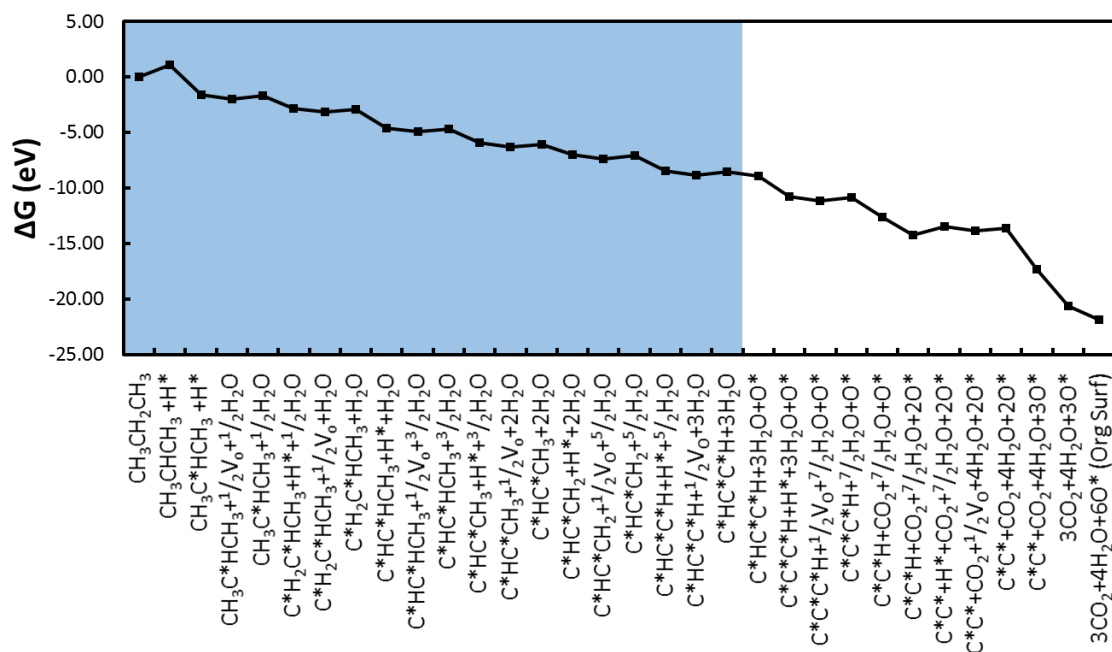


Figure 6-3. Propane reforming reaction energy diagram over Mn-doped CeO₂ (1 1 1) surface in an oxidizing environment (0.05 atm H₂O, 0.234 atm H₂, 0.1 atm O₂, 0.32 atm CO, 0.32 atm CO₂ and 0.1 atm propane at 1000 K). The blue (dark grey) denotes steps that are equivalent under more reducing environments in Figures 6-4 and 6-5.

As with our previous paper, breaking a C-H bond or a C-C bond, desorption of C₂ intermediate and the possibility of re-oxidizing the surface with oxygen was considered.²⁸ Desorption of the C₂ intermediate prior to the desorption of CO or CO₂ was at least 1.5 eV higher in energy than the surface reaction and therefore we conclude the only major C-containing products are CO and CO₂, and is more detailed in Section 6.3.5.

The following step after adsorption of the secondary propyl radical is the abstraction of a hydrogen atom from one of the primary carbon atoms and the bonding of the same carbon atom to a surface oxygen atom, forming C*H₂C*HCH₃. The asterisks refer to carbon atoms bound to a surface oxygen atoms. The following two steps, after H₂O desorption and oxygen vacancy refilling, involves the abstraction of a hydrogen from the primary carbon bound to the surface, and then the

abstraction of the hydrogen on the secondary carbon atom forming $C^*HC^*CH_3$, Figure 6-2b. Next, the abstraction of a hydrogen from the primary carbon atom not bound to a surface oxygen occurs, forming $C^*HC^*CH_2$. Another hydrogen is abstracted from the primary carbon atom not bound to the surface and the carbon atom forms a bond with a surface oxygen atom, $C^*HC^*C^*H$. A surface re-oxidation occurs next with the oxygen atom forming a bond with both of the primary carbon atoms forming an oxete like structure, Figure 6-2c.

A hydrogen abstraction occurs next and the oxete like structure is broken up and the primary carbon atom with no hydrogens has two carbon-oxygen bonds, with one resembling a carbon-oxygen double bond, Figure 6-2d. This primary carbon atom then breaks its C-C bond forming a CO_2 molecule, leaving behind C^*HC^* on the surface along with forming an oxygen vacancy. The surface is re-oxidized again with an oxygen atom and forms a bond with the carbon atom with no hydrogen atoms. The last hydrogen atom is abstracted from the carbon atom, following by a re-oxidation with an oxygen atom forming another bond with the carbon atom with only one oxygen. The carbon-carbon bond is then broken forming 2 CO_2 molecules, leaving behind an additional 2 surface oxygen vacancies (4 total). Completing the catalytic cycle, the surface is then re-oxidized with 3 oxygen atoms, re-oxidizing the surface to the initial starting surface (one surface oxygen vacancy present). Figures D-1 and D-2 contain all structures along this reforming path. A detailed examination of the electronic structure for reforming propane over Mn-doped CeO_2 in an oxidizing environment is contained in Section 6.3.5.

Reforming of propane over the Mn-doped CeO_2 (1 1 1) surface produced $3CO_2$ and $4H_2O$ molecules with an overall reaction free energy of -21.83 eV. Which is also very similar to the overall gas phase reaction energy based upon tabulated energies of formation of the gas phase species of -22.00 eV.⁵² The overall reaction rate for reforming of propane over Mn-doped CeO_2 would be mostly dictated by the initial first hydrogen abstraction from the propane forming a secondary propyl radical in the gas phase (0 K barrier of 0.63 eV, and free energy barrier relative

to gas phase propane of 1.07 eV) and the final product desorption of CO₂ (1.00 eV). As discussed in our previous paper, the surface would not be bare fully-oxidized surface.²⁸ We made one step closer to the active surface of the catalyst with the presence of the oxygen vacancy (2 surface oxygen vacancies would be in thermodynamic equilibrium with the O₂ chemical potential). However, the surface we used is not covered in hydrogen, as we stated the surface would be. Not including the hydrogen covered surface would lead to a higher degree of surface reduction and could raise the propane activation energy as well as slightly changing the elementary reaction energies and the reforming path. Though, overall we do not expect to have a great influence on the overall reaction path, but it could shift CO desorption to become more competitive with CO₂ desorption.

6.3.2. Propane reforming in a reducing environment (1x10⁻¹⁷ atm O₂)

The initial steps to reform propane over Mn-doped CeO₂ (1 1 1) in reducing environments is the same as in an oxidizing environment. In a reducing environment, the elementary steps are the same up until the formation of C*HC*C*H. The paths diverge at this point due to the lower partial pressure of oxygen, where surface re-oxidation is preferred over hydrogen abstractions in the oxidizing environment. The reaction free energy diagram under these reducing conditions is contained in Figure 6-4. In the reducing environment, the abstraction of the final two hydrogen atoms (forming a 3 carbon ring) is preferred over re-oxidizing the surface. The first and second re-oxidation steps occur next forming a carbon-oxygen bond with each of the primary carbon atoms. One of the carbon-carbon bonds are broken allowing the desorption of a CO₂ molecule from the surface, forming an additional oxygen vacancy. The surface is then re-oxidized again, forming a carbon-oxygen bond with the carbon atom with only one carbon-oxygen bond. Next, the carbon-carbon bond is broken and two CO₂ molecules desorb from the surface forming an additional two

surface oxygen vacancies (4 total). The catalytic cycle is then completed by the re-oxidation of the surface with 3 oxygen atoms.

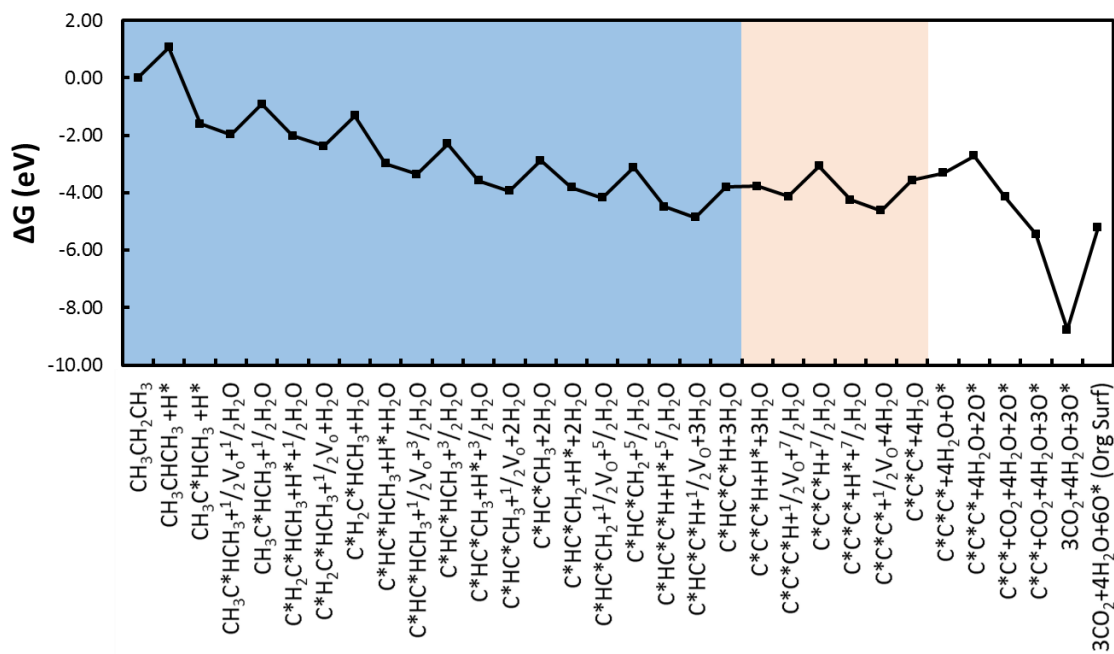


Figure 6-4. Propane reforming reaction energy diagram over Mn-doped CeO_2 (1 1 1) surface in a reducing environment (0.05 atm H_2O , 0.234 atm H_2 , 1×10^{-17} atm O_2 , 0.32 atm CO , 0.32 atm CO_2 and 0.1 atm propane at 1000 K). The blue (dark grey) denotes the steps that follow the same sequence regardless of oxidation conditions considered (equivalent in Figures 6-3 and 6-5) and the red (light grey) denotes steps that are equivalent under the more reducing conditions of Figure 6-5.

Under the reducing conditions presented here, there are three CO₂ and four H₂O molecules formed during the reforming of propane. Figures D-3 and D-4 contains all structures along this reforming path. The first hydrogen abstraction is not the highest energy sequence, as for the oxidative environment, but a series of steps in the middle of the overall reaction, giving a barrier of 1.89 eV with CO₂ desorption occurring immediately after with a 0 K desorption energy of 0.75 eV. This energy sequence involves the refilling of an oxygen vacancy from H₂O desorption and two from re-oxidizing the surface. This reforming path is very similar to the path in an oxidative environment, with the only major difference being the point at which the surface re-oxidizes. The desorption of CO₂ instead of CO, could be a result of the surface not being covered in hydrogen, as we showed in our previous paper.²⁸ The additional hydrogen on the surface would increase the overall reduction of the surface, which would prefer to desorb less oxidized products.

6.3.3. Propane reforming in an extremely reducing environment (8×10^{-22} atm O₂)

Dictating the oxygen partial pressure based upon the equilibrium between H₂O and H₂ at 1000 K, P_{H₂} = 0.234 atm, and P_{H₂O} = 0.05 atm, would give an oxygen an oxygen partial pressure of 8×10^{-22} atm. These conditions are similar to the effluent from a biomass gasifier.⁵ Under these conditions, the reforming path for propane is the same as the reducing environment, up until the surface re-oxidizes. The reaction free energy diagram under these extremely reducing conditions is contained in Figure 6-5, with all structures in Figures D-5 and D-6. Instead of the surface re-oxidizing, one of the carbon-carbon bonds break forming a CO in the gas phase and a surface oxygen vacancy. Followed by the breaking of the other carbon-carbon bond forming two more CO molecules and two more surface oxygen vacancies.

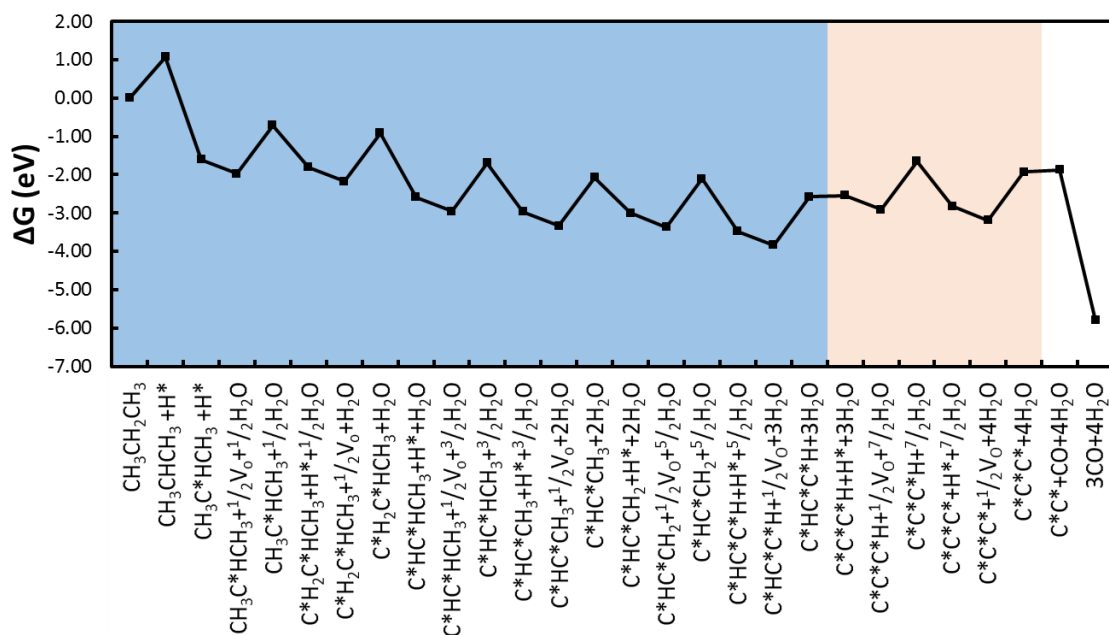


Figure 6-5. Propane reforming reaction energy diagram over Mn-doped CeO₂ (1 1 1) surface in an extremely reducing environment (0.05 atm H₂O, 0.234 atm H₂, 8x10⁻²² atm O₂, 0.32 atm CO, 0.32 atm CO₂ and 0.1 atm propane at 1000 K). The blue (dark grey) denotes steps equivalent to the more oxidizing conditions used in Figures 6-3 and 6-4 and the red (light grey) denotes steps equivalent under the more oxidizing conditions in Figure 6-4.

Under these extremely reducing conditions, the products are three CO and four H₂O molecules in the gas phase. As in the reducing environment, the initial hydrogen abstraction is not the highest energy sequence. The highest energy sequence is the refilling of the oxygen vacancy from H₂O desorption followed by the desorption of the first CO molecule, of 3.35 eV (2.09 eV CO 0 K desorption energy). The major differences between the extremely reducing environment and the previous two environments is the lack of surface re-oxidation and the production of CO instead of CO₂. The large endothermicity in the high energy sequence is the result of not starting with the active surface under these extremely reducing conditions. There will be more surface oxygen vacancies present, along with hydrogen adsorbed on the surface, would cause the surface to be further reduced. A surface that is further reduced would most likely increase the importance of the

initial hydrogen abstraction along with changing the reaction path and lowering the CO desorption energy. Overall our reforming path in oxidizing or a reducing environment is reasonable, our reaction path in an extremely reducing environment is highly misrepresented due to the use of a more oxidized surface compared with the reaction environment.

6.3.4. Differences between Mn- and Zr-doped CeO₂

Compared with Zr-doped CeO₂, reforming on Mn-doped CeO₂ is very similar. The initial hydrogen abstraction between the two surfaces are almost the same in energy, with only Mn-doped CeO₂ lower by only 0.05 eV. The first difference in the path, is the third hydrogen abstraction. On the Zr-doped surface, the third hydrogen abstraction involves the removal of a hydrogen from a primary carbon and the bonding of the carbon to a surface oxygen atom. The third hydrogen abstraction on the Mn-doped surface removes a hydrogen from the primary carbon atom already bound to a surface oxygen. The primary carbon not bound to an oxygen, binds to an oxygen during the sixth hydrogen abstraction, forming C*HC*C*H on the surface. In the oxidative and reducing environments, the point at which the surface first re-oxidizes is much later on the Mn-doped CeO₂ surface (after formation of C*HC*C*H in an oxidative environment) compared to the Zr-doped surface (after formation of C*H₂C*HC*H in an oxidative environment). This signifies that the Mn-doped surface is easier to create a further reduced surface compared to the Zr-doped surface, especially in the oxidative environment with the surface already in thermodynamic equilibrium with the O₂ chemical potential. The final products on both the Zr- and Mn-doped CeO₂ surface in the oxidizing and reducing environment is CO₂ and CO in the extremely reducing environment with the formation of H₂O in all environments.

The overall reaction free energy for reforming propane in an oxidative environment on both the Zr- and Mn-doped surface is about the same and in the reducing environment Zr-doped is

slightly more favorable and much more favorable in the extremely reducing environment. The initial reaction rate (abstraction of the first hydrogen) is about the same between Mn- and Zr-doped CeO₂ in the oxidative environment, along with the product desorption energy. In the reducing environment, a series of steps in the middle of the reaction path will dictate the reaction rate for both the Mn- and Zr-doped surfaces, with the series of steps on the Mn-doped surface occurring slightly later in the reaction path compared to Zr-doped surface. The series of steps on the Zr-doped surface is about 0.25 eV lower than on the Mn-doped surface and the desorption of CO₂ is 1.2 eV more favorable on the Mn-doped surface compared to the Zr-doped surface. In the extremely reducing environment, a series of steps in the middle also dictate the reaction rate for Mn- and Zr-doped CeO₂. The series of steps on the Zr-doped surface includes a hydrogen abstraction and H₂O formation and oxygen vacancy refilling, compared with the Mn-doped surface consists of refilling an oxygen vacancy and desorption of the first CO molecule, which occurs later in the reaction path. The energy involved on the Mn-doped surface is 3.35 eV (including the 0 K CO desorption energy) and on the Zr-doped surface is 2.03 eV and the CO desorption energy is 2.04 eV.

6.3.5. Desorption of intermediates and electronic structure analysis

For the reforming of propane in the oxidizing environment every hydrogen abstraction and re-oxidation step is exothermic in energy, with only the refilling of the ½ oxygen vacancy formed after the desorption of H₂O and the desorption energy of CO₂ being endothermic. Table 6-1 contains C_z intermediate desorption, hydrogen abstraction and re-oxidation energies for the reforming of propane in an oxidizing environment. The 0 K desorption energies for all of the intermediate species on the surface is more endothermic than the following hydrogen abstraction or surface re-oxidation. Therefore, the surface will fully oxidize the propane to either CO or CO₂, depending upon reaction conditions, and will not partially oxidize the propane. Under reducing conditions, the surface will

still fully oxidize the propane, as even though the energy to re-oxidize the surface with C*C*C* is endothermic, the 0 K desorption energy is more endothermic. However, for the extremely reducing conditions, the 0 K energy for the desorption of the C*C*C* species compared to the breaking of a C-C bond and desorption of the CO molecule is similar in energy (2.21 and 2.09 eV, respectively). Which is most likely an artifact of not starting with the active surface of the catalyst under these extremely reducing conditions.

Table 6-1. Energies for C_z intermediate desorption, abstracting a hydrogen and re-oxidizing the surface under oxidizing conditions

C _z Intermediate	0 K Desorption Energy (eV)	Energy to Abstract Next Hydrogen (eV)	Energy to Re-Oxidize the Surface (eV)
C*HC*HCH ₃	2.91	-1.28	1.56
C*HC*CH ₃	1.73	-0.93	-0.75
C*HC*CH ₂	2.04	-1.37	0.43
C*HC*C*H	3.00	0.03	-0.39
C*C*C*H ^a	2.40	-1.17	-0.66
C*C*C* ^a	2.21	-	0.26

^a Energies based upon a reducing environment

Figure 6-6 contains Lewis structures for the reforming of propane of the surface under oxidizing conditions. Each order of structures follows the same reaction path as described in Section 6.3.1 and either involves a hydrogen abstraction, re-oxidation or CO₂ desorption step. The number of reduced metal atoms was determined as discussed in Section 6.2.2, and is shown in the figure as a Ce[·]. This does not directly correspond to the number of cerium atoms that reduced, but a combination of Mn atoms reducing to Mn²⁺ and Ce atoms reducing to Ce³⁺. The bond orders were

determined using the bond lengths, the valency of the atoms and the number of reduced metal atoms to match up the total number of electrons in the system. A number near a partial bond is the total number of electrons associated with that partial bond. Figures 6e, 6i and 6k all had a partial radical electron on carbon and oxygen atoms, this has been signified by a partial bond between the atoms, along with an odd number of electrons associated with that bond. Oxygen atoms without full double bonds with a carbon atom, still has at least one bond with a cerium atom in the surface.

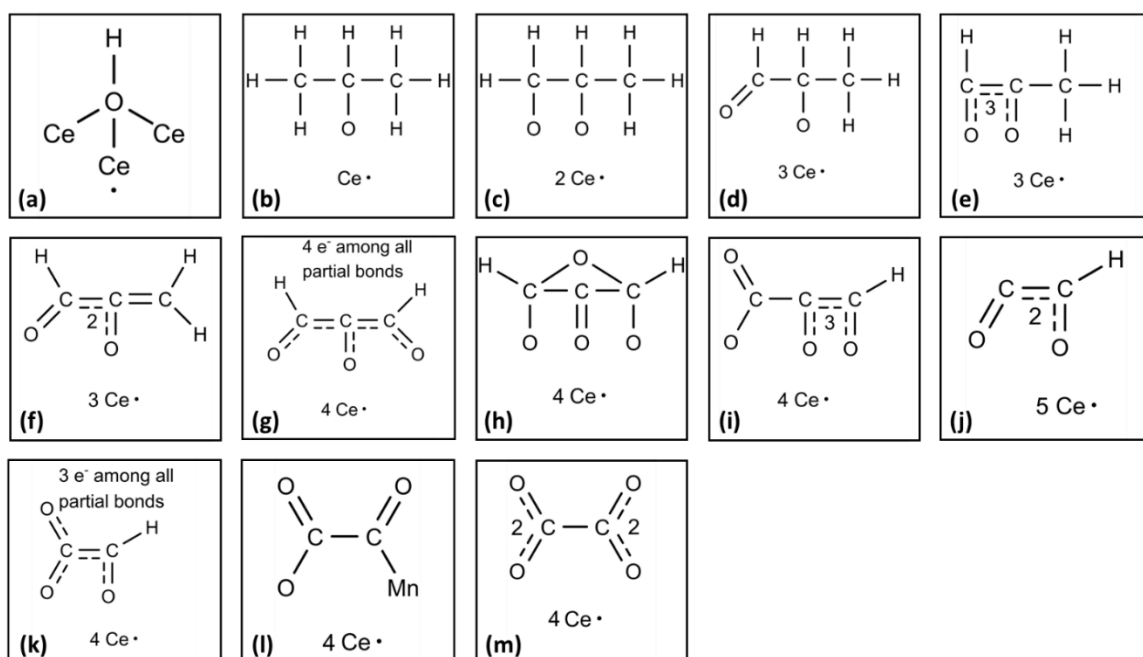


Figure 6-6. Lewis structures for propane reforming over Mn-doped CeO_2 (1 1 1) in an oxidizing environment. Numbers near partial bonds represent the total of electrons associated with the partial bonds.

6.4. Conclusions

The reforming path for propane over Mn-doped CeO₂ (1 1 1) is very similar to the reforming path over Zr-doped CeO₂. The initial hydrogen abstraction energy on the two surfaces are very similar with the only major differences between the two surfaces, the point at which the second primary carbon forms a bond with a surface oxygen is later on Mn-doped ceria and the point at which the surface re-oxidizes is also later on the Mn-doped surface under both oxidizing and reducing conditions. All possible intermediate desorption energies are more endothermic than a hydrogen abstraction or surface re-oxidation of the same species for the oxidizing and reducing environments, leading to only fully oxidizing the propane to CO₂. For the extremely reducing environment the desorption of the C*C*C* species on the surface and the desorption of the first CO molecule will complete, with their 0 K desorption energies being very similar in energy. On three of the intermediate species during the reforming of propane over the Mn-doped CeO₂ surface there is a radical electron delocalized across multiple bonds between carbon and oxygen atoms.

ACKNOWLEDGEMENTS: This material is based upon work supported as part of the Center for Atomic Level Design, an Energy Frontier Research Center funded by the U.S. Department of Energy, Office of Science, Office of Basic Energy Sciences under Award Number DE-SC0001058.

6.5. References

1. M. Abecassis-Wolfovich, M. V. Landau, A. Brenner, M. Herskowitz. *Journal of Catalysis* **2007**, *247*, 201-213.
2. H. F. Li, G. Z. Lu, Q. G. Dai, Y. Q. Wang, Y. Guo, Y. L. Guo. *Applied Catalysis B-Environmental* **2011**, *102*, 475-483.
3. M. D. Krcha, M. J. Janik. *Langmuir* **2013**, *29*, 10120-10131.
4. M. D. Krcha, A. D. Mayernick, M. J. Janik. *Journal of Catalysis* **2012**, *293*, 103-115.
5. R. Li, M. D. Krcha, M. J. Janik, A. D. Roy, K. M. Dooley. *Energy & Fuels* **2012**, *26*, 6765-6776.
6. D. Terribile, A. Trovarelli, C. de Leitenburg, A. Primavera, G. Dolcetti. *Catalysis Today* **1999**, *47*, 133-140.
7. D. Delimaris, T. Ioannides. *Applied Catalysis B-Environmental* **2008**, *84*, 303-312.
8. R. Li, A. Roy, J. Bridges, K. M. Dooley. *Industrial & Engineering Chemistry Research* **2014**, *53*, 7999-8011.
9. Y. N. Liao, M. L. Fu, L. M. Chen, J. L. Wu, B. C. Huang, D. Q. Ye. *Catalysis Today* **2013**, *216*, 220-228.
10. L. C. Hsu, M. K. Tsai, Y. H. Lu, H. T. Chen. *Journal of Physical Chemistry C* **2013**, *117*, 433-441.
11. M. L. Yang, Y. A. Zhu, C. Fan, Z. J. Sui, D. Chen, X. G. Zhou. *Journal of Molecular Catalysis A-Chemical* **2010**, *321*, 42-49.
12. M. L. Yang, Y. A. Zhu, C. Fan, Z. J. Sui, D. Chen, X. G. Zhou. *Physical Chemistry Chemical Physics* **2011**, *13*, 3257-3267.
13. K. Lee, E. Lee, C. Song, M. J. Janik. *Journal of Catalysis* **2014**, *309*, 248-259.
14. P. Gelin, M. Primet. *Applied Catalysis B-Environmental* **2002**, *39*, 1-37.

15. J. A. Labinger, J. E. Bercaw. *Nature* **2002**, *417*, 507-514.
16. G. C. Bond, D. T. Thompson. *Catalysis Reviews-Science and Engineering* **1999**, *41*, 319-388.
17. D. Knapp, T. Ziegler. *Journal of Physical Chemistry C* **2008**, *112*, 17311-17318.
18. A. D. Mayernick, M. J. Janik. *Journal of Physical Chemistry C* **2008**, *112*, 14955-14964.
19. A. D. Mayernick, M. J. Janik. *Journal of Catalysis* **2011**, *278*, 16-25.
20. W. Tang, Z. P. Hu, M. J. Wang, G. D. Stucky, H. Metiu, E. W. McFarland. *Journal of Catalysis* **2010**, *273*, 125-137.
21. L. H. Xiao, K. P. Sun, X. L. Xu, X. N. Li. *Catalysis Communications* **2005**, *6*, 796-801.
22. T. K. Das, E. L. Kugler, D. B. Dadyburjor. *Industrial & Engineering Chemistry Research* **2009**, *48*, 10796-10802.
23. C. deLeitenburg, A. Trovarelli, J. Llorca, F. Cavani, G. Bini. *Applied Catalysis a-General* **1996**, *139*, 161-173.
24. K. Alexopoulos, M. F. Reyniers, G. B. Marin. *Journal of Catalysis* **2012**, *289*, 127-139.
25. L. Cheng, G. A. Ferguson, S. A. Zygmunt, L. A. Curtiss. *Journal of Catalysis* **2013**, *302*, 31-36.
26. B. Beck, M. Harth, N. G. Hamilton, C. Carrero, J. J. Uhlrich, A. Trunschke, S. Shaikhutdinov, H. Schubert, H. J. Freund, R. Schlogl, J. Sauer, R. Schomacker. *Journal of Catalysis* **2012**, *296*, 120-131.
27. Y. Liu, Z. H. Li, J. Lu, K. N. Fan. *Journal of Physical Chemistry C* **2008**, *112*, 20382-20392.
28. M. D. Krcha, M. J. Janik. *Catalysis Science & Technology* **2014**, DOI: 10.1039/C4CY00619D.
29. M. R. Morales, F. N. Agüero, L. E. Cadus. *Catalysis Letters* **2013**, *143*, 1003-1011.
30. X. Y. Wang, Q. Kang, D. Li. *Applied Catalysis B-Environmental* **2009**, *86*, 166-175.

31. S. Colussi, A. Gayen, M. F. Camellone, M. Boaro, J. Llorca, S. Fabris, A. Trovarelli. *Angewandte Chemie-International Edition* **2009**, *48*, 8481-8484.
32. V. Shapovalov, H. Metiu. *Journal of Catalysis* **2007**, *245*, 205-214.
33. Z. P. Hu, H. Metiu. *Journal of Physical Chemistry C* **2011**, *115*, 17898-17909.
34. W. Cen, Y. Liu, Z. Wu, H. Wang, X. Weng. *Phys. Chem. Chem. Phys.* **2012**, *14*, 5769-5777.
35. A. Gupta, U. V. Waghmare, M. S. Hegde. *Chemistry of Materials* **2010**, *22*, 5184-5198.
36. Y. H. Tang, H. Zhang, L. X. Cui, C. Y. Ouyang, S. Q. Shi, W. H. Tang, H. Li, J. S. Lee, L. Q. Chen. *Physical Review B* **2010**, *82*, 125104.
37. G. Kresse, J. Furthmuller. *Computational Materials Science* **1996**, *6*, 15-50.
38. G. Kresse, J. Furthmuller. *Physical Review B* **1996**, *54*, 11169-11186.
39. G. Kresse, J. Hafner. *Physical Review B* **1993**, *47*, 558-561.
40. G. Kresse, D. Joubert. *Physical Review B* **1999**, *59*, 1758-1775.
41. J. P. Perdew, J. A. Chevary, S. H. Vosko, K. A. Jackson, M. R. Pederson, D. J. Singh, C. Fiolhais. *Physical Review B* **1992**, *46*, 6671-6687.
42. H. J. Monkhorst, J. D. Pack. *Physical Review B* **1976**, *13*, 5188-5192.
43. S. Fabris, S. de Gironcoli, S. Baroni, G. Vicario, G. Balducci. *Physical Review B* **2005**, *71*, 041102.
44. S. Fabris, S. de Gironcoli, S. Baroni, G. Vicario, G. Balducci. *Physical Review B* **2005**, *72*, 237102.
45. G. Kresse, P. Blaha, J. L. F. Da Silva, M. V. Ganduglia-Pirovano. *Physical Review B* **2005**, *72*, 237101.
46. A. D. Mayernick, M. J. Janik. *Journal of Chemical Physics* **2009**, *131*, 084701.
47. M. Nolan, V. S. Verdugo, H. Metiu. *Surface Science* **2008**, *602*, 2734-2742.

48. M. Nolan, S. Grigoleit, D. C. Sayle, S. C. Parker, G. W. Watson. *Surface Science* **2005**, 576, 217-229.
49. D. G. Pintos, A. Juan, B. Irigoyen. *Journal of Physical Chemistry C* **2013**, 117, 18063-18073.
50. M. Nolan, S. C. Parker, G. W. Watson. *Surface Science* **2005**, 595, 223-232.
51. L. Wang, T. Maxisch, G. Ceder. *Physical Review B* **2006**, 73, 195107.
52. J. A. Dean. *Lange's Handbook of Chemistry*. 15th ed.; McGraw-Hill, Inc.: 1999.

Chapter 7

Ce-Mn Oxides for High-Temperature Gasifier Effluent Desulfurization

This chapter was partially published as: R. Li, M. D. Krcha, M. J. Janik, A. D. Roy, K. M. Dooley. *Energy & Fuels* 2012, 26, 6765-6776.

ABSTRACT: $\text{MnO}_x - \text{CeO}_x$ mixed oxides can be used as high-temperature desulfurization sorbents. Our collaborators at Louisiana State University measured the sulfur capacities of various Mn/Ce ratios mixed with other oxides using a synthetic syngas mixture. A high sulfur capacity sorbent with low pre-breakthrough of H_2S is realized. Their XANES analysis identified the oxidation states of Ce and Mn in the calcined and sulfided (reduced) samples. Utilizing density functional theory, we determine that the high sulfur capacity of $\text{MnO}_x/\text{CeO}_x$ is a result of Mn lowering the oxygen vacancy formation energy of CeO_2 . Additionally, a larger number of active sites for sulfur adsorption are available due to manganese's ability to access multiple oxidation states compared to other dopants.

7.1. Introduction

H₂S can be adsorbed from the effluent of biomass gasification at high temperatures using mixed rare-earth oxides (REOs), like CeO₂/La₂O₃.¹⁻⁵ To adsorb sulfur using CeO₂, oxygen vacancies in ceria must be present.⁶ Pure ceria sulfides slowly with a mixture of H₂S/H₂, but the rate can be increased by an order of magnitude if it is mixed with another oxide, such as La₂O₃. To further stabilize the surface under repetitive redox reactions and to prevent REO crystal growth, ceria can be mixed with ZrO₂, Tb₂O₃, Gd₂O₃ or Al₂O₃.⁷⁻¹⁷ These mixed ceria-based oxides display rapid adsorption and an increased sulfur capacity compared to pure oxides, yet they do not meet the desired capacity.

MnO_x has the highest initial rate for sulfur adsorption of all pure oxides tested.¹⁸ MnO_x/Al₂O₃ had 100% initial oxide utilization and a high sulfur capacity with a synthetic syngas mixture at 770 to 970 K.¹⁹ During air regeneration of the sorbent, manganese sulfate is formed and is stable below 1070 K,²⁰ and this therefore causes problems for using MnO_x-based sorbents over the long-term. To partially alleviate this regeneration problem, MnO_x can be supported on Al₂O₃. However, when MnO_x is supported on Al₂O₃, formation of MnAl₂O₄ can occur and the sample cannot be fully sulfided, except above 1070 K.²¹ Unsupported MnO_x can adsorb more sulfur compared to the supported case;²¹ however, MnO_x supported on Al₂O₃ can rapidly react with sulfur and can be regenerated with air at 1073 K.²² Cycling MnO_x/Al₂O₃ for 300 cycles using a syngas mixture deactivated during the first 10 cycles.²³

Herein, we use a combination of the thermal stability and low H₂S equilibrium concentration of mixed REOs with the rapid sulfidation kinetics and high sulfur capacity of MnO_x to create a better sulfur sorbet from gasification effluent. Recently, mixtures of MnO_x and REOs have been shown to significantly outperform other mixed REOs in sulfur capacity using a model syngas effluent.^{1,24} Our collaborators examined the mixed MnO_x and REO mixture over a range of

MnO_x compositions and determine its sulfur capacities using a stream closely resembling the composition of effluent from a gasifier. X-ray adsorption near-edge spectroscopy (XANES) and density functional theory (DFT) are combined to understand the role Mn plays in the increased adsorption capacity of MnO_x/REO mixtures.

7.2. Methods

Calculations were carried out using the Vienna *ab initio* simulation program (VASP), an *ab initio* total energy and molecular dynamics program developed at the Institute for Material Physics at the University of Vienna.²⁵⁻²⁷ The projector augmented wave (PAW) method was used to represent the core region.²⁸ The valence electrons were represented with a tractable plane-wave basis set with an energy cutoff of 450 eV. Valence configurations were $5s^25p^66s^24f^15d^1$ for ceria, $2s^22p^4$ for oxygen, $1s^1$ for hydrogen, $3s^23p^4$ for sulfur, and $3d^64s^1$ for Mn. Structural optimizations were performed by minimizing the forces on all atoms to below $0.05 \text{ eV}\cdot\text{\AA}^{-1}$; k -point sampling of $(2 \times 2 \times 1)$ was performed using the Monkhorst Pack scheme,²⁹ with the third vector perpendicular to the surface. All calculations were spin polarized. The Perdew-Wang (PW91) version of the generalized gradient approximation (GGA) was used to incorporate exchange and correlation energies.³⁰

DFT has difficulties in representing the nature of the $4f$ orbitals of ceria,³¹⁻³³ hence we implemented the DFT+ U approach.³⁴⁻³⁵ The DFT+ U approach introduces the Hubbard U -term as an on-site Coulombic interaction in the f states of ceria, which localizes $4f$ electrons on Ce³⁺ in reduced ceria. A U -value of 5 was utilized, which is consistent with values used in previous DFT studies of ceria.^{6,36-45} Absolute reduction energies are a function of the U -value, though relative trends in reduction energies are preserved with varying U .⁴⁵ DFT also has difficulties representing electrons in localized d -states of metal oxides.⁴⁶⁻⁴⁷ As shown in Chapter 4 and other studies, the

inclusion of a U -term on the d -states of Mn becomes necessary to correctly represent the electronic structure of Mn doped in ceria.⁴⁸⁻⁴⁹ A U -value of 4 on the d -states of Mn is utilized as described by Wang, Maxish and Cedar.⁴⁶

A Mn-doped fluorite CeO_2 (1 1 1) surface model is used to examine the impact of Mn doping on surface reducibility and sulfur adsorption. The choice of a Mn-doped fluorite phase is motivated by characterization results presented below. The surface models used for ceria were mirrored 12-layer slabs doped with Mn. The (1 1 1) termination of ceria was used because it is the lowest energy surface of ceria.^{45,49-50} All atom positions are relaxed during structural optimizations. Though the XANES measurements, which are compared with DFT results, potentially measure bulk reduction processes, a surface model is used because of our direct desire to capture surface behavior of H_2S adsorption. We previously demonstrated surface energetics of H_2S adsorption as empirically relevant to predicting dopant effects on H_2S adsorption capacity.⁶ All structural optimizations and relative energy definitions follow the same procedure as described previously.^{6,49}

Details of the experimental procedures, including sample preparation, used by our collaborators are given in our full paper.⁵¹

7.3. Results and Discussion

7.3.1. Experimental Results

Table 7-1 contains the sample names, along with some of the basic properties of the samples (surface area and pre-breakthrough of H_2S). Figure 7-1 contains the sulfur adsorption capacities for a number of different mixtures of ceria with manganese oxide, zirconia, alumina, terbium oxide, lanthanum oxide, and gadolinium oxide. The adsorption capacities are an average of at least three adsorption/regeneration cycles. A synthetic syngas mixture was used with 1000

ppm sulfur and 32% CO₂. MnO_x supported on alumina has one of the lowest sulfur capacities of all samples tested due to the formation of manganese sulfate during sorbent regeneration. CeO₂ has a lower equilibrium pre-breakthrough H₂S concentration, but has a low and stable sulfur capacity. Combining MnO_x with CeO₂ yields the low pre-breakthrough of H₂S and the higher sulfur capacity of MnO_x. The sulfur capacity of Mn12/Ce3/La is much greater than expected based on a linear combination of CeO₂-La₂O₃ and MnO_x. The addition of either Tb or Gd to the sorbent did not further increase the sulfur capacity.

Table 7-1. Sample Names and Basic Properties.

Designation and Molar Ratios (wt % Al ₂ O ₃)	Surface area (m ² /g)		Pre-breakthrough H ₂ S (ppmv)
	As Calcined	Used ^a	
CeO ₂	220	190	10
Ce6/Tb	200	76	
Mn0.8/Al (75) ^b	150	120	
Mn1/Ce1	55	15	
Mn1/Ce4	150	59	
Mn4/Ce3/La	83	30	
Mn12/Ce3/La	60	10	13
Mn1.1/Ce3/La/Gd0.05	130	50	4.5
Mn1.4/Ce6/La/Gd0.10	190	12	
Mn0.8/Ce3/La/Al (89)	210	200	4.1
Mn0.4/Ce3/Zr/Al (81)	180	180	

^aUsed for at least three cycles of adsorption/regeneration. ^bValues in parentheses are wt % Al₂O₃ in supported materials.

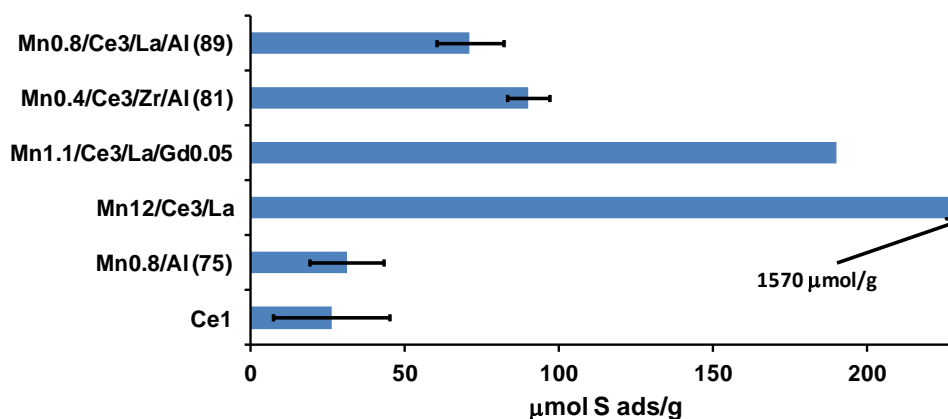


Figure 7-1. Sulfur adsorption capacity at 903 K using a synthetic gasifier effluent with 32% CO_2 . All capacities are the average of three cycle, not using the first cycle. Air regeneration was used at 873 K for 30 minutes. The numbers in parentheses are the wt% Al_2O_3 for supported materials.

In the Ce L_{III} XANES spectra (not shown here) there are fewer reduced cerium atoms (Ce^{3+}) in the as calcined or air regenerated samples, and far more reduced cerium in the sulfided (reduced) state. In the Mn-doped samples, there are more reduced cerium atoms compared to samples without Mn in the same state, with approximately three times more Ce^{3+} atoms in the Mn-doped samples. Figure 7-2 contains the Mn K-edge XANES results. The spectrum for the sulfided (reduced) sample of Mn0.8/Ce3/La/Al shows evidence that Mn is in a 2+ oxidation state based upon the center of the pre-edge, and the XRD suggests Mn is in a tetrahedral arrangement. In the calcined sample of Mn4/Ce3/La (not shown), the pre-edge region is more consistent with Mn^{2+} , however the breadth of the region suggests the presence of Mn^{3+} as well.

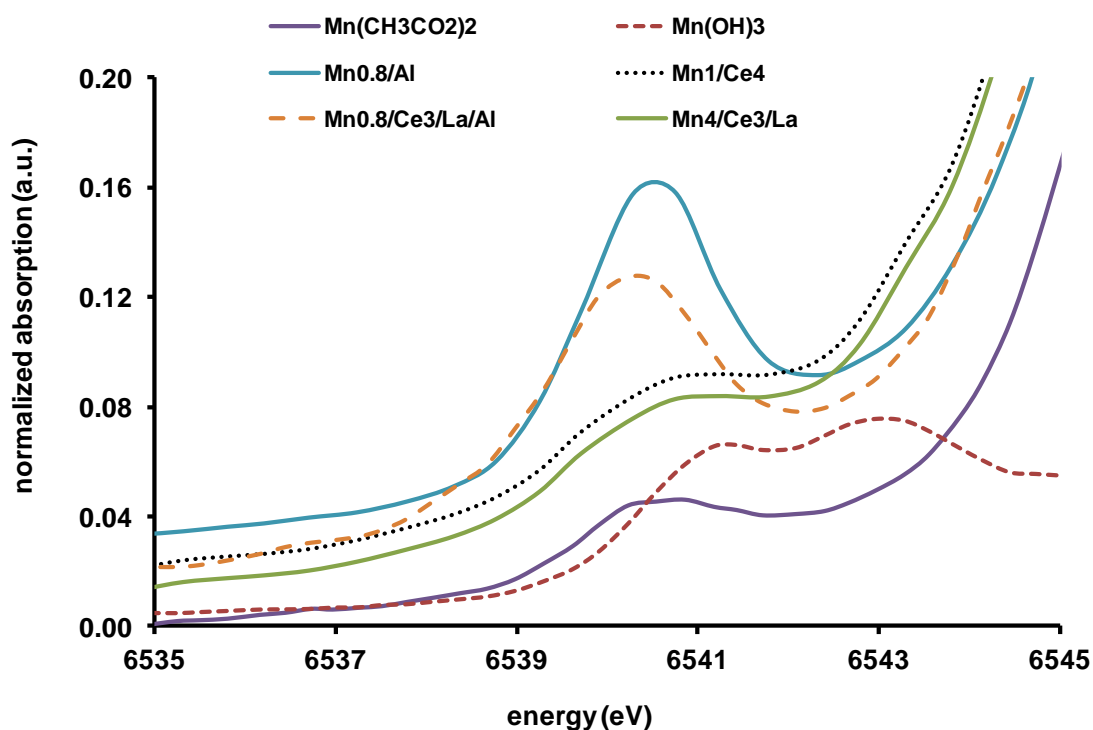


Figure 7-2. Normalized XANES spectra of Mn K pre-edge region. All samples were sulfided and reduced for several cycles prior to analysis.

7.3.2. DFT Results

In previous DFT modeling, we have found that the conversion of a CeO_2 (1 1 1) surface to an oxysulfide follows the formation of oxygen vacancies, with H_2S activated over an O vacancy and S eventually incorporated into a vacancy site. The addition of La^{3+} doped into CeO_2 promotes excess reduction to Ce^{3+} over a wide range of temperatures. Our DFT work shows that H_2S adsorbs and dissociates over sub-stoichiometric oxygen vacancies, and is rate-limited by a strongly endergonic molecular adsorption (low coverage) of H_2S . DFT-computed free energy and phase diagrams showed that sulfur incorporation is only favorable if multiple adjacent oxygen vacancies are present to accommodate the larger coordination shell of sulfur atoms.

Therefore it is not surprising that mixing MnO_x intimately with CeO_2 also greatly increased the sulfur capacity of a Mn-doped fluorite phase. Disordered, small particle CeO_2 , promoted by either Mn, Zr or La dopants, exhibits far more oxygen vacancies than larger particles of crystalline CeO_2 . The results of Figure 7-2 also suggest that Mn and La have synergistic (but not greatly so) effects on sulfur adsorption for the lower Mn-loading CeO_2 adsorbents. The lesser sulfur capacities for these materials when compared to the maximum theoretical capacities can be attributed to the poor diffusion of sulfide ions in the matrix, even as oxygen vacancies are eliminated by sulfur adsorption at the surface, coupled with the losses in surface area for those materials not supported on Al_2O_3 .

DFT calculations were used to examine the impact of Mn doping on CeO_2 (1 1 1) reducibility and H_2S adsorption. Models with one and two Mn doped into the CeO_2 (1 1 1) surface were considered. When one Mn atom is doped into the surface of CeO_2 , the Mn atom replaces one cerium atom in the 2x2 surface, as illustrated in Figure 7-3b. We refer to this structure as containing an “isolated” Mn dopant, as there are no O atoms bridging two Mn atoms. Doping two Mn atoms into the slab creates a non-isolated model, with one surface Ce atom and one sub-surface Ce atom replaced, as seen in Figure 7-3a.

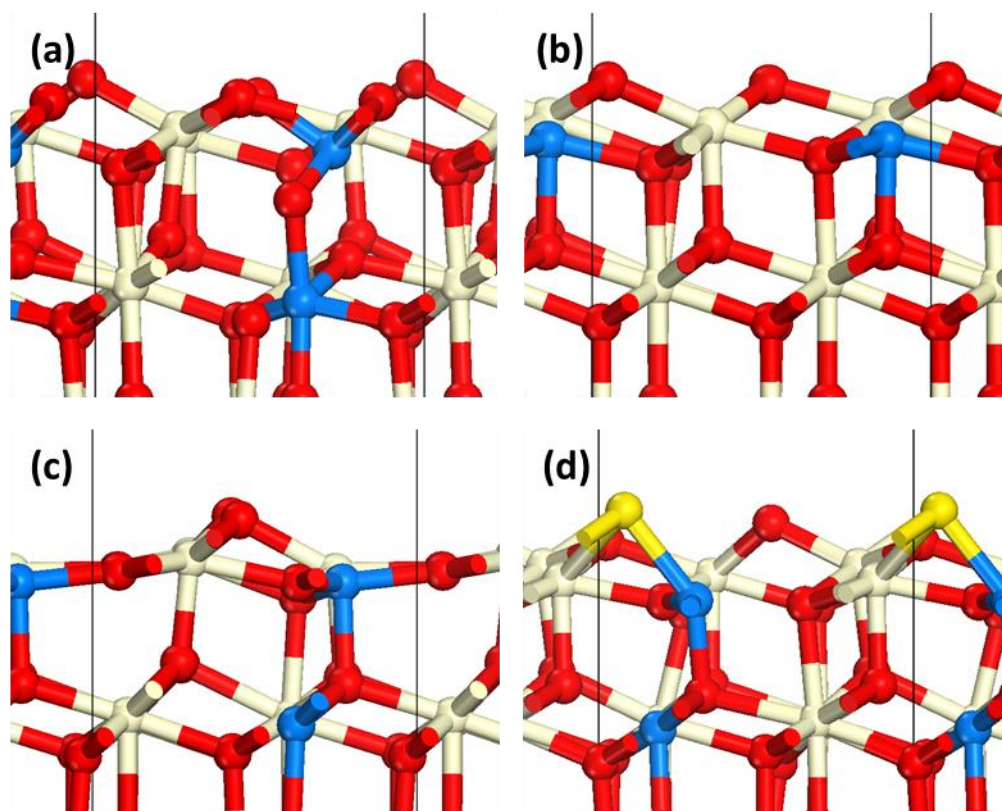


Figure 7-3. Side views of the surface unit cell for Mn-doped CeO₂ (1 1 1): (a) Intact 2 Mn-doped; (b) oxygen vacant 1 Mn-doped; (c) doubly oxygen vacant 2 Mn-doped; and (d) Sulfur adsorbed oxygen vacancy, 2 Mn-doped. Ce is displayed as tan (white), Mn as light blue (gray), O as red (dark), and S as yellow (light).

With two Mn atoms doped in the surface, the first surface oxygen vacancy is spontaneous, as evidenced by the exothermic vacancy formation energy given in Table 7-2. As vacancy formation, converting a surface oxygen atom to half an oxygen molecule, is driven entropically at non-zero temperatures, this spontaneous vacancy formation energy suggests that non-isolated Mn dopants will be accompanied by O vacancies following calcination. The two Mn atoms reduce to Mn³⁺ with the formation of this first oxygen vacancy, with oxidation states determined by atomic charge analysis as described previously. When one Mn atom is doped in the surface (isolated) the first oxygen vacancy formation energy is also slightly exothermic, and therefore likely present

following calcination. This oxygen vacancy reduces the surface Mn dopant to the Mn^{2+} oxidation state. In the Mn K-edge XANES, the calcined adsorbents Mn1/Ce4 and Mn4/Ce3/La contained Mn in both Mn^{2+} and Mn^{3+} states (Figure 7-2). This DFT analysis suggests Mn^{3+} species may result from Mn atoms that are non-isolated and Mn^{2+} may result from Mn atoms that are isolated. The spontaneity of “first vacancy” formation is consistent with the lack of Mn^{4+} observed in the as-calcined samples. These “first vacancies” reduce only Mn atoms, and no Ce^{4+} atoms are reduced to Ce^{3+} . The Ce L_{III} XANES spectra showed very little Ce^{3+} in the as-calcined samples, in agreement with the DFT calculations.

Table 7-2. Oxygen vacancy formation (ΔE_{vac}) and H_2S adsorption (ΔE_{ads}) energies for CeO_2 (1 1 1) with 1 Mn atom doped in the surface (isolated) and 2 Mn atoms doped in the surface (non-isolated), with one and two oxygen vacancies in the surface. The oxidation states of Mn are listed for each case, as well as the number of cerium atoms that reduce from Ce^{4+} to Ce^{3+} .

	Number of Vacancies	ΔE_{vac} (eV)	ΔE_{ads} (eV)	Oxidation State of Mn	Number of Ce atoms Reduced
1 Mn Dopant	0	-	-0.38	4+	0
	1	-0.14	-0.40	2+	0
	2	1.75	-1.40	2+	2
2 Mn Dopants	0	-	-0.27	4+	0
	1	-1.01	-0.49	3+	0
	2	1.69	-0.50	2+	0

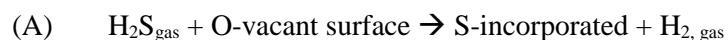
Forming a second surface oxygen vacancy with two doped Mn atoms reduces the Mn atoms from the Mn^{3+} to Mn^{2+} oxidation state. As given in Table 7-2, this second vacancy formation energy is endothermic. For an isolated Mn atom at the surface, the formation of a second surface oxygen vacancy does not reduce the Mn any further, instead reducing two Ce^{4+} atoms to Ce^{3+} , characterized by a positive oxygen vacancy formation energy. Though these second vacancy formation energies are significantly positive (Table 7-2), they are still substantially less than the first vacancy formation energy in the undoped CeO_2 (1 1 1) surface (+2.67 eV). In a reducing environment, the formation of both types of second oxygen vacancies will be entropically driven, further reducing non-isolated Mn atoms to the 2+ state and reducing some Ce^{4+} to Ce^{3+} states. The Mn XANES results did show reduction of Mn^{3+} to Mn^{2+} in the reduced/sulfided samples (Figure 7-2), which might be interpreted as the further reduction of Mn atoms that are non-isolated. The Ce XANES results showed more Ce^{3+} in the reduced sample, and TPR (not shown) indicated a greater reducibility of the Mn-doped sample compared to a non-doped sample. These results are in agreement with the DFT results, suggesting that vacancy formation beyond the initial reduction of Mn^{4+} accounts for the greater extent of reduction, affecting both Mn and Ce.

Table 7-2 also lists the H_2S adsorption energies to the Mn-doped CeO_2 (1 1 1) surfaces at various oxidation states. H_2S adsorption is considerably stronger to the vacant surfaces, further corroborating the role of O vacancies in desulfurization. We previously reported that stronger H_2S adsorption correlated with greater experimental sulfur capacities for un-doped, Tb-doped, and La-doped CeO_2 (1 1 1) surfaces, suggesting that the rate of uptake determined by the H_2S adsorption energy dictated ultimate sulfur capacity. However, all of the H_2S adsorption capacities listed in Table 7-2 are weaker than those for La- and Tb-doped CeO_2 (1 1 1), suggesting the further increases in Mn-doped ceria sulfur capacities cannot be attributed to a stronger H_2S adsorption.

The enhanced sulfur adsorption capacity of the Mn-doped system may instead arise from a greater number of “active” O-vacancy sites and a greater driving force to S^* formation at O-

vacancies. For La- and Tb-doped surfaces, each dopant pair forms a stoichiometric vacancy, allowing La and Tb to occupy 3+ oxidation states as opposed to the inaccessible 4+ state. The formation of “second oxygen vacancies” in the Mn system may be compared with the formation of sub-stoichiometric vacancies in the La- and Tb-doped systems. For the Mn doped system, the second vacancy formation energies are more favorable than the sub-stoichiometric vacancy formation energies in the La- and Tb-doped surfaces. Though additional vacancy formation in La- and Tb-doped surfaces was not examined, this result suggests the concentration of O vacancies will be greater in the Mn-doped system. Therefore, one explanation for the greater capacity of Mn-doped CeO₂ adsorbents is their greater reducibility compared to the Tb- and La-doped systems.

A second factor that may explain the enhanced Mn-doped ceria sulfur capacities is that a larger fraction of the vacancies formed may be considered as “active sites” for H₂S conversion. In the La- and Tb-doped surfaces, the first stoichiometric vacancy is not active for H₂S conversion to S*, as such activation would require these dopants to occupy a 4+ oxidation state. However, the 4+ oxidation state is accessible for Mn-dopants, providing the possibility that this “first vacancy” can also be active for H₂S conversion. This possibility was evaluated computationally by considering the reaction energy of



where “S-incorporated” represents a surface with a S atom filling the oxygen vacancy. The reaction energy for this reaction was calculated considering the “first vacancy” for the Mn-doped surface and the stoichiometric vacancy for the La- and Tb-doped surfaces. Table 7-3 reports these reaction energies. For the La- and Tb-doped systems, these reaction energies are highly endothermic, indicating that the stoichiometric vacancies cannot serve as active sites for H₂S conversion. For the isolated Mn-doped system, this reaction energy is exothermic, whereas it is mildly endothermic for

the non-isolated doped system. For the Mn-doped system, these “first vacancies” can serve as active sites, with H₂S adsorption and S incorporation reasonably favorable. Though these sites would be active for H₂S conversion, we would not expect to observe Mn⁴⁺ in highly sulfided samples (and indeed did not), because S incorporation would engender further surface reduction, as vacancy formation from this S-incorporated surface would be highly favorable. Table 7-2 also indicates that “first vacancies” would also be active for the pure CeO₂ (1 1 1) surface, however, the concentration of these vacancies would be considerably reduced compared to the doped surface, due to the substantially higher vacancy formation energy.

Table 7-3. Reaction energies ($\Delta E_{\text{reaction}}$, in eV) for conversion of H₂S_{gas} and O-vacant surfaces to H₂gas and an S-incorporated surface (Reaction A).

Surface	$\Delta E_{\text{reaction}}$
CeO ₂ (111)	-0.51
La ₂ -doped CeO ₂ (111)	2.21
Tb ₂ -doped CeO ₂ (111)	2.33
Mn ₁ -doped CeO ₂ (111)	-1.31
Mn ₂ -doped CeO ₂ (111)	0.67

7.4. Conclusions

Combining MnO_x with CeO_2 yields a sulfur sorbent with low pre-breakthrough H_2S from CeO_2 and the high sulfur capacity from MnO_x , but with higher than expected sulfur capacities. XANES shows the presence of Mn^{3+} and Mn^{2+} in as calcined samples and after sulfidation, XANES shows Mn^{2+} and Ce^{3+} . Two reasons, based on insight from DFT, why Mn-doped CeO_2 (1 1 1) has a higher sulfur capacity compared with ceria doped with other oxides, is the ability of Mn to decrease the oxygen vacancy formation energy of CeO_2 and the favorable H_2S adsorption energies, even without sub-stoichiometric oxygen vacancies. The favorable H_2S adsorption energy without sub-stoichiometric oxygen vacancies leads to a larger number of active sites for H_2S adsorption compared to other dopants, due to manganese's ability to access multiple oxidation states.

ACKNOWLEDGEMENTS: This material is based upon work supported as part of the Center for Atomic Level Design, an Energy Frontier Research Center funded by the U.S. Department of Energy, Office of Science, Office of Basic Energy Sciences under Award Number DE-SC0001058.

7.5. References

1. K. M. Dooley, V. Kalakota, S. Adusumilli. *Energy & Fuels* **2011**, *25*, 1213-1220.
2. K. B. Yi, E. J. Podlaha, D. P. Harrison. *Industrial & Engineering Chemistry Research* **2005**, *44*, 7086-7091.
3. Y. Zeng, S. Kaytakoglu, D. P. Harrison. *Chemical Engineering Science* **2000**, *55*, 4893-4900.
4. Y. Zeng, S. Zhang, F. R. Groves, D. P. Harrison. *Chemical Engineering Science* **1999**, *54*, 3007-3017.
5. M. Kobayashi, M. Flytzani-Stephanopoulos. *Industrial & Engineering Chemistry Research* **2002**, *41*, 3115-3123.
6. A. D. Mayernick, R. Li, K. M. Dooley, M. J. Janik. *Journal of Physical Chemistry C* **2011**, *115*, 24178-24188.
7. M. Pijolat, M. Prin, M. Soustelle, O. Touret, P. Nortier. *Journal of the Chemical Society, Faraday Transactions* **1995**, *91*, 3941-3948.
8. P. D. L. Mercera, J. G. v. Ommen, E. B. M. Doesburg, A. J. Burggraaf, J. R. H. Ross. *Applied Catalysis* **1991**, *71*, 363-391.
9. A. Martinez-Arias, A. B. Hungria, M. Fernandez-Garcia, A. Iglesias-Juez, J. C. Conesa, G. C. Mather, G. Munuerac. *Journal of Power Sources* **2005**, *151*, 43-51.
10. F. Ye, T. Mori, D. R. Ou, J. Zou, G. Auchterlonie, J. Drennan. *Solid State Ionics* **2008**, *179*, 827-831.
11. X. Wang, J. C. Hanson, G. Liu, J. A. Rodriguez, A. Iglesias-Juez, M. Fernandez-Garcia. *Journal of Chemical Physics* **2004**, *121*, 5434-5444.
12. G. Zhou, P. R. Shah, T. Kim, P. Fornasiero, R. J. Gorte. *Catalysis Today* **2007**, *123*, 86-93.

13. B. M. Reddy, P. Saikia, P. Bharali, S.-E. Park, M. Muhler, W. Grunert. *Journal of Physical Chemistry C* **2009**, *113*, 2452–2462.
14. S. Bernal, G. Blanco, G. A. Cifredo, J. J. Delgado, D. Finol, J. M. Gatica, J. M. Rodriguez-Izquierdo, H. Vidal. *Chemistry of Materials* **2002**, *14*, 844-850.
15. A. Trovarelli, F. Zamar, J. Llorca, C. de Leitenburg, G. Dolcetti, J. T. Kiss. *Journal of Catalysis* **1997**, *169*, 490-502.
16. G. Colon, M. Pijolat, F. Valdivieso, H. Vidal, J. Kaspar, E. Finocchio, M. Daturi, C. Binet, J. C. Lavalley, R. T. Baker, S. Bernal. *Journal of the Chemical Society, Faraday Transactions* **1998**, *94*, 3717-3726.
17. M. A. Malecka, L. Kepinski, W. Mista. *Applied Catalysis B: Environmental* **2007**, *74*, 290-298.
18. P. R. Westmoreland, D. P. Harrison. *Environmental Science & Technology* **1976**, *10*, 659-661.
19. T. H. Ko, H. Chu, L. K. Chaung. *Chemosphere* **2005**, *58*, 467-474.
20. E. Garcia, J. M. Palacios, L. Alonso, R. Moliner. *Energy and Fuels* **2000**, *14*, 1296-1303.
21. W. J. W. Bakker, F. Kapteijn, J. A. Moulijn. *Chemical Engineering Journal* **2003**, *96*, 223-235.
22. E. Turkdogan, R. Olsson, J. Vinters. *Metallurgical and Materials Transactions B* **1977**, *8*, 59-65.
23. J. P. Wakker, A. W. Gerritsen, J. A. Moulijn. *Industrial & Engineering Chemistry Research* **1993**, *32*, 139-149.
24. S. Yasyerli. *Chemical Engineering and Processing* **2008**, *47*, 577-584.
25. G. Kresse, J. Furthmuller. *Computational Materials Science* **1996**, *6*, 15-50.
26. G. Kresse, J. Furthmuller. *Physical Review B* **1996**, *54*, 11169-11186.
27. G. Kresse, J. Hafner. *Physical Review B* **1993**, *47*, 558-561.

28. G. Kresse, D. Joubert. *Physical Review B* **1999**, *59*, 1758-1775.
29. H. J. Monkhorst, J. D. Pack. *Physical Review B* **1976**, *13*, 5188-5192.
30. J. P. Perdew, J. A. Chevary, S. H. Vosko, K. A. Jackson, M. R. Pederson, D. J. Singh, C. Fiolhais. *Physical Review B* **1992**, *46*, 6671-6687.
31. S. Fabris, S. de Gironcoli, S. Baroni, G. Vicario, G. Balducci. *Physical Review B* **2005**, *71*, 041102.
32. S. Fabris, S. de Gironcoli, S. Baroni, G. Vicario, G. Balducci. *Physical Review B* **2005**, *72*, 237102.
33. G. Kresse, P. Blaha, J. L. F. Da Silva, M. V. Ganduglia-Pirovano. *Physical Review B* **2005**, *72*, 237101.
34. V. I. Anisimov, O. Gunnarsson. *Physical Review B* **1991**, *43*, 7570-7574.
35. J. F. Herbst, R. E. Watson, J. W. Wilkins. *Physical Review B* **1978**, *17*, 3089-3098.
36. Y. Chen, J. Cheng, P. Hu, H. F. Wang. *Surface Science* **2008**, *602*, 2828-2834.
37. Y. Chen, P. Hu, M. H. Lee, H. F. Wang. *Surface Science* **2008**, *602*, 1736-1741.
38. N. C. Hernandez, R. Grau-Crespo, N. H. de Leeuw, J. F. Sanz. *Physical Chemistry Chemical Physics* **2009**, *11*, 5246-5252.
39. M. Nolan. *Journal of Chemical Physics* **2009**, *130*, 144702.
40. Z. X. Yang, G. X. Luo, Z. S. Lu, K. Hermansson. *Journal of Chemical Physics* **2007**, *127*, 074704.
41. Z. X. Yang, Z. M. Fu, Y. N. Zhang, R. Q. Wu. *Catalysis Letters* **2011**, *141*, 78-82.
42. H. T. Chen, J. G. Chang. *Journal of Chemical Physics* **2010**, *132*, 214702.
43. A. D. Mayernick, M. J. Janik. *Journal of Chemical Physics* **2009**, *131*, 084701.
44. A. D. Mayernick, M. J. Janik. *Journal of Catalysis* **2011**, *278*, 16-25.
45. A. D. Mayernick, M. J. Janik. *Journal of Physical Chemistry C* **2008**, *112*, 14955-14964.
46. L. Wang, T. Maxisch, G. Ceder. *Physical Review B* **2006**, *73*, 195107.

47. Z. X. Yang, Q. G. Wang, S. Y. Wei. *Physical Chemistry Chemical Physics* **2011**, *13*, 9363-9373.
48. W. L. Cen, Y. Liu, Z. B. Wu, H. Q. Wang, X. L. Weng. *Physical Chemistry Chemical Physics* **2012**, *14*, 5769-5777.
49. M. D. Krcha, A. D. Mayernick, M. J. Janik. *Journal of Catalysis* **2012**, *293*, 103-115.
50. M. Nolan, S. C. Parker, G. W. Watson. *Surface Science* **2005**, *595*, 223-232.
51. R. Li, M. D. Krcha, M. J. Janik, A. D. Roy, K. M. Dooley. *Energy & Fuels* **2012**, *26*, 6765-6776.

Chapter 8

Alkane Reforming on Partially Sulfided CeO₂ (1 1 1) Surfaces

ABSTRACT: Cleanup of biomass gasification effluent requires a catalyst that can reform methane and larger hydrocarbons while tolerating the presence of H₂S or, ideally acting as a sulfur sorbent while reforming hydrocarbons. We utilize density functional theory (DFT) methods to examine the impact of oxide sulfidation on the reforming of methane and the initial steps of propane reforming, using M-doped CeO₂ catalysts. On a ceria oxy-sulfide surface, surface oxygen atoms remain active for C-H bond activation via hydride abstraction whereas surface sulfur atoms are significantly less active. Methyl adsorption slightly favors a surface sulfur site, and through subsequent dehydrogenation steps remain viable, the final steps of methane decomposition lead to carbon buildup on the surface. Collectively, surface sulfur sites will be less active for the initial rate limiting H abstraction step and can nucleate carbon buildup. The extent of reduction in the ceria surface is also examined along the methane decomposition path.

8.1. Introduction

Cleanup of gasifier effluents requires both reforming of hydrocarbons and removal of sulfur species. A single material capable of performing both cleanup steps at gasifier effluent temperatures would aid process integration.¹⁻² $\text{MO}_x\text{-CeO}_2$ materials can be used to absorb sulfur³⁻⁸ as well as reform hydrocarbons.⁸⁻¹³ These two processes have mostly been studied independently from one another on oxides, though reforming in the presence of sulfur species has been examined on metal catalysts.¹⁴⁻¹⁵ There are several studies (both experimental and computational) examining hydrocarbon reforming over ceria, with most of them focused on methane.^{9-13,16-18} The overall mechanism to reform methane over a ceria surface is established,^{11,19-20} however, the impact of each intermediate on the extent of surface reduction is not well established. The adsorption of sulfur using M-doped ceria has also been examined using both experimental and computational techniques.³⁻⁷ Dooley and coworkers recently examined the impact of partial sulfidation of an oxide on reforming catalysis chemistry on ceria.⁸ The mechanistic impact of partial sulfidation on hydrocarbon conversion catalyzed by CeO_x and $\text{MO}_x\text{-CeO}_x$ remains unclear. We use density functional theory (DFT) to examine the reforming of methane, in addition to the initial steps in the reforming of propane, over M-doped ceria with sulfur present in the surface. We further establish the electronic reduction state of the ceria surface with methyl intermediates (CH_3 , CH_2 , CH and C) adsorbed, both with and without sulfur present in the surface.

Currently biomass gasification cleanup process first remove sulfur from the effluent then reform the methane and other larger hydrocarbons.¹⁻² Sulfur typically has to be removed prior to catalysis processes due its corrosive nature and its poisoning of many industrial catalysts. In gasifier effluent cleanup, the absorption step is typically performed at temperatures lower than those coming off the gasifier and subsequent catalysis steps, leading to process energy inefficiencies.¹ M-doped ceria has shown promise as a high temperature sulfur sorbent³⁻⁷ as well as a hydrocarbon

reforming catalyst.^{9-13,16-18} Li et al. recently examined the reforming of tar ($C_{10}H_8$) with and without H_2S present over mixed oxides with ceria.⁸ The presence of sulfur (H_2S) caused a partial deactivation of the catalyst for reforming of tars, though catalysts remained active for several turnovers. Mn-doped supported REOs showed promise for tar reforming in the presence of sulfur as they exhibited high sulfur tolerance, less coking and less methanation than the typical Ni-based reforming catalysts.

Ceria absorbs sulfur, forming oxy-sulfides, and doping ceria can increase its sulfur capacity.³⁻⁷ CeO_2-ZrO_2 has a higher sulfur capacity compared to CeO_2 alone and the additional sulfur capacity is thought to be a result of the increased surface area of CeO_2-ZrO_2 compared to pure ceria.⁷ $Ce_{0.7}La_{0.3}O_y$ has a greater sulfur capacity than either pure CeO_2 or pure La_2O_3 .⁵ The addition of either MnO_x or FeO_x to CeO_2/La_2O_3 mixtures further increases the sulfur capacity.⁶ Our group previously applied DFT methods to show that the greater sulfur capacity of La-doped CeO_2 compared to pure ceria is a result of the activation barrier of the H_2S adsorption and dissociation and can be associated with the fast surface kinetics over La-doped CeO_2 .⁴ We have also shown that Mn-doped CeO_2 has an even greater sulfur capacity compared to La-doped CeO_2 , which is a result of having more active oxygen vacancies for the adsorption of H_2S in those vacancies.³

To our knowledge, DFT has not been previously employed to consider how the presence of sulfur affects the hydrocarbon oxidation/reforming ability of metal oxides. DFT studies have examined how sulfur affects hydrocarbon reforming over metals.¹⁴⁻¹⁵ The presence of sulfur on Ni (1 1 1) will deactivate the step sites on Ni, leaving only terrace sites active for the activation of methane.¹⁴ Rh has a low sulfur resistance, which can be improved with the addition of Ni forming a bimetallic surface.¹⁵

Our previous DFT work has established the rate limiting step for the oxidation of methane on pure and M-doped CeO_2 to be the initial abstraction of a hydrogen from methane.^{16,19} This step reduces the surface, converting M^{n+} atoms to $M^{(n-1)+}$ through occupation of an electron in a localized

d- or *f*-orbital. Depending upon the dopant in the surface of ceria, the dopant can either alter the reducibility of cerium atoms or become the reduction center. Whether it becomes the reduction center or alters the reducibility, all transition metal dopants lower the activation barrier compared to pure ceria.¹⁷ We have also established the reforming mechanism for propane over Zr-doped CeO₂.¹⁸

In our previous work with pure, La-, Tb-, and Mn-doped ceria (1 1 1) surfaces, we established the thermodynamic equilibrium in the presence of biomass gasifier effluent to be CeO_{1.25}S_{0.25} for pure ceria and M_{0.25}Ce_{0.75}O_{1.25}S_{0.25} for M-doped ceria.³⁻⁴ The equilibrium CeO₂ (1 1 1) surface has one surface oxygen atom replaced by a sulfur atom, with one surface and one subsurface oxygen vacancy. The M-doped ceria structure also has one surface oxygen atom replaced with a sulfur atom with two oxygen vacancies, one surface and one subsurface, and two of the cerium atoms substitutionally replaced with the dopant atom (one surface and one subsurface).³⁻⁴ Further sulfidation of the surface and subsurface layers is endogenic, such that this reduced oxysulfide surface would be stable under gasifier effluent conditions.

Herein, we utilize the aforementioned thermodynamically stable surface models to compare the reforming of methane and the initial steps of reforming propane over sulfided and unsulfided pure and M-doped CeO₂ (1 1 1) (M = La, Tb, Mn). Our initial structure contains one subsurface oxygen vacancy with no surface oxygen vacancies, so the catalyst will cycle between having a surface oxygen vacancy and not having a surface oxygen vacancy. We show that the initial steps for the reforming of methane over the sulfided surfaces (methyl group bound to sulfur) are similar in energy and only the later oxidation steps are energetically impacted compared to the unsulfided surfaces. We also further examine how the state of the reduction of the ceria surface changes along the methane reforming path.

8.2. Methods

8.2.1. Electronic structure method

Calculations were carried out using the Vienna *ab initio* simulation program (VASP), an *ab initio* total energy, and molecular dynamics program developed at the Institute for Material Physics at the University of Vienna.²¹⁻²³ A plane wave basis set was used to represent the valence electrons with a cutoff of 450 eV. The core region was represented using the projector augmented wave (PAW) method.²⁴ The valence configurations were $5s^25p^66s^24f^15d^1$ for cerium, $5s^25p^65d^16s^2$ for lanthanum, $4f^9$ for terbium, $3d^64s^1$ for manganese, $2s^22p^4$ for oxygen, $3s^23p^4$ for sulfur, $2s^22p^2$ for carbon, and $1s^1$ for hydrogen. All DFT calculations were spin polarized. The exchange and correlations energies were represented using the Perdew-Wang (PW91) version of the generalized gradient approximation (GGA).²⁵ The Monkhorst Pack k -point sampling scheme was utilized with a $(2 \times 2 \times 1)$ grid, with the third vector perpendicular to the surface.²⁶ All forces were converged to $0.05 \text{ eV} \cdot \text{\AA}^{-1}$ for structural optimizations, and previously a force criteria of $0.02 \text{ eV} \cdot \text{\AA}^{-1}$ was tested and both the structures and energetics were converged at the coarser value.¹⁷

We implemented the DFT+ U approach due to well established difficulties that DFT has in representing the nature of the $4f$ orbitals of cerium.²⁷⁻²⁹ A Hubbard U -correction adds an on-site Coulombic interaction term that penalizes non-integer occupation of localized orbitals.³⁰⁻³¹ This correction effectively penalizes the delocalization of Ce f electrons. We utilized a U -value of 5 eV on the f orbitals of cerium which is consistent with previous DFT studies of ceria.^{9-13,16-20,32-34} The oxygen vacancy formation and methane activation energies depend on the value of U chosen for the f -states of Ce in CeO_2 and $\text{M}_x\text{Ce}_{1-x}\text{O}_2$. The two energies increase in exothermicity linearly with increasing the U -value on the f -states of Ce, though there is only a slight slope when the M atom serves as the reduction center.¹⁶ With the dependence of vacancy formation and methane activation

energies on the chosen U -value, the quantitative analysis presented herein is U -dependent. Utilizing a U -value of 5 eV provides an accurate description of the electronic structure of reduced ceria and provides reliable qualitative results for alkane adsorption with and without sulfur present.

DFT with typical GGA exchange-correlation functions is also known to have difficulties representing localized d -states on metal oxides.³⁵⁻³⁶ Therefore, we included a U -value of 4 eV on the d -states of Mn. This U -value correctly predicts the oxidation states for Mn in the intact and oxygen vacant surfaces, as shown through comparison with XANES results, and provides a relative energy between Mn^{2+} and Mn^{3+} states in agreement with HSE06 hybrid functionals.³⁷ We did not include a U -value on either the La or Tb dopants, because these dopants retain their 3+ oxidation state throughout the hydrocarbon oxidation catalytic process.

8.2.2. Surface models

The cubic fluorite structure of ceria is utilized as in our previous studies^{3-4,16-19,37} and the bulk lattice constant is reproduced within 1% of experimental values.¹⁶ A $p(2 \times 2)$ ($\text{Ce}_{16}\text{O}_{32}$) unit cell expansion (Figure 8-1) is used with 4 CeO_2 layers (12 atomic layers) which are converged to surface formation and oxygen vacancy formation energies. Mirrored slabs were used to minimize the slab-to-slab interactions that could result from a net surface dipole due to reduction of metal atoms. The (1 1 1) surface is used because it is the lowest energy surface among single crystal terminations of ceria.^{16,38-39} This termination of ceria results in four oxygen atoms per side of the unit cell and four cerium atom in the layer below. 15 Å of vacuum space is utilized perpendicular to the surface.

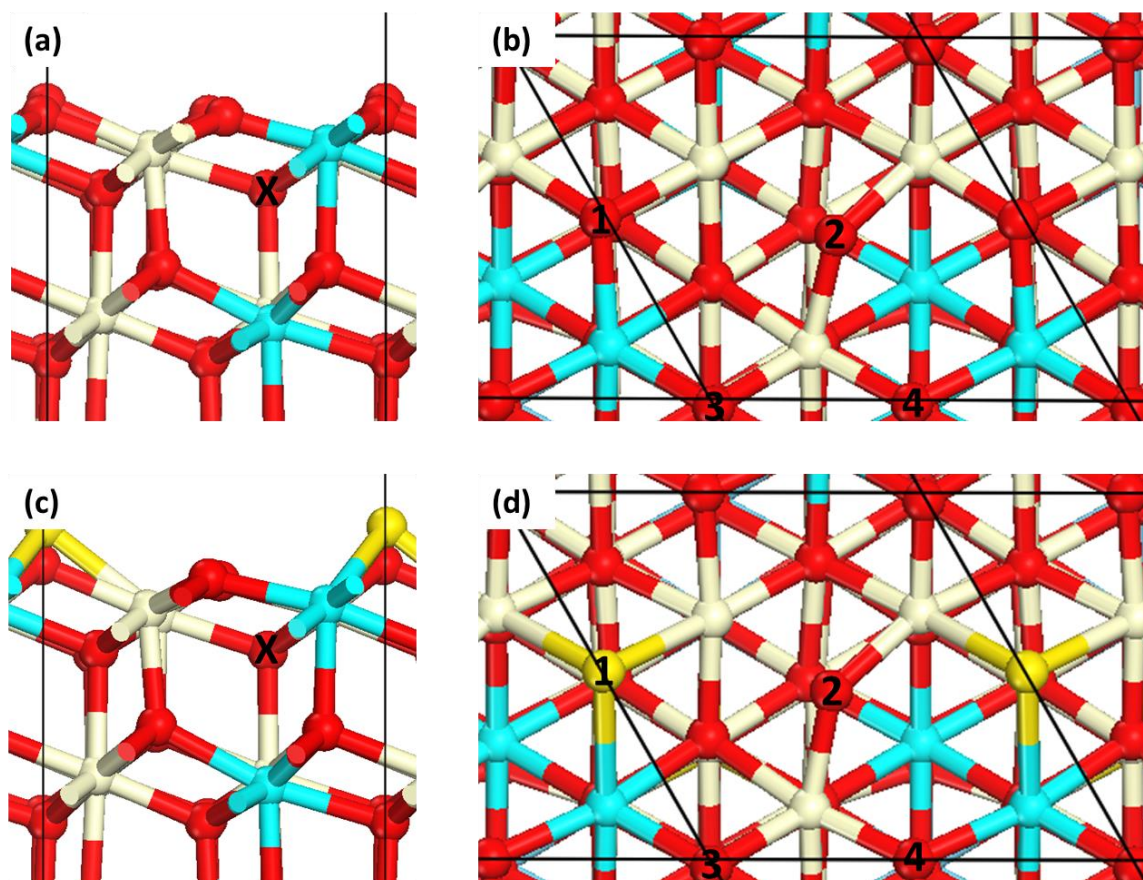


Figure 8-1. Top and side views of the $p(2 \times 2)$ unit cell expansion of sulfided M-doped CeO_2 (1 1 1). (a) side view, and (b) top view. The X is the position of the subsurface oxygen vacancy (the X denotes an oxygen vacancy in front of the labeled oxygen). The oxygen /sulfur atoms 1-4 labels are used in referring to surface adsorbate positions. Ce is displayed at tan (light), M as light blue (light gray), O as red (dark) and S as yellow (dark gray).

The sulfided surfaces used in this study would be in thermodynamic equilibrium with effluent from a biomass gasifier, as shown previously with an *ab initio* thermodynamic approach.⁴ This sulfided structure has one oxygen atom replaced by a sulfur atom, and there are two oxygen vacancies in the surface slab, one in the outermost surface layer and one in the first subsurface layer. The doped surface has two cerium atoms substitutionally replaced with a dopant atom (Tb, La, or Mn), with one of the replaced cerium atoms in the first layer and the second atom in the layer

below. During the catalytic cycle for the reforming of methane, the surface will cycle between two states, as the reforming of methane (desorption of CO) removes a lattice oxygen atom. We use an initial surface modeled with one sulfur replacing a surface oxygen atom and one subsurface oxygen vacancy (Figures 8-1c-d). Reaction transforms the surface to the thermodynamic equilibrium state with two oxygen vacancies. Another choice, cycling through the thermodynamic equilibrium state and the further reduced state, would reduce the surface to an extent that would be physically unreasonable given our surface model with 16 CeO₂ units. The un-sulfided modeled surface also has one subsurface oxygen vacancy, matching the state of reduction in the sulfided case (Figures 8-1a-b). The presence of an oxygen vacancy in the un-doped ceria surface causes reduction of two cerium atoms (Ce³⁺). In the doped system, the oxygen vacancy allows both of the dopant atoms to have a 3+ oxidation state, and none of the cerium atoms are reduced. As we have previously shown, Mn will not dope into the ceria surface without the formation of an oxygen vacancy and will only be stable when doped in with an oxygen vacancy present (Mn²⁺ or Mn³⁺).³⁷ The level of doping was considered low enough not to affect the lattice parameters.

8.2.3. Reaction Energies

All chemical reactions and their reaction energy formulas considered in this study are listed in Table 8-1.

The variables used in Table 8-1 are listed below:

E_S is the energy of the surface slab

$E_{S/(n-1)V_O}$ is the energy of a surface unit cell with $(n-1)$ oxygen vacancies on each side of the unit slab

E_{S/nV_O} is the energy of a surface unit cell with n oxygen vacancies on each side of the unit slab

$E_{S/C_zH_y^*}$ is the energy of the surface slab with a hydrocarbon molecule bound to the surface

E_{S/H^*} is the energy of the surface slab with a hydrogen bound to the surface

E_{O_2} is the energy of a gas phase O_2 molecule

E_{H_2} is the energy of a hydrogen molecule in the gas phase

$E_{C_zH_y}$ is the energy of a hydrocarbon molecule in the gas phase

$E_{C_zH_{y-1}\cdot}$ is the energy of a hydrocarbon radical in the gas phase

E_{S/C^*} is the energy of the surface slab with a carbon molecule bound to the surface

Table 8-1. Reaction types and reaction energy definitions for all reactions included in this paper.

Reaction Type	Chemical Reaction	Reaction Energy
(A) Oxygen Vacancy Formation	(A) $M_xCe_{1-x}O_{2-(n-1)} \rightarrow M_xCe_{1-x}O_{2-n} + \frac{n}{2}O_2(g)$	$\Delta E_{vac} = \frac{E_{S/nV_0} + E_{O_2} - E_{S/(n-1)V_0}}{2}$ (1)
(B) Pseudo-Transition State	(B) $C_zH_y(g) + * \rightarrow H^* + C_zH_{y-1}\cdot(g)$	$E_{act} = \frac{(E_{S/H^*} + 2*E_{C_zH_{y-1}\cdot}) - (E_S + 2*E_{C_zH_y})}{2}$ (2)
(C) Hydrocarbon Adsorption	(C) $C_zH_y(g) + * \rightarrow C_zH_{y-1}* + \frac{1}{2}H_2(g)$	$\Delta E_{ads} = \frac{(E_{S/C_zH_{y-1}*} + E_{H_2}) - (E_S + 2*E_{C_zH_y})}{2}$ (3)
(D) Hydrogen Abstraction	(D) $C_zH_y* \rightarrow C_zH_{y-1} + \frac{1}{2}H_2(g)$	$\Delta E_{abs} = \frac{(E_{S/C_zH_{y-1}*} + E_{H_2}) - (E_{S/C_zH_y*})}{2}$ (4)
(E) Desorption of species	(E) $C^* \rightarrow CO(g) + * + V_o$	$\Delta E_{CO} = \frac{(E_{S/nV_0} + 2*E_{CO}) - (E_{S/C^*})}{2}$ (5)

The factors of 2 listed in the reaction energies of Table 8-1 are a result of using mirrored slabs. Even though it is known that DFT overestimates the O₂ binding energy, in Equation 1 the DFT energy for O₂ is utilized.³⁶ We did not add in a correction to better match the experimental binding energy because we only are using the oxygen vacancy formation energies for qualitative trends and a constant correction term would not alter these trends. For all gas phase molecules, the ZPVE and temperature dependent free energy terms were not added. All energies reported herein are used to compare between the sulfided and un-sulfided surfaces and these corrections would only alter the absolute adsorption energies and not the differences between these two cases. The dehydrogenation of CH_x* intermediates on the surface would produce surface bound H* atoms that would then pair and desorb as H₂ during a reforming process. As our emphasis is on the hydrocarbon surface chemistry, we consider dehydrogenation (CH_x* → CH_{x-1}*) to directly produce half of an H₂ molecule without considering the H₂ desorption process. This allows us to isolate the impact of sulfidation on H* or CH_x* adsorbates without considering co-adsorption of both in the

same unit cell. The desorption energies (Equation 5) can represent the desorption of a CO molecule or of a CS molecule from the sulfided surface.

8.2.4. Determination of oxidation states

We utilize the site projected charge method to identify the number of cerium atoms in the Ce^{4+} and Ce^{3+} oxidation states, as described in our previous study.¹⁷ The formal oxidation states of La and Tb were assigned to 3+, as the formation of a single oxygen vacancy with two La/Tb doped into the surface didn't reduce the cerium atoms, but did increase the electron density on the La and Tb atoms. The formal oxidation state of Mn was identified using the site projected charge method (RWIGS of 0.7 for Mn) and the spin state of each Mn atom. Using this method, obtaining the number of valence electrons on the Mn to be ~3.5 indicated the Mn^{3+} oxidation state and ~3.7 electrons indicated an oxidation state of Mn^{2+} . For all structures, metal oxidation state changes were clear and localized orbitals appeared in the band gap region, indicating surface reduction occurred through reduction of localized metal centers.

8.3. Results and discussion

8.3.1. Initial C-H bond activation

Table 8-2 reports the hydrogen abstraction, methane decomposition and propane decomposition energies, with and without partial sulfidation of the oxide surface. The initial hydrogen abstraction from methane (or any alkane) onto the surface of M-doped CeO_2 leaves a hydrogen bound to an oxygen atom (labeled O1-O4 in Figure 8-1) on the surface and a methyl (alkyl) radical in the gas phase. The energy to abstract a H atom on a surface oxygen has only a

slight variance if a nearby O atom has been replaced with a S atom. However, abstraction of the first hydrogen from the methane on a sulfur atom (Figures 8-2a-b) causes the extraction to be less favorable by 0.34-0.46 eV than abstraction onto an oxygen atom in the same position (O1/S1). As this H-abstraction energy is used as a pseudo-activation barrier for the initial C-H bond activation,¹⁷ this increase is kinetically significant and we conclude substitution of surface oxygen atoms by sulfur atoms will leave less active sites (sulfur atoms) for the methane abstraction. This will impact the overall rate of alkane oxidation through lowering the number of sites, but the barrier on the remaining active sites (surface oxygen atoms) is unperturbed by sulfidation. Our previous thermodynamic analysis suggested the surface saturates with 25% substitution of oxygen to sulfur under typical biomass gasifier effluents. Sulfidation will effectively remove 25% of the surface oxygen sites for C-H bond activation. All structures for the adsorption of H* on the surface can be seen in Figures E-1 and E-4.

Table 8-2. Adsorption and dehydrogenation energies for methane and propane reforming on sulfided and un-sulfided surfaces of pure, La-, Tb- and Mn-doped CeO₂ (1 1 1). The oxygen numbers refer to which oxygen the species is adsorbed to from the labels in Figure 8-1. O1 is the sulfur atom position in the sulfided cases. The * represent which carbon(s) or hydrogen are bound to oxygen or sulfur atoms. Reaction types are defined in Table 8-1.

Reaction Type	Product Surface Species	Oxygen Numbers	CeO ₂		La-Doped CeO ₂		Tb-Doped CeO ₂		Mn-Doped CeO ₂	
			Un-Sulfided (eV)	Sulfided (eV)	Un-Sulfided (eV)	Sulfided (eV)	Un-Sulfided (eV)	Sulfided (eV)	Un-Sulfided (eV)	Sulfided (eV)
B	H*	O1 (S1)	1.28	1.64	1.61	1.95	1.30	1.76	0.84	1.23
B	H*	O2	1.22	1.15	1.54	1.52	1.38	1.45	1.51	1.34
B	H*	O4	1.24	1.13	1.48	1.40	1.23	1.19	0.98	0.75
B	H*	O3	1.27	1.22	1.62	1.60	1.30	1.40	0.83	0.77
C	C*H ₃	O1 (S1)	0.13	0.00	0.41	0.33	0.24	0.20	-0.13	-0.14
D	C*H ₂	O1 (S1)	1.81	1.85	1.99	1.76	1.91	1.69	0.29	1.25
D	C*H	O1 (S1)	1.48	1.69	1.01	1.94	1.13	2.43	2.18	2.43
D	C*	O1 (S1)	0.19	0.42	0.53	0.24	0.26	-0.22	-0.39	-0.33
E	Desorb CO/CS	O1 (S1)	0.56	1.70	0.17	1.32	0.35	1.44	0.06	0.67
C	CH ₃ C*HCH ₃	O4	-0.09	-0.35	0.07	0.00	-0.21	-0.19	-0.51	-0.60
D	C*H ₂ C*HCH ₃	O3,O4	0.49	1.18	0.45	1.04	0.32	0.83	0.15	0.23
D	C*HC*HCH ₃	O3,O4	0.48	-0.06	0.34	0.85	0.50	0.66	0.79	0.43
D	C*H ₂ C*HC*H ₂	O2,O3,O4	0.30	-0.33	0.33	-0.26	0.51	0.02	0.63	0.46
D	C*H ₂ C*HC*H ₂	O1,O3,O4	0.47	0.02	0.96	0.21	0.74	0.35	0.38	0.41

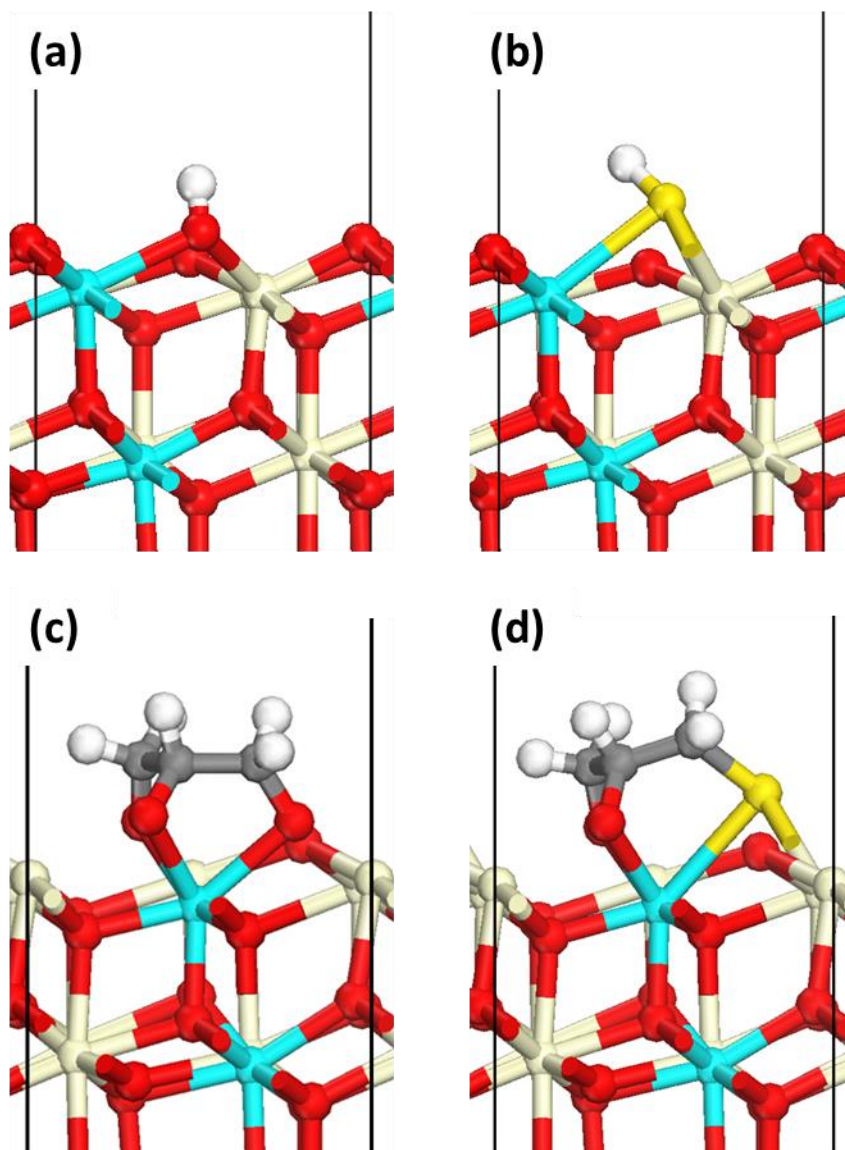


Figure 8-2. Four selected structures of hydrogen and a propyl derivative adsorbed onto the surfaces of sulfided and un-sulfided M-doped CeO_2 . (a) H^* (on O1) on the un-sulfided surface, (b) H^* (on S1 (O1 position)) on the sulfided surface, (c) $\text{C}^*\text{H}_2\text{C}^*\text{HC}^*\text{H}_2$ (on O1, O3, and O4) on the un-sulfided surface, (d) $\text{C}^*\text{H}_2\text{C}^*\text{HC}^*\text{H}_2$ (on S1 (O1), O3, and O4) on the sulfided surface. Ce is displayed as tan (light), M as light blue (light gray), O as red (dark) and S as yellow (dark gray).

A thermodynamic cycle decomposition of the process involved in the abstraction of a hydrogen/alkyl fragment from a hydrocarbon is given in Figure 8-3. The overall reaction abstracts a hydrogen/alkyl fragment from a hydrocarbon, and we term this abstraction energy as E_{act} given the pseudo-transition state assumption. Table 8-3 contains the energies associated with each step of Figure 8-3 for the abstraction of a hydrogen from methane for pure, La-, Tb- and Mn-doped CeO_2 (1 1 1). For the abstraction of a hydrogen from methane, R_1 would represent CH_3 and R_2 would represent H.

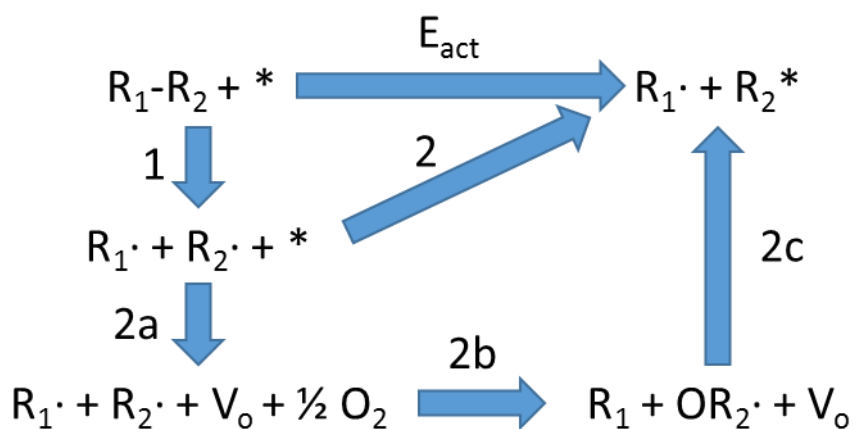


Figure 8-3. Thermodynamic cycle decomposition of the steps involved in the abstraction of R_2 from R_1 forming a R_1 radical in the gas phase. On the sulfided case where R_2 is bound to a sulfur, the O would be replaced with S.

We decompose formation of the pseudo-transition states into two steps, (1) forming of a CH_3 radical and a hydrogen radical in the gas phase and the (2) adsorption of the hydrogen on an oxygen or sulfur in the surface. Step 1 does not depend on the surface and the energy required to break this bond is therefore independent of whether the surface is partially sulfided. The energy for reaction 2 will depend on whether the hydrogen binds to a sulfur or an oxygen atom. We further split step 2 into 3 processes: (2a) removing an oxygen (or sulfur) from the surface forming a vacancy, (2b) oxidizing (or sulfiding) the hydrogen radical in the gas phase, and (2c) adsorbing the hydroxyl (or sulfided radical) into the surface vacancy. The O-H bond in the gas phase is 0.42 eV stronger than an equivalent S-H bond (both forming radicals in the gas phase, step 2b.) This step is surface independent. The difference in the overall hydrogen abstraction energy occurring on a surface sulfur versus oxygen on the four surfaces ranges from 0.34 to 0.46 eV. This difference is similar to the O-H and S-H bond energy difference. There is a large energy difference between the sulfur and oxygen atoms for steps 2a (breaking M-S or M-O interactions) and 2c (reforming the M-S or M-O interactions), however the difference in the sum of steps 2a and 2c for oxygen versus sulfur ranges from -0.08 to 0.04 eV. The difference in absolute energies between 2a and 2c result from differences in the surface redox processes, as forming an oxygen vacancy (2a) is a 2 electron reduction process whereas adsorbing OH^* (SH^*) is a one electron process. We conclude from this analysis that the preferable (faster) abstraction of hydrogen from hydrocarbons on surface oxygen atoms versus surface sulfur atoms occurs due to the stronger O-H versus S-H bond formed.

Table 8-3. Energies associated with the thermodynamic cycle decomposition of the abstraction of a hydrogen from a methane forming a methyl radical in the gas phase and a hydrogen adsorbed on the surface (on O1 for un-sulfided or S1 for sulfided) for pure, La-, Tb- and Mn-doped CeO₂ (1 1 1). This cycle is represented graphically in Figure 8-3, if the R₁ represents CH₃ and R₂ represents hydrogen. Step 2 is the sum of steps 2a-c and E_{act} is the sum of steps 1 and 2. Step 2b and 2c are the energies associated with the thermodynamic cycle breakdown for the adsorption of a methyl radical on the surface.

	CeO ₂		La-Doped CeO ₂		Tb-Doped CeO ₂		Mn-Doped CeO ₂	
	Un-Sulfided (eV)	Sulfided (eV)	Un-Sulfided (eV)	Sulfided (eV)	Un-Sulfided (eV)	Sulfided (eV)	Un-Sulfided (eV)	Sulfided (eV)
Step 1	4.81	4.81	4.81	4.81	4.81	4.81	4.81	4.81
Step 2a	3.53	1.80	3.48	1.74	3.25	1.69	1.37	0.02
Step 2b	-1.66	-1.24	-1.66	-1.24	-1.66	-1.24	-1.66	-1.24
Step 2c	-5.41	-3.72	-5.02	-3.36	-5.10	-3.49	-3.68	-2.36
Step 2	-3.54	-3.17	-3.20	-2.86	-3.51	-3.05	-3.98	-3.58
E _{act}	1.28	1.64	1.61	1.95	1.30	1.76	0.84	1.23
Step 2b for CH ₃	-1.41	-0.96	-1.41	-0.96	-1.41	-0.96	-1.41	-0.96
Step 2c for CH ₃	-4.52	-3.38	-4.19	-2.99	-4.13	-3.07	-2.62	-1.74
Step 2 for CH ₃ *	-5.94	-4.33	-5.61	-3.94	-5.55	-4.03	-4.04	-2.70

Contrasting the surface O-H/S-H bonding, adsorbing a methyl species on the surface onto a sulfur atom (S1) is slightly more favorable than to adsorb the methyl group onto an oxygen atom (O1). We can again use the thermodynamic cycle in Figure 8-3 to analyze this difference, with R₂ now representing the methyl species and R₁ representing a H atom. Steps 1 and 2a are unchanged from surface H abstraction. The O-CH₃/S-CH₃ difference in step 2b is surface independent, and as for the O-H/C-H, the O-CH₃ bond is 0.46 eV more stable than the S-CH₃ bond. Contrary to H abstraction, the differences in energy for steps 2a and 2c does not cancel for methyl adsorption. The sum of 2a and 2c is 0.46 to 0.59 eV more stable on the sulfided case whereas this difference was ~ 0 eV for H abstraction. This leads to CH₃ adsorption on the sulfur atom versus oxygen atom.

This indicates the CH_3 species weakens the metal-oxygen bonds more than the metal-sulfur bonds. The slightly stronger adsorption of CH_3 to surface sulfur atoms over oxygen atoms may lead to eventual carbon buildup on the sulfided surface, as discussed in Section 8.3.2. All structures for reforming of methane on the surface can be seen in Figures E-2 and E-5.

The data in Table 8-2 allows for consideration of how La-, Tb-, or Mn-doping impact C-H bond activation kinetics. Using the H^* pseudo-transition state assumption, Tb- or La-doping increase the activation barrier relative to pure CeO_2 (1 1 1) on all surface oxygen atoms or sulfur atoms, with an average increase of 0.31 eV (0.70 eV for sulfur) for La-doping and 0.05 eV (0.12 eV for sulfur) for Tb-doping. As H abstraction is occurring on a surface with a subsurface oxygen vacancy already present, La- and Tb-dopants are reduced to a 3+ state prior to C-H activation. La- and Tb- doping appear to increase the activation barrier by making the adjacent Ce atoms slightly less reducible. Contrarily, Mn-doping lowers the barrier for H abstraction on O1 (S1), O3 and O4. Prior to H abstraction, Mn atoms are in a 3+ oxidation state, but their accessible 2+ state helps promote C-H bond activation. The barrier for H abstraction on O2 for the Mn-doped surface is higher than pure CeO_2 . O1 (S1), O3 and O4 are all nearest neighbors to the Mn dopant and O2 is a next nearest neighbor (doesn't share any bonds with the Mn atom). This suggests that Mn-doping promotion of C-H activation is a local affect, only promoting C-H activation on oxygens bound to surface-doped Mn atoms.

8.3.2. Complete methane dehydrogenation with and without sulfur present

Figure 8-4 contains the 0 K reaction energy diagram for methane reforming over pure CeO_2 (1 1 1) and sulfided CeO_2 (1 1 1). All CH_x species are taken to adsorb on O1 or S1. The pseudo-transition state (for hydrogen abstraction on a sulfur and oxygen) as described in the section before, is included on the reaction energy diagram. H abstraction on a surface sulfur or oxygen can lead to

CH_3^* formation on either site, as the radical may move along the surface to find a binding site. The 0 K reaction energy diagram of Figure 8-4 suggest CH_4 surface decomposition and subsequent CO desorption is highly unfavorable, uphill in energy by ~ 4 eV. This should not be taken to indicate a lack of favorability under reforming conditions. The standard state reaction free energy to partially oxidize methane to carbon monoxide and hydrogen is -0.89 eV (exergonic),⁴⁰ and the unfavorable overall process in 0 K stem from not including the large entropy gain associated with the conversion of methane and a lattice oxygen to H_2 and CO. Additionally, the 0 K dissociative adsorption energy of $\frac{1}{2} \text{H}_2$ to form H^* on a CeO_2 (1 1 1) surface is -1.14 eV (exothermic), such that elementary reaction producing H^* versus $\frac{1}{2} \text{H}_2$ would be more favorable. We have chosen to use 0 K energies and production of H_2 gas versus H^* to allow for simple and consistent comparison between dehydrogenation of the different CH_x species and between the sulfided and un-sulfided surface, at the expense of providing realistic energetics at reaction conditions.

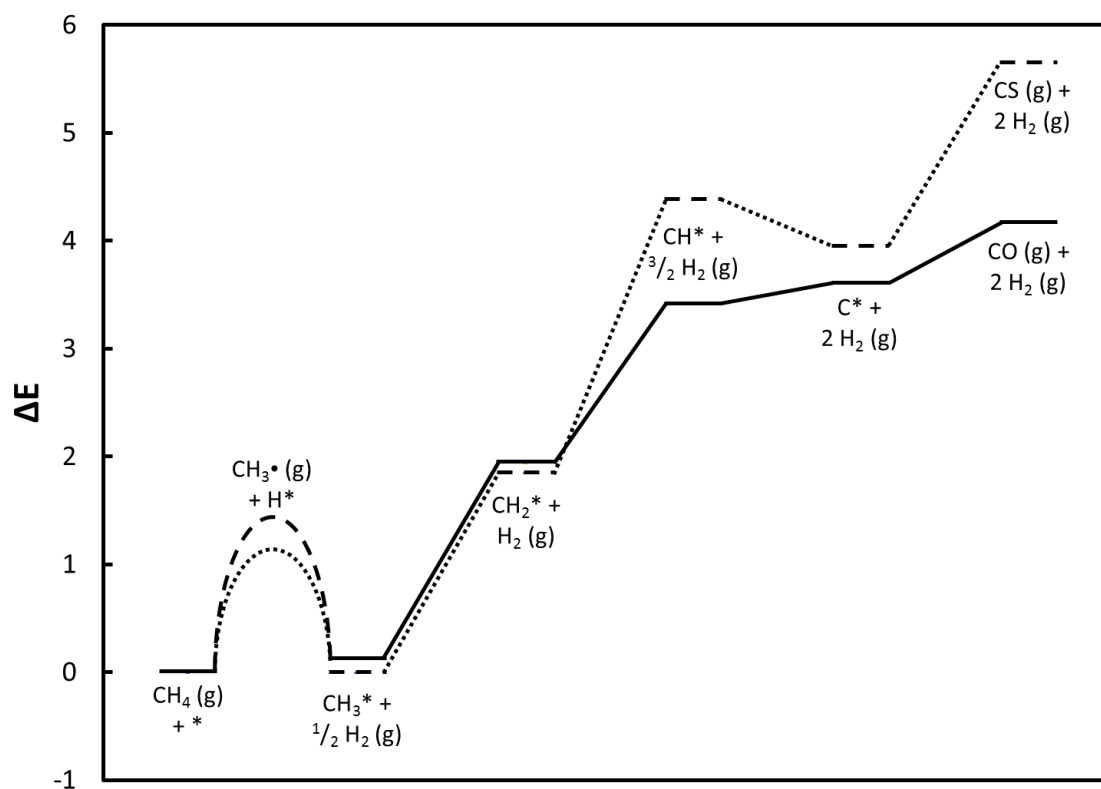


Figure 8-4. Reaction energy diagram of methane decomposition over sulfided and un-sulfided surfaces of pure CeO_2 (1 1 1). The solid lines represent each hydrogen abstraction (product desorption) on the un-sulfided surface and the dashed lines for the sulfided surface. For the pseudo-transition state ($\text{CH}_3\cdot + \text{H}^*$), the long dash represents H abstraction on a sulfur atom and the short dash represents on an oxygen atom.

The CH_3^* species has a small preference to adsorb to a surface sulfur atom. The CH_2^* product of the second hydrogen abstraction also has a small preference to bond to a sulfur atom. The subsequent CH^* and C^* intermediates show a strong preference to bond to surface oxygen atoms, indicating complete methyl decomposition will be less favorable on surface sulfur sites. The largest difference between methane decomposition on an oxygen atom compared to a sulfur atom is the desorption of the final products, with the desorption of the CO molecule being 1.13 eV more favorable than desorption of the CS molecule. The large discrepancy between these two desorption

energies is mostly a result of the CS molecule before desorption has a radical on the carbon atom, with one less cerium reduced compared to the CO molecule. This radical on the carbon atom and the electronic structure of the C_1 intermediate during every step of the decomposition will be discussed in the next section. The similar first and second hydrogen abstraction energy on an oxygen atom compared to a sulfur atom will allow the methane species to start to dehydrogenate on either atom. However, after the first two abstractions, the second two hydrogen abstractions and product desorption is much higher on the sulfur atom compared to the oxygen atom, which can lead to coking of the ceria surface when the surface is sulfided.

For the methyl decomposition on an oxygen site, the oxygen atom bound to the carbon is always towards the surface, Figure 8-5. For the CH_3^* , CH_2^* and CH^* intermediates on the sulfur atom, the sulfur is in the same orientation as the oxygen atom case (towards the surface). However, for the C^* bound to a sulfur atom (CS^*) the CS molecule is flipped and has the carbon atom pointing towards the surface, instead of the sulfur.

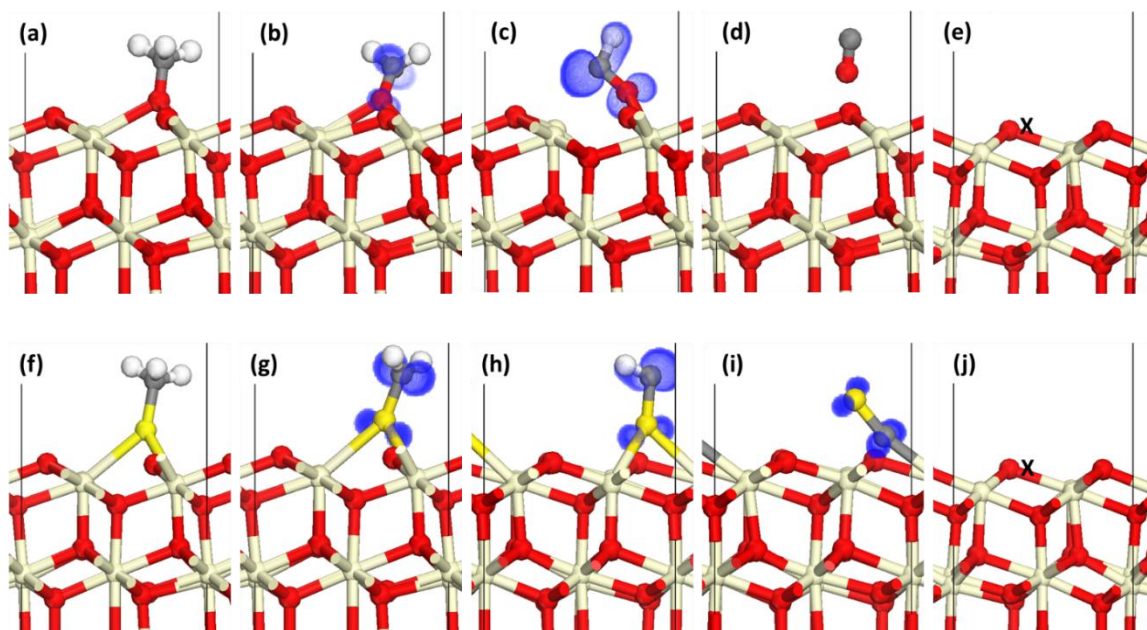


Figure 8-5. Structures of methane decomposition intermediates over (a-e) un-sulfided and (f-j) sulfided (1 1 1) surfaces of pure CeO_2 . Isodensity surfaces representing isolated electron states on adsorbates are displayed in (b-c) and (g-i). The represent state appearing in the ceria band gap in the energy ranges of (b) -0.72 to -0.60 eV, (c) -1.24 to -1.10 eV, (g) -0.48 to -0.36 eV, (h) -0.55 to -0.35 eV, and (i) -0.36 to -0.13 eV (relative to the Fermi level). Total density of states for these structures are given as Figures E-9 and E-10. Ce is displayed as tan (light), O as red (dark), S as yellow (dark grey).

Appendix E contains the 0 K reaction energy diagrams for methane decomposition over the sulfided and the un-sulfided La- and Tb-doped CeO_2 (1 1 1) surface. The reaction energy diagrams for La- and Tb-doped CeO_2 (1 1 1) are very similar to the reaction energy diagram for pure CeO_2 . With the adsorption of CH_3^* and CH_2^* intermediates having a slight preference on the sulfur atom and the adsorption of CH^* and C^* intermediates has a strong preference on the oxygen atom. The desorption of the CO molecule is significantly more favorable than the desorption of the CS molecule leaving behind and oxygen vacancy.

The 0 K reaction energy diagram is illustrated in Figure 8-6 for the methane decomposition over the sulfided and the un-sulfided surface of Mn-doped CeO_2 (1 1 1). A significant difference

with the pure CeO₂ or Tb, La-doped surfaces is that the initial C-H activation barrier is low and the initial CH₃* adsorption is more favorable by 0.15 – 0.5 eV. The CH₂* state is also more stable on the un-sulfided Mn-doped CeO₂ (1 1 1) surface, though the sulfided surface shows less difference. The CH₃* (slightly) and the CH₂* (considerably) prefer to bind to surface oxygen atoms on Mn-doped ceria, suggesting Mn-doping may induce a sulfur tolerant property. The CH* species is less stable on the Mn-doped surface than the other dopants. The C* species is more stable on the Mn-doped surface, and the CO or CS product, leaving a surface oxygen vacancy, is significantly preferred on the Mn-doped surface due to the significantly more favorable oxygen (sulfur) vacancy formation energy with the Mn-dopant. As for the other dopants, the desorption of the CS molecule is more endergonic compared to the desorption of the CO molecule. Most of these differences can be accounted for by the difference in electronic behavior between the Mn-doped surface and the three other surfaces, as described in the following section.

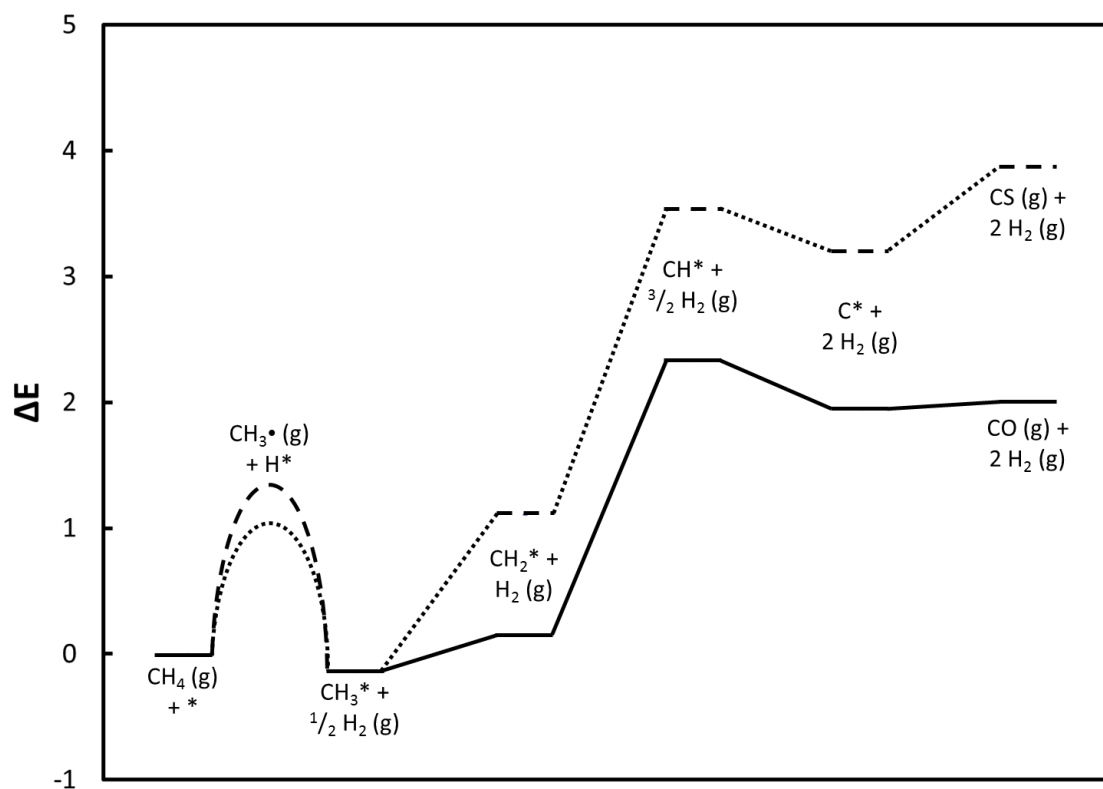


Figure 8-6. Reaction energy diagram of methane decomposition over sulfided and un-sulfided surfaces of Mn-doped CeO_2 (1 1 1). The solid lines represents each hydrogen abstraction (product desorption) on the un-sulfided surface and the dashed lines for the sulfided surface. For the pseudo-transition state ($\text{CH}_3\bullet + \text{H}^*$), the long dash represents H abstraction on a sulfur atom and the short dash represents on an oxygen atom.

8.3.3. Electronic structure analysis during dehydrogenation on CeO₂

Lewis structures for each surface intermediate along the decomposition of methane over the sulfided and un-sulfided surfaces of pure CeO₂ (1 1 1) are illustrated in Figure 8-7. Table 8-4 contains the number of reduced (3+) cerium atoms at each intermediate, along with Figures E-9 and S10 containing the total density of states for each intermediate. The adsorption of the methyl radical on the ceria surface forms a C-O (C-S) bond and reduces one cerium atom to Ce³⁺. Abstracting the second hydrogen from the C₁ intermediate to form CH₂* leaves an unpaired electron on the carbon atom. All efforts to motivate H₂C=O (H₂C=S) formation and localize the unpaired electron to form an additional Ce³⁺ were unsuccessful and we conclude that the CH₂* adsorbed state is more favorable than the state with a C-O (C-S) double bond and two reduced cerium atoms. The third hydrogen abstraction forms a C-O (C-S) double bond and leaves a lone pair of electrons on the carbon atom. No additional cerium atoms reduce. The O-C-H bond angle is indicative of an sp² hybridized carbon atom. Conversion of CH₄ (g) to CH* + ³/₂ H₂ leads to only a 1 electron reduction of the surface, occurring upon O-CH₃/S-CH₃ formation.

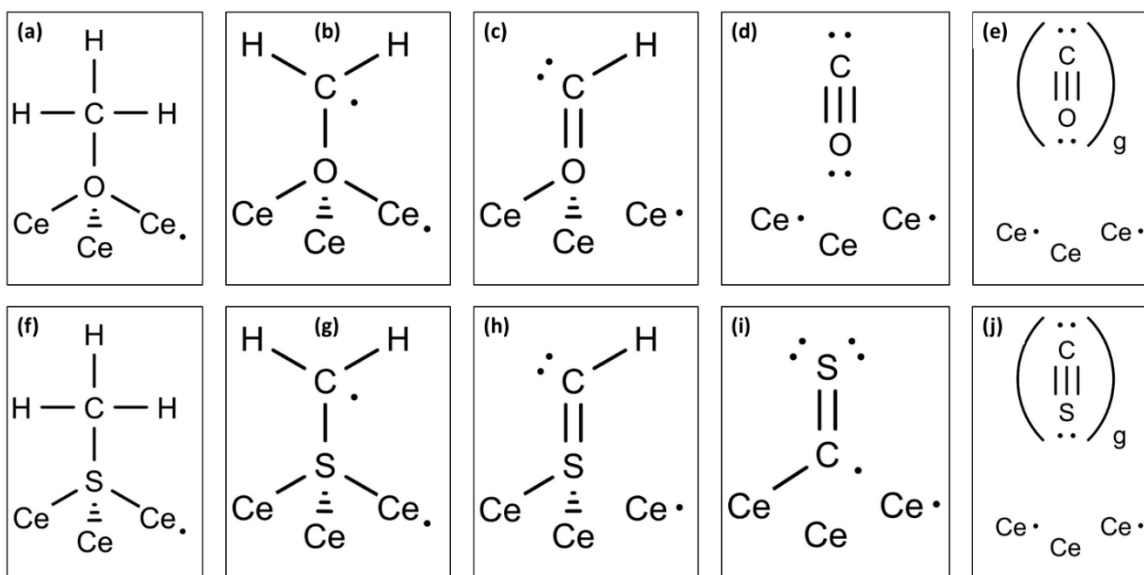


Figure 8-7. Lewis structures for methane decomposition surface intermediates over (a-e) surface oxygen atoms and (f-j) surface sulfur atoms over pure CeO_2 (1 1 1). Every image corresponds to the structure with the same letter displayed in Figure 8-5.

In progressing to the CH^* species, the surface and adsorbate electronic structure did not differ between the O-CH_x^* or S-CH_x^* species. The last hydrogen abstraction from the C_1 intermediate bound to the oxygen atom forms a CO molecule, “ C^* ”, with the CO species having little interaction with the surface. An additional cerium is reduced (2 Ce^{3+}) on converting CH^* to $\text{C}^* + \frac{1}{2} \text{ H}_2$. C^* on a sulfur atom prefers instead to flip to put the carbon end down, and the CS species has a strong interaction with the surface with one bond to a cerium atom and an unpaired electron left on the carbon atom. The product desorption of the CO, as surface oxygen vacancy, molecule keeps the same extent of surface reduction as the previous C^* state. The desorption of the CS molecule breaks the C-Ce bond and reduces an additional Ce (2 Ce^{3+}). After either desorption, the surface has a vacancy with 2 reduced cerium atoms. La- and Tb-doped ceria showed no difference in the state of reduction or character of surface intermediates from the pure CeO_2 surfaces.

Table 8-4. The number of reduced cerium atoms and the oxidation state of the dopant atoms for methane and propane reforming surface intermediate over sulfided and un-sulfided surfaces of pure, La-, Tb- and Mn-doped CeO₂ (1 1 1). La- and Tb-doped ceria had the same extent of reduction in the surface for every step and the dopant is represented by M. The oxygen numbers refer to which oxygen the species is adsorbed to from the labels in Figure 8-1. O1 is the sulfur atom in the sulfided surfaces. The * represent which carbon or hydrogen is bound to the oxygen or sulfur atom, and the oxygen numbers represent which oxygen (sulfur) the carbon or hydrogen are bound to.

	Oxygen Numbers	CeO ₂		La/Tb-Doped CeO ₂ ^a		Mn-Doped CeO ₂			
		Un-Sulfided	Sulfided	Un-Sulfided	Sulfided	Un-Sulfided		Sulfided	
		# Ce ³⁺	# Ce ³⁺	# Ce ³⁺	# Ce ³⁺	Mn States	# Ce ³⁺	Mn States	# Ce ³⁺
Starting Surface	-	2	2	0	0	2 Mn ³⁺	0	2 Mn ³⁺	0
H* On O1(S1)	O1	3	3	1	1	2 Mn ³⁺	1	2 Mn ³⁺	1
H* On O2	O2	3	3	1	1	2 Mn ³⁺	1	2 Mn ³⁺	1
H* On O3	O3	3	3	1	1	2 Mn ³⁺	1	2 Mn ³⁺	1
H* On O4	O4	3	3	1	1	2 Mn ³⁺	1	2 Mn ³⁺	1
C*H ₃	O1	3	3	1	1	1 Mn ²⁺ & 1 Mn ³⁺	0	1 Mn ²⁺ & 1 Mn ³⁺	0
C*H ₂	O1	3	3	1	1	1 Mn ²⁺ & 1 Mn ³⁺	1	1 Mn ²⁺ & 1 Mn ³⁺	1
C*H	O1	3	3	1	1	1 Mn ²⁺ & 1 Mn ³⁺	0	1 Mn ²⁺ & 1 Mn ³⁺	0
C*	O1	4	3	2	1	1 Mn ²⁺ & 1 Mn ³⁺	1	1 Mn ²⁺ & 1 Mn ³⁺	1
Desorb CO/CS	O1	4	4	2	2	1 Mn ²⁺ & 1 Mn ³⁺	1	1 Mn ²⁺ & 1 Mn ³⁺	1
CH ₃ C*HCH ₃	O4	3	3	1	1	1 Mn ²⁺ & 1 Mn ³⁺	0	1 Mn ²⁺ & 1 Mn ³⁺	0
C*H ₂ C*HCH ₃	O3, O4	4	4	2	2	2Mn ²⁺	0	1 Mn ²⁺ & 1 Mn ³⁺	1
C*HC*HCH ₃	O3, O4	5	5	3	3	2Mn ²⁺	1	2Mn ²⁺	1
C*H ₂ C*HC*H ₂	O2, O3, O4	5	5	3	3	1 Mn ²⁺ & 1 Mn ³⁺	2	1 Mn ²⁺ & 1 Mn ³⁺	2
C*H ₂ C*HC*H ₂	O1, O3, O4	5	5	3	3	1 Mn ²⁺ & 1 Mn ³⁺	2	1 Mn ²⁺ & 1 Mn ³⁺	2

^aLa- and Tb-dopants remained in the 3+ oxidation state in all intermediates along the methane/propane decomposition paths.

For the Mn-doped surface, the initial CH_3^* adsorption reduces a Mn atom from $3+$ to $2+$ rather than reducing a Ce atom. The Mn-doped ceria surface, compared to pure CeO_2 or La-, Tb-doped CeO_2 (1 1 1), shows additional differences in electronic structure after the second hydrogen abstraction (CH_2^*) (Table 8-4). For CH_2^* , the unpaired electron localized onto a cerium atom rather than the adsorbate C atom. This allowed the formation of a double bond between the carbon and the oxygen atom in the surface. The next hydrogen abstraction left a lone pair of electrons on the sp^2 hybridized carbon atom and maintained its double bond with the oxygen atom. The cerium atom reduced in the CH_2^* state re-oxidized to Ce^{4+} in the CH^* state. Contrary to the pure CeO_2 surface, the final C^* (CO or CS formation) both have two electrons reducing atoms in the surface and both adsorbates have an interaction with the surface. Collectively, the main impacts of Mn-doping for CH_4 conversion is the initial reduction of Mn^{3+} to Mn^{2+} on C-H abstraction and in stabilizing the eventual oxygen vacancy when CO/CS is formed. The accessible Mn^{2+} oxidation state also facilitates various propane oxidation intermediates.

8.3.4. Initial reforming of propane over a sulfided surface

The surface chemistry of propane oxidation is more complex due to the potential for adsorbates with multiple points of surface interaction and the mixing of C-H and C-C dissociation with C-O formation and surface re-oxidation. We have examined this complex reaction process over Zr-doped CeO_2 (1 1 1) previously.¹⁸ Here, we consider only the initial step of propane oxidation to explore the impact of a partially sulfided surface. Energetics of surface intermediates are reported in Table 8-2 and two key intermediates are included in Figure 8-2. Table 8-4 includes the extent of surface reduction for each propane derived surface intermediate. All structures for the first three steps of reforming propane can be seen in Figures E-3 and E-6.

The dissociative adsorption of propane, forming a $\frac{1}{2}$ H₂ and a propyl species adsorbed at the second carbon atom to O4 is slightly more favorable when there is sulfur present in the surface. The second hydrogen abstraction from the propyl intermediate is from a primary carbon, and when the hydrogen is abstracted the primary carbon forms a bond with a second surface oxygen atom (O3), forming the C*H₂C*HCH₃ intermediate and $\frac{1}{2}$ H₂ (g). Our previous paper showed this was more favorable than C-C dissociation.¹⁸ This second hydrogen abstraction is less favorable with sulfur present. We did not examine binding of these intermediates with surface sulfur atoms. For the abstraction of a 3rd hydrogen atom we considered: (1) abstracting the hydrogen from the primary carbon already bound to an oxygen atom, (2) abstracting the hydrogen from the other primary carbon atom and binding the 3rd carbon atom to an oxygen atom, and (3) abstracting the hydrogen from the other primary carbon atom and binding it to a sulfur atom (Figures 8-2c-d). The following H abstraction (either removing H from primary bound to surface (C*HC*HCH₃), or forming an additional carbon-oxygen bond with the other primary carbon (C*H₂C*HC*H₂ on O2, O3 and O4)) is slightly more favorable on the sulfided surface for the pure CeO₂ and Mn-doped CeO₂ (1 1 1) surfaces, but less favorable on the La- and Tb-doped CeO₂ (1 1 1) surfaces. Removal of the third hydrogen either forming a C-O or a C-S bond with the other primary carbon is more favorable on the sulfur atom, except for the Mn-doped CeO₂ surface.

8.4. Conclusions

The presence of sulfur in the partially sulfided CeO₂ or M-CeO₂ (1 1 1) surfaces will decrease the number of active sites for the activation of hydrocarbons in the gas phase. Surface sulfur sites are less active for the rate limiting step of C-H activation, through partial sulfidation has little effect on the remaining surface oxygen atoms. Though H* formation preferably occurs on surface oxygen atoms, there is a slight preference for CH₃* species to bind to surface sulfur atoms.

The hydrocarbon species and their subsequent dehydrogenation to surface CS species represent a potential deactivation route, as CS desorption is significantly less favorable than CO desorption. The highly endergonic desorption energy of CS will result in the surface of the sulfided case to have carbon buildup more rapidly compared to the un-sulfided surface. La- and Tb-doping have little effect on the surface chemistry, though Mn-doping accelerates C-H activation through Mn^{3+} reduction to Mn^{2+} . Mn-doping similarly promotes eventual CO product desorption, and also shows a greater preference for some hydrocarbon species to bind to surface oxygen atoms versus sulfur atoms, suggesting potential enhanced tolerance against surface poisoning. The complete catalytic cycle, including refilling oxygen vacancies, with free energies considered under reaction conditions are not considered and would be necessary to definitively conclude that Mn-doping would accelerate the oxidation rate.

ACKNOWLEDGEMENTS: This material is based upon work supported as part of the Center for Atomic Level Design, an Energy Frontier Research Center funded by the U.S. Department of Energy, Office of Science, Office of Basic Energy Sciences under Award Number DE-SC0001058.

8.5. References

1. X. M. Meng, W. De Jong, A. H. M. Verkooijen. *Environmental Progress & Sustainable Energy* **2009**, 28, 360-371.
2. L. Devi, K. J. Ptasinski, F. Janssen. *Biomass & Bioenergy* **2003**, 24, 125-140.
3. R. Li, M. D. Krcha, M. J. Janik, A. D. Roy, K. M. Dooley. *Energy & Fuels* **2012**, 26, 6765-6776.
4. A. D. Mayernick, R. Li, K. M. Dooley, M. J. Janik. *Journal of Physical Chemistry C* **2011**, 115, 24178-24188.
5. M. Flytzani-Stephanopoulos, M. Sakbodin, Z. Wang. *Science* **2006**, 312, 1508-1510.
6. K. M. Dooley, V. Kalakota, S. Adusumilli. *Energy & Fuels* **2011**, 25, 1213-1220.
7. K. B. Yi, E. J. Podlaha, D. P. Harrison. *Industrial & Engineering Chemistry Research* **2005**, 44, 7086-7091.
8. R. Li, A. Roy, J. Bridges, K. M. Dooley. *Industrial & Engineering Chemistry Research* **2014**, 53, 7999-8011.
9. S. Colussi, A. Gayen, M. F. Camellone, M. Boaro, J. Llorca, S. Fabris, A. Trovarelli. *Angewandte Chemie-International Edition* **2009**, 48, 8481-8484.
10. S. Colussi, A. Trovarelli, C. Cristiani, L. Lietti, G. Groppi. *Catalysis Today* **2012**, 180, 124-130.
11. D. Knapp, T. Ziegler. *Journal of Physical Chemistry C* **2008**, 112, 17311-17318.
12. W. Tang, Z. P. Hu, M. J. Wang, G. D. Stucky, H. Metiu, E. W. McFarland. *Journal of Catalysis* **2010**, 273, 125-137.
13. N. Laosiripojana, W. Sutthisripok, P. Kim-Lohsoontorn, S. Assabumrungrat. *International Journal of Hydrogen Energy* **2010**, 35, 6747-6756.

14. F. Abild-Pedersen, O. Lytken, J. Engbaek, G. Nielsen, I. Chorkendorff, J. K. Nørskov. *Surface Science* **2005**, *590*, 127-137.
15. K. Lee, E. Lee, C. Song, M. J. Janik. *Journal of Catalysis* **2014**, *309*, 248-259.
16. A. D. Mayernick, M. J. Janik. *Journal of Physical Chemistry C* **2008**, *112*, 14955-14964.
17. M. D. Krcha, A. D. Mayernick, M. J. Janik. *Journal of Catalysis* **2012**, *293*, 103-115.
18. M. D. Krcha, M. J. Janik. *Catalysis Science & Technology* **2014**, DOI: 10.1039/C4CY00619D.
19. A. D. Mayernick, M. J. Janik. *Journal of Catalysis* **2011**, *278*, 16-25.
20. M. Fronzi, S. Piccinin, B. Delley, E. Traversa, C. Stampfl. *Rsc Advances* **2014**, *4*, 12245-12251.
21. G. Kresse, J. Furthmüller. *Computational Materials Science* **1996**, *6*, 15-50.
22. G. Kresse, J. Furthmüller. *Physical Review B* **1996**, *54*, 11169-11186.
23. G. Kresse, J. Hafner. *Physical Review B* **1993**, *47*, 558-561.
24. G. Kresse, D. Joubert. *Physical Review B* **1999**, *59*, 1758-1775.
25. J. P. Perdew, J. A. Chevary, S. H. Vosko, K. A. Jackson, M. R. Pederson, D. J. Singh, C. Fiolhais. *Physical Review B* **1992**, *46*, 6671-6687.
26. H. J. Monkhorst, J. D. Pack. *Physical Review B* **1976**, *13*, 5188-5192.
27. S. Fabris, S. d. Gironcoli, S. Baroni, G. Vicario, G. Balducci. *Physical Review B* **2005**, *71*, 041102.
28. S. Fabris, S. d. Gironcoli, S. Baroni, G. Vicario, G. Balducci. *Physical Review B* **2005**, *72*, 237102.
29. G. Kresse, P. Blaha, J. L. F. Da Silva, M. V. Ganduglia-Pirovano. *Physical Review B* **2005**, *72*, 237101.
30. V. I. Anisimov, O. Gunnarsson. *Physical Review B* **1991**, *43*, 7570-7574.
31. J. F. Herbst, R. E. Watson, J. W. Wilkins. *Physical Review B* **1978**, *17*, 3089-3098.

32. C. deLeitenburg, A. Trovarelli, J. Llorca, F. Cavani, G. Bini. *Applied Catalysis a-General* **1996**, *139*, 161-173.
33. Q. Y. Wang, B. Zhao, G. F. Li, R. X. Zhou. *Environmental Science & Technology* **2010**, *44*, 3870-3875.
34. M. Fernandez-Garcia, A. Martinez-Arias, A. Iglesias-Juez, A. B. Hungria, J. A. Anderson, J. C. Conesa, J. Soria. *Journal of Catalysis* **2003**, *214*, 220-233.
35. S. L. Dudarev, G. A. Botton, S. Y. Savrasov, C. J. Humphreys, A. P. Sutton. *Physical Review B* **1998**, *57*, 1505-1509.
36. L. Wang, T. Maxisch, G. Ceder. *Physical Review B* **2006**, *73*, 195107.
37. M. D. Krcha, M. J. Janik. *Langmuir* **2013**, *29*, 10120-10131.
38. M. Nolan, V. S. Verdugo, H. Metiu. *Surface Science* **2008**, *602*, 2734-2742.
39. M. Nolan, S. C. Parker, G. W. Watson. *Surface Science* **2005**, *595*, 223-232.
40. J. A. Dean. *Lange's Handbook of Chemistry*. 15th ed.; McGraw-Hill, Inc.: 1999.

Chapter 9

Summary, Conclusions, and Recommendations for Future Study

This dissertation used density functional theory (DFT+*U*) to examine the electronic structure and quantify the catalytic activity of M-doped CeO₂ (1 1 1) surfaces for use in the cleanup of effluent from biomass gasification. Chapter 2 examined the difficulties in using DFT methods to model these M-doped ceria surfaces. Chapters 3-6 focused on using these M-doped ceria surfaces for methane and propane reforming. A correlation exists between the reducibility and C-H bond activation energies on these surfaces, with trends appearing whether the cerium or dopant atoms reduce. Mn-doped CeO₂ shows promise for hydrocarbon oxidation. The stability of Mn-doped into the ceria surface is examined and found Mn will only dope into the surface with oxygen vacancies present. A mechanism to reform propane over Zr- and Mn-doped ceria is established in Chapters 5 and 6. In addition to hydrocarbon reforming ceria can also absorb sulfur. Chapters 7 and 8 illustrated the sulfur capacity of M-doped ceria along with examining the ability of a sulfided surface to reform methane and propane.

9.1. Hydrocarbon activity on M-doped CeO₂ (1 1 1) surfaces

Before directly considering surface reactivity, Chapter 2 provided perspective on the difficulties of applying DFT methods to examine oxide catalyzed redox processes. Chapter 2 showed DFT+*U* and hybrid functional methods can be chosen to match experimental properties of ceria and M-doped ceria systems, though the transferability to surface catalytic activity is unclear. For catalytic studies, accurate reaction energies and activation barriers for transforming among reactant, adsorbed species and products is needed. These transformations include reduction and re-

oxidation of the M-doped CeO₂ surface, challenging accurate energetics determination with tractable DFT methods. Despite these limitations, DFT+*U* methods have provided qualitative insight into catalytic mechanisms and trends with dopant variations for methane and carbon monoxide oxidation and desulfurization.

Utilizing the DFT+*U* methods described in Chapter 2, Chapter 3 examined the electronic structure of transition metal doped CeO₂ (1 1 1) surfaces in the fully oxidized, reduced, and CH₃+H adsorbed states. *We established periodic trends in the role of surface dopants on redox catalysis for M-doped CeO₂ systems.* Upon the formation of a surface oxygen vacancy in the surface of M-doped CeO₂, the dopant can either become the reduction center or can serve to alter the reducibility of the cerium atoms. On the left side of the periodic table, dopants act to alter the reducibility of the cerium atoms, whereas late transition metals serve as the reduction center. When methane adsorption reduces the surface, the dopants serve the same role. The *U*-value on the *d*-states of the dopant can change both the vacancy formation energy as well as the electronic role the dopant plays in surface reduction. The effect of the dopant has local and smaller non-local effects. The lowest oxygen vacancy formation and methane adsorption energies occur for the nearest neighbor to the dopant atom with a higher vacancy formation for the next nearest neighbor.

A series of energetic correlations were established for relating C-H activation to surface reducibility. The vacancy formation energy and dissociative methane adsorption energy correlate across transition metal doped CeO₂ (1 1 1) surfaces. A BEP relationship exists for the activation of the C-H bond in methane over M-doped CeO₂ surfaces, with the activation of the C-H bond being the rate limiting step for methane reforming over pure and Pd-doped CeO₂.¹ Using this BEP relationship we determine that the methane activation and vacancy formation energies are also correlated.

The established correlations provide a qualitative and quantitative connection between surface reducibility and hydrocarbon oxidation activity. For dopants with the most exothermic

(lowest) vacancy formation energy, hydrocarbon oxidation will be limited by oxygen vacancy refilling. For higher vacancy formation energies, methane activation will become rate limiting, *leading to a volcano relationship between methane conversion activity and surface reducibility*. Some of the dopants that look promising for hydrocarbon conversion are Ag, Au, Ni, Co, Pt, Pd, and Mn. These dopants have lower barriers for methane activation, but they are not so low that oxygen vacancy refilling will become rate limiting. The optimal dopant will depend on hydrocarbon pressure as well as the redox environment.

The establishments of these design criteria lead to the conclusion that Mn-doped ceria catalyst hold promise for hydrocarbon conversion. We then focus on examining the effect of the Mn-dopant in ceria for Chapter 4. With the correlation between the dissociative methane adsorption and vacancy formation energies, the vacancy formation energy is used to describe the catalytic activity of the Mn-doped surface. *Chapter 4 shows to correctly represent the electronic structure and behavior of Mn in Mn-doped CeO₂ (111) surface, a U-correction on the d-states of Mn must be included*. Depending upon the *U*-value chosen, the most stable oxidation state for Mn can vary. At low *U*-values, a $p(2 \times 2)$ unit cell expansion with 25% Mn concentration reduces Mn⁴⁺ to Mn³⁺ upon formation of an oxygen vacancy. Mn reduces instead to Mn²⁺ at high *U*-values. Using a *U*-value of 4 eV, as recommended by Wang et al.,² the most stable oxidation state for isolated Mn atoms in a reduced surface is Mn²⁺. The difference in energy between Mn reducing to Mn²⁺ and Mn³⁺ at a *U*-value of 4 eV is closely matched to the equivalent difference in energy as predicted by the HSE06 hybrid functional. This helps to confirm that a *U*-value of 4 eV is reasonable.

Though the previous work established the potential for C-H activation, the stability of the Mn-dopant in ceria has not been established. For all concentrations and arrangements of Mn atoms in the doped CeO₂ (1 1 1) surface without oxygen vacancies, the formation energy is endergonic and therefore Mn does not favorably dope into the surface. *Under sufficiently reducing conditions, the formation energy is favorable for doping Mn into CeO₂ (1 1 1) with oxygen vacancies,*

indicating that Mn will dope into the reduced surface. The most favorable concentration and arrangement for Mn to dope into CeO₂ occurs when Mn atoms are diagonal to one another or when Mn atoms form a continuous row (short row). As Mn is not stable doped into the surface of CeO₂ without oxygen vacancies, the first oxygen vacancy is not catalytically important. The second oxygen vacancy becomes catalytically important as it may form and re-oxidize during catalyzed redox processes. The second oxygen vacancy formation energy is highly dependent upon the concentration and orientation of Mn atoms.

Chapter 5 is the first study to apply DFT to the complete oxidation of a hydrocarbon larger than methane over any oxide. *We developed an approach using DFT and ab-initio thermodynamics to model the reaction path along with all possible intermediate reaction steps including re-oxidation and intermediate product desorption (partial oxidation).* In the cleanup of effluent from biomass gasification, hydrocarbon larger than methane will have to be reformed. Propane is used as a model hydrocarbon to examine the ability of M-doped CeO₂ (1 1 1) to reform larger hydrocarbons. Chapter 5 first examines the reaction path of reforming propane over a bare fully-oxidized Zr-doped CeO₂ (1 1 1) in oxidizing, reducing and extremely reducing environments. *We then show that the bare, fully-oxidized Zr-doped CeO₂ (1 1 1) surface is not the active surface during the reforming of propane under the oxidizing, reducing or extremely reducing environments.* Instead the surface will be either covered in hydrogen (oxidizing and reducing environments) or have half of the surface oxygen atoms covered in hydrogen and the other half vacant (extremely reducing environment). Therefore, for propane oxidation to occur, surface oxygen sites need to become available through either vacancy refilling, H₂ desorption, or H₂O desorption followed by vacancy refilling. Requiring these processes will alter the reaction path and could slow down the overall rate relative to a surface model where all surface O are available to reactants. Further reforming steps will also require the opening of additional oxygen sites which could also impact the rate. With the surface also being in a further reduced state, the reaction path in all of the

environments could be altered. Our reaction path analysis, including re-oxidation, captures the oxidizing and reducing environments reasonably well, however, the reaction path under extremely reducing (gasifier effluent) conditions is highly misrepresented. The approach utilized in this study is able to differentiate the preferred oxidation products (H_2O or H_2 , CO or CO_2) based on the reaction environment, and connect this distribution to elementary reaction processes. The oxidation environment influences the points during the propane decomposition path at which surface re-oxidation occurs. Our results demonstrate that erroneous mechanistic conclusions can be reached when examining redox catalysis over oxide surfaces if the initial surface oxidation state about which the catalytic cycle oscillates is not properly utilized.

As shown in Chapter 2 and described in more detail in Chapter 3, Mn-doped CeO_2 (1 1 1) is a promising surface for hydrocarbon reforming. Chapter 6 uses the model hydrocarbon of propane to examine the reaction path for reforming of propane over the surface. The reforming path for propane over Mn-doped CeO_2 (1 1 1) is very similar to the reforming path over Zr-doped CeO_2 as described in Chapter 5. The initial hydrogen abstraction energy on the two surfaces are very similar with the only major differences between the two surfaces, the point at which the second primary carbon forms a bond with a surface oxygen is later on Mn-doped ceria and the point at which the surface re-oxidizes is also later on the Mn-doped surface under both oxidizing and reducing conditions. All possible intermediate desorption energies are more endothermic than a hydrogen abstraction or surface re-oxidation of the same species for the oxidizing and reducing environments, leading to only fully oxidizing the propane to CO_2 . For the extremely reducing environment the desorption of the $\text{C}^*\text{C}^*\text{C}^*$ species on the surface and the desorption of the first CO molecule will complete, with their 0 K desorption energies being very similar in energy. On three of the intermediate species during the reforming of propane over the Mn-doped CeO_2 surface there is a radical electron delocalized across multiple bonds between carbon and oxygen atoms.

9.2. Effect of sulfur in effluent from biomass gasification

Cleanup of the effluent from biomass gasification also requires the removal of sulfur from the stream in the form of H_2S . Previously it was shown that La- and Tb-doped CeO_2 have a higher sulfur capacity compared to pure ceria due to faster surface kinetics over La- and Tb-doped CeO_2 .³ Chapter 7 showed that combining MnO_x with CeO_2 yields a sulfur sorbent with low pre-breakthrough H_2S from CeO_2 and the high sulfur capacity from MnO_x , but with higher than expected sulfur capacities. XANES shows the presence of Mn^{3+} and Mn^{2+} in as calcined samples and after sulfidation, XANES shows Mn^{2+} and Ce^{3+} . Two reasons, based on insight from DFT, why Mn-doped CeO_2 (1 1 1) has a higher sulfur capacity compared with ceria doped with other oxides, is the ability of Mn to decrease the oxygen vacancy formation energy of CeO_2 and the favorable H_2S adsorption energies, even without sub-stoichiometric oxygen vacancies. *The favorable H_2S adsorption energy without sub-stoichiometric oxygen vacancies leads to a larger number of active sites for H_2S adsorption compared to other dopants, due to manganese's ability to access multiple oxidation states.*

Our goal is to design a catalyst that can act as a sulfur sorbent and reform hydrocarbons. Chapter 8 examines the ability of pure, La-, Tb-, and Mn-doped CeO_2 (1 1 1) to reform methane and propane over these sulfided surfaces. *The presence of sulfur in the partially sulfided CeO_2 or M- CeO_2 (1 1 1) surfaces will decrease the number of active sites for the activation of hydrocarbons in the gas phase.* Surface sulfur sites are less active for the rate limiting stem of C-H activation, through partial sulfidation has little effect on the remaining surface oxygen atoms. Though H^* formation preferably occurs on surface oxygen atoms, there is a slight preference for CH_3^* species to bind to surface sulfur atoms. The hydrocarbon species and their subsequent dehydrogenation to surface CS species represent a potential deactivation route, as CS desorption is significantly less favorable than CO desorption. The highly endergonic desorption energy of CS will result in the

surface of the sulfided case to have carbon buildup more rapidly compared to the un-sulfided surface. La- and Tb-doping have little effect on the surface chemistry, though Mn-doping accelerates C-H activation through Mn^{3+} reduction to Mn^{2+} . *Mn-doping similarly promotes eventual CO product desorption, and also shows a greater preference for some hydrocarbon species to bind to surface oxygen atoms versus sulfur atoms, suggesting potential enhanced tolerance against surface poisoning.* The complete catalytic cycle, including refilling oxygen vacancies, with free energies considered under reaction conditions are not considered and would be necessary to definitively conclude that Mn-doping would accelerate the oxidation rate.

9.3. Perspectives and Suggestions for Future Studies

Chapter 2 illustrated the difficulty in using DFT to model surfaces of CeO_2 (1 1 1) and Chapters 3-8 used a constant U -value of 5 eV on the f -states of cerium and Chapters 4, 7 and 8 used a constant U -value of 4 eV on the d -states of Mn. Instead of using a constant U -values on cerium or other dopants the DFT+ $U(\mathbf{R})$ method can be used.⁴ This method uses the linear-response value of U with respect to every atom, and every atom can have a different U -value. However, the value of U on every atom can change throughout the reaction coordinate and comparison in energies between different U -values is not trivial. Therefore, a constant U -value would have to be chosen and could be chosen by using an average between the two states or using the U -value at the initial or final states. Even though the U -value would change throughout the reaction coordinate, the electronic structure of the system using this method could be more accurate, providing a better understanding of the reaction environment. Though it would be expected using the constant U -value of 5 eV to provide very similar electronic structure compared to the DFT+ $U(\mathbf{R})$ method, as the U -value determined by the linear-response method in other studies all were around 5 eV.⁵ The

DFT+ $U(\mathbf{R})$ method could also be used to verify the U -value of 5 eV on the f -states of ceria systems, to confirm the correct electronic structure behavior of the system.

Instead of using the DFT+ $U(\mathbf{R})$ method to obtain a more accurate electronic structure picture of a ceria system, along with reaction energies, a hybrid functional can be used, like HSE06 (as described in Chapters 2 and 4). A hybrid functional combines a specified amount of nonlocal exact exchange with a GGA functional to help alleviate the self-interaction error present in normal DFT. Energies obtained using a hybrid functional along a reaction coordinate can be directly compared, unlike DFT+ $U(\mathbf{R})$ and can produce correct electronic structure behavior of ceria systems. A hybrid functional also removes the empiricism of selecting U -value (an empirical correction itself), but one must instead select the amount of nonlocal exact exchange to include. The main difficulty in expanding the use of hybrid functionals is its computationally tractability. Hybrid functionals can take an order of magnitude longer to converge along with extra difficulties in getting these hybrid functionals to converge. If these hybrid functionals become more computationally tractable, these functionals could provide a better picture of the electronic structure and reaction energies for these M-doped ceria surfaces.

Instead of using DFT or its variants, a reactive force field could be used, like ReaxFF. A ReaxFF reactive force field can provide energetics sufficiently accurately to model doped ceria systems and sulfided ceria systems. DFT can provide energies and a picture of the electronic structure of the ceria system, however it is only computationally tractable to <200 atoms. With ReaxFF, large scale MD-simulations of ~10,000 atoms for nanoseconds can be performed. These large scale MD-simulations could provide insight into the long range ordering of the dopants in the systems, as well as possible restructuring of the surface when phase separation occurs. With the long range interactions and possible restructuring of the system now evident with ReaxFF, more structures that might not have been found by only using DFT+ U and can be further examined.

These new structures can help to further the understanding of structure-composition-function relationships that exists for M-doped CeO₂.

As described in Chapter 5, the active surface of M-doped CeO₂ is not a bare fully oxidized surface under oxidizing, reducing or extremely reducing conditions. Under oxidation conditions, the surface will mostly be covered in hydrogen and under reducing conditions, the surface will have hydrogens on the surface along with many oxygen vacancies. To better model the active surface of ceria, the reforming of hydrocarbons and the formation of oxygen vacancies should be considered with hydrogens on the surface, along with oxygen vacancies depending upon the reaction environment. The hydrogen on the surface will increase the starting number of reduced cerium (or dopant) atoms present. This increased number of reduced cerium atoms would most likely increase the activation barriers along with the possibility of change the reaction path for methane and propane reforming. Starting with oxygen vacancies in the surface (reducing conditions) will also increase the number of reduced cerium atoms present, thereby increasing the activation barrier and possibly changing the reaction path. Under extremely reducing conditions, the number of oxygen vacancies present will reduce almost every cerium atom to Ce³⁺ in the model used. This reduction of almost every Ce atom would make the surface more likely to resemble the Ce₂O₃ structure compared to the fluorite CeO₂ structure. This restructuring was not allowed to occur and could also change the reaction energies for reforming hydrocarbons. With most every cerium atom reduced in the 4 CeO₂ layered model, a greater number of CeO₂ layers should be used to allow the bulk of the model to maintain its bulk fluorite lattice. ReaxFF could also be used in this case to obtain a clearer picture of what the surface of CeO₂ would look like under reducing and extremely reducing conditions.

Using these surfaces with either hydrogen present or oxygen vacancies and hydrogen present can cause difficulties in trying to model hydrocarbon reforming on these surfaces. With these extremely reduced surfaces, almost all of the cerium atoms will be reduced, as described

above. Activating and then reforming hydrocarbons on this surface, with almost all of the cerium atoms reduced might no longer represent the correct electronic behavior of the system. Increasing the number of layers could help alleviate this problem, however, it still might not be electronically correct. The hydrogen on the surface can cause other difficulties, where either the desorption of hydrogen or oxygen vacancy refilling on the surface would have to occur to open oxygen sites for C-H bond activation of a hydrocarbon and then an additional oxygen sites would have to open up for the hydrocarbon to adsorb to the surface. For further reforming of the hydrocarbon, hydrogen atoms on nearby oxygen atoms would have to desorb or refill nearby oxygen vacancies to allow further reforming steps to occur. A model would have to be developed to describe the desorption of hydrogen atoms and vacancy refilling, and how it would affect the energy of the C-H bond activation and subsequent reforming steps.

Chapters 5 and 6 examined the complete oxidation of propane of Zr- and Mn-doped CeO_2 (1 1 1) surfaces. The Zr- and Mn-doped surface of ceria would be expected to completely oxidize propane, but on other surfaces, partial oxidation of propane could occur. For every step of the propane reforming mechanism of Zr- and Mn-doped CeO_2 , we examined if the hydrocarbon intermediate would 1) dissociate to $\text{C}_z\text{H}_{n-1}^* + \text{H}^*$ (considering all non-equivalent H's and numerous adsorption configurations for $\text{C}_z\text{H}_{n-1}^*$), (2) to dissociate to $\text{C}_{z-1}\text{H}_{n-x}^*$ and CH_x^* , (3) to add an oxygen atom to the surface, or (4) to desorb C_zH_n^* , CO, or CO_2 . If step 4 is more favorable than the other 3 steps for the C_zH_n intermediate, the catalyst would only partially oxidize the hydrocarbon. Step 4 was only considered more favorable if the 0 K energy for the desorbed product was more favorable than all other steps. This assumption reflects the need for desorption to overcome an activation barrier similar to the 0 K unimolecular desorption energy. Using these 4 steps, a catalyst that would only partially oxidize a hydrocarbon can be identified. Catalysts that would be identified a partial oxidation catalyst are ones where the catalyst is only able to reduce by a couple of electrons and then cannot be reduced any further. This would cause any further reforming of the hydrocarbon to

be much higher in energy compared to the desorption of the intermediate. A catalyst where this could occur is where there is only one or two atoms that could reduce in the surface or in a small particle. Another case would be if the adsorbed intermediate is highly stable in the gas phase, which would make the 0 K energy of the desorbed product more favorable than subsequent reforming on the surface.

An extreme case of partial oxidation is the oxidative coupling of methane (OCM). In this mechanism, the catalyst surface abstracts a hydrogen from a methane leaving a methyl radical in the gas phase. Then, instead of the methyl radical adsorbing onto the catalyst surface, the methyl radical would bond with another methyl radical in the gas phase forming ethane. Figure 9-1 illustrates the C-H bond activation of methane, and $\text{CH}_3\bullet$ adsorption onto various oxide surfaces. Most points on the left side are M-doped ceria surfaces and on the right are M-doped MgO surfaces. For an active catalyst for OCM, the C-H bond activation should be as low as possible, but the adsorption of $\text{CH}_3\bullet$ should be higher than the C_2H_6 formation energy. The surfaces to the left side have the lowest C-H bond activation energies, but they are more favorable to adsorb $\text{CH}_3\bullet$ and therefore will not couple $\text{CH}_3\bullet$ in the gas phase. The surfaces to the right would prefer to couple $\text{CH}_3\bullet$ in the gas phase, but are not active enough for the C-H bond activation. Surfaces in the middle should couple $\text{CH}_3\bullet$ in the gas phase, but are also active enough to activate the C-H bond, forming a volcano plot for OCM. Oxides need to be found that are more in the middle of this plot and would therefore be near the top of the volcano plot. Figure 9-1 is an extension to Figure 3-2 which shows a correlation between the dissociative adsorption energy of methane and oxygen vacancy formation. This shows that the correlation between the dissociative adsorption energies of methane and oxygen vacancy formation energies, holds across other oxides besides M-doped ceria and they continue along the same trend line.

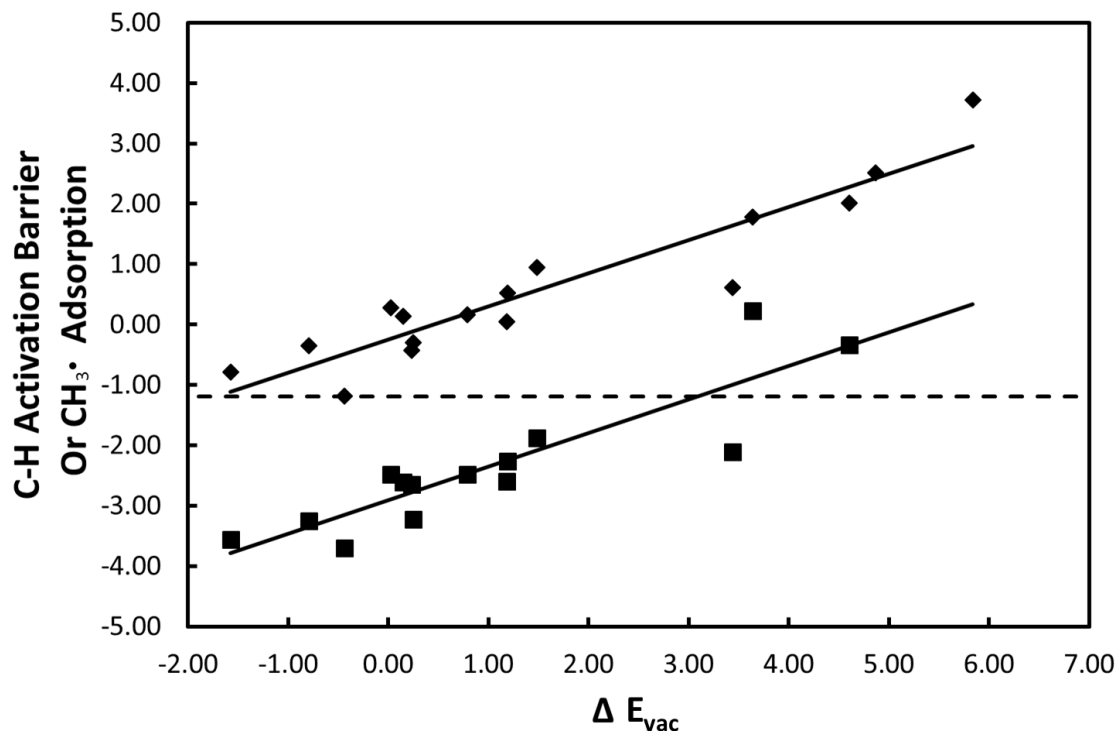


Figure 9-1. C-H activation of methane and $CH_3\bullet$ adsorption energies versus the oxygen vacancy formation energy of various oxide surfaces for oxidative coupling of methane. (\blacklozenge) C-H activation energy of methane, (\blacksquare) adsorption energy of $CH_3\bullet$, (—) best fit line for C-H activation and $CH_3\bullet$ adsorption, (----) C_2H_6 formation energy in gas phase.

The results in this dissertation are encouraging for the use of ceria based catalysts to adsorb sulfur and to reform hydrocarbons from the effluent from biomass gasifiers and provides insight to the electronic nature and energetics of these systems. Further studies will examine the oxidative coupling of methane and partial oxidation of hydrocarbons on oxides, as well as using ReaxFF to obtain a better understanding of the active surfaces on these M-doped ceria surfaces along with other oxides. To improve the efficiencies of conversion of hydrocarbons to other hydrocarbon fuels relies on the ability improve the activity of catalysts. Increasing the activity of these catalysts will depend upon improvements in the ability of DFT to better model oxide surfaces, along with improvements in identifying active sites on heterogeneous oxide surfaces.

9.4. References

1. A. D. Mayernick, M. J. Janik. *Journal of Catalysis* **2011**, 278, 16-25.
2. L. Wang, T. Maxisch, G. Ceder. *Physical Review B* **2006**, 73, 195107.
3. A. D. Mayernick, R. Li, K. M. Dooley, M. J. Janik. *Journal of Physical Chemistry C* **2011**, 115, 24178-24188.
4. H. J. Kulik, N. Marzari. *The Journal of Chemical Physics* **2011**, 135, 194105.
5. D. Y. Lu, P. Liu. *Journal of Chemical Physics* **2014**, 140, 084101.

Appendix A
Supplemental Material for Chapter 3

Table A-1. Subsurface oxygen vacancy formation energies.

Dopant	ΔE_{vac} Surface (eV)	ΔE_{vac} Subsurface (eV)
Ir	1.05	0.95
Os	1.32	1.22
Re	1.99	1.00*
Ru	1.35	1.19

*Dramatic restructuring observed.

Table A-2. Valence configurations for the transition metal dopants used in this study.

Dopant	Valence Configuration
Ag	$4d^{10}5s^1$
Au	$5d^{10}6s^1$
Cd	$4d^{10}5s^2$
Co	$3d^84s^1$
Cr	$3d^44s^2$
Cu	$3d^{10}4p^1$
Fe	$3d^64s^2$
Hf	$5d^26s^2$
Hg	$5d^{10}6s^2$
Ir	$5d^86s^1$
Mn	$3d^64s^1$
Mo	$4d^45s^2$
Nb	$4p^64d^45s^1$
Ni	$3d^84s^2$
Os	$5d^66s^2$
Pd	$4d^{10}$
Pt	$5d^86s^2$
Re	$5d^66s^1$
Rh	$4d^85s^1$
Ru	$4d^65s^2$
Ta	$4d^45s^1$
Ti	$3d^24s^2$
V	$3d^44s^1$
W	$5d^46s^2$
Zn	$3d^{10}4s^2$
Zr	$4s^24p^64d^25s^2$

Table A-3. Number of layers convergence. Vacancy formation energies are not calculated for non-mirrored slabs.

Slab	Dopant	Number of Atomic Layers	ΔE_{ads} (eV)	ΔE_{vac} (eV)
Mirrored	Ag	12	-3.29	-0.35
		15	-3.17	-0.32
		18	-3.27	-0.33
	V	12	-2.07	1.23
		15	-1.96	1.43*
		18	-1.98	1.27
	W	12	-0.82	1.93
		15	-0.75	1.99
		18	-0.77	2.00
Non-Mirrored	V	6	-0.17	-
		9	-1.13	-
		12	-1.09	-
	W	6	-2.23	-
		9	-2.00	-
		12	-2.26	-

* Unable to find lower energy for oxygen vacancy for V with 15 atomic layers

Table A-4. Nearest neighbor oxygen vacancy formation energy and nearest neighbor dissociative methane adsorption energy.

Dopant	ΔE_{vac} (eV)	ΔE_{ads} (eV)
Ag	-0.35	-3.29
Au	-0.08	-1.87
Cd	-0.82	-3.94
Co	0.42	-2.54
Cr	1.23	-1.97
Cu	-0.83	-4.24
Fe	1.09	-1.88
Hf	1.82	-1.63
Hg	-0.56	-3.59
Ir	1.05	-1.64
Mn	0.68	-2.14
Mo	2.34	-0.71
Nb	1.89	-0.96
Ni	0.01	-3.70
Os	1.32	-1.01
Pd	0.59	-2.15
Pt	0.47	-2.52
Re	2.08	-0.13
Rh	1.52	-1.12
Ru	1.35	-1.82
Ta	1.68	-1.31
Ti	1.31	-1.86
V	1.23	-2.07
W	1.93	-0.82
Zn	-1.13	-4.19
Zr	1.63	-1.39

(15 Layers)

(18 Layers)

A.1. Site Projected Charge Method

The optimal value of Wigner-Seitz radii (RWIGS) for Ce atoms was chosen by manipulating the value and quantifying the difference in the number of electrons assigned between Ce^{3+} and Ce^{4+} species. This was done for a system in which PDOS and orbital analysis already revealed which Ce atoms were reduced upon vacancy formation. The charge difference upon reduction (diamonds in Figure A-1) was examined by taking the Ce^{3+} atom with the smallest charge and subtracting the largest value of the charges on the Ce^{4+} atoms, representing the smallest change in reduced cerium atoms. The charge variation among Ce^{4+} atoms was determined by subtracting the smallest charge on a Ce^{4+} in the slab from the largest charge on the Ce^{4+} atom (squares in Figure A-1). The value of RWIGS that is chosen for providing Ce atom oxidation state assignments is 0.7 Å. This value gives good contrast for the cerium atoms that reduced compared to the cerium atoms that did not reduce, as it represents the minimum in variation among Ce^{4+} atoms and shows significant Ce^{4+} to Ce^{3+} differentiation.

Decreasing the value of RWIGS will decrease the total number of electrons associated with each cerium atom. As the reduced cerium atoms have an electron in the f orbital which is tight to the cerium atom, a small RWIGS value allows easy identification of the presence of this electron. A RWIGS value below 0.7 was not chosen because the number of electrons counted in the d orbital becomes negative for values smaller than 0.7 Å, as an artifact from this method.

In Figure A-2, charges from the Bader atoms-in-molecules method are compared to the site projected charge method. Cerium atoms number 10 and 18 are reduced to Ce^{3+} in the structure considered. The variance among cerium atoms that did not reduce is much greater in the Bader method than the site projected charge method (RWIGS = 0.7). The site-projected breakdown of s , p , d , and f electrons is given in Figure A-3. The number of electrons counted in the s , p , and d orbitals of cerium, for either Ce^{4+} or Ce^{3+} , stays relatively constant. However the number of

electrons counted in the f orbital of Ce^{3+} versus the number electrons in Ce^{4+} varies significantly. This further illustrates the reliability of using the site-projected method with an RWIGS value of 0.7 in determining which Ce atoms reduce.

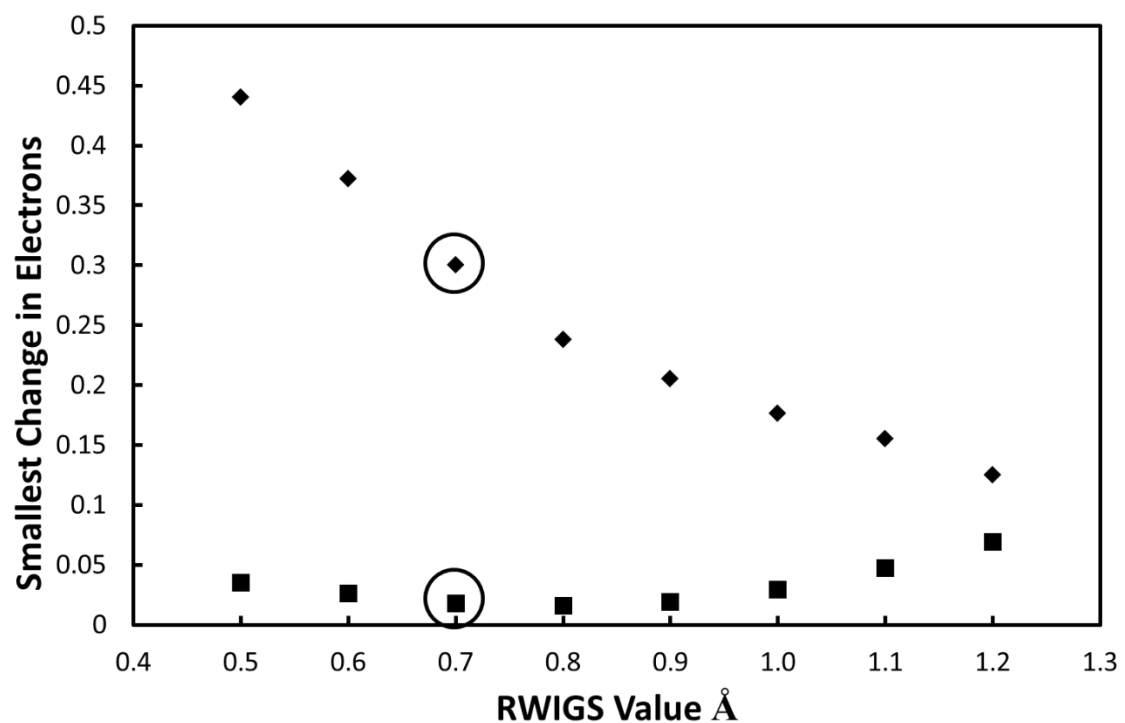


Figure A-2. Difference in number of electrons between a Ce^{4+} atom and Ce^{3+} atom (◆) and maximum variation of number of electrons counted for all Ce^{4+} (■) vs. the RWIGS value on Ce. An RWIGS value of 0.7 was used to determine which cerium atoms reduced in this study.

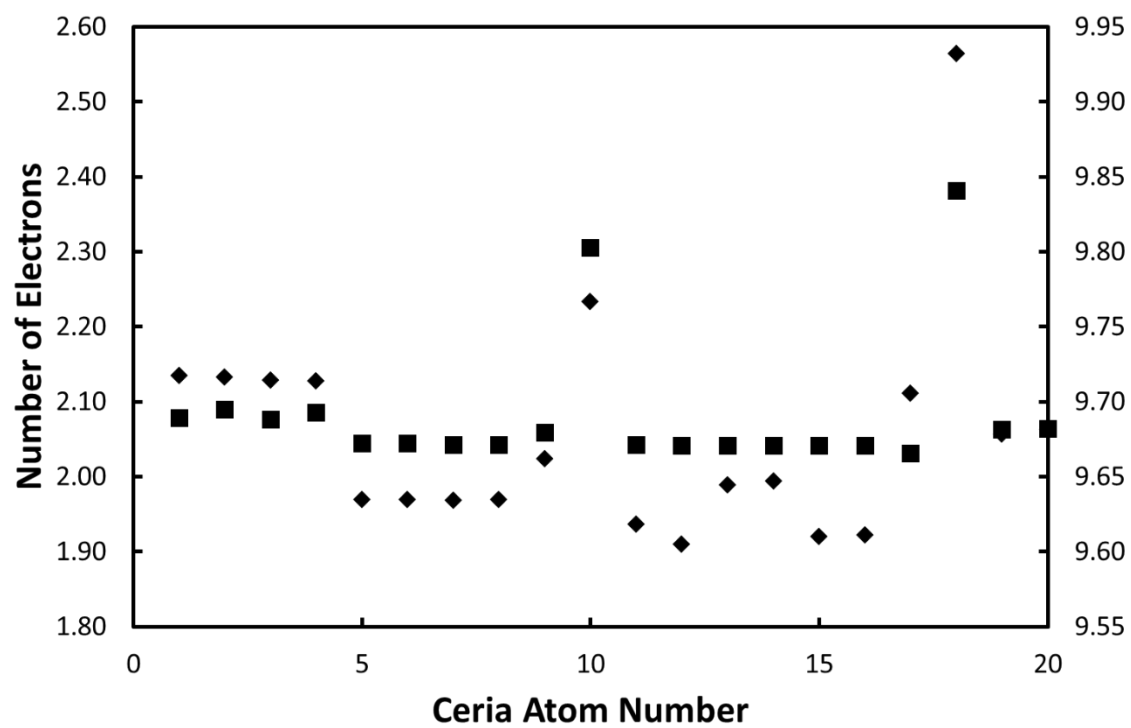


Figure A-3. Number of electrons around every cerium atom in a reduced CeO_2 (1 1 1) surface counted by the site projected method using an RWIGS value of 0.7 (■) and the Bader atoms-in-molecules method (◆). Ce atoms number 10 and 18 are Ce^{3+} and all others are Ce^{4+} .

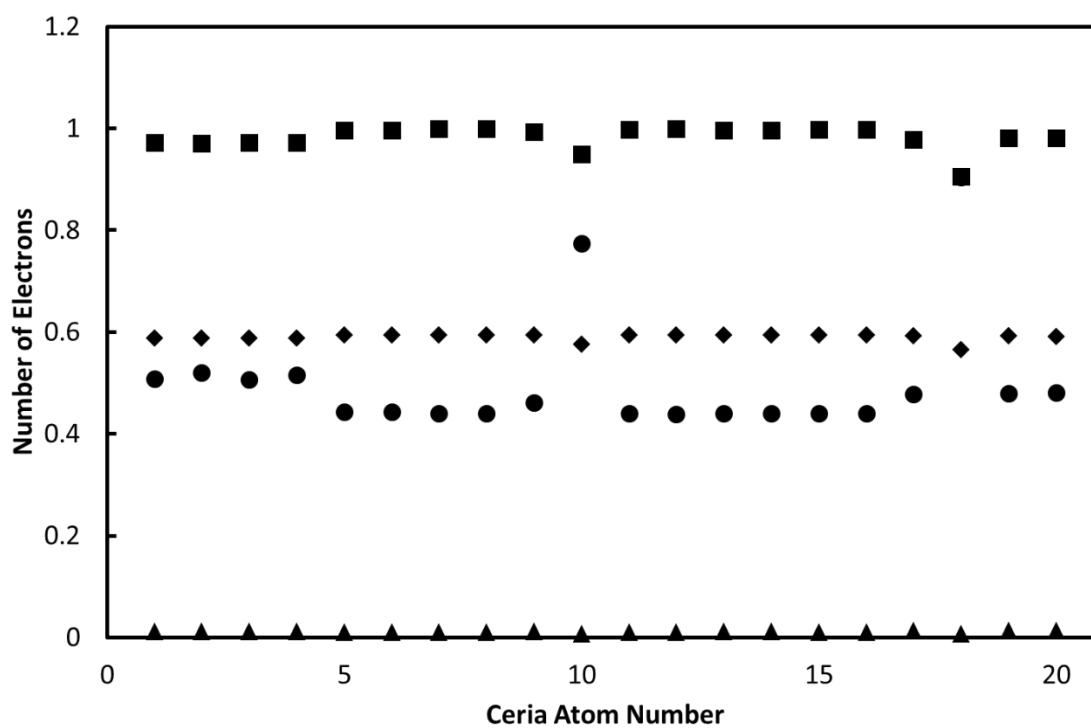


Figure A-4. Number of electrons counted in each orbital of the cerium atoms by the site projected charge method (RWIGS = 0.7). The number of s (◆), p (■) and d (▲) electrons is relatively constant, whereas the f (●) electron count changes significantly for the two Ce^{3+} atoms (10 and 18 (for 18, the circle and square overlap)) and is relatively constant for all other non-reduced cerium atoms (Ce^{4+}).

A.2. Structural Assignment Categorization Scheme

The oxygen coordination number of M-dopants in CeO₂ (1 1 1), either in fully oxidized or reduced form, was determined by first calculating the average of the three shortest M-dopant to oxygen distances. Three M-O distances were used as it was found that no M-O first-coordination shell had less than three O-atoms. A cut-off distance for the first M-O coordination shell was then established by considering any O within a certain multiple of this averaged distance as bound. Based on a visual scan of structures, we determined that any M-O distance within 9% of this shortest difference average could be taken to be bonded. For a value of 9%, an increase or decrease of this value results in the smallest number of dopants changing their coordination numbers. The bond lengths for the seven (six for oxygen vacancy) closest dopant oxygen distances are included in Table A-8. Using the dopant coordination number, the arrangement of the bonded oxygen atoms around the dopant is examined and a structure is assigned. Table A-5 contains the dopant coordination number, along with the structural assignment of the dopant coordination environment. The possible structures for intact M-doped CeO₂ are illustrated in Figure A-4. Structures for an oxygen-vacancy containing M-doped CeO₂ (1 1 1) surface are in Figure A-5, and structures for methane dissociatively adsorbed onto M-doped CeO₂ (1 1 1) are in Figure A-6.

Table A-5. Number of layers convergence. Vacancy formation energies are not calculated for non-mirrored slabs.

Dopant	Intact		Oxygen Vacant		Methane Adsorbed	
	Coordination Number	Structure	Coordination Number	Structure	Coordination Number	Structure
Ag	5	Square Planar	4	Square Planar	4	See-Saw*
Au	4	Square Planar	4	Square Planar	4	Square Planar
Cd	6	Octahedral	6	Trigonal Prismatic	5	2
Co	3	Pyramidal	4	Trigonal Pyramidal	4	Trigonal Pyramidal
Cr	4	Trigonal Pyramidal	4	Trigonal Pyramidal*	5	2
Cu	4	Trigonal Pyramidal	3	T-Shaped	4	Square Planar
Fe	4	Square Planar*	4	Square Planar	4	Trigonal Pyramidal
Hf	4	Tetrahedral	6	Trigonal Prismatic	5	2
Hg	6	Octahedral	5	Square Pyramidal*	4	See-Saw*
Ir	6	Octahedral	4	Square Planar	6	Octahedral
Mn	3	Pyramidal	4	Square Planar*	4	Square Planar*
Mo	4	Tetrahedral	6	Trigonal Prismatic	5	2
Nb	4	Tetrahedral	6	Trigonal Prismatic	5	2
Ni	4	Trigonal Pyramidal	4	Trigonal Pyramidal	4	Square Planar
Os	4	Tetrahedral	6	Trigonal Prismatic	4	See-Saw*
Pd	6	Octahedral	3	Square Pyramidal	4	Square Planar
Pt	6	Octahedral	4	Square Planar	4	Square Planar
Re	4	Tetrahedral	6	Trigonal Prismatic	5	1
Rh	6	Octahedral	4	Square Planar	4	Square Planar
Ru	4	Tetrahedral	5	3	5	Square Pyramidal
Ta	4	Tetrahedral	6	Trigonal Prismatic	4	Trigonal Pyramidal
Ti	4	Trigonal Pyramidal	4	Trigonal Pyramidal	5	2
V	4	Trigonal Pyramidal	4	Trigonal Pyramidal	4	Trigonal Pyramidal
W	4	Tetrahedral	6	Trigonal Prismatic	5	1
Zn	4	Trigonal Pyramidal	4	Trigonal Pyramidal	4	Trigonal Pyramidal
Zr	4	Tetrahedral	6	Trigonal Prismatic	5	2
Ce	7	Cubic	6	Trigonal Prismatic	5	2

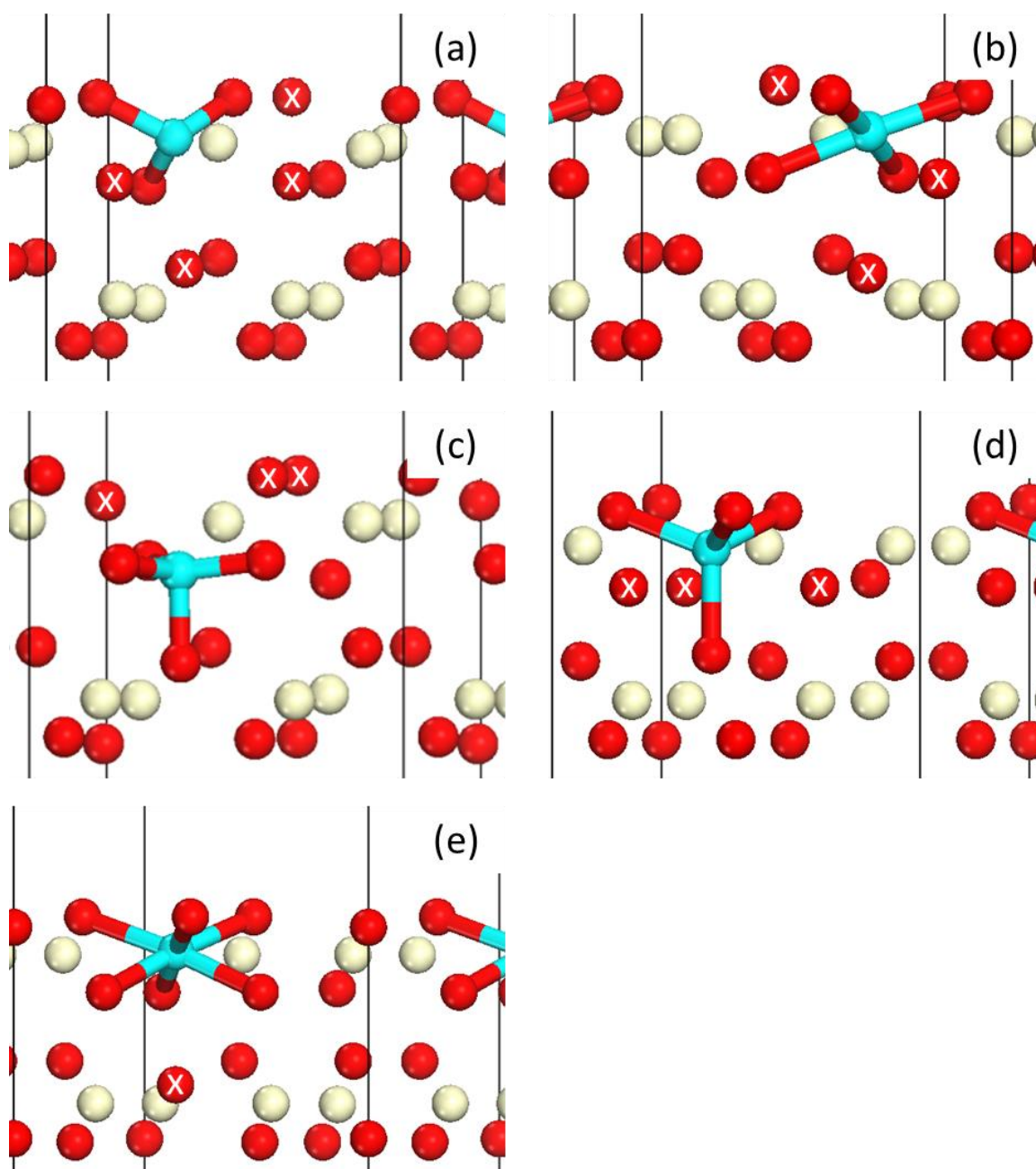


Figure A-5. Five possible oxygen coordination environments about an intact M-dopant in CeO₂ (1 1 1). (a) Mn coordinated in pyramidal, (b) Ag coordinated in square planar, (c) V coordinated in trigonal pyramidal, (d) Zr coordinated in tetrahedral, and (e) Pd coordinated in octahedral. Ce is displayed as tan (light), M-dopant as light blue (gray), and O as red (dark). The oxygen atoms labeled with X's are the oxygen atoms not bonded, but are part of the 7 closest oxygen atoms.

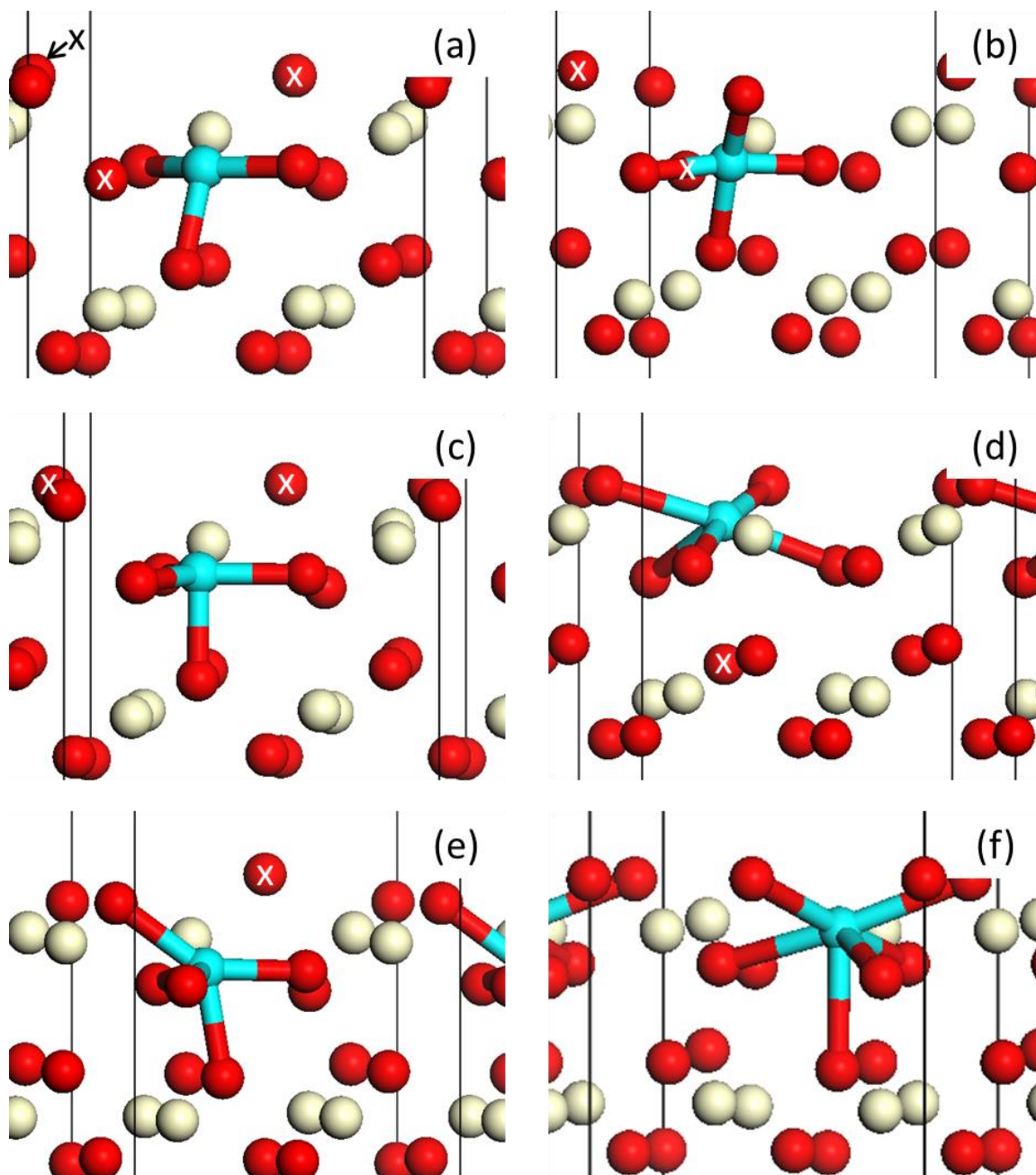


Figure A-6. Six oxygen coordination environments with an oxygen vacancy in M-doped in CeO_2 (1 1 1). (a) Cu coordinated in T-shaped, (b) Fe coordinated in square planar, (c) Ni coordinated in trigonal pyramidal, (d) Hg coordinated in square pyramidal, (e) Ru coordinated in 4, and (f) Cd coordinated in trigonal prismatic. Ce is displayed as tan (light), M-dopant as light blue (gray), and O as red (dark). The oxygen atoms labeled with X's are the oxygen atoms not bonded, but are part of the 6 closest oxygen atoms.

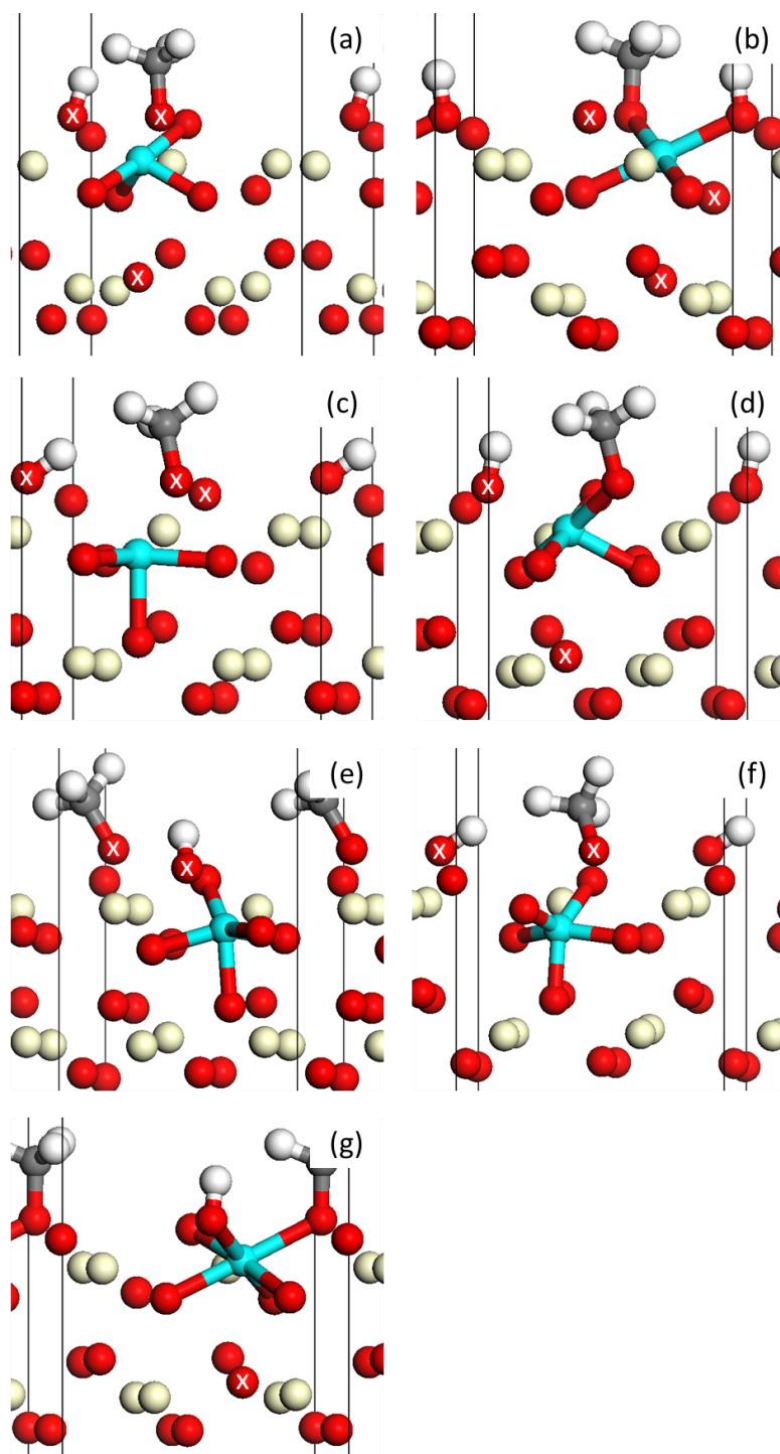


Figure A-7. Seven oxygen coordination environments with methane dissociatively adsorbed on M-doped CeO_2 (1 1 1). (a) Os coordinated in see-saw, (b) Fe coordinated in square planar, (c) Ni coordinated in trigonal pyramidal, (d) Ru coordinated in square pyramidal, (e) W coordinated in 1, (f) Cr coordinated in 2, (g) Ir coordinated in octahedral. Ce is displayed as tan (light), M-dopant as light blue (gray), and O as red (dark). The oxygen atoms labeled with X's are the oxygen atoms not bonded, but are part of the 7 closest oxygen atoms.

Table A-6. Bond lengths for dopant to 7 closest oxygens (6 with oxygen vacancy). Highlighted ones for the methane adsorbed structure are oxygens with the hydrogen or the methyl radical adsorbed to.

Dopant	Intact Structure Bond Lengths (Å)							Oxygen Vacant Structure Bond Lengths (Å)						Methane Adsorbed Structure Bond Lengths (Å)						
	1	2	3	4	5	6	7	1	2	3	4	5	6	1	2	3	4	5	6	7
Ag	2.162	2.165	2.192	2.196	2.354	2.756	2.832	2.261	2.261	2.392	2.395	2.519	2.726	2.214	2.272	2.342	2.361	2.586	2.836	3.102
Au	2.110	2.113	2.136	2.136	2.348	2.856	2.930	2.079	2.083	2.085	2.088	2.772	2.851	2.041	2.044	2.126	2.136	2.688	2.964	3.056
Cd	2.330	2.330	2.331	2.393	2.395	2.395	2.622	2.294	2.310	2.310	2.469	2.469	2.477	2.331	2.341	2.351	2.434	2.478	2.580	2.712
Co	1.844	1.847	1.847	2.077	2.731	2.736	2.749	1.836	1.875	1.948	2.024	3.168	3.215	1.800	1.914	1.943	1.951	3.088	3.298	3.305
Cr	1.786	1.785	1.786	1.847	3.136	3.136	3.138	1.625	1.793	1.883	1.891	1.936	3.156	1.644	1.844	1.844	1.860	1.911	3.581	3.674
Cu	1.909	1.909	1.910	1.965	3.060	3.065	3.072	1.859	1.860	1.920	2.819	3.474	3.475	1.924	1.933	1.960	2.056	3.110	3.483	3.683
Fe	1.784	1.814	1.817	1.908	2.957	3.468	3.480	1.799	1.804	1.862	1.909	3.125	3.820	1.890	1.914	1.914	1.938	3.021	3.262	3.333
Hf	2.087	2.095	2.096	2.096	2.438	2.438	2.438	2.040	2.108	2.137	2.138	2.143	2.143	2.076	2.106	2.124	2.146	2.179	2.368	2.369
Hg	2.335	2.335	2.335	2.384	2.385	2.385	2.776	2.370	2.371	2.419	2.419	2.452	2.747	2.241	2.275	2.455	2.466	2.619	2.859	2.903
Ir	2.119	2.119	2.119	2.185	2.186	2.186	2.558	1.914	1.921	1.972	2.008	2.869	3.005	2.085	2.098	2.110	2.187	2.190	2.193	2.992
Mn	1.736	1.737	1.794	2.736	2.739	2.774	3.365	1.849	1.864	1.906	1.944	2.932	3.660	1.861	1.889	1.889	2.033	2.646	3.343	3.513
Mo	1.818	1.818	1.829	1.956	2.409	2.546	2.562	1.885	1.889	1.938	2.018	2.024	2.058	1.863	1.878	1.909	1.909	2.033	2.297	3.889
Nb	1.916	1.924	1.927	2.064	2.482	2.490	2.628	1.960	1.962	1.994	2.114	2.120	2.139	1.975	1.991	2.024	2.033	2.087	2.571	2.664
Ni	1.820	1.862	1.864	1.940	3.110	3.111	3.161	1.947	1.960	1.970	2.068	3.095	3.163	1.859	1.859	1.863	1.882	3.525	3.673	3.900
Os	1.836	1.850	1.878	1.956	2.205	2.370	2.489	1.938	1.937	1.964	1.978	1.978	1.997	1.949	1.953	1.978	2.007	2.169	2.174	3.055
Pd	2.134	2.135	2.135	2.259	2.259	2.285	2.853	2.143	2.179	2.198	2.484	2.598	2.622	2.077	2.123	2.128	2.180	2.742	2.788	3.353
Pt	2.109	2.109	2.109	2.221	2.221	2.221	2.907	1.986	1.998	2.027	2.027	3.382	3.825	2.006	2.063	2.155	2.162	2.313	2.950	2.954
Re	1.809	1.809	1.810	1.903	2.338	2.340	2.349	1.911	1.926	1.960	1.974	1.974	1.979	1.885	1.900	1.927	1.943	1.945	2.162	3.854
Rh	2.161	2.163	2.163	2.206	2.207	2.260	2.485	1.952	1.998	2.026	2.077	3.262	3.761	2.161	2.173	2.211	2.213	2.408	2.742	2.859
Ru	1.949	1.955	1.958	2.012	2.522	2.533	2.559	1.922	1.925	1.966	2.032	2.038	3.616	1.968	2.027	2.067	2.103	2.118	2.225	3.031
Ta	1.911	1.921	1.921	2.032	2.440	2.440	2.666	1.968	2.010	2.017	2.027	2.029	2.115	1.907	1.949	1.954	1.955	2.226	2.333	3.469
Ti	1.905	1.917	1.920	1.953	2.170	3.206	3.262	1.830	1.830	1.904	1.925	2.924	3.029	1.863	1.919	1.944	1.952	2.065	3.453	3.570
V	1.731	1.733	1.738	1.767	3.206	3.245	3.245	1.706	1.707	1.760	1.781	3.323	3.341	1.723	1.729	1.734	1.755	3.245	3.436	3.449
W	1.826	1.827	1.838	1.962	2.339	2.516	2.541	1.903	1.907	1.949	1.970	2.006	2.009	1.884	1.893	1.914	1.935	1.960	2.195	3.823
Zn	1.994	1.995	1.995	2.074	3.297	3.311	3.337	1.996	1.997	2.047	2.082	3.086	3.086	2.024	2.026	2.031	2.067	2.940	3.170	3.267
Zr	2.141	2.141	2.141	2.141	2.430	2.431	2.431	2.105	2.116	2.144	2.156	2.160	2.170	2.103	2.138	2.142	2.168	2.195	2.421	2.472
Ce	2.353	2.354	2.357	2.359	2.359	2.359	2.362	2.228	2.362	2.372	2.426	2.433	2.445	2.335	2.340	2.412	2.443	2.450	2.603	2.605

Table A-7. Adsorption energies and vacancy formation energies demonstrating the increasing of the number of layers in slab used to correct non-symmetries.

Dopant	Number of Atomic Layers	ΔE_{ads} (eV)	ΔE_{vac} (eV)	Adsorption	Vacancy
Au	12	-1.88	0.19	Au^{3+}	Not Symmetric
	15	-1.87	-0.08	Au^{3+}	Au^{3+}
	18	-1.90	0.61	Au^{3+}	Au^{2+}
	21	-1.88	-0.08	Au^{3+}	Au^{3+}
	24	-1.87	-0.09	Au^{3+}	Au^{3+}
Re	12	-0.44	1.99	Re^{6+}	Re^{6+}
	15	-0.20	2.07	Re^{6+}	Re^{6+}
	18	-0.13	2.08	Re^{6+}	Re^{6+}

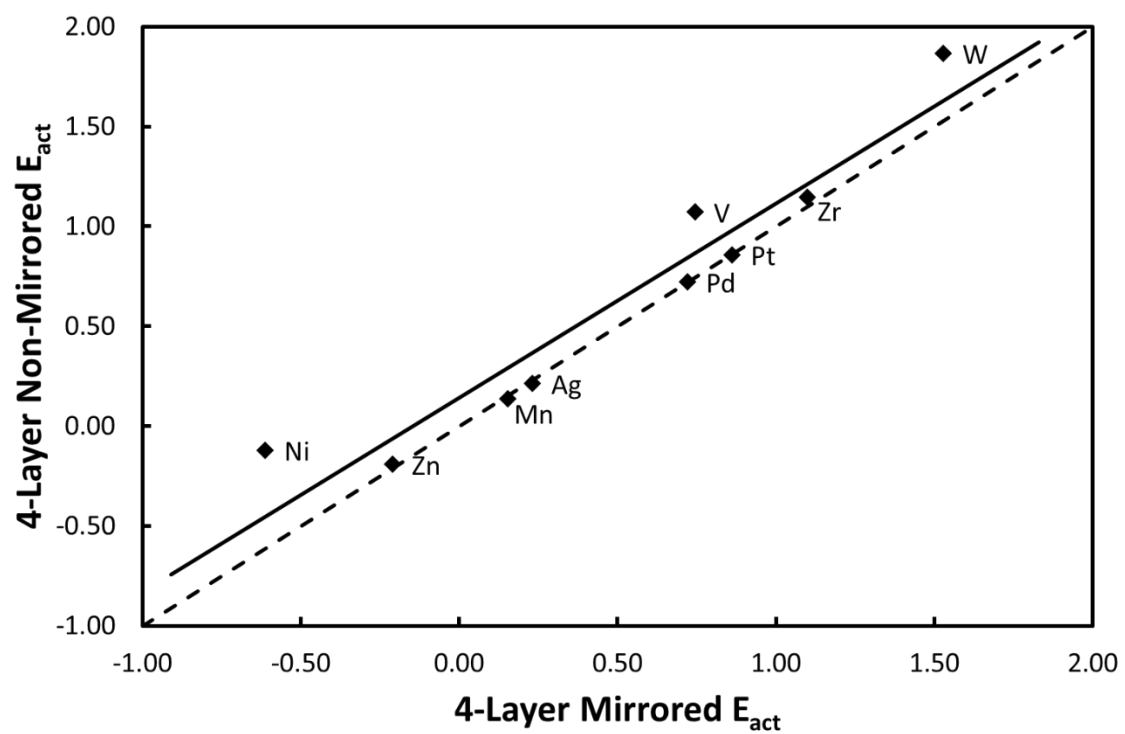


Figure A-8. Hydrogen absorption and methyl radical formation energies (E_{act}) on 4-layer non-mirrored M-doped CeO₂ versus 4-layer mirrored M-doped CeO₂. (----) E_{act} non-mirrored = E_{act} mirrored, (—) best fit line.

Table A-8. Activation barriers to the pseudo-transition and true transition states as well as the dissociative methane adsorption energies.

Dopant	True Transition State (eV)	Pseudo-Transition State (eV)	ΔE_{ads} (eV)
Ag	0.39	0.21	-3.35
Mn	-	0.14	-2.68
Ni	0.29	-0.12	-3.41
Pd	-	0.72	-1.73
Pt	-	0.86	-2.82
V	1.07	1.07	-2.26
W	1.90	1.87	-1.09
Zn	0.17	-0.19	-4.04
Zr	1.42	1.14	-1.48

Appendix B**Supplemental Material for Chapter 4**

Table B-1. Surface oxygen vacancy formation energies at different values of U on d -states of Mn in a $p(2 \times 2)$ unit cell expansion with a 25% surface Mn concentration.

U -value	Mn ²⁺ (eV)	Mn ³⁺ (eV)	Mn ⁴⁺ (eV)
0.0	1.47	0.74	1.08
2.0	0.65	0.31	1.05
3.0	0.22	0.08	-
3.5	0.00	-0.02	-
4.0	-0.13	-0.03	-
4.5	-0.33	-0.13	-
5.0	-0.48	-0.16	-

Table B-2. Surface, subsurface and 2nd oxygen vacancy formation energies for Mn-doped CeO₂ (1 1 1) with $U = 4$ eV on d -states of Mn. The second oxygen vacancy is calculated relative to a structure with the first surface oxygen vacancy formed.

	ΔE_{vac} Surface Oxygen Vacancy (eV)	ΔE_{vac} Subsurface Oxygen Vacancy (eV)	ΔE_{vac} 2 Surface Oxygen Vacancies (eV)	ΔE_{vac} 1 Surface and 1 Subsurface Oxygen Vacancies (eV)
2x2 – 1Mn (Mn ³⁺)	-0.03	0.05	1.65	1.40
2x2 – 1Mn (Mn ²⁺)	-0.13	-	1.75	1.50
2x3 – 1Mn (Mn ²⁺)	-0.20	-0.11	1.65	1.72
2x3 – 2Mn Diagonal	-1.66	3.30	1.65	2.72
2x3 – 2Mn Short Row	-2.03	1.03	0.56	3.26
2x3 – 2Mn Long Row	-1.28	-0.70	0.12	0.67
2x3 – 2Mn Sub-Row	-1.55	-0.56	1.30	1.02
2x3 – 2Mn Sub-Diagonal	-1.18	3.44	2.64	2.23

Appendix C

Supplemental Material for Chapter 5

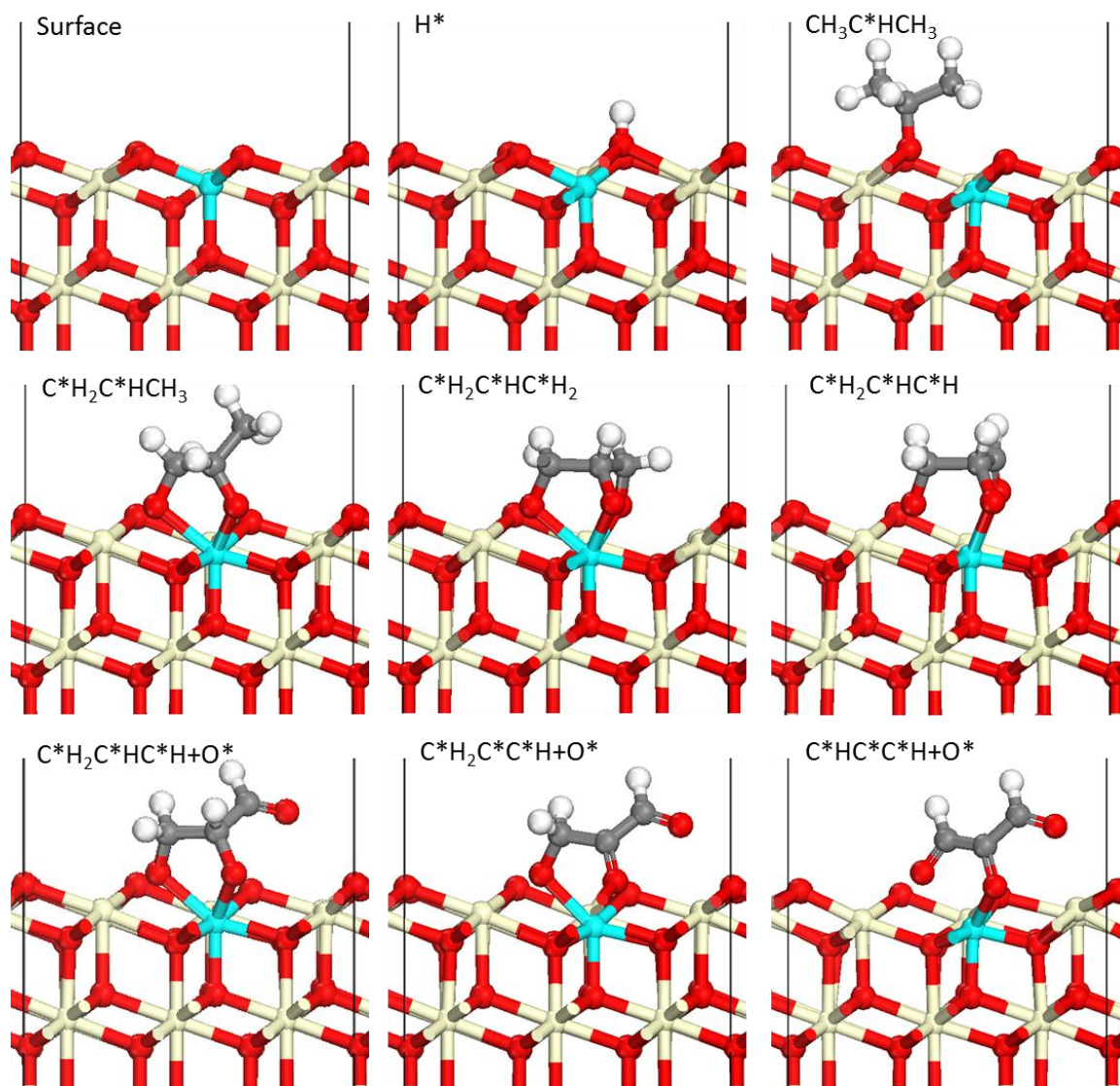


Figure C-1. Structures for first 9 steps (excluding desorption of H* as H₂O and refilling of the 1/2 V_O) to reform propane in an oxidizing environment. Ce is displayed as tan (light), Zr as light blue (gray), O as red (dark).

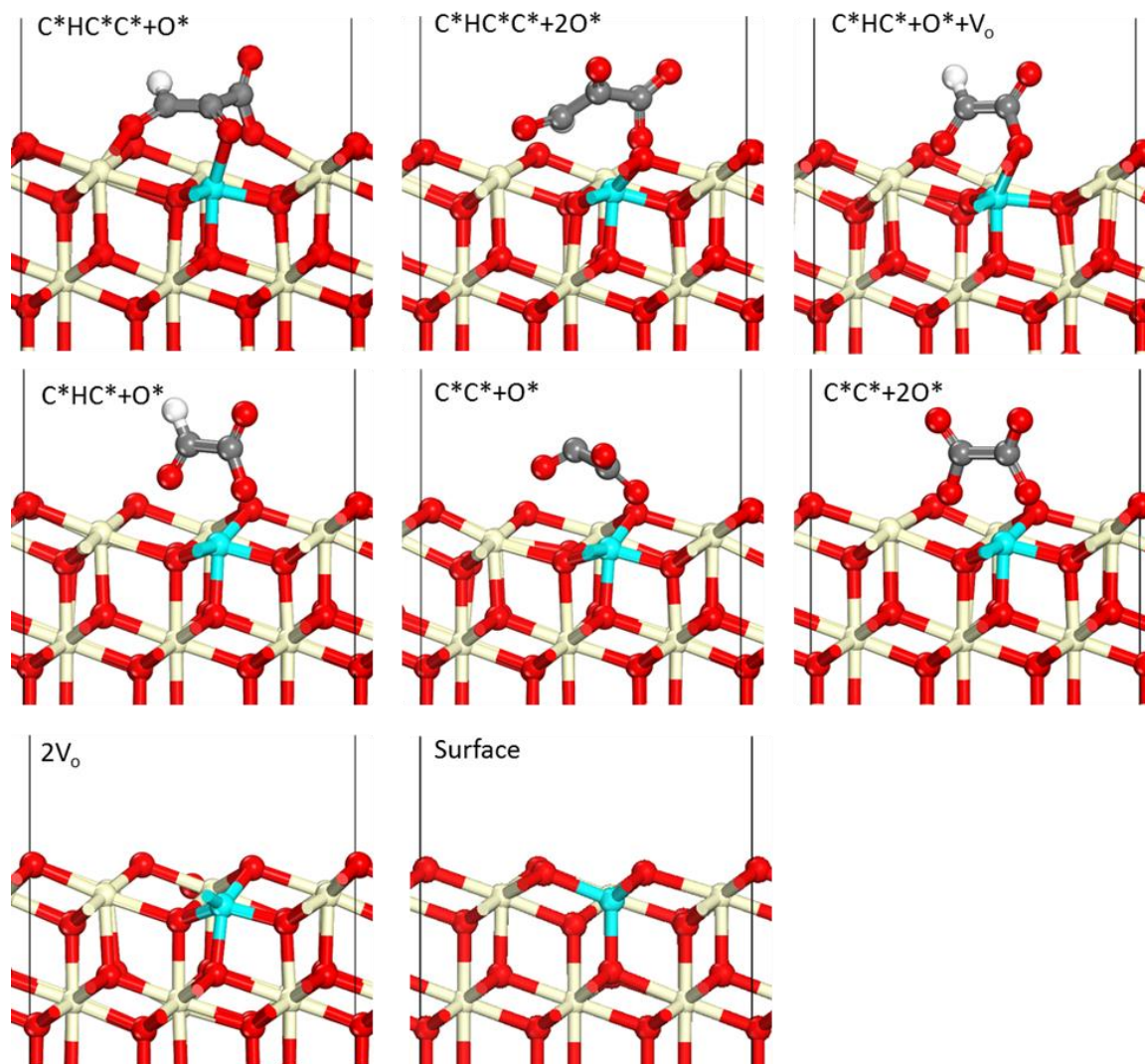


Figure C-2. Structures for last 8 steps (excluding desorption of H^* as H_2O and refilling of the $\frac{1}{2} V_O$) to reform propane in an oxidizing environment. Ce is displayed as tan (light), Zr as light blue (gray), O as red (dark).

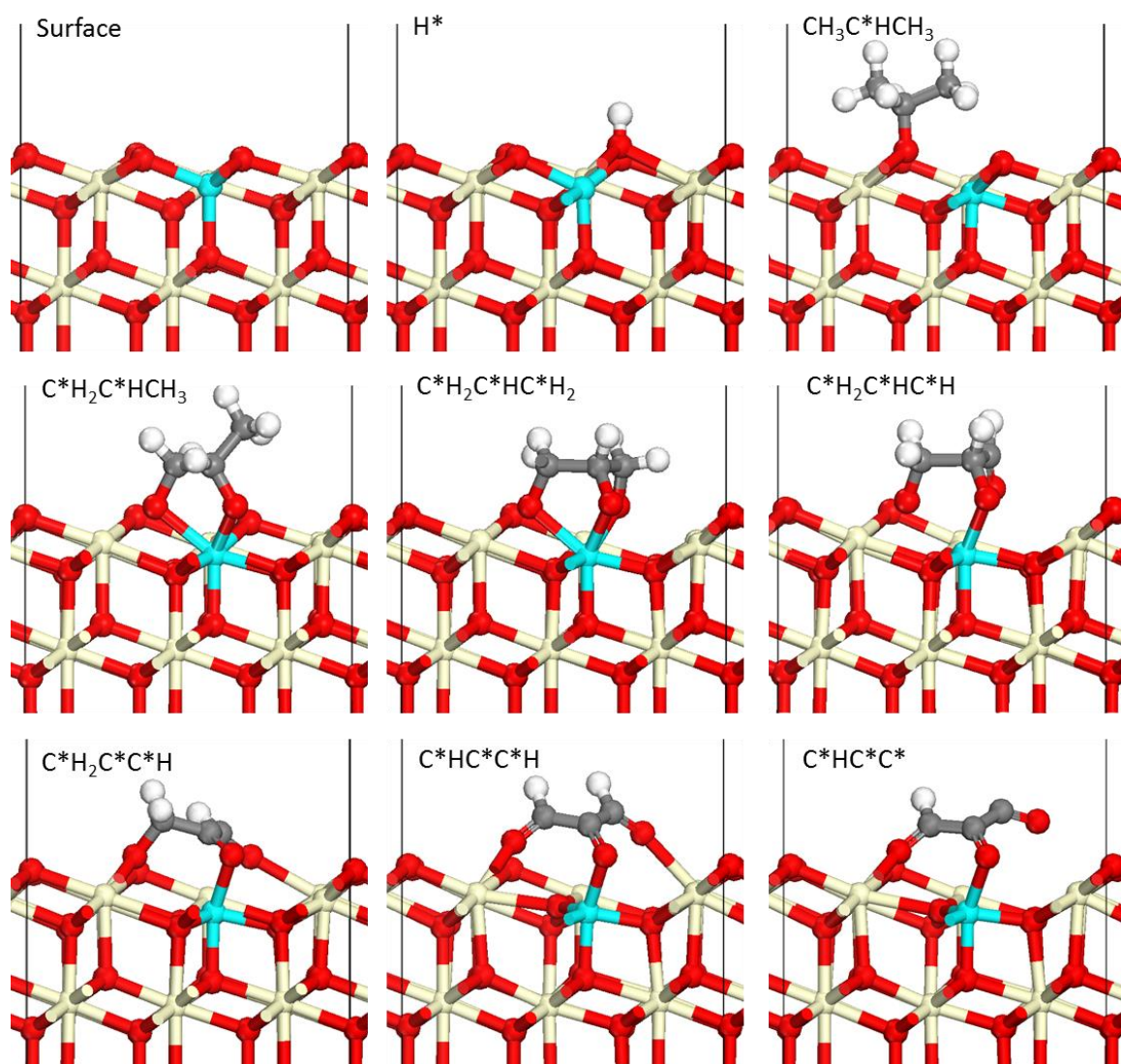


Figure C-3. Structures for first 9 steps (excluding desorption of H* as H₂O and refilling of the 1/2 V_O) to reform propane in a reducing environment. Ce is displayed as tan (light), Zr as light blue (gray), O as red (dark).

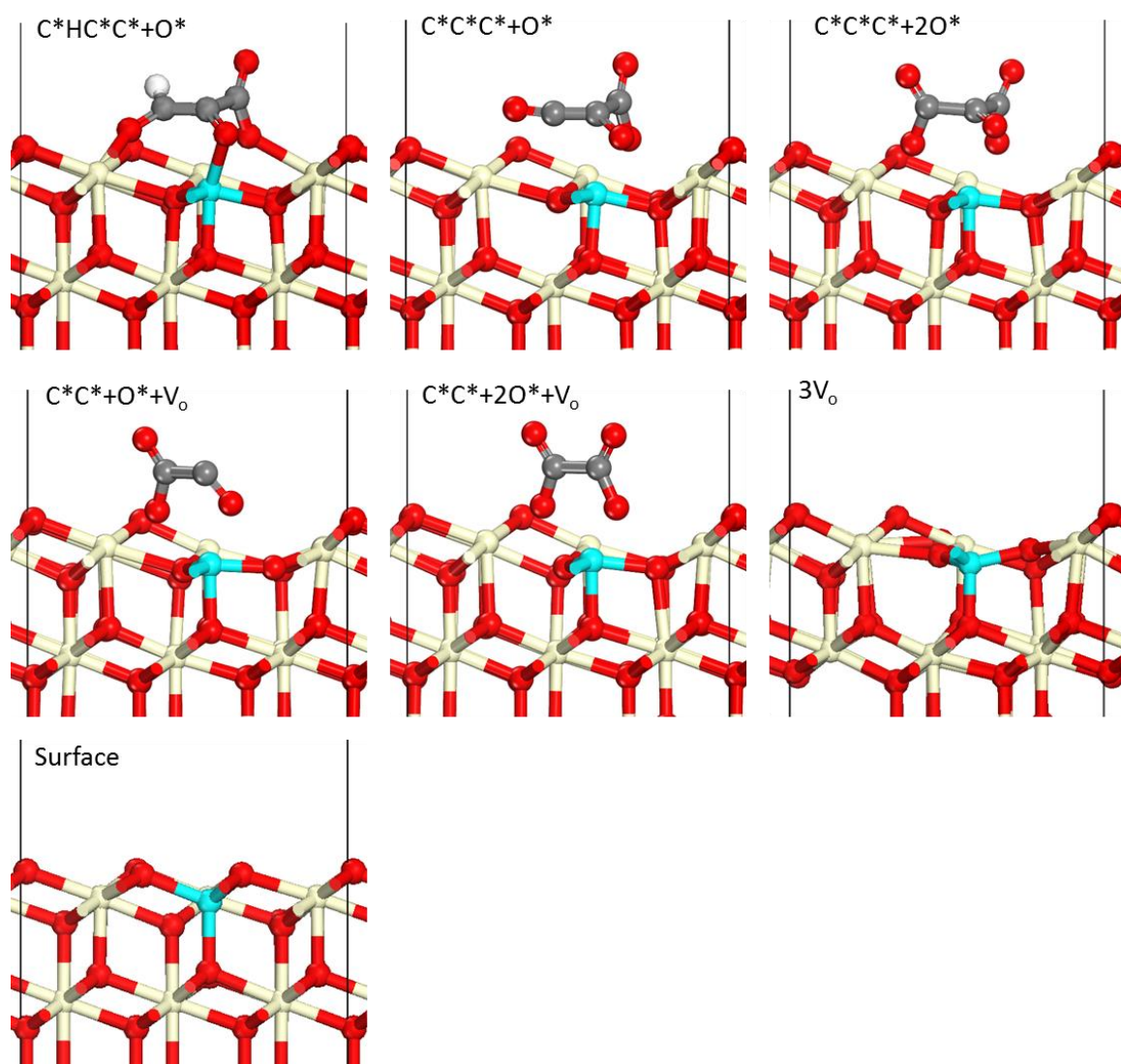


Figure C-4. Structures for last 7 steps (excluding desorption of H^* as H_2O and refilling of the $\frac{1}{2} V_o$) to reform propane in a reducing environment. Ce is displayed as tan (light), Zr as light blue (gray), O as red (dark).

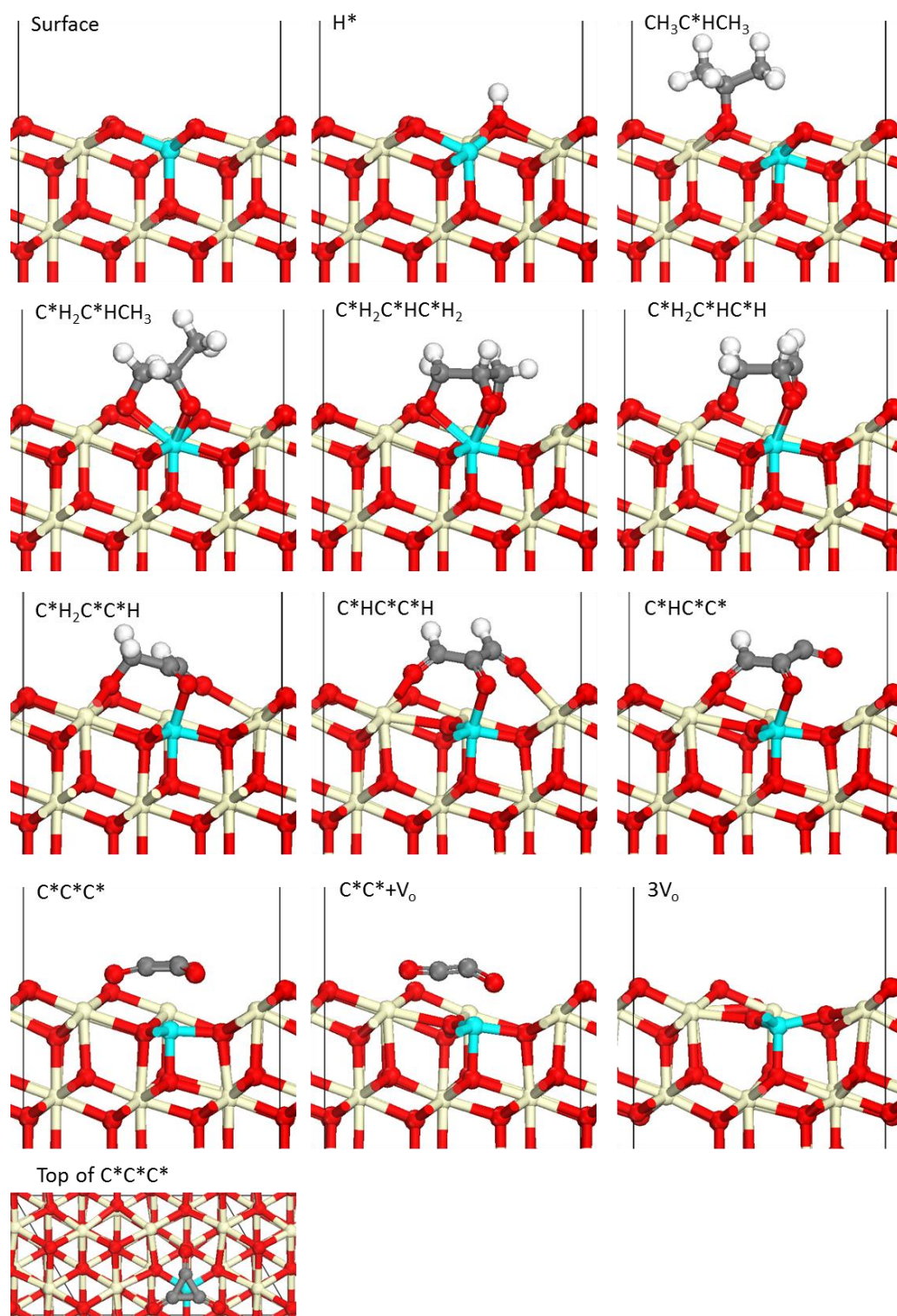


Figure C-5. Structures for all of the steps (excluding desorption of H^* as H_2O and refilling of the $\frac{1}{2} V_O$) to reform propane under extremely reducing (gasifier effluent) conditions. Ce is displayed as tan (light), Zr as light blue (gray), O as red (dark).

Table C-1. 0 K oxygen vacancy formation energies for pure CeO₂ (111) and Zr-doped CeO₂ (111). Each successive oxygen vacancy formation energy is calculated relative to a surface with one less vacancy. The 6th oxygen vacancy in Zr-doped CeO₂ is not electronically possible due the number of cerium atoms that would have to reduce, see Section 5.3.4.

Number of Oxygen Vacancies	Pure CeO ₂ (eV)	Zr-doped CeO ₂ (eV)
1	2.57	1.86
2	2.59	1.69
3	2.73	2.74
4	2.34	2.39
5	2.56	3.07
6	2.63	-

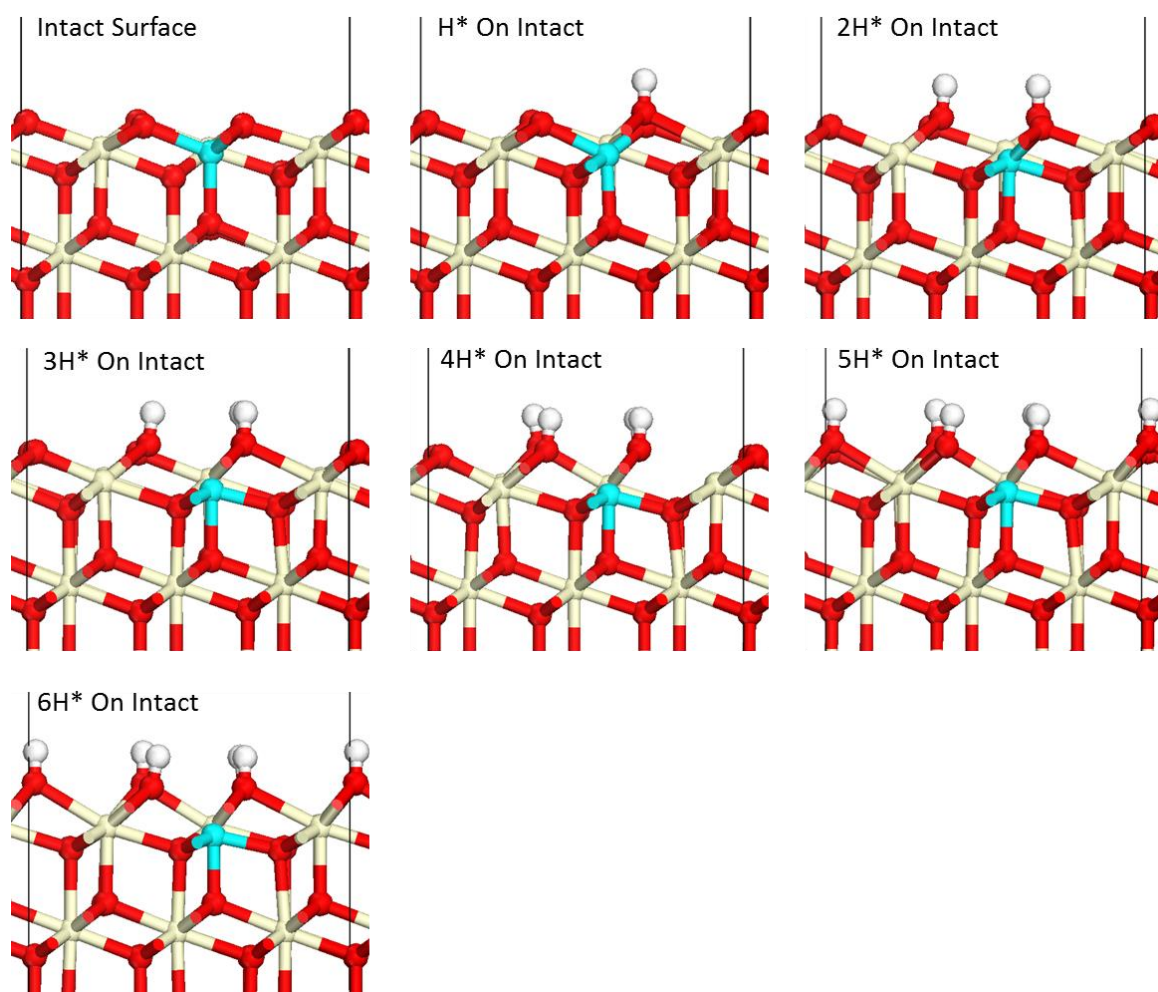


Figure C-6. Structures for hydrogen adsorption on an intact Zr-doped CeO₂ surface. Ce is displayed as tan (light), Zr as light blue (gray), O as red (dark).

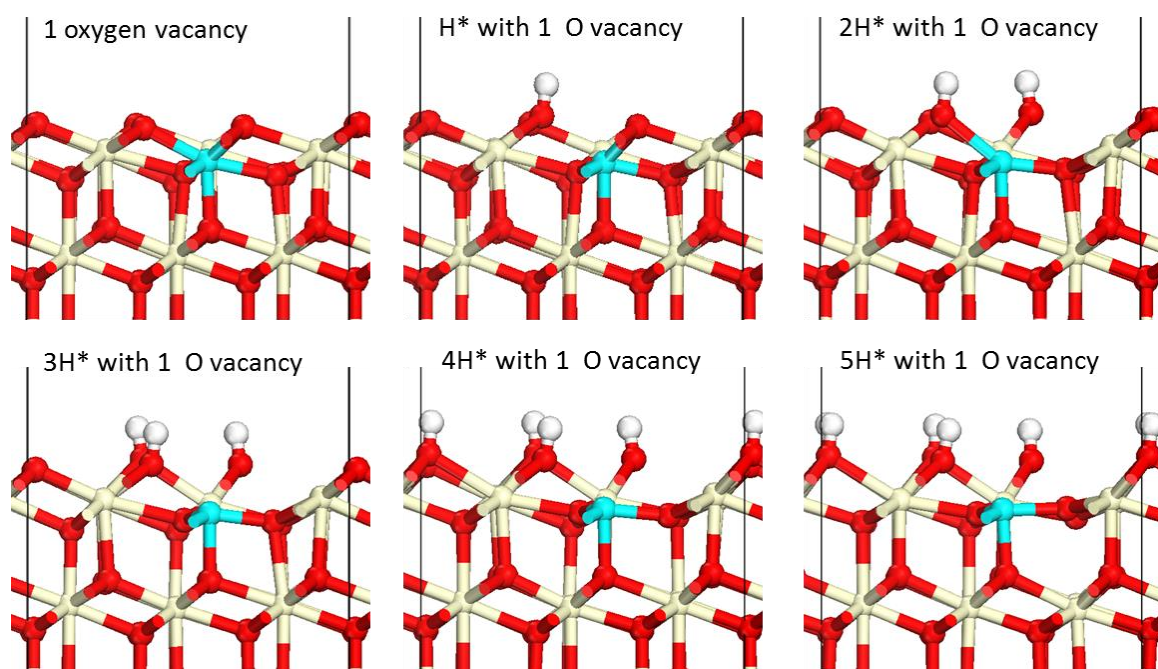


Figure C-7. Structures for hydrogen adsorption on a Zr-doped CeO₂ surface with 1 oxygen vacancy. Ce is displayed as tan (light), Zr as light blue (gray), O as red (dark).

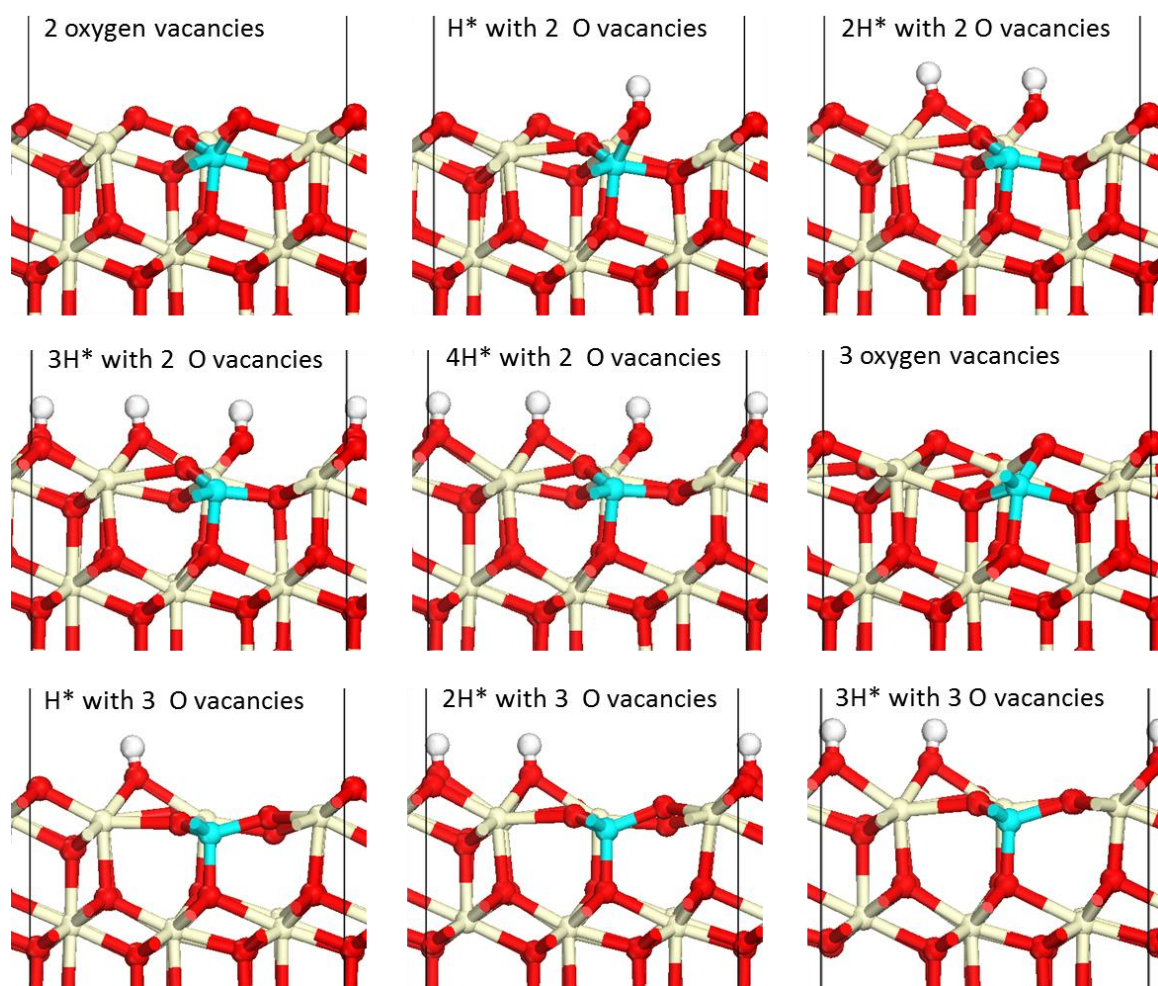


Figure C-8. Structures for hydrogen adsorption on a Zr-doped CeO_2 surface with 2 and 3 oxygen vacancy. Ce is displayed as tan (light), Zr as light blue (gray), O as red (dark).

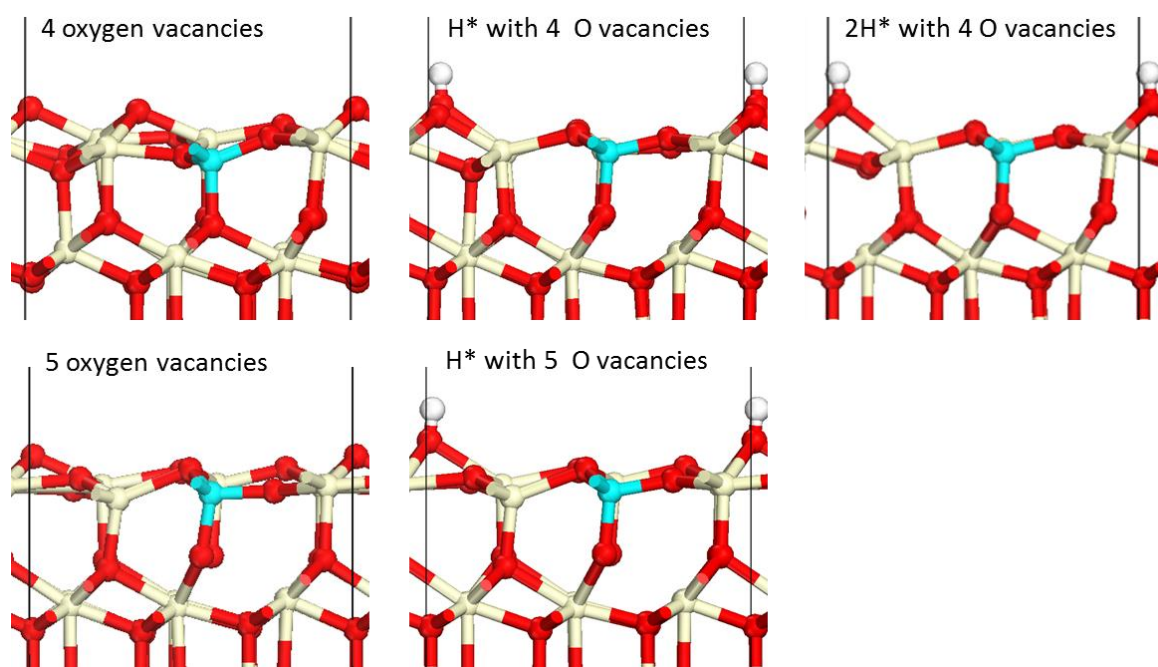


Figure C-9. Structures for hydrogen adsorption on a Zr-doped CeO₂ surface with 4 and 5 oxygen vacancy. Ce is displayed as tan (light), Zr as light blue (gray), O as red (dark).

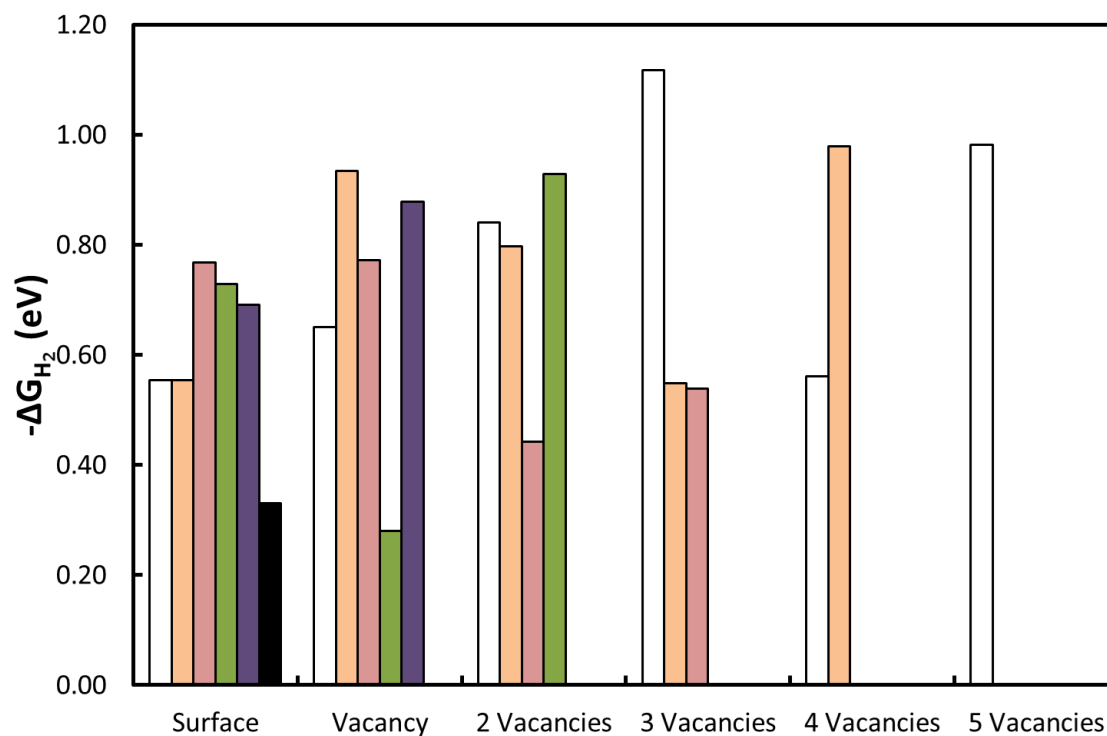


Figure C-10. The energy to absorb $\frac{1}{2}$ H_2 (g) onto the surface of pure CeO_2 varying number of surface oxygen vacancies and number of hydrogen atoms on the surface. The energy to absorb each hydrogen atom is calculated progressively in each step. The partial pressure of hydrogen is 0.234 atm and for oxygen is 6×10^{-20} atm. (white) 1 hydrogens, (orange or lightest gray) 2 hydrogens, (red or light gray) 3 hydrogens, (green or medium gray) 4 hydrogens, (purple or dark gray) 5 hydrogens, (black) 6 hydrogens.

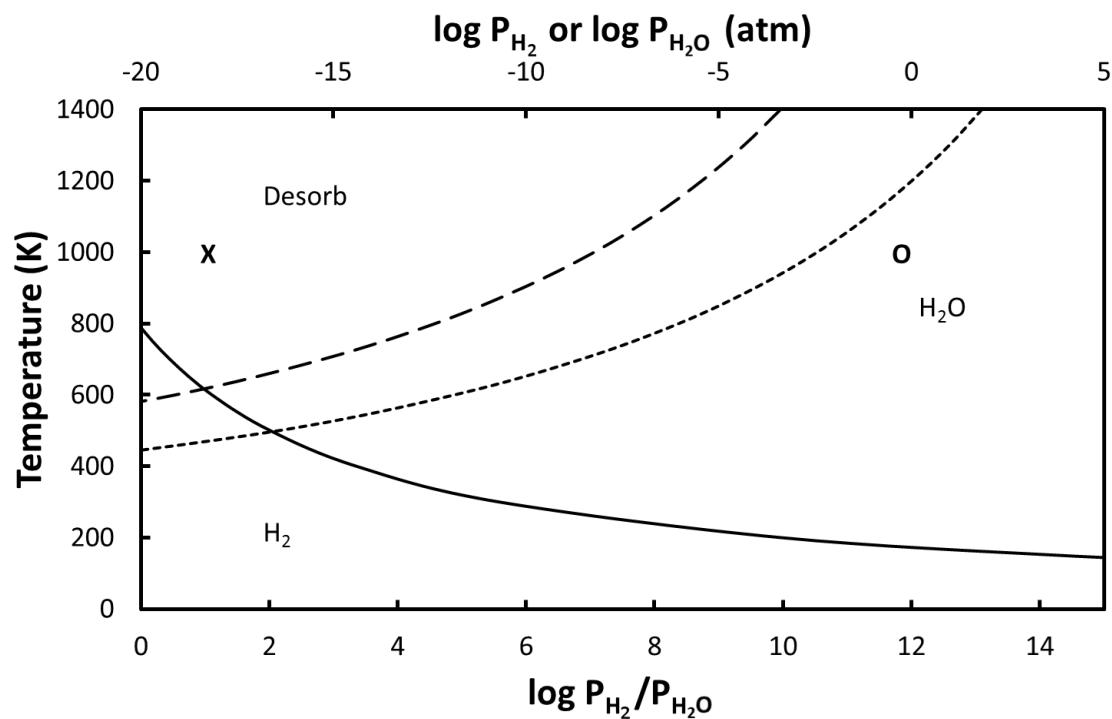


Figure C-11. The pressure-temperature curves as to whether the hydrogen on the surface of pure ceria will desorb as H₂ or H₂O for a pure ceria surface with 6 hydrogens. (—) the division between whether the hydrogen will desorb as H₂ (lower) or H₂O (upper) based on the lower axes. The division on whether the hydrogen will desorb as (---) H₂, or (-·-·-) H₂O, upper axes. Above these lines the hydrogen will desorb and below they will not. The X's represent the composition of the gas when the H₂ or H₂O will desorb and the O's represent the conditions if the hydrogen will desorb.

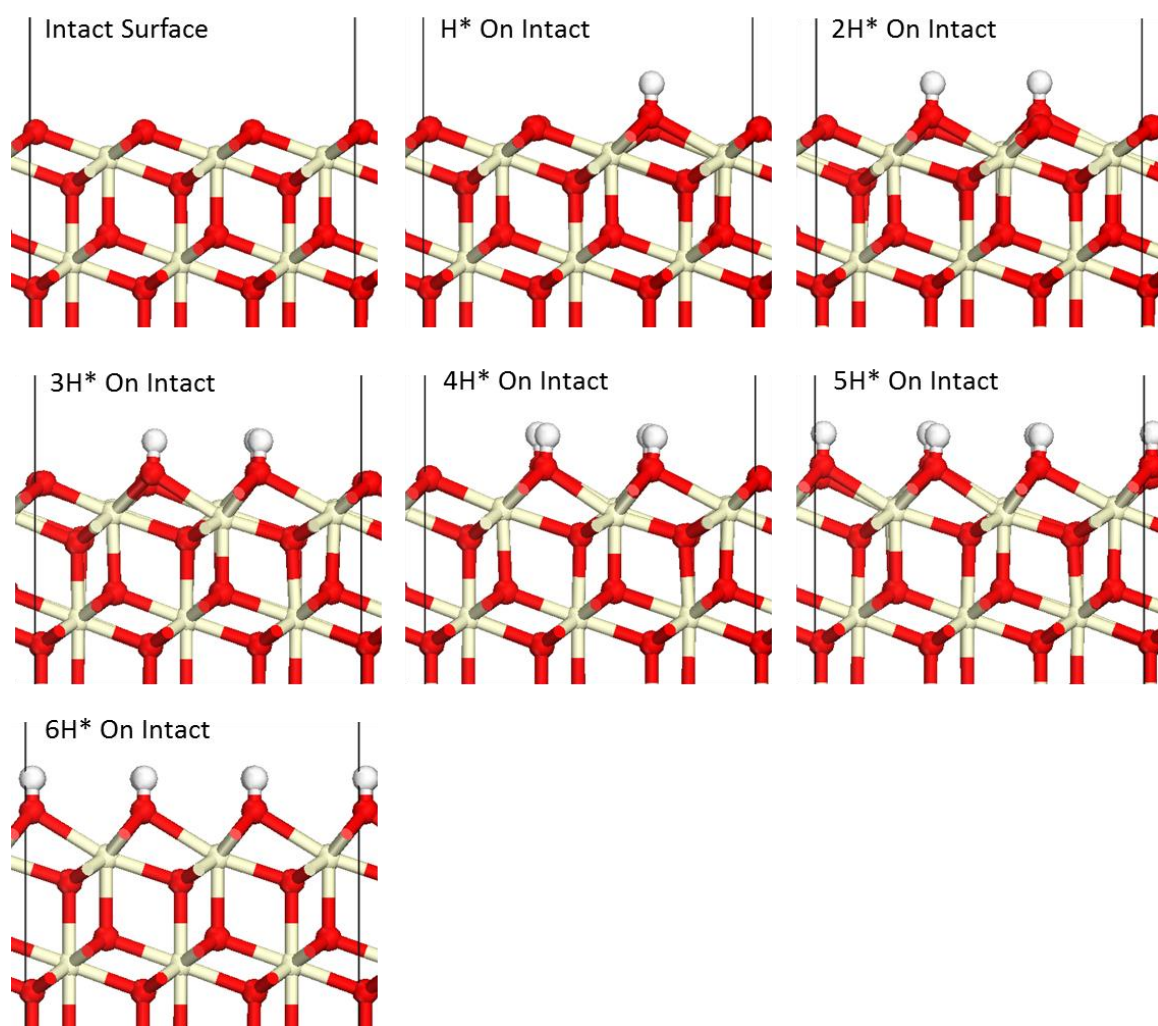


Figure C-12. Structures for hydrogen adsorption on an intact CeO_2 surface. Ce is displayed as tan (light), O as red (dark).

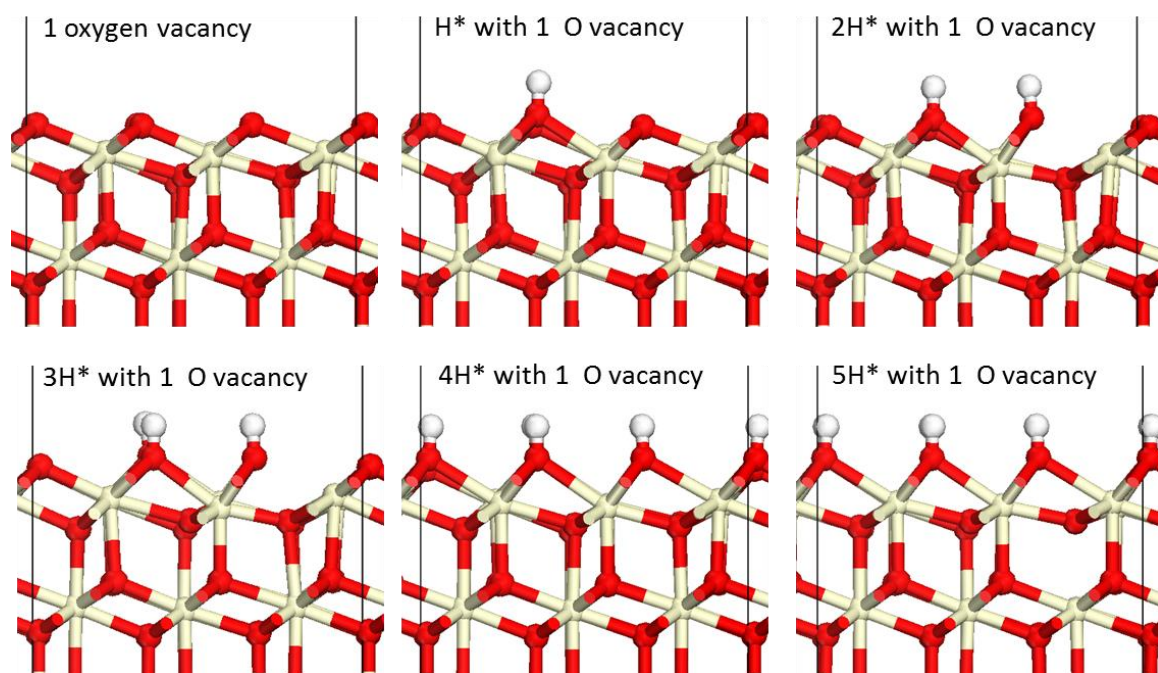


Figure C-13. Structures for hydrogen adsorption on a CeO₂ surface with 1 oxygen vacancy. Ce is displayed as tan (light), O as red (dark).

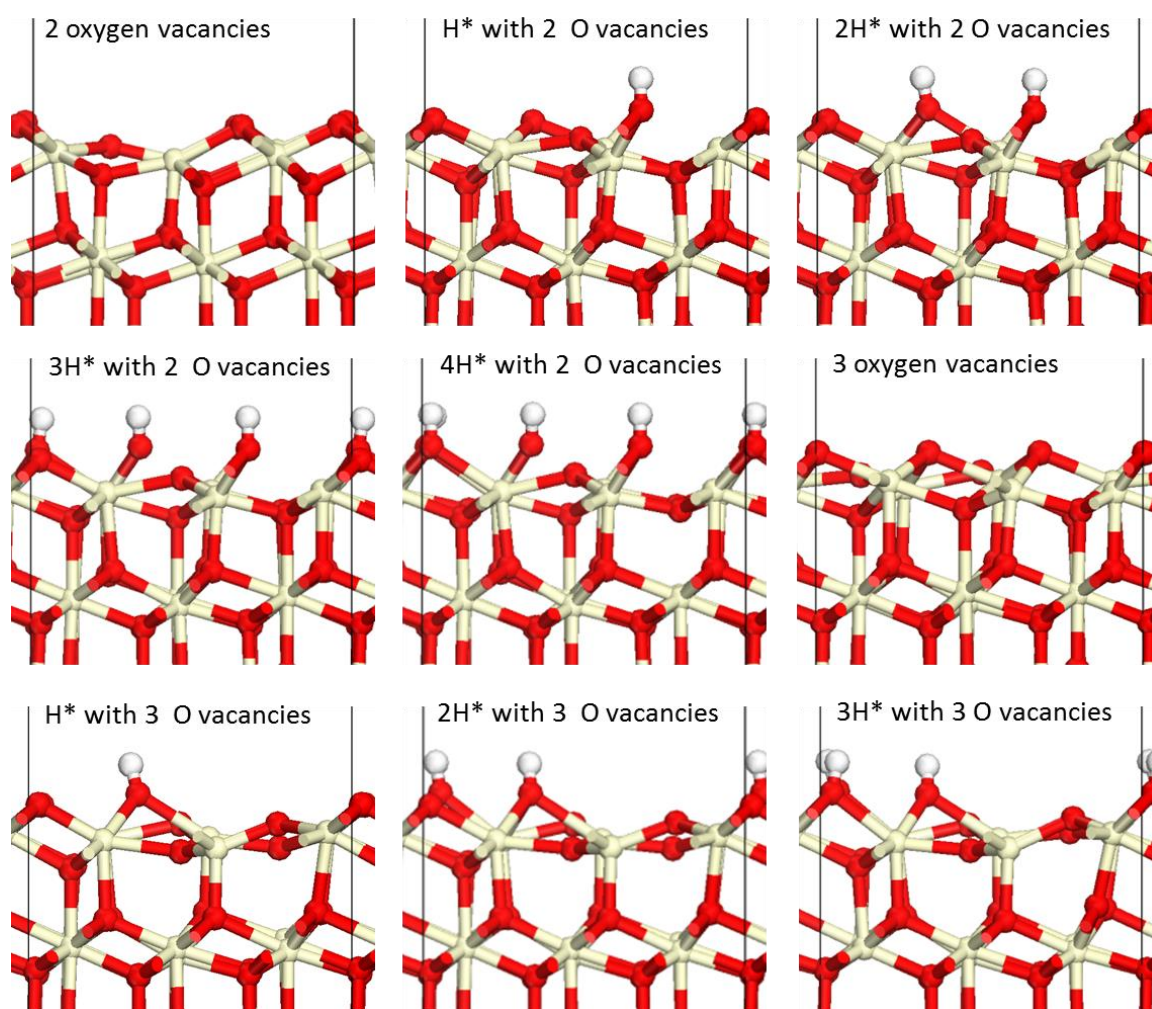


Figure C-14. Structures for hydrogen adsorption on a CeO₂ surface with 2 and 3 oxygen vacancy. Ce is displayed as tan (light), O as red (dark).

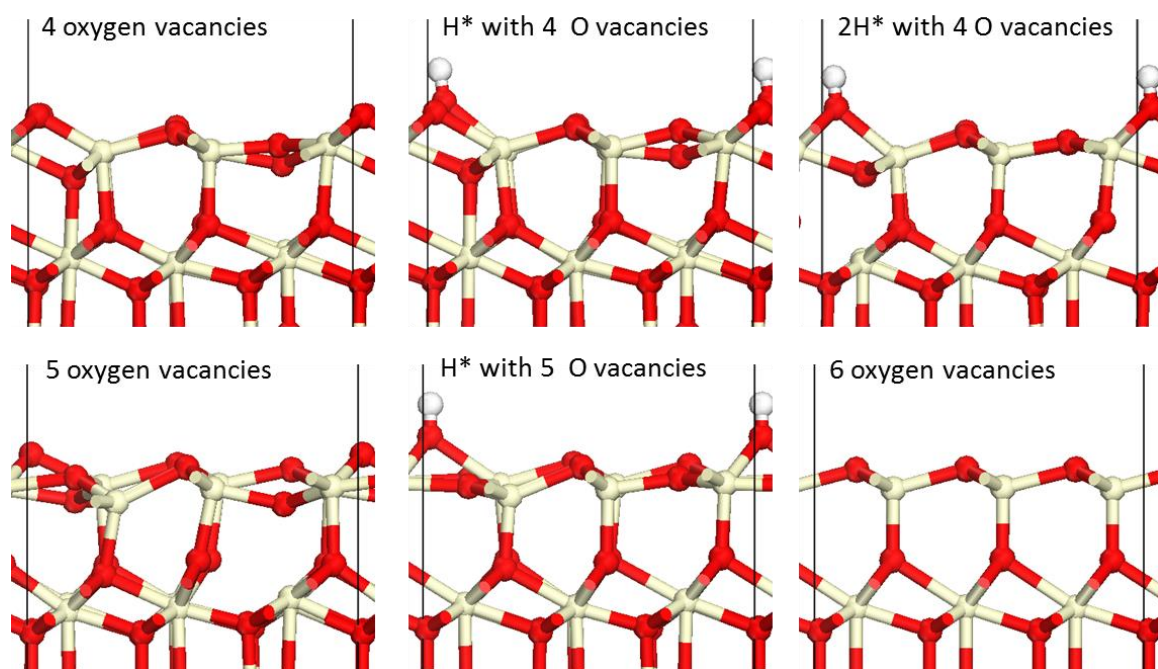


Figure C-15. Structures for hydrogen adsorption on a CeO_2 surface with 4, 5 and 6 oxygen vacancy. Ce is displayed as tan (light), O as red (dark).

Appendix D

Supplemental Material for Chapter 6

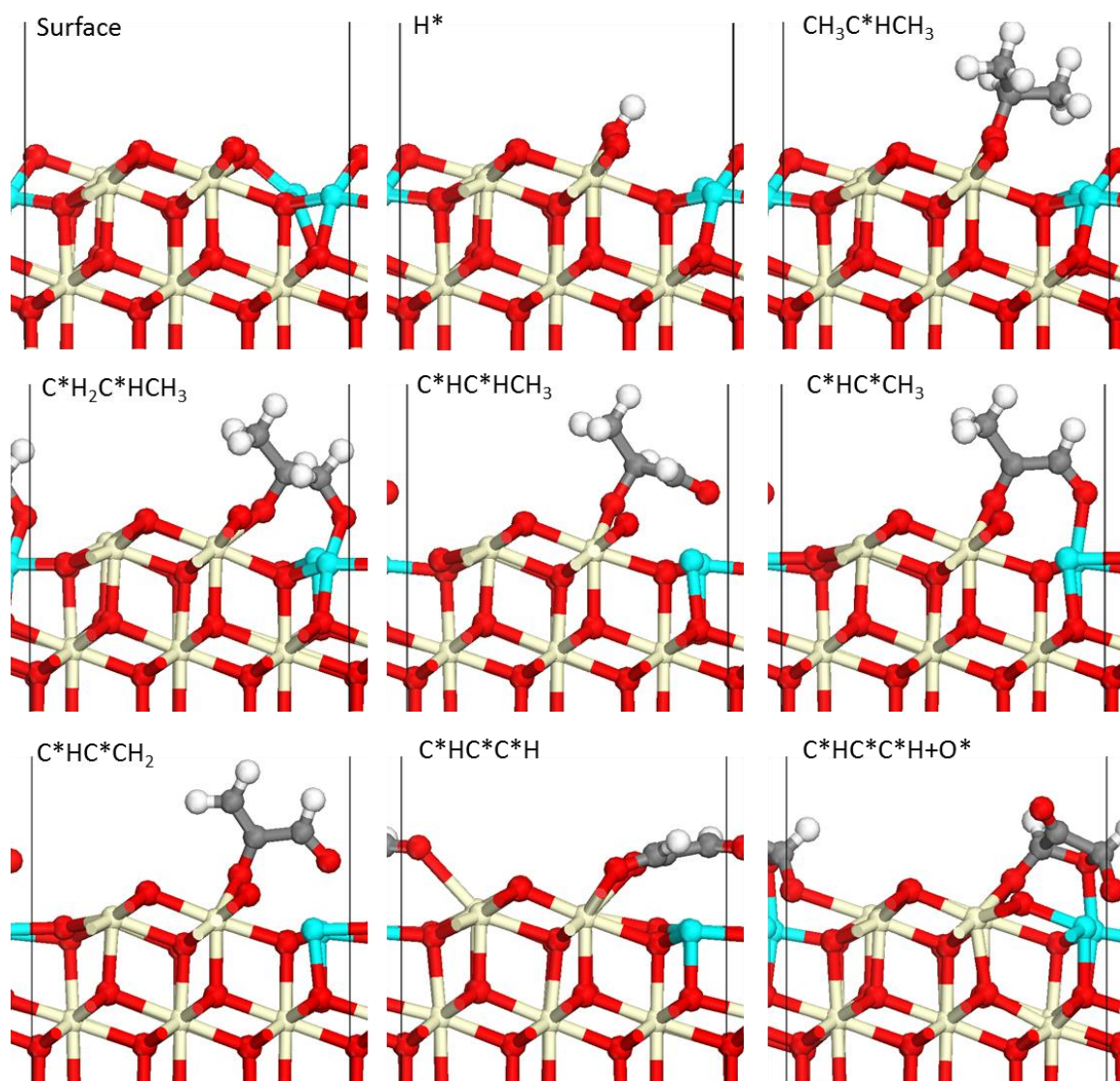


Figure D-1. Structures for the first 9 steps (excluding desorption of H^* as H_2O and refilling of the $\frac{1}{2} V_{\text{O}}$) to reform propane in an oxidizing environment. Ce is displayed as tan (light), Zr as light blue (gray), O as red (dark).

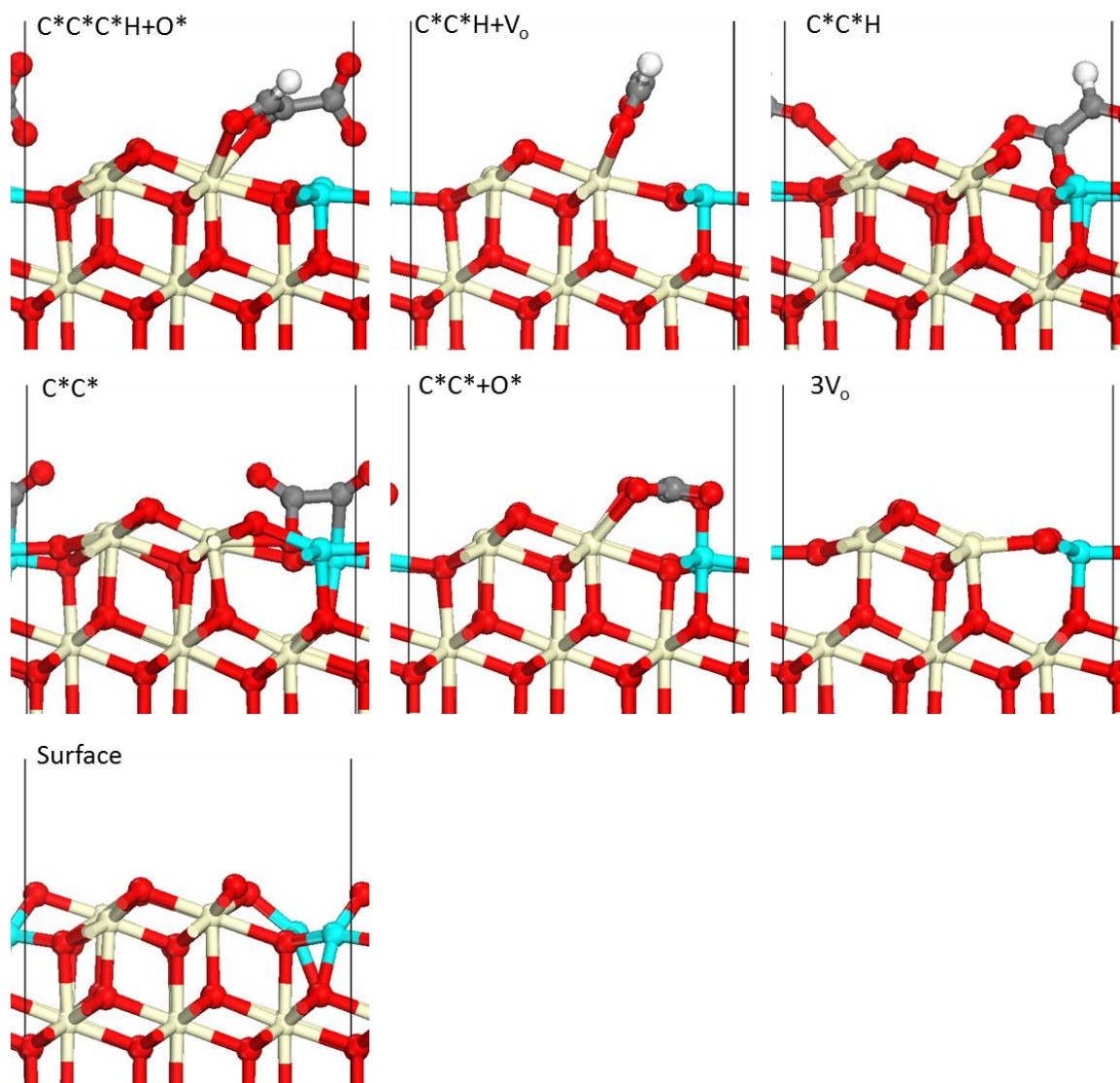


Figure D-2. Structures for the last 7 steps (excluding desorption of H^* as H_2O and refilling of the $\frac{1}{2} V_o$) to reform propane in an oxidizing environment. Ce is displayed as tan (light), Zr as light blue (gray), O as red (dark).

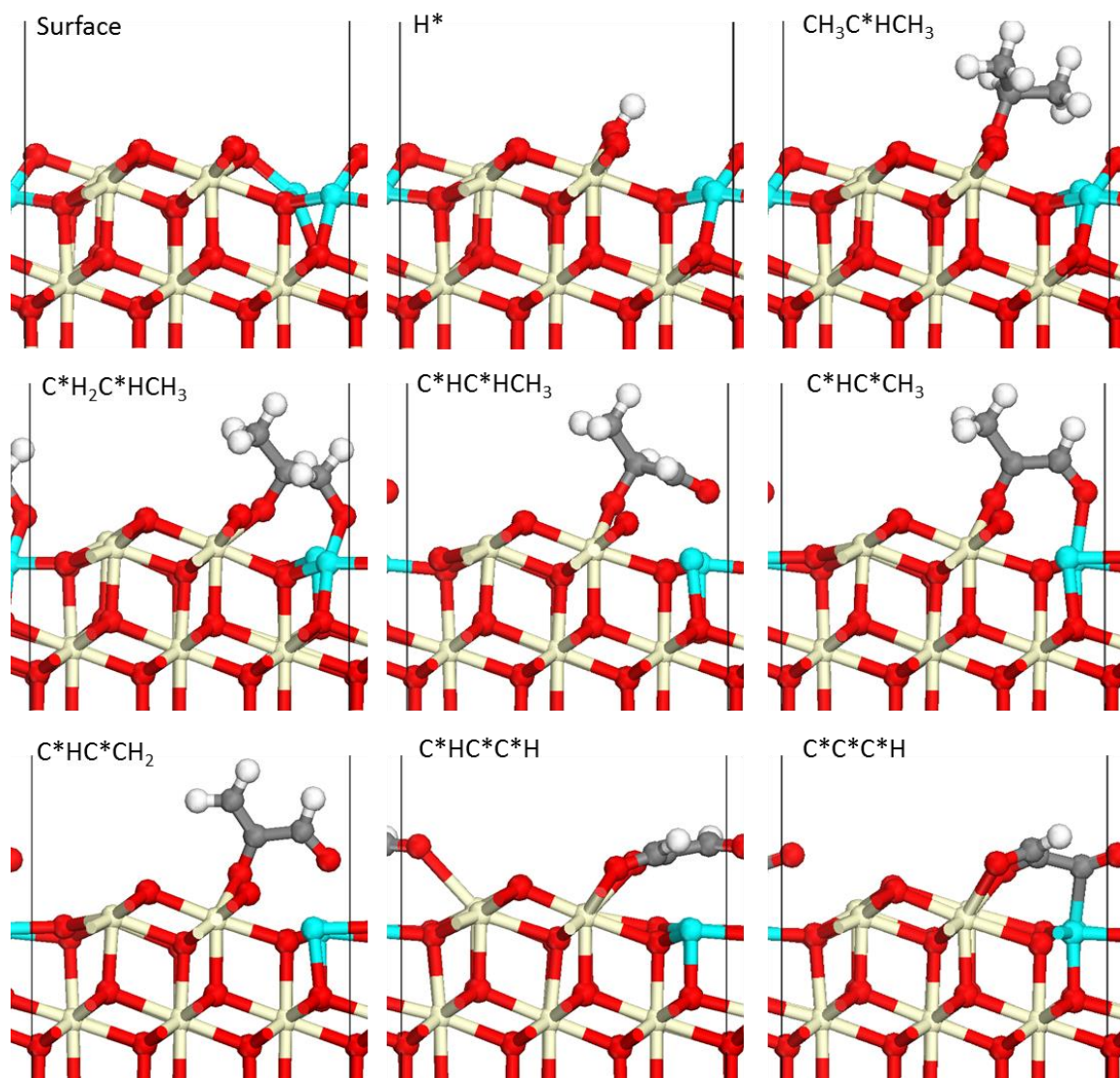


Figure D-3. Structures for the first 9 steps (excluding desorption of H^* as H_2O and refilling of the $\frac{1}{2} V_O$) to reform propane in a reducing environment. Ce is displayed as tan (light), Zr as light blue (gray), O as red (dark).

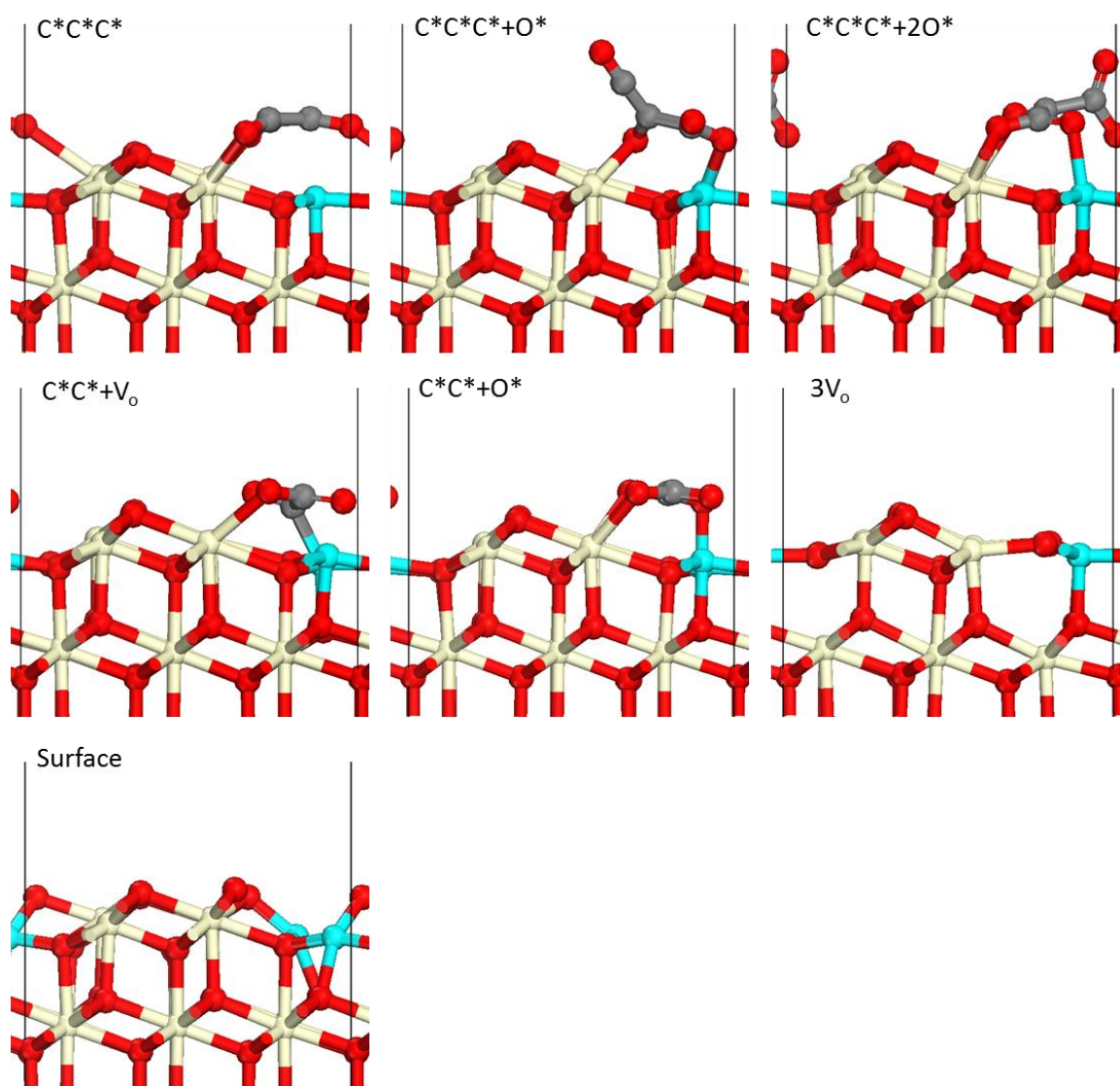


Figure D-4. Structures for the last 7 steps (excluding desorption of H^* as H_2O and refilling of the $\frac{1}{2} V_o$) to reform propane in a reducing environment. Ce is displayed as tan (light), Zr as light blue (gray), O as red (dark).

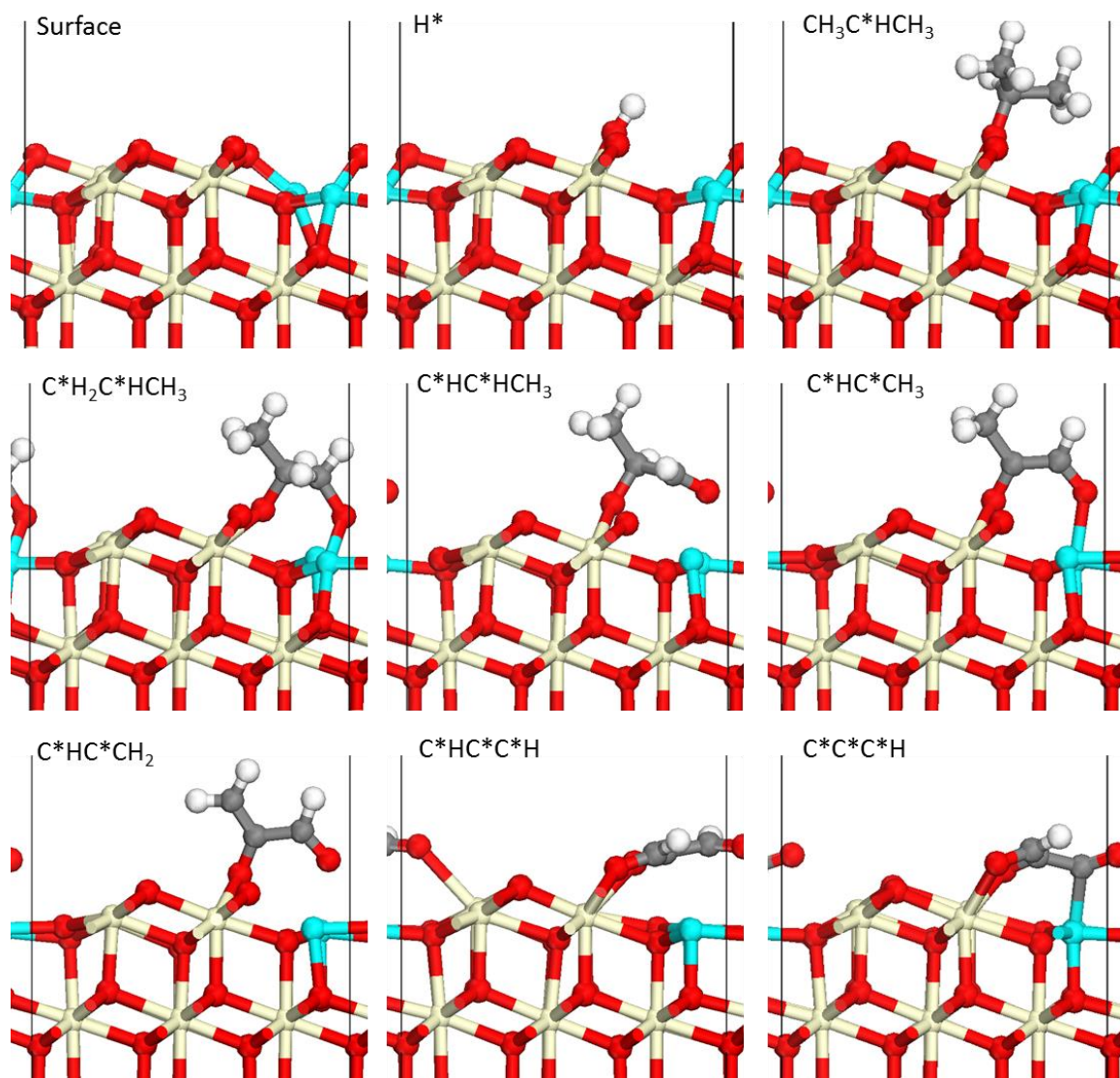


Figure D-5. Structures for the first 9 steps (excluding desorption of H* as H₂O and refilling of the 1/2 V_O) to reform propane under extremely reducing (gasifier effluent) conditions. Ce is displayed as tan (light), Zr as light blue (gray), O as red (dark).

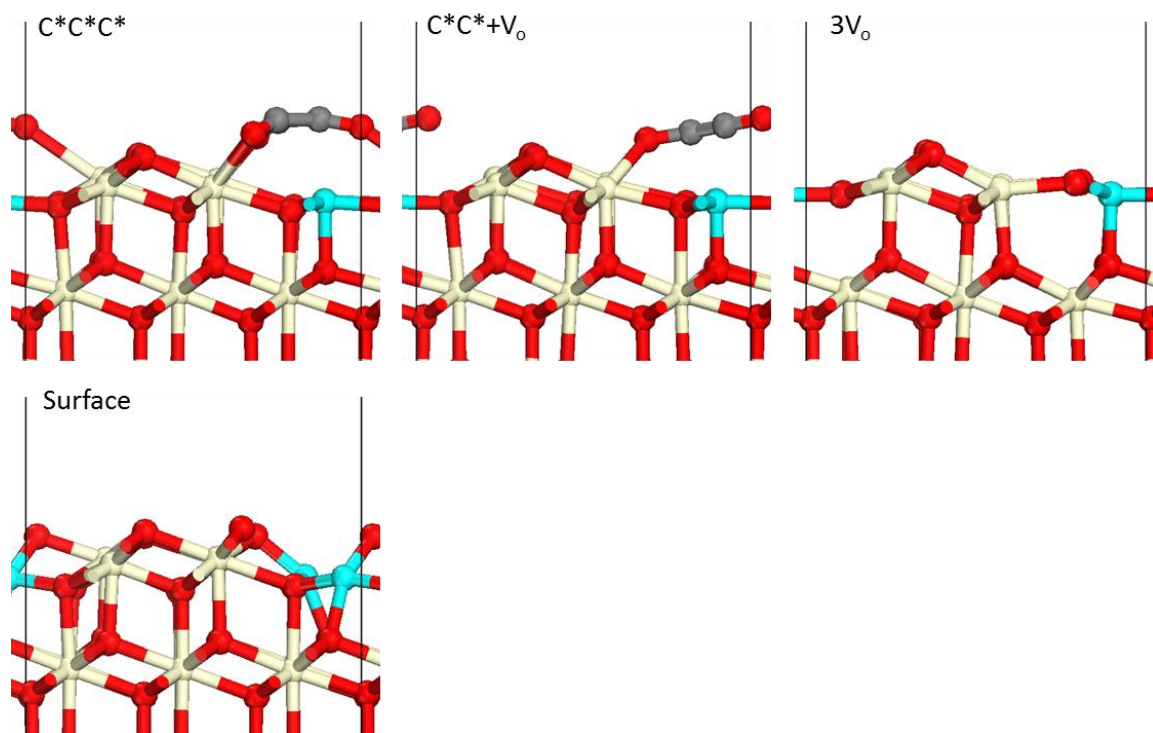


Figure D-6. Structures for the last 4 steps (excluding desorption of H* as H₂O and refilling of the $\frac{1}{2} V_o$) to reform propane under extremely reducing (gasifier effluent) conditions. Ce is displayed as tan (light), Zr as light blue (gray), O as red (dark).

Appendix E

Supplemental Material for Chapter 8

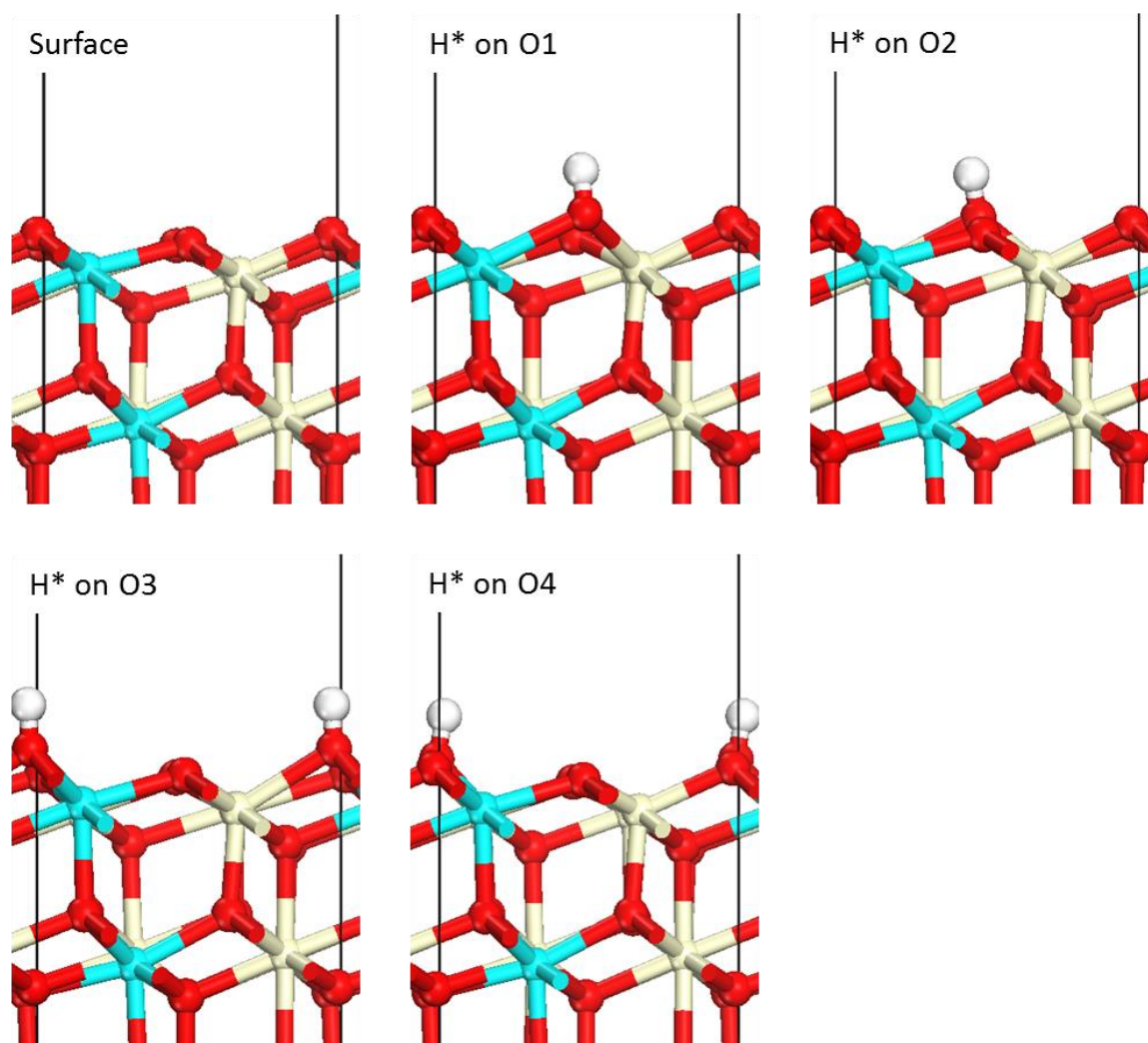


Figure E-1. Structures of the adsorption of H* onto the 4 surface oxygens in the un-sulfided surface of M-doped CeO₂. Ce is displayed as tan (light), M as light blue (gray) and O as red (dark).

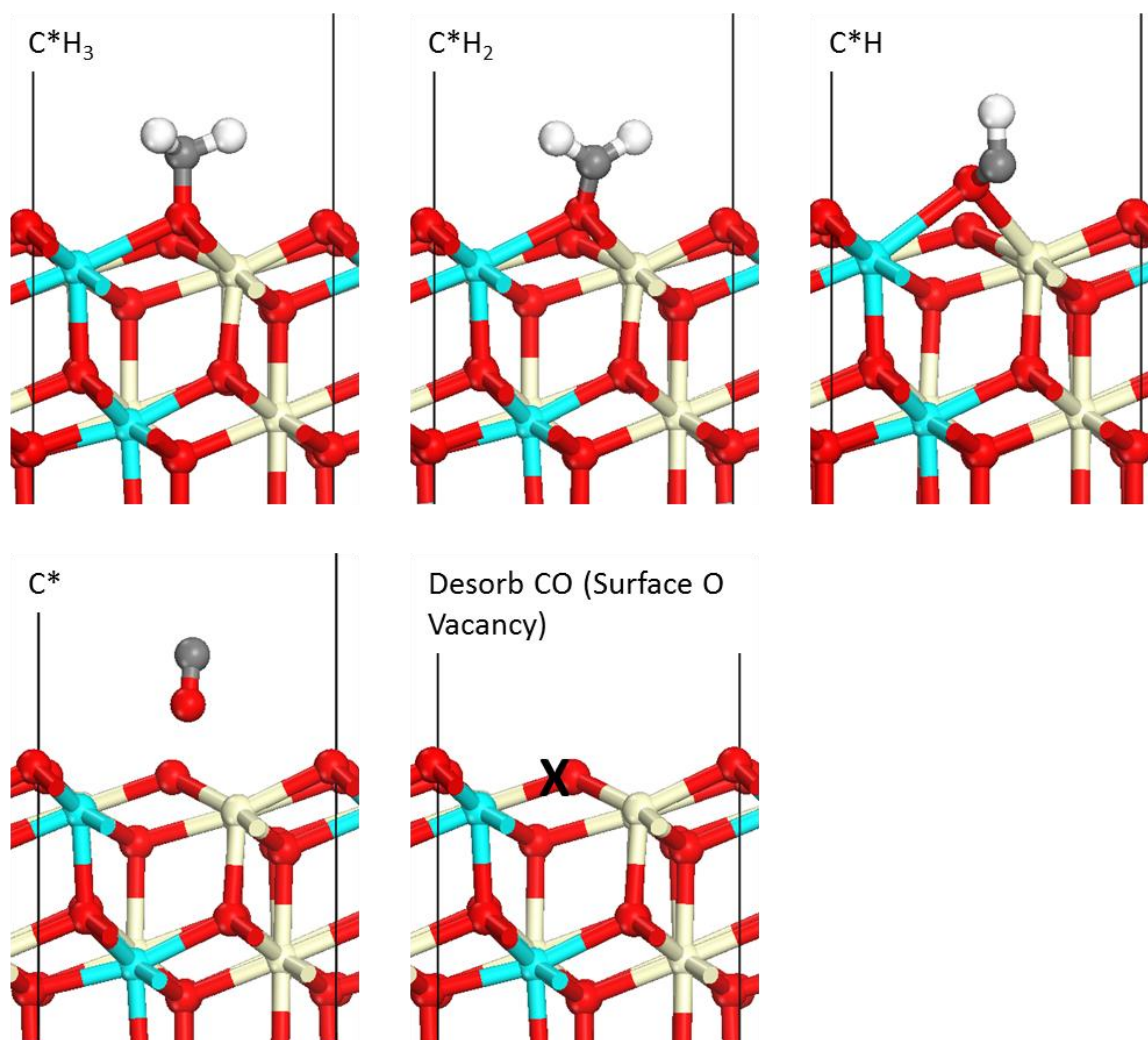


Figure E-2. Structures of the reforming of methane on the un-sulfided surface of M-doped CeO₂. Ce is displayed as tan (light), M as light blue (gray) and O as red (dark). The X represents the position of the additional surface oxygen vacancy.

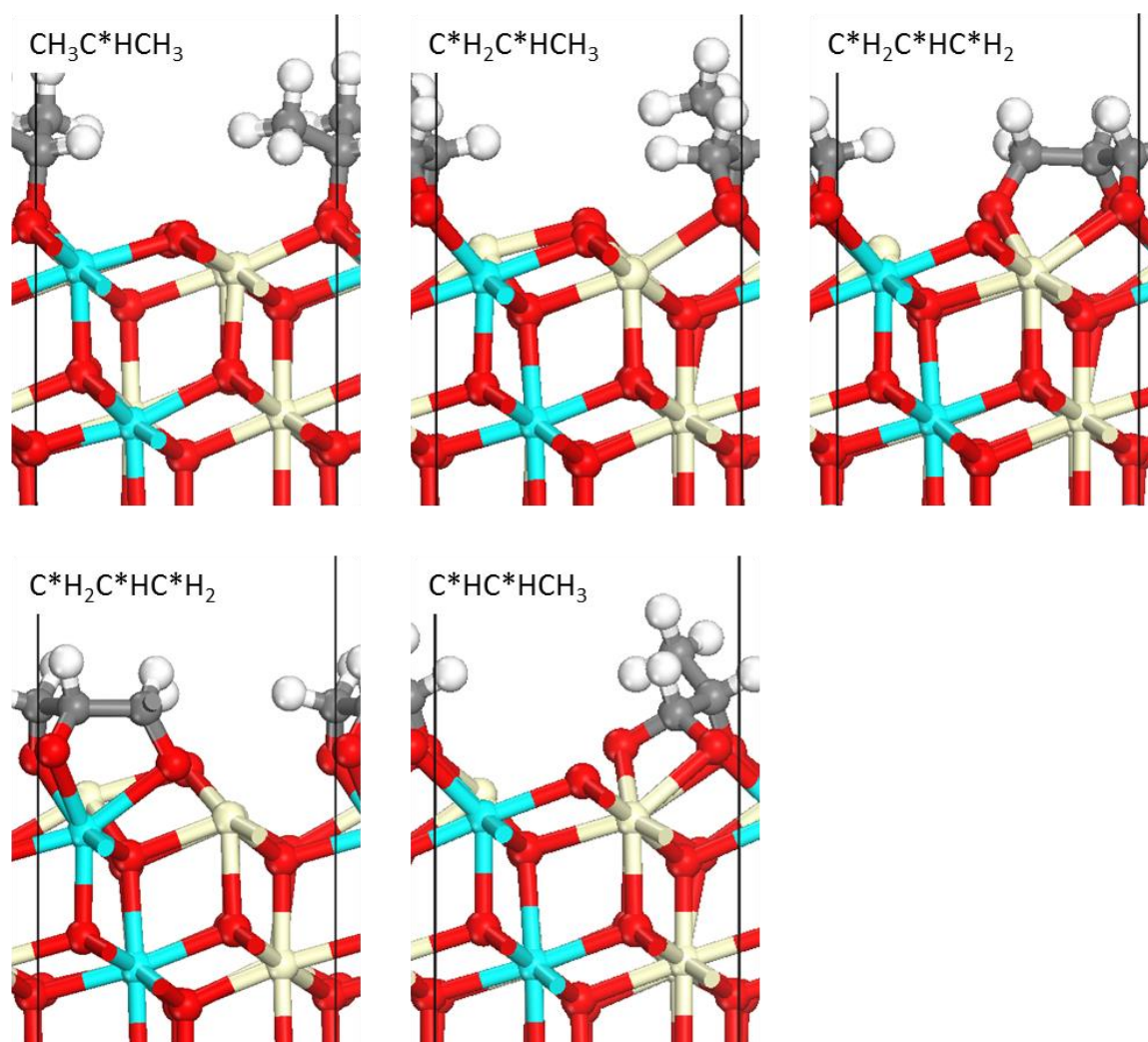


Figure E-3. Structures of the first three steps in the reforming of propane on the un-sulfided surface of M-doped CeO₂. Ce is displayed as tan (light), M as light blue (gray) and O as red (dark).

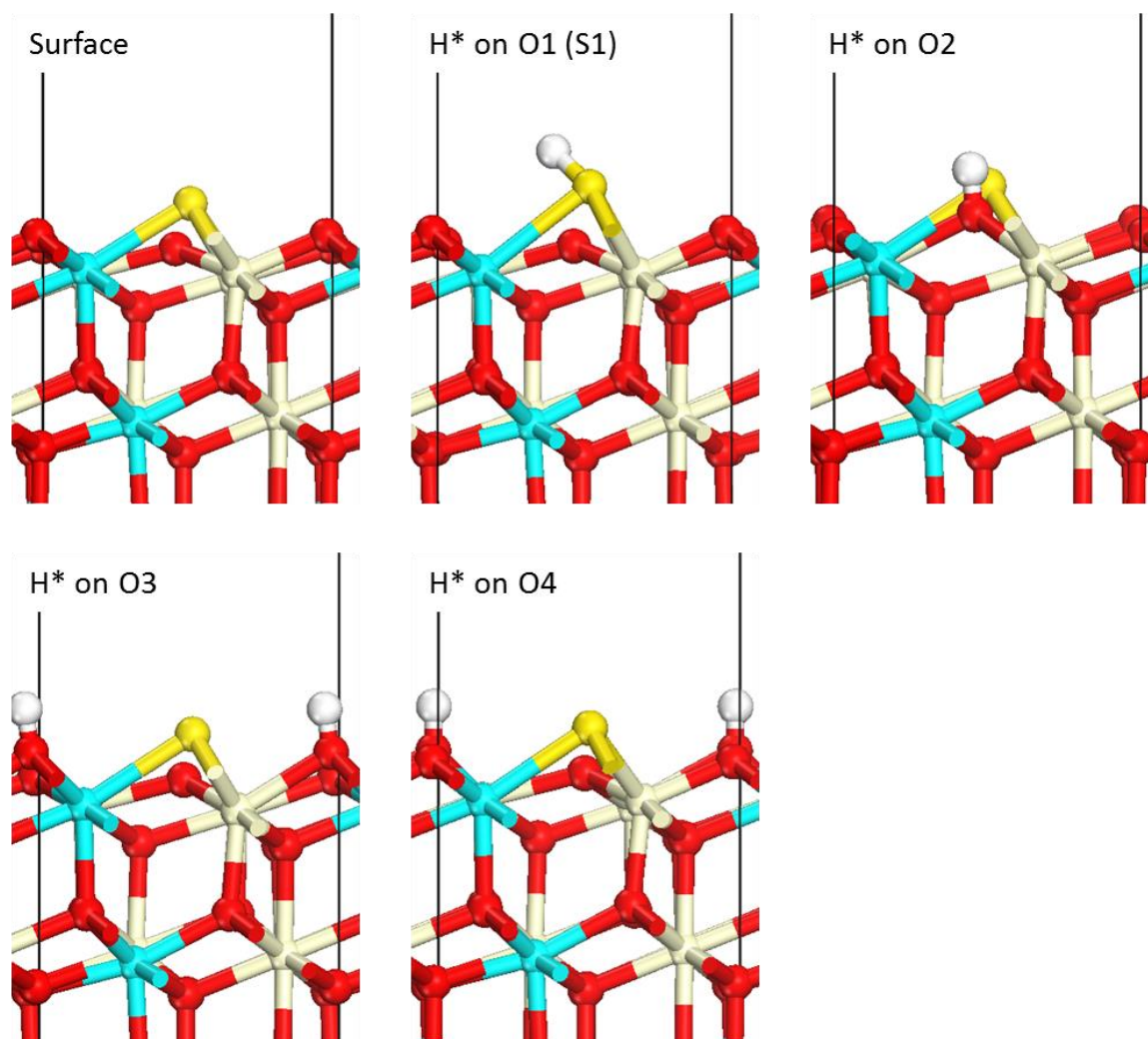


Figure E-4. Structures of the adsorption of H* onto the 4 surface oxygens in the sulfided surface of M-doped CeO₂. Ce is displayed as tan (light), M as light blue (light gray), O as red (dark) and S as yellow (dark gray).

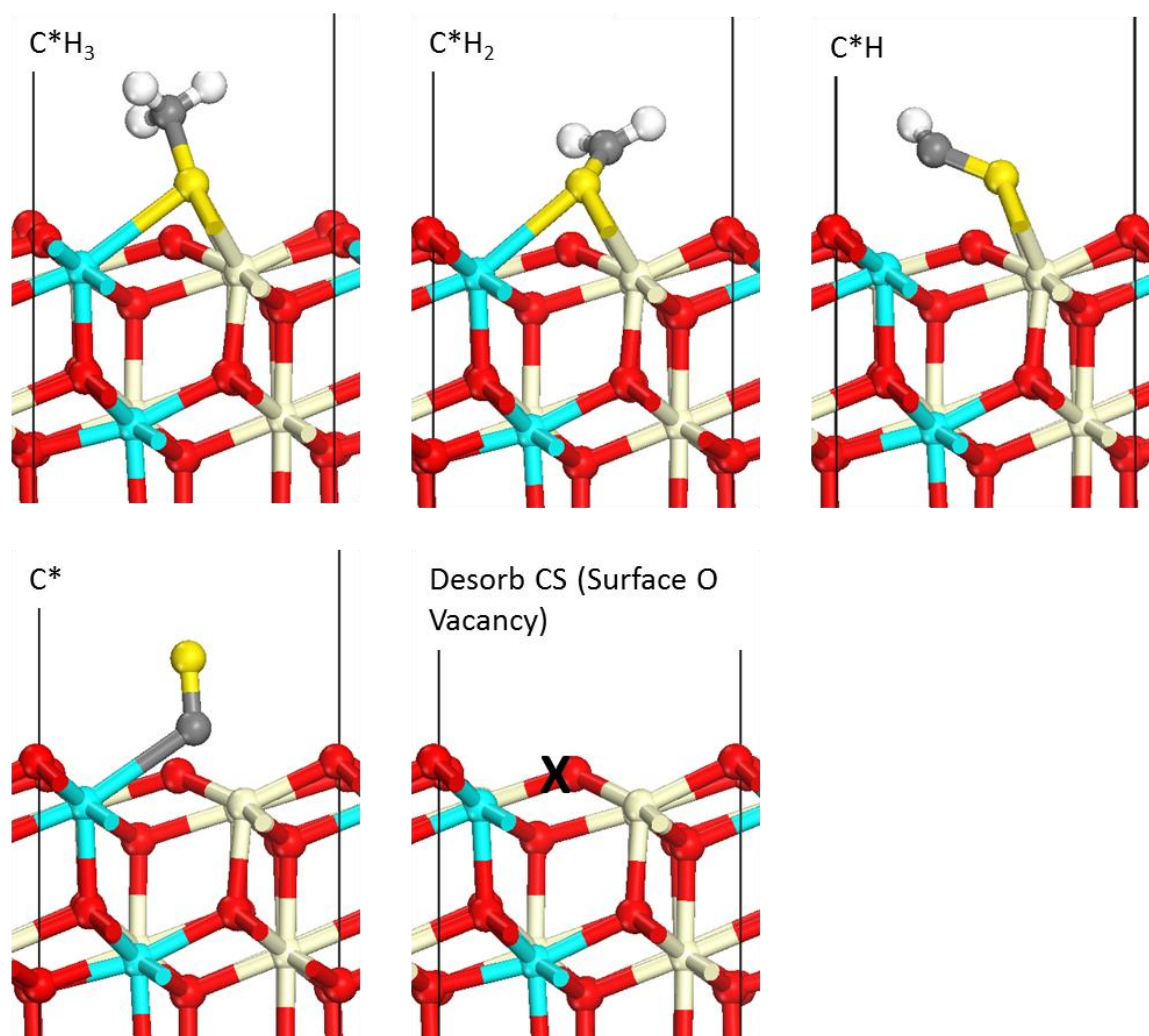


Figure E-5. Structures of the reforming of methane on the sulfided surface of M-doped CeO₂. Ce is displayed as tan (light), M as light blue (light gray), O as red (dark) and S as yellow (dark gray). The X represents the position of the additional surface oxygen vacancy.

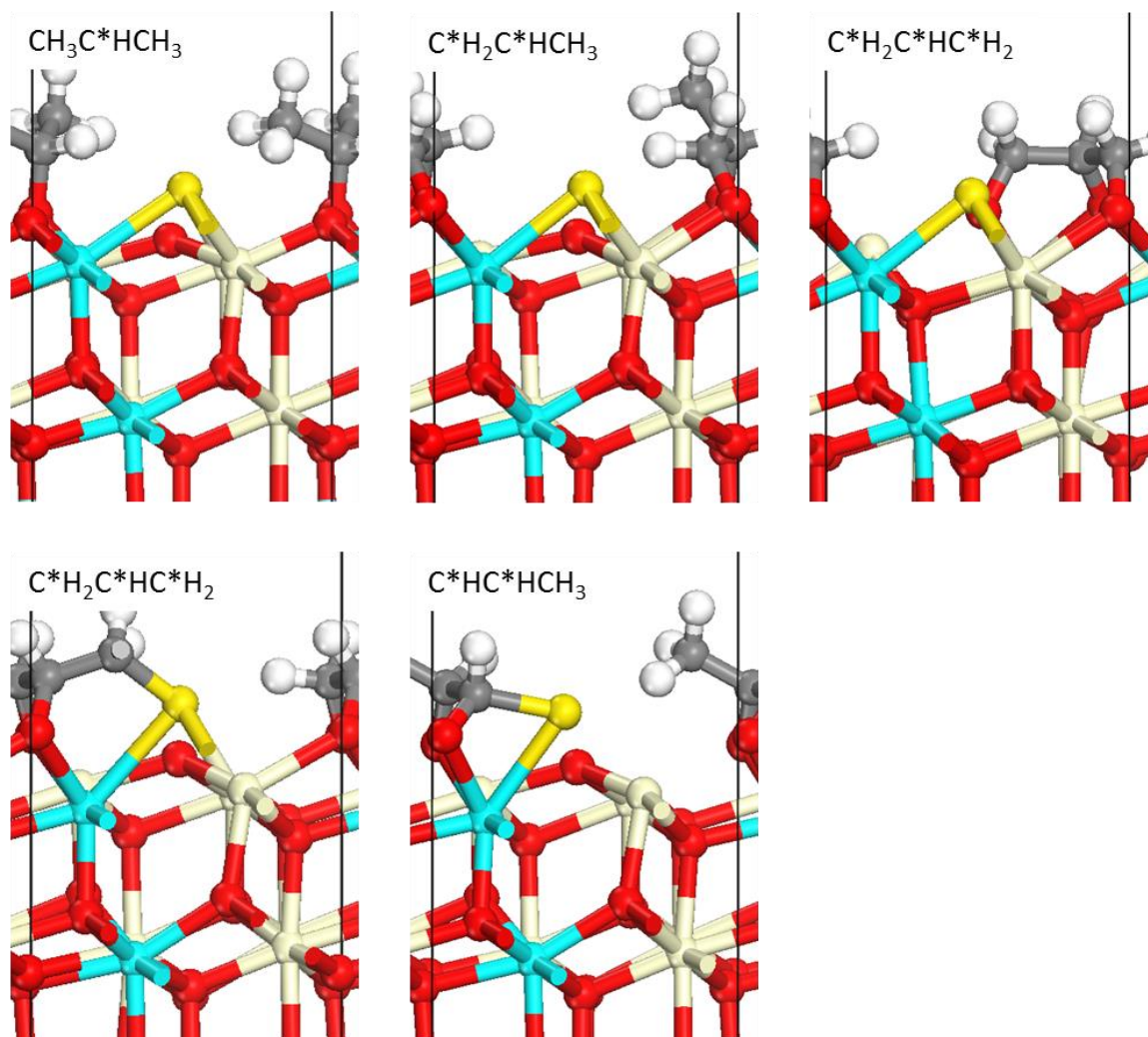


Figure E-6. Structures of the first three steps in the reforming of propane on the sulfided surface of M-doped CeO₂. Ce is displayed as tan (light), M as light blue (light gray), O as red (dark) and S as yellow (dark gray).

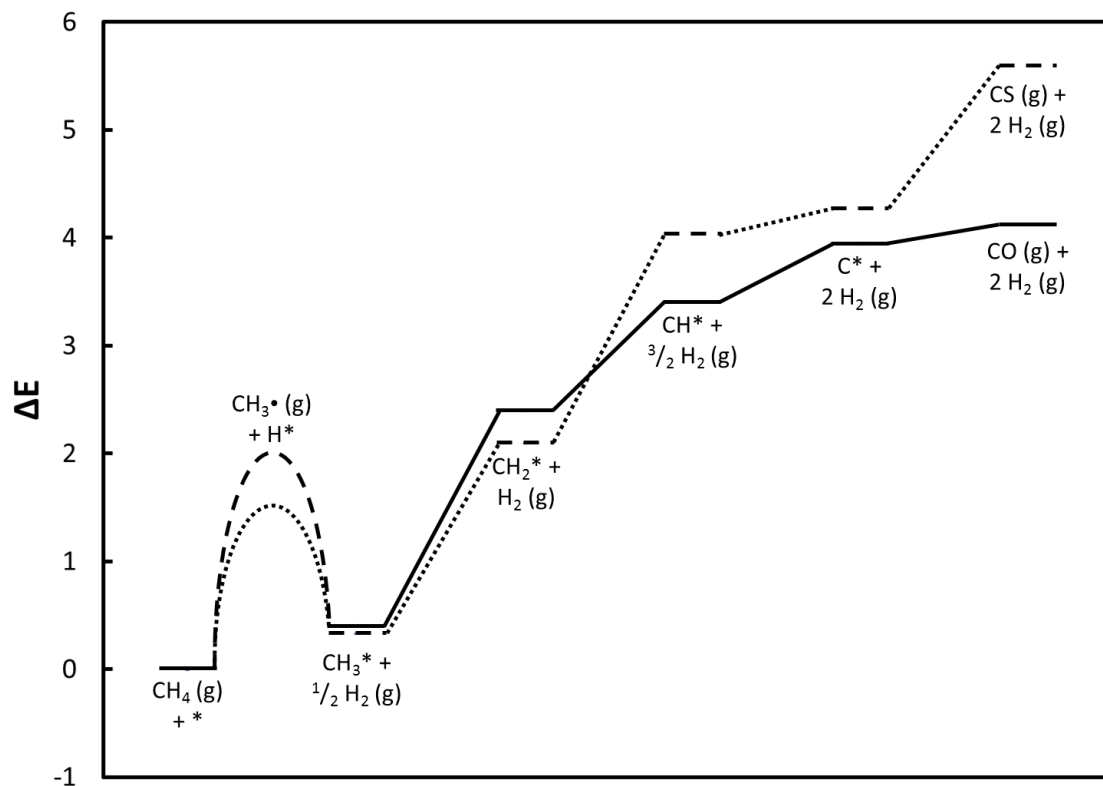


Figure E-7. Reaction energy diagram of methane decomposition over sulfided and un-sulfided surfaces of La-doped CeO_2 (1 1 1). The solid lines represent each hydrogen abstraction (product desorption) on the un-sulfided surface and the dashed lines for the sulfided surface. For the pseudo-transition state ($\text{CH}_3\cdot + \text{H}^*$), the long dash represents H abstraction on a sulfur atom and the short dash represents on an oxygen atom.

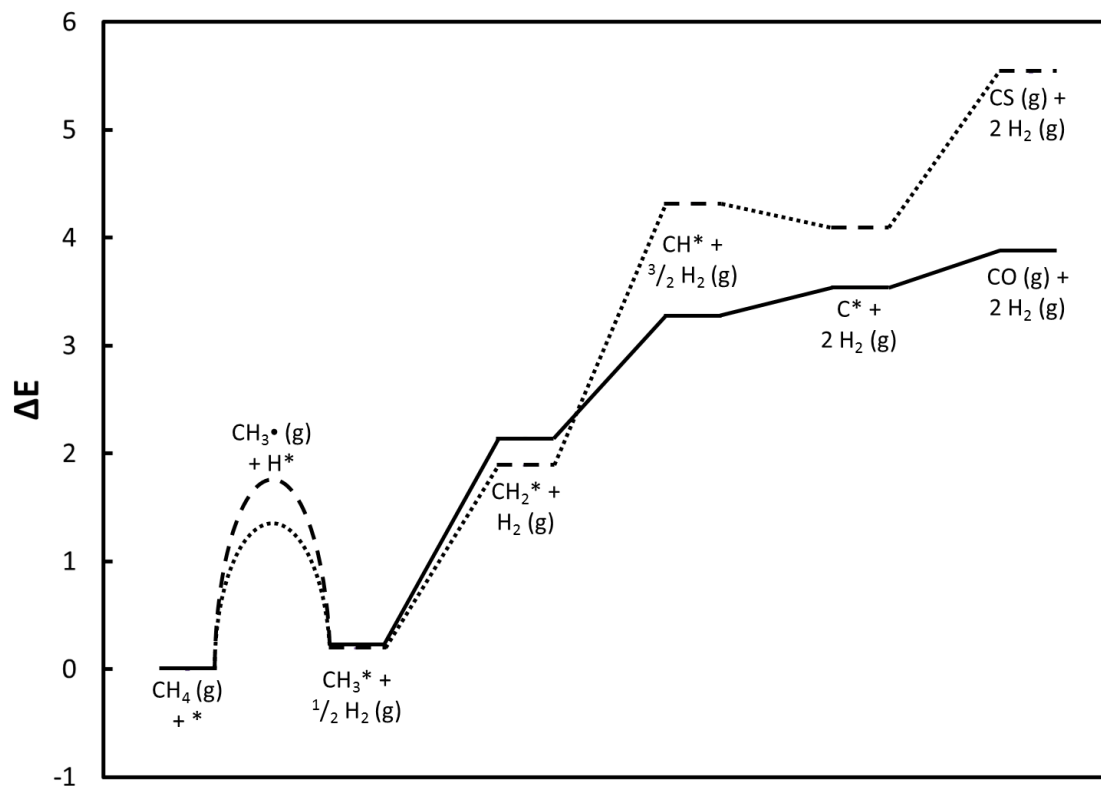


Figure E-8. Reaction energy diagram of methane decomposition over sulfided and un-sulfided surfaces of Tb-doped CeO_2 (1 1 1). The solid lines represents each hydrogen abstraction (product desorption) on the un-sulfided surface and the dashed lines for the sulfided surface. For the pseudo-transition state ($\text{CH}_3\cdot + \text{H}^*$), the long dash represents H abstraction on a sulfur atom and the short dash represents on an oxygen atom.

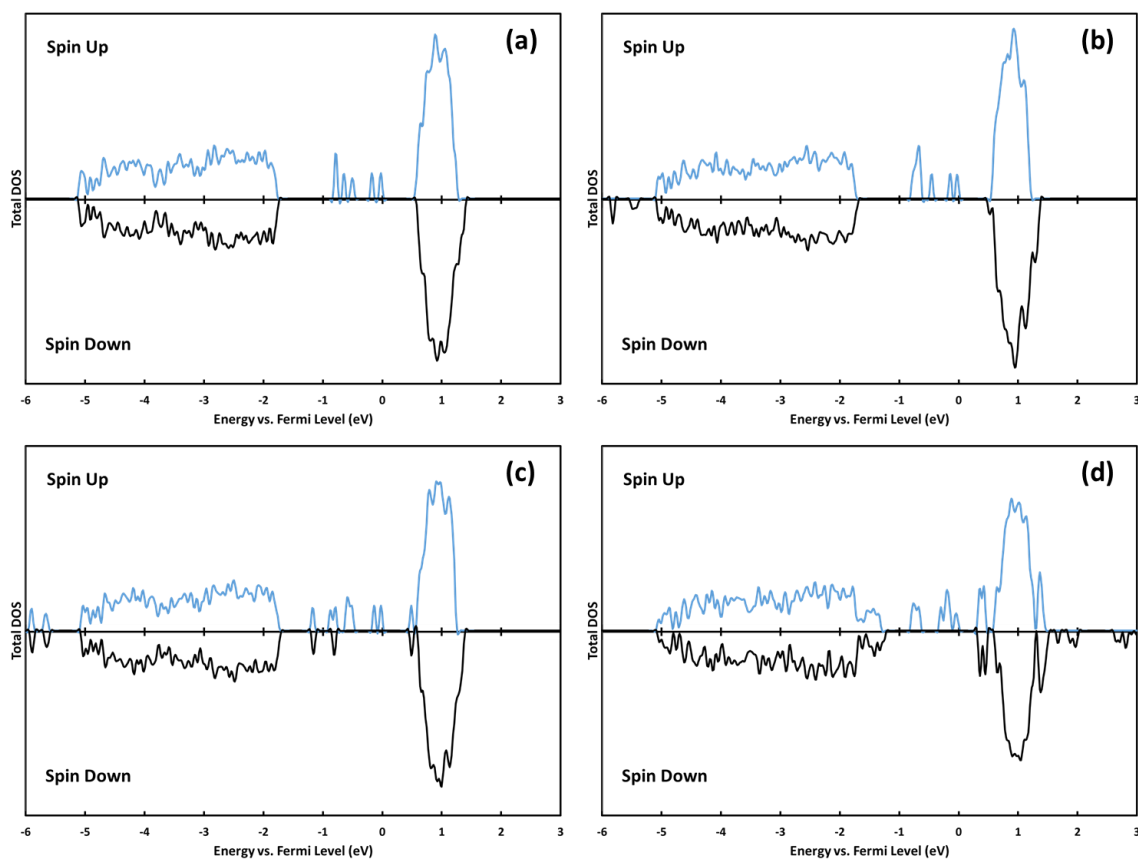


Figure E-9. Total density of states (DOS) plotted versus energy (referenced to Fermi level) for (a) C*H₃, (b) C*H₂, (c) C*H, and (d) C* on the un-sulfided pure CeO₂ (1 1 1) surface. Spin-down density of states is plotted on the negative y axis. All reduced cerium atoms have a spin-up *f* electron, and any spin paired states below the Fermi level and above the valence band are associated with electrons on the carbon atom.

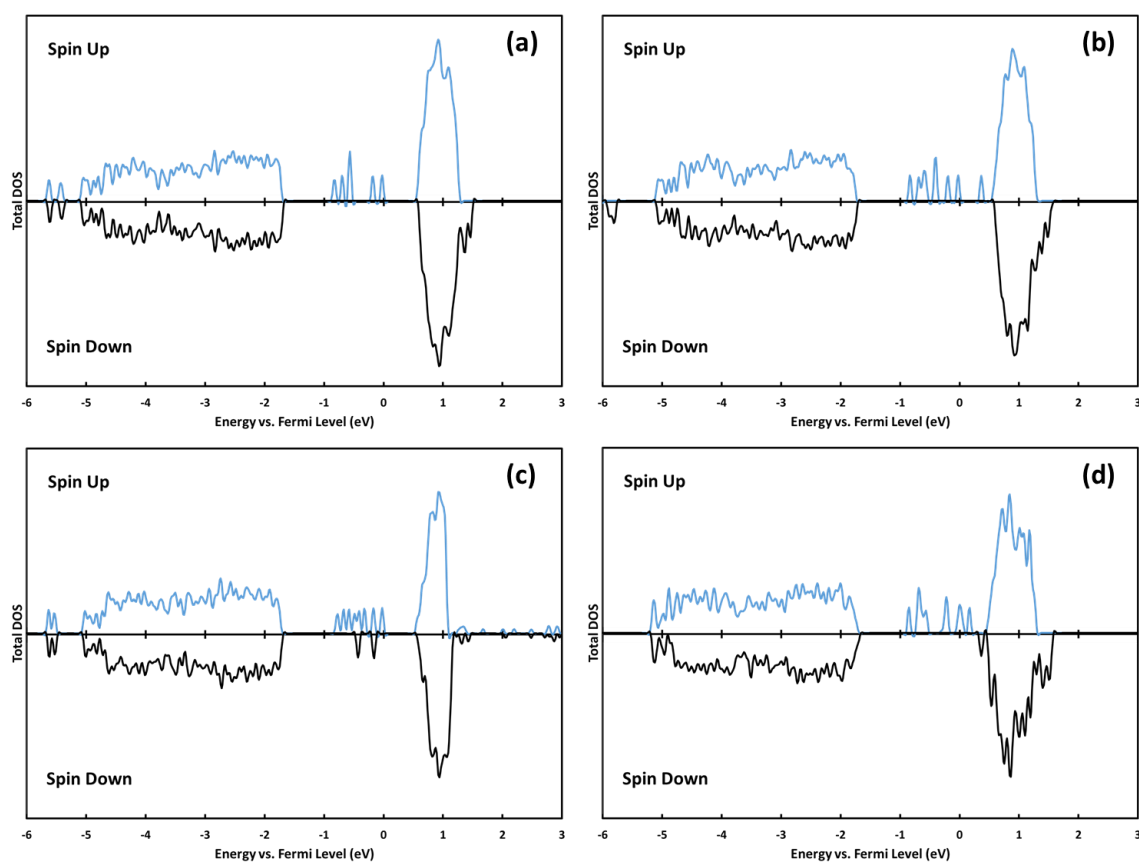


Figure E-10. Total density of states (DOS) plotted versus energy (referenced to Fermi level) for (a) C*H₃, (b) C*H₂, (c) C*H, and (d) C* on the sulfided pure CeO₂ (1 1 1) surface. Spin-down density of states is plotted on the negative y axis. All reduced cerium atoms have a spin-up *f* electron, and any spin paired states below the Fermi level and above the valence band are associated with electrons on the carbon atom.

VITA

Matthew D. Krcha

Education

B.S. Chemical Engineering – Clarkson University 2010

Ph.D. Chemical Engineering – The Pennsylvania State University 2014

Honors and Awards

Featured on the cover of the first issue of International Journal of Quantum Chemistry (2014)

Outstanding Chemical Engineering Teaching Assistant Award (2013)

Second place for best presentation for Center for Atomic Level Design Theory Day at Georgia Tech (2012)

Clarkson University Achievement Award Scholarship (2006)

Publications

1. **M. D. Krcha**, A. D. Mayernick, M. J. Janik. “Periodic trends of oxygen vacancy formation and C-H bond activation over transition metal-doped CeO₂ (1 1 1) surfaces” *Journal of Catalysis* 293 (2012) 103-115.
2. R. Li, **M. D. Krcha**, M. J. Janik, A. D. Roy, K. M. Dooley. “Ce-Mn oxides for high-temperature gasifier effluent desulfurization” *Energy & Fuels* 26 (2012) 6765-6776.
3. **M. D. Krcha**, M. J. Janik. “Examination of oxygen vacancy formation in Mn-doped CeO₂ (1 1 1) using DFT+*U* and the hybrid functional HSE06” *Langmuir* 29 (2013) 10120-10131.
4. **M. D. Krcha**, M. J. Janik. “Challenges in the use of density functional theory to examine catalysis by M-doped ceria surfaces” *International Journal of Quantum Chemistry* 114 (2014) 8-13.
5. **M. D. Krcha**, M. J. Janik. “Catalytic propane reforming mechanism over Zr-doped CeO₂ (1 1 1)” *Catalysis Science & Technology* (2014) DOI: 10.1039/C4CY00619D.